Dissertation
submitted to the
Combined Faculties of the Natural Sciences and Mathematics
of the Ruperto-Carola-University of Heidelberg, Germany
for the degree of
Doctor of Natural Sciences

Put forward by
Dipl.-Phys. Diana Nanova
Born in Sofia, Bulgaria

Oral examination: 29. 04. 2015

Intermolecular Ordering in Organic Semiconductor Layers and its Correlation to Electronic Properties

Referees: Prof. Dr. Wolfgang Kowalsky
Prof. Dr. Albrecht Winnacker

Zusammenhang zwischen Struktur und elektronischen Eigenschaften organischer Halbleiterschichten – Im Rahmen dieser Arbeit wird der Einfluss der Morphologie organischer Halbleiter auf ihre elektronischen Eigenschaften mittels analytischer Transmissionselektronenmikroskopie (TEM) untersucht. Dabei werden erstmalig die dielektrischen Eigenschaften organischer Halbleiter aus Elektronenenergieverlustspektroskopie bestimmt. Eine gefundene Korrelation zwischen Elektronendiffraktion und Stromtransienten-Messungen zeigt, dass die semikristalline Struktur des flüssigprozessierten Polymers Poly(3-hexylthiophen) zu einem anisotropen Ladungstransport führt. Des Weiteren werden die Struktureigenschaften co-verdampfter Heterostrukturen, bestehend aus kleinen Molekülen von fluoriertem Zinkphtalocyanin (F_4ZnPc) und Fullerenen (C_{60}), auf unterschiedlichen Substraten analysiert. Mittels energiegefilterter TEM wird gezeigt, dass das Heizen des Substrates auf 100 °C während des Aufdampfens zu Fullerenagglomeration führt. Diese Fullerenagglomerate sind weitestgehend amorph, sofern die Heterostruktur auf einem F_4ZnPc Untergrund aufgedampft wird, der typisch für nicht invertierte Solarzellenstrukturen ist. Im Gegensatz hierzu ist auf einem C_{60}-Untergrund, der in invertierten Solarzellen Anwendung findet, eine hohe Ordnung innerhalb der Agglomerate zu beobachten. Aus der elektrischen Charakterisierung von Solarzellen wird deutlich, dass die kristallinen C_{60}-Domänen zu einer verbesserten Ladungstrennung und einer höheren Bauteileffizienz führen. Somit kann im Rahmen dieser Arbeit erstmals nachgewiesen werden, warum Rekordeffizienzen nur in invertierter Bauteilstruktur kleiner Molekülsolarzellen erreicht werden.

Intermolecular Ordering in Organic Semiconductor Layers and its Correlation to Electronic Properties – This thesis examines the influence of the morphology of organic semiconductors on their electronic properties using analytical transmission electron microscopy (TEM). For the first time, the dielectric properties of organic materials are derived from electron energy loss spectroscopy. A correlation between electron diffraction and current transient measurements of the solution processed polymer poly(3-hexylthiophene) indicates that the semicrystalline structure of the polymer leads to anisotropic charge transport. The study further investigates the structural properties of co-evaporated small molecule blends of fluorinated zincphtalocyanine (F_4ZnPc) and fullerene (C_{60}) on different substrates. Energy filtered TEM reveales strong fullerene agglomeration for all substrates considered here, which is shown to be facilitated by an elevated substrate temperature (100 °C). These agglomerates are still largely amorphous if the blend is grown on a pristine F_4ZnPc layer as required for non-inverted solar cells. However, on an underlying C_{60}-layer, as is typically used for inverted devices, a pronounced order of the fullerene is observed. Device characterization indicates that the highly pure and crystalline C_{60} domains improve free charge carrier generation and solar cell efficiency. This thesis therefore provides a novel explanation why record efficiencies in small molecule solar cells are only achieved in inverted devices.

Contents

1. Introduction **1**

2. Theoretical Fundamentals **5**
2.1. Fundamentals of Organic Semiconductors 5
2.1.1. Basics of Organic Solar Cells 6
2.1.2. Solar Cell Characteristics 9
2.1.3. Charge Transport in Organic Semiconductors 12
2.1.4. Phase Separation in Molecular Crystals 13
2.2. Electron Interaction with Matter 14

3. Experimental Details **21**
3.1. Transmission Electron Microscopy (TEM) 21
3.1.1. Bright-Field Mode 21
3.1.2. Electron Diffraction 23
3.2. Analytical TEM 24
3.2.1. Electron Energy Loss Spectroscopy (EELS) 24
3.2.1.1. Deconvolution 26
3.2.1.2. Kramers-Kronig-Relation 28
3.2.2. Electron Spectroscopic Imaging 31
3.2.2.1. ESI Series 32
3.2.2.2. Data Analysis 33
3.3. Charge Carrier Mobility Measurements 35
3.3.1. Charge Extraction by Linear Increasing Voltage 35
3.3.2. Field-Effect Mobilities 36

4. Organic Semiconductors and Sample Preparation **39**
4.1. Materials 39
4.2. Devices 42
4.2.1. P3HT Diodes 42
4.2.2. P3HT Transistors 42
4.2.3. Small Molecule Solar Cells 43

4.3. TEM Sample Preparation 44
4.3.1. Floating 44
4.3.2. Cross-Sections by Focused Ion Beam Milling 45

5. Preparatory Study on Beam Damage: Polymers vs. Small Molecules 49

6. Correlation between Structural and Electronic Properties of P3HT Thin Films 57
6.1. State of the Art 57
6.2. Structural Properties of Pure P3HT Layers from TEM Measurements 59
6.2.1. Annealing 59
6.2.2. Molecular Weight Dependence 65
6.2.3. Conclusion: P3HT Structure 70
6.3. Electrical Characterization of P3HT Devices 71
6.3.1. Mobilities Extracted from CELIV Measurements 71
6.3.2. Field-Effect Mobilities 73
6.3.3. Conclusion: Charge Carrier Mobilities 77
6.4. Discussion: Crystallinity Impact on Charge Carrier Mobilities 77
6.5. Structural Properties of P3HT Doped with F_4TCNQ from TEM Measurements 80
6.5.1. Electron Diffraction 80
6.5.2. EELS and Energy Filtered TEM 83
6.5.3. Conclusion: TEM Measurements 88
6.6. Charge Transfer Determined by Infrared Spectroscopy 88
6.6.1. Conclusion: Infrared Spectroscopy 93
6.7. Discussion: Crystallinity Impact on Charge Transfer 94

7. The Decisive Role of Active Layer Morphology for Solar Cell Performance 97
7.1. State of the Art 97
7.2. TEM Measurements on Small Molecule OPV Cells: F_4ZnPc:C_{60} 100
7.2.1. Pristine F_4ZnPc Layers Grown at Different Temperatures 101
7.2.2. Pristine C_{60} Layers Grown at Different Temperatures . 108
7.2.3. F_4ZnPc:C_{60} Blends Deposited on Different Substrates at Varied Temperatures 115
7.2.3.1. EELS 115
7.2.3.2. Energy Filtered TEM 119

7.2.3.3. ESI Series 123
7.2.3.4. Plasmon Peak Map 126
7.2.3.5. Electron Diffraction 134
7.2.4. Conclusion: TEM Measurements 137
7.2.5. Correlation to Structural Properties Obtained by Infrared Spectroscopy 138
7.3. I-V Characteristics of F_4ZnPc:C_{60} Solar Cells 140
7.3.1. Non-inverted vs. Inverted Devices 141
7.3.2. Conclusion: Device Characteristics 143
7.4. Discussion: Structure-Function-Relationship 144
7.5. Proposed Model for the Solar Cell Functionality Based on Structural and Electronic Properties 149

8. Conclusion and Outlook **151**

A. Appendix **155**

Bibliography **161**

B. Journal Publications, Conference Presentations, Supervised Theses **189**

List of Abbreviations

TEM:	Transmission electron microscopy
EFTEM:	Energy filtered TEM
BFTEM:	Bright-field TEM
EELS:	Electron energy loss spectroscopy
ESI.	Electron spectroscopic imaging
BHJ:	Bulk heterojunction
P3HT:	Poly(3-hexylthiophen)
F_4ZnPc:	Fluorinated zincphtalocyanine
C_{60}:	Buckminster fullerene
PCE:	Power conversion efficiency
CELIV;	Charge extraction by linear increasing voltage
FFT:	Fast-Fourier-Transformation
IR:	Infrared
F_4TCNQ:	2,3,5,6-Tetrafluoro-7,7,8,8-tetracynoquinodimethane
PEDOT:PSS:	Poly(3,4-ethylenedioxythiophene):poly-(styrenesulfonate)
RT:	Room temperature
HOMO:	Highest occupied molecular orbital
LUMO:	Lowest unoccupied molecular orbital
OFET:	Organic field-effect transistor
CT:	Charge transfer

1. Introduction

The development of inorganic semiconductor technology is, beyond doubt, amongst the most significant technological accomplishments of the 20th century. Through their countless applications in solar cells, light emitting diodes (LED) or transistors, inorganic semiconductors have become an indispensable part of the information age. However, the fairly complex production process of inorganic semiconductors, often silicon-based, still requires high temperatures and extensive cleaning procedures for material purity. Hence, a more versatile and less costly technology is demanded, and organic semiconductors are considered to be a promising candidate.

While the electroluminescent properties of organic semiconductors were discovered as early as in the 1960s [1], for a long time they remained confined to the realm of fundamental research. This changed only after the discovery of the conducting polymer polyacetylene by Heeger et al. [2]. Ever since, and in particular in reaction to their first applications in LEDs (OLEDs) and solar cells (OPVs) in the mid 1980s [3, 4], organic semiconducting materials have undergone a remarkable development. In part due to their low power consumption and color fastness, OLEDs have been successfully commercialized and are presently used in screens for television sets and mobile devices [5]. Future applications are expected to exploit the potential of organic semiconductors for low temperature processing on various substrates, allowing low-cost manufacturing of lightweight, flexible and transparent electronics. That said, owing to some intrinsic limitations, organic semiconductors cannot be expected to completely replace silicon-based technology, but instead to complement existing technologies and add important innovative components. In conjunction with inorganic semiconductors, high-performance organic materials have the potential to greatly expand the range of possible applications. However, in order to fully exploit the potential of organic materials, a deeper understanding of the fundamental properties is necessary.

One of the pivotal aspects that has not been fully understand yet are the underlying processes of charge transport mechanisms. These properties markedly deviate from those of inorganic semiconductors due to a lack of long-range order in most organic materials. Most unexplained effects reported in the literature are simply attributed to the complex “morphology” of the

organic materials, often without any further specification.

The purpose of this thesis is to directly correlate the morphology with the electronic properties of organic semiconductor devices. In particular, it is specified what is referred to as "morphology" in terms of long- and short-range intermolecular order. For this purpose diverse organic material systems, including polymers and small molecules, which constitute the main material classes in organic semiconductors, are analyzed by advanced analytical methods.

More precisely, in this thesis one of the most prominent semiconducting polymers poly(3-hexylthiophene) (P3HT), which is considered the "work-horse" or the "fruit fly" by the organic electronics community, is investigated [6]. The literature suggests that P3HT exhibits a complex semicrystalline microstructure constituted by crystalline domains, which are surrounded by amorphous regions. Hence, the charge transport properties are strongly affected by the structure both on the macroscopic and intra- and intermolecular scale [6]. Therefore, P3HT is an appropriate model system to study the complex structure-function relationship of polymers. In addition, due to the wide literature that exists on P3HT, it is the ideal candidate to serve as a reference system for the establishment of new experimental techniques for the investigation of charge carrier mobilities. Moreover, doped P3HT is used for novel analytical transmission electron microscopy (TEM) measurements, complemented by infrared spectroscopy, to gain a deeper understanding of solution-doping processes.

In the second part of this thesis, vacuum-deposited organic semiconductors are investigated. Small molecule organic solar cells are still a highly active field of research despite the recent boost of organo-metallic perovskite solar cells [7]. The development of the photo conversion efficiencies (PCE) up to 8.3 % for single junctions [8] and certified 12 % for a multi bulk-heterojunctions (BHJ) stack reported by Heliatek GmbH[1] is impressive. The improved device performance is mainly due to progress in material design, processing and device architecture [9–11]. However, the role of substrate heating during or after BHJ deposition for the active layer morphology and its impact on PCE remains a matter of debate. So far publications have led to mixed results where a clear improvement [12, 13], no change or even a decrease of efficiency is reported [14, 15]. Possible morphological changes upon heat treatment of BHJs comprise the relative orientation of the donor/acceptor molecules, phase separation and ordering in pure phase-separated regions [15–17]. The possible influence of device architecture (e.g. the underlying layer) on BHJ

[1] Pressrelease 2013, http://www.heliatek.com

morphology and crystallization has so far not been considered in the literature and is one of the main aspects investigated in this thesis. Here, the effect of substrate heating is shown on the exemplary donor/acceptor blend of fluorinated zincphtalocyanine (F_4ZnPc)/fullerene (C_{60}). This effect is closely related to improved free charge generation in ordered acceptor domains, which leads to an increase of the PCE. Fullerene ordering, recently reported to be beneficial for charge separation [18–20], strongly depends on device architecture, namely whether the cell is built in inverted or non-inverted architecture. In this thesis, novel results from analytical TEM, supported by infrared (IR) spectroscopy and combined with device characterization, unravel the crucial morphology factors that affect the PCE.

Few experimental techniques are able to spatially resolve the nanoscale morphology of organic materials. This is especially true for BHJs which consist of blended species [17]. For this purpose, the main experimental technique used in this thesis is analytical TEM, since analytical TEM enables the distinction of different material domains by their characteristic energy loss from electron energy loss spectroscopy (EELS) and energy-filtering [17]. The benefits of this technique have already been shown by Pfannmöller et al., who demonstrated how the phase-separated donor and acceptor domains can be discriminated in an organic BHJ [17]. Furthermore, the dielectric function and the absorption properties of the organic materials from EELS are derived and compared for the first time to optical measurements. In addition, the crystallinity is studied by electron diffraction. The combination of all measuring modes in one instrument allows the investigation of distinct characteristics on the exact same sample, which is especially profitable for the correlation of the different properties. To ensure the comparability between the structural and device properties, the TEM measurements are performed on samples close to the actual device structure, which is the unique feature of the present work. Complemented with the electrical characterization of devices, analytical TEM is a very powerful technique which contributes to a novel and comprehensive understanding of the decisive role of morphology for the performance of organic electronic devices.

The present work is carried out within a cooperation between the Technical University of Braunschweig, also based at the InnovationLab GmbH (sample preparation and electrical characterization) and Heidelberg University (TEM measurements). This collaboration is part of the "Leading-Edge Cluster Forum Organic Electronics" [2] founded by the Federal Ministry of Education and Research (BMBF), which combines the value chain of organic electronics

[2] http://www.innovationlab.de/en/cluster-foe/

from fundamental research to products and their industrial application. The main research activities are conducted at the InnovationLab GmbH, which is a joint transfer platform allowing to merge substantial competences such as synthesis, simulation, analytics, device physics and printing of organic electronics.

Outline

The present thesis is structured as follows: Chapter 2 gives a brief introduction to the fundamentals of organic semiconductors and the underlying processes in organic solar cells, followed by the physics of electron scattering and interaction with matter. Chapter 3 focuses on the basics of analytical transmission electron microscopy (TEM) including bright-field (BFTEM) and energy filtered (EFTEM) imaging, electron energy loss spectroscopy and electron diffraction. Kramers-Kronig analysis of EELS data and different data analysis approaches for EFTEM image stacks are also presented within this chapter. At the end of chapter 3 two common experimental methods for charge carrier mobility characterization are explained. In the following chapter (4) the used organic semiconductors and the sample processing is described in detail. In chapter 5 the stability of the organic materials used in this thesis under electron beam exposure is investigated. Chapter 6 comprises experimental results on the structural properties and charge carrier mobilities of the widely investigated polymer P3HT, which is eligible for the direct comparison with literature results. The chapter is supplemented with preliminary results on charge transfer characteristics of doped P3HT measured by infrared (IR) spectroscopy. The following chapter (7) constitutes the main part of this thesis as novel results from TEM measurements on the structure-function relationship of F_4ZnPc:C_{60} small molecule solar cells are presented. A comparison with IR measurements complete the results. At the end of the chapter the influence of layer crystallinity on solar cell performance is discussed. Finally, chapter 8 summarizes the results of this thesis and gives a brief outlook on future research topics.

2. Theoretical Fundamentals

The following chapter gives an overview on the basic theoretical concepts needed for a comprehensive understanding of this thesis. After a short introduction to organic semiconductors, the basics of organic solar cells are presented. The important factors affecting the solar cell characteristics are discussed. In addition, fundamentals of electron scattering and interaction are introduced as they play a key role in transmission electron microscopy.

2.1. Fundamentals of Organic Semiconductors

The present work focuses on the properties of organic semiconductors and their applications. Organic semiconductors are carbon based and comprise mainly three classes of materials: polymers, oligomers and small molecules. Roughly speaking, the widespread use of organic semiconductors results from their electronic properties which originate from the configuration of the carbon atoms. The planar sp^2-orbitals of the atom caused by hybridization, can overlap and form localized σ-bonds. Additionally, the p_z-orbitals, perpendicular to the sp^2-orbitals, form strongly delocalized π-bonds in the plane of the σ-bonds [21]. The delocalized π-electrons build a so called conjugated system and are mainly responsible for the conducting properties of the materials. Defects or twisting of the molecules, which especially occur in long polymer chains, usually interrupt the conjugation and lead to a decreased electrical conductivity. Moreover, it can be distinguished between a π-bonding orbital, also known as the highest occupied molecular orbital (HOMO) and a π^*-antibonding orbital, the lowest unoccupied molecular orbital (LUMO) [22]. Transitions between the HOMO and the LUMO have to overcome the energy gap of 1.5 eV to 3 eV [22]. This size of the energy gap explains the semiconducting properties of the materials. However, the already mentioned defects and twists lead to a broadened distribution of the energetic states. The resulting density of states can be described by a Gaussian distribution and has typically a width of around 100 meV [22].

2.1.1. Basics of Organic Solar Cells

Solar cells, inorganic or organic, convert the energy of photons into electrical energy. If the energy of the photons exceeds the energy of the band gap of the absorbing material, then an electron is excited from the HOMO (or valence band in inorganic materials) to the LUMO (conduction band). The electrons in the LUMO and the holes in the HOMO form pairs, also called excitons, which are bound by Coulomb interaction. The binding energy of the excitons in organic materials (also known as Frenkel excitons) is relatively high ($0.1\,\mathrm{eV} - 1\,\mathrm{eV}$). This is the case as the electrostatic shielding is very weak due to the low dielectric constant of organic materials in comparison to inorganic compounds, which is inversely proportional to the Coulomb attraction [23]. Additionally, the effective electron mass in organic materials is relatively high. Frenkel excitons are localized on one molecule. Due to the high binding energy of the exciton, thermal energy is not sufficient to cause its dissociation, which is crucial for the generation of free charge carriers. One way to overcome this barrier in organic solar cells is combining hole- and electron transporting materials in the active layer. The LUMO energy of the electron transporting material is low (acceptor) compared to the LUMO of the hole transporting material (donor), and respectively, the HOMO energy of the donor is high compared to the HOMO of the acceptor. Therefore, the exciton is likely to separate when reaching the donor-acceptor interface. The electron and the hole form a so called charge transfer (CT) state, which extends over more than one molecule. The separation of the charge transfer state into free charge carriers is affected by different factors, which are currently widely discussed. This process is explained in detail in the following section. A discussion about the role of CT states in charge separation mechanisms that considers the results of this thesis follows in section 7.4.

Assuming a successful charge separation, the holes and the electrons are extracted at the respective electrodes if the energy levels at the organic/electrode interfaces match. In figure 2.1 a) the basic working principle of an organic solar cell is shown, indicating the photon absorption, the exciton diffusion and dissociation at the interface, the charge transfer state and the charge extraction at the contacts [24]. From the presented working principle it becomes clear that there are several conditions that need to be considered, including the active layer morphology, for an optimized organic solar cell:

- In order to achieve good absorption properties the active layer needs to be sufficiently thick. However, as the exciton diffusion length in organic materials ranges between 3 nm and 40 nm, layer thickness is a tradeoff: it has to be enough for sufficient absorption but is limited by the diffusion

length [25].

- A suitable energy level alignment between the donor and acceptor material along with a significant amount of donor-acceptor interfaces is required for an efficient exciton dissociation. For this purpose an interpenetrating donor-acceptor network (bulk heterojunction) is introduced, which is usually achieved by co-evaporating or mixing the donor and acceptor in solution in a ratio close to 1:1 [26].

- The resulting rather complex structure of the BHJ is a tradeoff between sufficient interface areas and well formed percolation paths without dead ends that enables charge transport directly to the respective contact. To this end, the morphology of the active layer plays a key role, in terms of phase separation between the donor and acceptor phase.

- Ordering in pure phase-separated regions is aspired in an optimized active layer morphology as crystallinity is beneficial for charge mobility, and hence for efficient charge transport along the paths.

- The separation of the CT state into free charge carriers is crucial for the device function and is still a matter of controversy [27]. Some publications claim that the charge separation is triggered by the internal electric field that is caused by the work function difference of the contacts [24]; others attach importance to the delocalization of the higher energetic CT states [27]. Furthermore, it is assumed that the delocalization of the states is stronger in crystalline materials with long-range order [19, 27].

- Another requirement for well performing solar cells is the energy level alignment at the selective contacts. For this purpose, electron and transport layers are introduced that resemble a p-i-n-solar cell structure [28]. A further approach is changing the electrode work function by surface modification of the electrodes, e.g. with self-assembled monolayers [29].

The present work focuses on understanding the complex structure-function-relationship in organic solar cells. Therefore, considering the conditions mentioned above, mainly the impact of morphology, in terms of phase separation and crystallinity, on the device performance is addressed in this thesis.

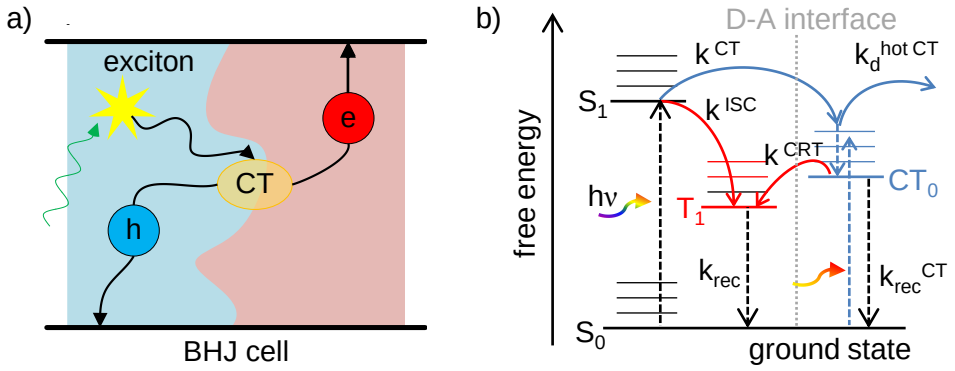

Figure 2.1: Basic working principle of an organic solar cell. a) Photon absorption, exciton diffusion, and charge separation at the donor-acceptor interface (donor material blue; acceptor material red). Based on [24]. Energy level diagram of the excited states after photon absorption ($S_0 \rightarrow S_1$) including the CT state at the donor-acceptor interface. The most important recombination and dissociation rates are indicated. Based on [30].

Charge Transfer State and Charge Carrier Recombination

The presented idealized case that the CT state separation directly creates free charge carriers, is limited by recombination. A schematic of the energy levels is shown in figure 2.1 b). Photon absorption leads to transition from the singlet state S_0 to S_1, which corresponds to the HOMO-LUMO transition of the absorbing material, e.g. the donor [31]. The energy of the transition is determined by the band gap E_g of the compound [31]. If the CT state energy is lower than the energy of S_1, charge transfer occurs between S_1 and the CT state (k^{CT}). The CT state is mainly determined by the HOMO of the donor and the acceptor of the LUMO:

$$E_{CT} = |E(D)_{\mathrm{HOMO}} - E(A)_{\mathrm{LUMO}}| - \triangle, \tag{2.1}$$

where $\triangle$ describes the Coulomb attraction [31]. The driving force for the transition into the CT state is ΔG_{CT}, which is defined by $\Delta G_{\mathrm{CT}} = E_{\mathrm{CT}} - E_{\mathrm{g}}$ [31]. In case of a "hot" CT state the electron does not relax into the ground state of the CT state (CT_0). It uses the excess energy to thermalize away from the hole which leads directly to dissociation of the charge pair ($k_{\mathrm{d}}^{\mathrm{hot,CT}}$) [30]. On the contrary, a "cold" CT state refers to the relaxation of the electron into CT_0. Then, charge separation can only happen with additional thermal energy or upon the application of an electric field [30]. However, the CT state

can recombine (k^{CRT}) into a triplet excited state T_1 (shown in figure 2.1 b)) of the donor or acceptor if this is energetically favorable. From here, the so called geminate recombination competes with charge pair dissociation into free carriers with an electric field-dependent rate that follows the Onsager-Braun Model [27, 32]. Geminate recombination is localized on one molecule, and the electron and the hole have the same origin. However, few recent publications demonstrated that in efficient BHJs the photocurrent generation does not depend on the electric-field [33, 34]. Therefore, charge separation through a hot CT state is the dominant process and geminate recombination is ruled out [33, 34]. In efficient BHJ systems materials exhibit a higher order, which leads to strongly delocalized states that enable the direct charge separation [18–20]. After charge separation, however, recombination is still possible. This is the so called non-geminate biomolecular recombination. It describes the case in which already separated free charge carriers that come from a different precursor state, recombine on their way to the electrodes. In that case the so called Langevin recombination rate R describes the probability of the two free charge carriers to find each other [35]:

$$R = \frac{e}{\epsilon_r \epsilon_0}(\mu_{\mathrm{e}} + \mu_{\mathrm{h}})(n \cdot p - n_{\mathrm{i}}^2). \tag{2.2}$$

Here the recombination rate depends mainly on the electron and hole mobilities (μ_{e}, μ_{h}), the electron and hole concentration (n, p), and the intrinsic charge carrier concentration n_{i}.

2.1.2. Solar Cell Characteristics

All important parameters of a solar cell can be derived from current-voltage (I-V) characteristics. In inorganic solar cells the current is described by the Shockley equation [35]:

$$j(V) = j_0 \left[\exp\left(\frac{e\,(V - jR_{\mathrm{s}})}{nkT} \right) - 1 \right] - \frac{V - jR_{\mathbf{s}}}{R_{\mathbf{p}}} + j_{\mathrm{ph}}. \tag{2.3}$$

where j_0 describes the reverse saturation current, j_{ph} the photocurrent, kT the thermal energy, and n is the ideality factor of the diode. Basically, the Shockley equation describes an equivalent circuit of a single diode model as shown in figure 2.2 a). For a more accurate description of real devices, two resistors are added in euqation (2.3). The series resistance R_{s} considers the finite conductivity of the materials and the contact resistance, which must be low. The parallel resistance R_{p}, also called shunt resistance, is in the ideal

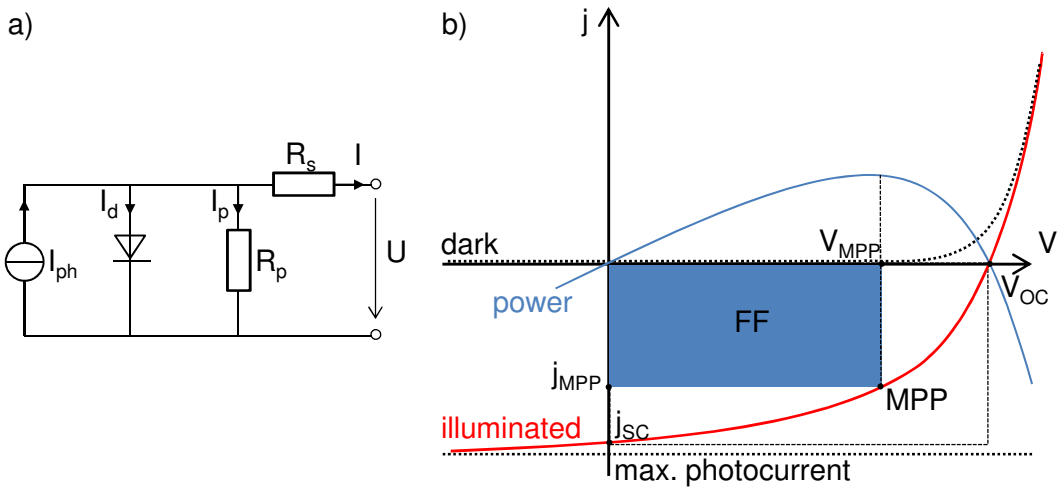

Figure 2.2: Solar cell characteristics. a) Equivalent circuit of a single diode describing the working principle of a solar cell. The diode current I_{d} together with the current through the parallel resistance I_{p} represent the dark current in a solar cell. R_s and R_p represent basically the contact resistance. b) Typical I-V curve of a solar cell under dark conditions (black, dashed line) or under illumination (red). The important characteristics such as j_{sc}, V_{oc}, the maximum power point (MPP) and the fill factor (FF) are indicated. The resulting output power is plotted in blue. Both figures are based on [36].

case high and takes leakage paths of the charge carriers into account. However, equation (2.3) does not describe the current-voltage characteristics of organic solar cells perfectly due to the field dependence of R_{s}, R_{p} and j_{ph} in this kind of devices. In figure 2.2 b) a typical I-V curve of an organic solar cell is shown. It indicates that the j_{ph} is not constant for negative voltages and does not reach the maximum value at short-circuit conditions j_{sc}. The maximum power point (MPP) defines the point with the maximal output of the solar cell $P_{\mathrm{MPP}} = j \cdot V$. In the following further important parameters of the solar cell such as FF, V_{oc}, and j_{sc} will be explained in detail.

Short Circuit Current

The short circuit current $j_{\mathbf{sc}}$ describes the current at $V = 0$, when the cell is not connected to an external load. The current depends on the charge carrier mobility, which in turn often depends on the active layer morphology, e.g. long range order of the materials. As charge transport in organic materials is described by thermally activated hopping transport, the current as well

can depend on temperature. Furthermore, since the charge carrier density is limited by the number of absorbed photons, the current also depends on the absorption behavior of the active material. Charge carrier recombination, which hinders the generation of free charges, is expected to lower the short circuit current.

Open Circuit Voltage

Assuming successful charge carrier generation after illumination of the solar cell, excess electrons are created in the acceptor and holes are created in the donor. This leads to a quasi-Fermi level splitting of the energy levels for the holes (E_{Fp}) and electrons (E_{Fn}). Therefore, the open circuit voltage V_{oc} can be described by the splitting [37]:

$$eV_{\mathrm{oc}} = E_{\mathrm{Fn}} - E_{\mathrm{Fp}}. \tag{2.4}$$

If one assumes the ideal case of Ohmic contacts then the open circuit voltage V_{oc} is mainly limited to the bandgap, as the quasi Fermi levels cannot move into the conduction or valence band [37]. In organic materials the band gap, or also called effective band gap, is related to the energetic distance of the donor HOMO and acceptor LUMO. Additionally, the Gaussian distribution of the density of states in the HOMO and LUMO must be considered. The energetic disorder of organic compounds is manifested in the Gaussian tail. Therefore, a possible approach for the description of V_{oc} in organic solar cells is given by [37]:

$$eV_{\mathrm{oc}} = E_{\mathrm{g}} - \frac{s_{\mathrm{n}} s_{\mathrm{p}}}{2k_{\mathrm{B}}\mathrm{T}} - k_{\mathrm{B}}T \ln \frac{N_{\mathrm{n}} N_{\mathrm{p}}}{np}, \tag{2.5}$$

where the equilibration energy in the Gaussian tail is described by $s_{\mathrm{n}}/k_{\mathrm{B}}T$ below the LUMO and $s_{\mathrm{p}}/k_{\mathrm{B}}T$ below the HOMO. N_{n} and N_{p} describe the effective density of states of the electrons in the LUMO of the acceptor and respectively of the holes in the HOMO of the donor, whereas n and p describe the electron and hole density. The energetic disorder considered in equation (2.5) might explain why V_{oc} in real devices is often lower as expected from the effective band gap of the donor-acceptor composite. However, the exact description of the distribution of tail states in organic materials is still of interest in ongoing research [38].

Fill factor

The fill factor (FF), marked with a blue square in figure 2.2 b), is a further parameter that describes the quality of the cell:

$$FF = \frac{P_{\mathrm{MPP}}}{j_{\mathrm{sc}} V_{\mathrm{oc}}}. \tag{2.6}$$

It is mainly determined by the amount of extracted charges that reach the electrodes and the field assisted charge separation. For a high FF the series resistance should be reduced and the parallel resistance should be increased. Additionally, short cuts or dead ends of the percolation paths that increase the charge carrier recombination, decrease FF. The overall power conversion efficiency η (PCE) of the cell can be described as:

$$\eta = FF \cdot \frac{V_{\mathrm{oc}} j_{\mathrm{sc}}}{P_{\mathrm{in}}}, \tag{2.7}$$

where P_{in} is the power of the incident light.

2.1.3. Charge Transport in Organic Semiconductors

In the scope of this work, the charge carrier mobilities in polymers are investigated. Furthermore, the charge mobility plays a major role in solar cells as the charges need to reach the electrodes once excitons are separated [35]. Due to the lack of long-range order that causes a weak overlap of the orbitals wavefunctions in most organic materials, charge transport is governed by hopping of localized charges from site to site. Therefore, the transport is thermally activated and strongly depends on the transfer integral between the corresponding wavefunctions. It is described by the Miller-Abrahams hopping rate [35, 39]:

$$\nu_{ij} = \nu_0 \exp\left(-\gamma r_{ij}\right) \begin{cases} \exp\left(-\frac{\Delta E}{kT}\right) & \Delta E_{ij} > 0 \\ 1 & \Delta E_{ij} \leq 0 \end{cases}, \tag{2.8}$$

where ν_0 describes the attempt-to-escape frequency, γ the inverse localization radius proportional to the transfer integral and r_{ij} the spatial distance between the sites i and j. The first exponential term describes the contribution of tunneling. For jumps upwards in energy the second term is described by a Boltzmann factor and with factor 1 for jumps downwards, respectively. Here, ΔE_{ij} describes the energy difference between the sites. Bässler uses Monte

Carlo simulations in order to simulate the hopping process that is described in equation (2.8). As an outcome he obtains for the mobility [39]:

$$\mu = \mu_0 \exp\left(-\left(\frac{2\sigma}{3kT}\right)^2 + C\left(\left(\frac{\sigma}{kT}\right)^2 - \Sigma\right)F^{1/2}\right). \tag{2.9}$$

Here a Gaussian distribution of the density of states is assumed, where the width σ is a measure for the energetic disorder. Furthermore, Σ describes the spatial disorder, F the electric field and C is a scaling factor from the fit. Equation (2.9) clarifies that the mobility is temperature- and field-depended. This is expected if the mobility is described by hopping, since the applied electric field lowers the energetic barriers in the direction of the field. Further models exist that additionally consider the correlation between energetic and spatial disorder and polaronic effects [35]. However, most proposed models so far describe only molecule-molecule interaction on the mesoscopic scale. An universal model that describes charge transport on a multiscale connecting microscopic to macroscopic transport properties of organic semiconductors is still a matter of discussion [35].

2.1.4. Phase Separation in Molecular Crystals

An important aspect investigated in this thesis is the phase separation of the donor and acceptor molecules in blended systems, e.g. active layers in organic solar cells. By means of equilibrium thermodynamics, the different mixing scenarios of molecules species A and B can be described by minimizing the free energy of the system F [40]:

$$\frac{F_{\text{mix}}}{k_{\text{B}}T} = x_{\text{A}} \ln x_{\text{A}} + x_{\text{B}} \ln x_{\text{B}} + \chi x_{\text{A}} x_{\text{B}}, \tag{2.10}$$

where x_{A} and x_{B} describe the concentration of the two species. The first two terms describe the change in entropy that favors mixing. The dimensionless interaction parameter is defined as [40]:

$$\chi = \frac{1}{k_{\text{B}}T}\left[W_{\text{AA}} + W_{\text{BB}} - 2W_{\text{AB}}\right] = \frac{1}{k_{\text{B}}T}W. \tag{2.11}$$

W_{AA} and W_{BB} describe the interaction energy between the same molecule species, whereas W_{AB} describes the interaction between molecule A and B. The sign of χ can serve as a measure for the mixture. There are four distinct cases [40]. For high temperatures ($\chi \to 0$) the effect due to entropy dominates

equation (2.10) and leads to a statistical intermixing. At low temperatures for $\chi \simeq 0$ the attraction between A and B is similar to the attraction between the pure compounds W_{AA} and W_{BB}, which results also in intermixing. At low temperatures and $\chi < 0$ an ordered molecular complex is formed as the attraction between A and B (W_{AB}) dominates. This leads to strong bonding between the two species. The last case at low temperatures considers $\chi > 2$ which means that the interaction between the two species is unfavorable. Hence, the interaction between the same species is large and exceeds the entropic contribution. This kind of strong interaction can be e.g. driven by crystallization and results in phase separation.

The presented model assumes thermal equilibrium. However, thermal equilibrium is not necessarily reached during the sample preparation by thermal co-evaporation as used in this thesis. During thermal evaporation in vacuum the two species can mainly diffuse along the substrate. Additional substrate heating can allow diffusion in the bulk as the molecules are thermally activated in a near equilibrium condition [40]. Therefore, phase separation is likely to occur upon substrate heating if the co-evaporated molecules favor crystallization. In this work this is likely to be the case as phtalocyanines and fullerenes, which are crystalline, are used [40].

2.2. Electron Interaction with Matter

Electron interaction with solids represent the most important basic concepts in transmission electron microscopy, which is the main experimental technique used in this thesis. In order to describe the interaction of fast electrons with matter, it is distinguished between elastic and inelastic scattering processes. The main difference between the two processes is defined by the energy loss of the electron. All presented relationships in the following are taken from the Electron Energy Loss Spectroscopy (EELS) basics provided by Egerton [41].

Elastic Scattering

Elastic scattering is caused by the electrostatic field of the atomic nuclei. As the mass of the nucleus is significantly higher than the mass of an electron, the energy transfer is negligible. Hence, elastically scattered electrons do not loose energy after the interaction with matter. The simplest model to describe elastic scattering is presented by Rutherford [41]:

$$\frac{d\sigma}{d\Omega} = \frac{4\gamma^2 Z^2}{a_0^2 q^4}, \tag{2.12}$$

where $d\sigma/d\Omega$ represents the differential cross-section, γ the relativistic factor, Z the atomic number, a_0 the first Bohr radius ($a_0 = 4\pi\epsilon_0\hbar^2/m_0e^2$), and q the scattering vector given by $q = 2k_0 \sin(\theta/2)$. However, equation (2.12) is an approximation that is appropriate for high scattering angles θ only. For a more accurate model the atomic potential has to be considered. Among others, a model was presented by Langmore et al. that determines the total cross section σ_e by calculating the potential from an iterative solution of the Schrödinger equation on the basis of Hartree-Fock wavefunctions [42]:

$$\sigma_{\mathrm{e}} = \frac{(1.5 \cdot 10^{-24} m^2)\, Z^{3/2}}{(v/c)^2} \left[1 - \frac{Z}{596 \cdot (v/c)}\right]. \tag{2.13}$$

The term in brackets is a correction to the Born approximation and v represents the velocity of the incident electron. Basically, the cross section for elastic scattering depends on the atomic number and the mass density. It is important to consider that the described scattering theory takes into account only scattering of electrons on an isolated single atom. In molecules the cross section per atom is reduced due to bondings. A further measure, the so called mean free path λ_e, considers the cross section per atom σ_e and can be calculated as follows:

$$\lambda_{\mathrm{e}} = \frac{1}{\sigma_{\mathrm{e}} n_{\mathrm{a}}}, \tag{2.14}$$

where n_{a} is the number of atoms per unit volume. If one assumes that the considered molecular materials are mostly amorphous such that diffraction effects can be neglected, λ_{e} describes the mean distance between elastic collisions.

A further important elastic scattering process is diffraction. If the incident electrons are scattered on a material that exhibits a regular atomic (or molecular) arrangement then the diffracted (outgoing) wave and the incident plane wave are different in phase. The so called scattering vector $\boldsymbol{\Delta k}$ is described by:

$$\boldsymbol{\Delta k} = \boldsymbol{k} - \boldsymbol{k_0}, \tag{2.15}$$

where $\boldsymbol{k_0}$ is the wavevector of the incident beam and $\boldsymbol{k}$ the wavevector of the diffracted (outgoing) beam. By introducing the primitive vectors of the crystal lattice $\boldsymbol{a}$, $\boldsymbol{b}$ and $\boldsymbol{c}$, and the reciprocal lattice indices (h, k, l), the conditions for the orientation of the scattering vector (Laue equations) are obtained:

$$\boldsymbol{a}\boldsymbol{\Delta k} = 2\pi h, \tag{2.16}$$

$$\boldsymbol{b}\boldsymbol{\Delta k} = 2\pi k, \tag{2.17}$$

$$\boldsymbol{c\Delta k} = 2\pi l. \tag{2.18}$$

Including θ, which describes the scattering angle relative to the incident beam, then, after some mathematical transformations (explained in detail in [41, 43]), the well-known Bragg's Law can be derived from the Laue equations:

$$\lambda = 2d \sin\theta_{\mathrm{B}}, \tag{2.19}$$

where λ is the electron wavelength and θ_{B} is twice the scattering angle θ. Here, the waves are reflected at the atomic planes that have a particular spacing d. Bragg's Law describes one of the most important relationships for diffraction experiments. For a more detailed description of diffraction fundamentals the so called structure factor $F(\theta)$ must be introduced. As $F(\theta)$ relates to the amplitude of the scattered wave, the intensity of the scattered wave is proportional to $|F(\theta)|^2$. The intensity then peaks at values of θ for which the scattered waves from the periodically arranged atoms are in phase with one another. A more detailed description of the structure factor is given in [44].

Inelastic Scattering

After inelastic scattering on outer- and inner-shell electrons of the atom, electrons loose a certain amount of energy. In light elements, like the constituents of organic materials, scattering on the outer-shell electrons is predominant. More precisely, the cross section for scattering on the inner-shell is less than 15 % of the total cross-section for inelastic scattering. The latter can be described by the transition of each electron of the atom from an initial state, described by the wavefunction ψ_0, to a final state described by the wavefunction ψ_n:

$$\frac{d\sigma_n}{d\Omega} = \left(\frac{m_0}{2\pi\hbar^2}\right)^2 \frac{k_1}{k_0} \left| \int V(r)\psi_0\psi_n^* \exp(\mathrm{i}\boldsymbol{kr}) \cdot d\tau \right|^2. \tag{2.20}$$

Here $\hbar\boldsymbol{k} = \hbar(\boldsymbol{k_0} - \boldsymbol{k_1})$ indicates the momentum transferred to the atom, $\boldsymbol{k_0}$ and $\boldsymbol{k_1}$ the wavevectors of the electron before and after scattering,$\mathbf{r}$ the coordinate of the electron and $d\tau$ the volume elements. $V(r)$ represents the potential, which is responsible for the interaction:

$$V(r) = \frac{Ze^2}{4\pi\epsilon_0 r} - \frac{1}{4\pi\epsilon_0} \sum_{j=1}^{Z} \frac{e^2}{|\boldsymbol{r} - \boldsymbol{r_j}|}. \tag{2.21}$$

The first term represents the Coulomb potential. The second term describes the repulsive interaction of the electrons in the atom with a coordinate r_j.

Additionally, it is considered that the electron transition is a transition into a continuum of states, as the energy loss spectrum is not a discrete function of energy loss. Hence, substituting $V(r)$ from equation (2.21) into equation (2.20) and considering the continuous energy loss function, the differential cross section is transformed to a double-differential cross section. It includes the angular and energy dependence of scattering:

$$\frac{d^2\sigma}{d\Omega dE} = \frac{8a_0^2R^2}{Em_0v^2}\left(\frac{1}{\theta^2+\theta_E^2}\right)\frac{df}{dE}. \tag{2.22}$$

Here, R is the Rydberg energy ($R = \hbar^2/(2m_0a^2)$), θ_E the characteristic angle ($\theta_E = E/(\gamma m_0 v^2)$) and df/dE describes the generalized oscillator strength per unit energy loss.

In analogy to elastic scattering, equation (2.22) describes inelastic scattering on single molecules. In order to describe the interaction of the electrons with the entire solid more accurately, the dielectric response function $\epsilon(k,\omega)$ is introduced. The latter is also used to describe the interaction of photons with solids. Therefore, the energy-loss data can be compared with data from optical measurements. The derivation of the relationship between the dielectric response function and the cross section for inelastic scattering is based on the Poisson equation (assuming the charge distribution for a point charge):

$$\epsilon_0\epsilon(\boldsymbol{k},\omega)\nabla^2\phi(\boldsymbol{r},t) = e\delta(\boldsymbol{r},t). \tag{2.23}$$

Its transformation in the frequency space leads to the following expression for the potential [45]:

$$\phi(\boldsymbol{k},\omega) = -\frac{8\pi^2 e}{\epsilon(\boldsymbol{k},\omega)}\frac{\delta(\boldsymbol{kv}+\omega)}{k^2}, \tag{2.24}$$

with the Fourier transformation:

$$\phi(\boldsymbol{r},t) = \frac{1}{(2\pi)^4}\int d\boldsymbol{k}\int d\omega\,\exp(\mathrm{i}\boldsymbol{kr}+\omega t)\phi(\boldsymbol{k},\omega). \tag{2.25}$$

Furthermore, the energy loss per unit path, also known as the stopping power, is equal to the backward force on the transmitted electron in the direction of motion [41]. It can be expressed as:

$$-dW/dx = \frac{e}{v}\boldsymbol{vE}, \tag{2.26}$$

where $\boldsymbol{E}$ describes the electric field. Considering that the electric field is the

potential gradient, equations (2.24) and (2.25) can be inserted in the expression for the energy loss per unit length $-dW/dx$ in equation (2.26). Additionally, $-dW/dx$ is proportional to the integrated double-differential cross section from equation (2.22). The mathematical transformation of all mentioned equations leads to the following expression:

$$\frac{d^2\sigma}{d\Omega dE} \approx \frac{\mathrm{Im}\left[-1/\epsilon(k,E)\right]}{\pi^2 a_0 m_0 v^2 n_a} \left(\frac{1}{\theta^2+\theta_E^2}\right). \tag{2.27}$$

$\mathrm{Im}[-1/\epsilon(k,E)]$ is also known as the energy-loss function. For small angles $\epsilon(k,E)$ can be approximated by $\epsilon(0,E)$ which describes the relative permittivity of the solid at a certain energy. After a Kramers-Kronig transformation the real and imaginary part of the dielectric function ϵ_1 and ϵ_2 can be determined. The collection of small angles in the electron energy loss measurement is guaranteed by a small semi collecting angle determined by the objective aperture. Further details on how the loss-function and the dielectric function (including the Kramers-Kronig relation) are derived from the measured energy loss spectrum are explained in chapter 3.

Dielectric Function

The dielectric function $\epsilon(\omega)$ describes the response of a medium to external electric fields. It depends on the frequency of the field as there are different processes contributing to material polarization. The main contributions comprise electronic, lattice and orientation polarizability:

$$\epsilon(\omega) = 1 + \chi_{\text{electronic}} + \chi_{\text{lattice}} + \chi_{\text{orientation}}. \tag{2.28}$$

A schematic of the real part of the dielectric function of an insulator is shown in figure 2.3. The different contributions are indicated. With increasing frequencies towards x-rays the medium cannot respond fast enough. Thus, the dielectric function approaches 1. For the materials investigated in this thesis mainly the electronic polarization is of interest.

$\epsilon(\omega)$ can be derived from Maxwell's equations in matter including additionally:

$$\boldsymbol{D} = \epsilon_0 \boldsymbol{E} + \boldsymbol{P} = \epsilon_1 \epsilon_0 \boldsymbol{E}, \tag{2.29}$$

$$\boldsymbol{P} = (\epsilon_1 - 1)\epsilon_0 \boldsymbol{E} = \chi \epsilon_0 \boldsymbol{E}. \tag{2.30}$$

Here $\boldsymbol{D}$ describes the dielectric displacement, $\boldsymbol{E}$ the electric field and $\boldsymbol{P}$ the

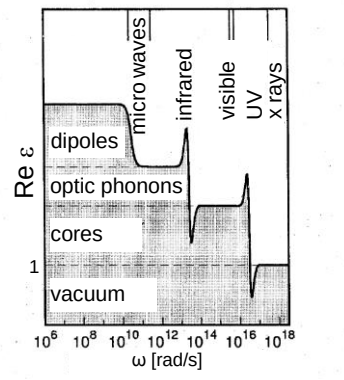

Figure 2.3: The real part of the dielectric function depending on the frequency for an insulator. The contributions of dipoles (orientation polarizability), optic phonons (lattice polarizability) and cores (electronic polarizability) are indicated. For high frequencies Re ϵ approaches 1. Based on [43].

polarization. χ denotes the dielectric susceptibility. The equations lead after some mathematical transformations to the expression for the wave equation in matter:

$$0 = \Delta \boldsymbol{E} - \frac{\epsilon}{c^2}\frac{\partial^2 \boldsymbol{E}}{\partial t^2} - \frac{1}{\epsilon_0 c^2}\sigma\frac{\partial \boldsymbol{E}}{\partial t}. \tag{2.31}$$

The solution of the differential equation (2.31) is given by the plane wave:

$$\boldsymbol{E}(\omega) = \boldsymbol{E_0}\exp \mathrm{i}(\boldsymbol{kr} - \omega t), \tag{2.32}$$

with

$$k^2 = \frac{\omega^2}{c^2}(\epsilon_1 + \frac{\mathrm{i}\sigma}{\epsilon_0\omega}) \tag{2.33}$$

and

$$\tilde{n}^2 = \epsilon_1 + \frac{\mathrm{i}\sigma}{\epsilon_0\omega} = \epsilon(\omega) = \epsilon_1 + \mathrm{i}\epsilon_2. \tag{2.34}$$

Additionally, $\epsilon_1 = n^2 - \kappa^2$ and $\epsilon_2 = 2n\kappa$ are defined, which are also used in this thesis to correlate electron energy loss measurements with optical measurements as will be explained in section 3.2.1.2. Here the complex index of refraction $\tilde{n} = n + \mathrm{i}\kappa$ is introduced, where n describes the real refractive index and κ describes the extinction coefficient. By inserting the complex wave number $\tilde{k} = \frac{2\pi\kappa}{\lambda}$ in the plane wave expression and considering that the intensity is proportional to the square of the electric field an exponential decay with $\mathrm{e}^{(-4\pi\kappa r/\lambda)}$ is obtained. From here the absorption coefficient of the material is derived as:

$$\alpha = \frac{4\pi\kappa}{\lambda}. \tag{2.35}$$

3. Experimental Details

This chapter focuses on the working principle of transmission electron microscopy (TEM), which is the main characterization method applied in this work. TEM is a very powerful technique, as it enables direct imaging of the morphology. However, gaining material contrast, especially for organic materials, is not straight-forward. In this case the so called analytical TEM is applied, which takes advantage of the specific material information carried by the inelastically scattered electrons. The first part of this chapter addresses conventional TEM imaging techniques, whereas the second part addresses analytical TEM. In particular, electron energy loss spectroscopy is discussed in detail.

3.1. Transmission Electron Microscopy (TEM)

All TEM measurements in this thesis were performed with a Carl Zeiss Libra 200 MC Cryo DMU (Kronos). In this kind of TEM electrons are emitted from a field emission gun and extracted by an applied voltage. After extraction the electrons are accelerated to 60 kV or 200 kV (not relevant in this work). In order to narrow the energetic width of the beam the electrons surpass a monochromator. After the interaction of the incident beam with the sample the electrons are scattered elastically or inelastically. One method to use the TEM is to only detect the elastically scattered electrons at small scattering angles in order to obtain a so called bright-field (BF) image or diffraction patterns. The image acquisition is carried out by a CCD camera (TemCam F416,TVIPS GmbH, Germany).

3.1.1. Bright-Field Mode

In the bright-field mode only the elastically scattered electrons contribute to the image. As explained in section 2.2 electrons are scattered elastically by the Coulomb field of the nuclei of the atoms in the specimen. Due to the interaction the incident electron wave changes its amplitude and phase.

Both, the amplitude and phase contrast contribute to an image. The scattered electron wave $\psi_{\mathrm{Sc}}(\boldsymbol{r})$ can be described as follows [46]:

$$\psi_{\mathrm{Sc}}(\boldsymbol{r}) = \psi_0 \exp\left[\mathrm{i}\phi(\boldsymbol{r}) + \mu(\boldsymbol{r})\right], \tag{3.1}$$

where the vector $\boldsymbol{r}$ in the sample plane is perpendicular to the incident beam. $\phi(\boldsymbol{r})$ denotes the value of the integral over the distribution of the Coulomb potential of the scattering object. $\mu(\boldsymbol{r})$ is the part that describes the change in the amplitude. In the case of organic materials, which mainly consists of light atoms like carbon and hydrogen, the amplitude contrast is very low and the contrast in the image is dominated by the phase contrast [47]. Thus, for $\phi(\boldsymbol{r}) \ll 1$ and $\mu(\boldsymbol{r}) \ll 1$ equation (3.1) can be approximated to:

$$\psi_{\mathrm{Sc}}(\boldsymbol{r}) = 1 + \mathrm{i}\phi(\boldsymbol{r}) + \mu(\boldsymbol{r}), \tag{3.2}$$

with the amplitude of the incident wave being normalized to 1. The corresponding description of $\psi_{\mathrm{Sc}}(\boldsymbol{r})$ in the frequency space is obtained by a Fourier transformation. Furthermore, the additional term $\gamma(\boldsymbol{k})$ considers the aberration effects from the electron optics:

$$\Psi_{\mathrm{Sc}}(\boldsymbol{k}) = (\delta(\boldsymbol{k}) + \mathrm{i}\Phi(\boldsymbol{k}) + M(\boldsymbol{k}))\exp(\mathrm{i}\gamma(\boldsymbol{k})), \tag{3.3}$$

with

$$\gamma(\boldsymbol{k}) = \frac{\pi}{2}\left(C_{\mathrm{s}}\lambda^3\boldsymbol{k}^4 - \Delta z\lambda\boldsymbol{k}^2\right). \tag{3.4}$$

λ is the electron wavelength, C_{s} is the coefficient of the spherical aberration and Δz describes the defocus. The intensity of an image is the product of the scattered wave with its complex conjugation: $I(\boldsymbol{k}) = \Psi_{\mathrm{Sc}}(\boldsymbol{k}) \otimes \Psi_{\mathrm{Sc}}(-\boldsymbol{k})$, where $I(\boldsymbol{k})$ is the density in the frequency space. From equations (3.3) and (3.4) the intensity is described as follows:

$$I(\boldsymbol{k}) = \delta(\boldsymbol{k}) + 2\Phi(\boldsymbol{k})(\sin\gamma(\boldsymbol{k}) - W\cos\gamma(\boldsymbol{k})) = CTF(k)\Phi(\boldsymbol{k}), \tag{3.5}$$

where CTF describes the so called contrast transfer function [44, 46, 48]:

$$CTF(k) = 2(\sin\gamma(k) - W\cos\gamma(k)), \tag{3.6}$$

The CTF is understood as the operator for the phase and is mainly dependent of the spherical aberration C_{s}. Therefore, for high-resolution images C_{s} has to be minimized. As already proposed by Scherzer et al. in 1936 the rotationally

symmetric electron lenses used in non-corrected TEMs induce spherical C_s aberrations [49]. Thus, the correction of the TEM used in this work is realized by a complex system of non-rotational symmetric hexapol lenses implemented by CEOS GmbH [50–52]. Further defects that limit the practical resolution of a TEM are chromatic aberration C_c and astigmatism. The former is caused by the distinct refraction of the electrons in the lenses depending on the electron energy. This can be corrected by a monochromator. The origin of astigmatism are inhomogeneities of the magnetic field which channels the electrons. It is corrected by so called stigmators, which consist of small octupoles that induce a compensating field to balance the non-uniformity. The theoretical resolution of a TEM is described by the diffraction limit $r_{th} = 1.22\frac{\lambda}{\beta}$, where β describes the collection angle of the aperture [44]. However, with an increasing diameter of the aperture, which theoretically would increase the resolution, the discussed lens aberrations increase. Therefore, lens correction mechanisms are still a matter of interest in ongoing instrument development.[1]

3.1.2. Electron Diffraction

In the presented work electron diffraction is applied for the examination of the crystal structure of materials. Hence, the TEM is operated in the diffraction mode. The diffraction pattern is created in the back focal plane, which acts as the object plane and is then projected on the CCD camera. In highly ordered samples discrete diffraction spots are observed. However, as organic thin films are usually amorphous or polycrystalline with small ordered domains and arbitrary orientation, the diffraction pattern consists of concentric rings. Depending on the degree of crystallinity the rings appear sharper and sometimes contain speckles, which are discrete spots caused by diffraction from larger crystallites [44]. The distance of the rings from the non-diffracted beam in the center are reciprocal to the spacings in the film. In the experimental section typically the radial profile of a diffraction pattern is shown for a more descriptive representation of the diffraction data. In order to obtain a radial profile the intensity of the diffraction rings is integrated and plotted vs. reciprocal nanometers. For the camera length used in this work (225 mm), which determines the magnification of the pattern on the screen, the calibration of the spacings was done by means of an Au [111] sample before the actual measurement.

[1] A further promising, but not yet established method in order to enhance the phase contrast of weak phase objects is the use of phase plates. As this technique was not available for this work, a more detailed explanation of the working principle can be found in the work of Frindt et al. and Schultheiss et al. [53, 54].

As the diffracted beam is also partially inelastically scattered in the specimen, each Bragg spot in the diffraction pattern is surrounded by a halo [41]. In order to get rid of inelastic scattering, a zero-loss filtering slit (explained in detail in the next section) is inserted for the measurement. This sharpens the pattern and reduces the background noise [41]. A monochromator (2 µm) is used for all diffraction measurements, in order to further reduce the background noise and to minimize the electron dose down to 300 e/nm^2 (exposure 500 ms). This is necessary, as the investigated organic materials in this thesis are susceptible to beam damage.

3.2. Analytical TEM

As mentioned in 3.1.1 organic materials are weak phase objects, thus contrast in bright-field images can also originate from thickness variations or electron channeling through crystalline domains in the sample [41, 44]. In order to gain true material contrast analytical TEM is applied. In analytical TEM, in contrast to the conventional techniques, the information carried by the inelastically scattered electrons is used. A schematic of the method is shown in figure 3.1. The ideally monochromatic incident electron beam is scattered inelastically on the sample. As all electrons loose different amounts of energy during the scattering process, the beam is polychromatic after the interaction. By a magnetic field (analogous to a prism) the electrons are forced on a circular path with a radius that depends on their energy. This leads to the desired spectroscopic splitting [55].

3.2.1. Electron Energy Loss Spectroscopy (EELS)

To collect spectral information of the sample the whole energetic spectrum of the electrons can be used, as depicted on the left-hand side in figure 3.1. This technique is also known as EELS. In this case, both the elastically and inelastically scattered electrons reach the CCD camera. The elastically scattered electrons form the so called zero-loss (ZL) peak in the spectrum at 0 eV. The ZL-peak exhibits the highest intensity as the major percentage of all electrons are scattered elastically. The full width at half maximum (FWHM) of the ZL-peak is determined by the monochromator, which directly affects the energy resolution. In the present work all EELS measurements were performed with a very narrow monochromator (0.5 µm) with a resulting energy resolution of around 80 meV for 60 kV accelerating voltage. A typical EEL-spectrum is shown in figure 3.1 on the bottom left (ZL-peak is cut off for

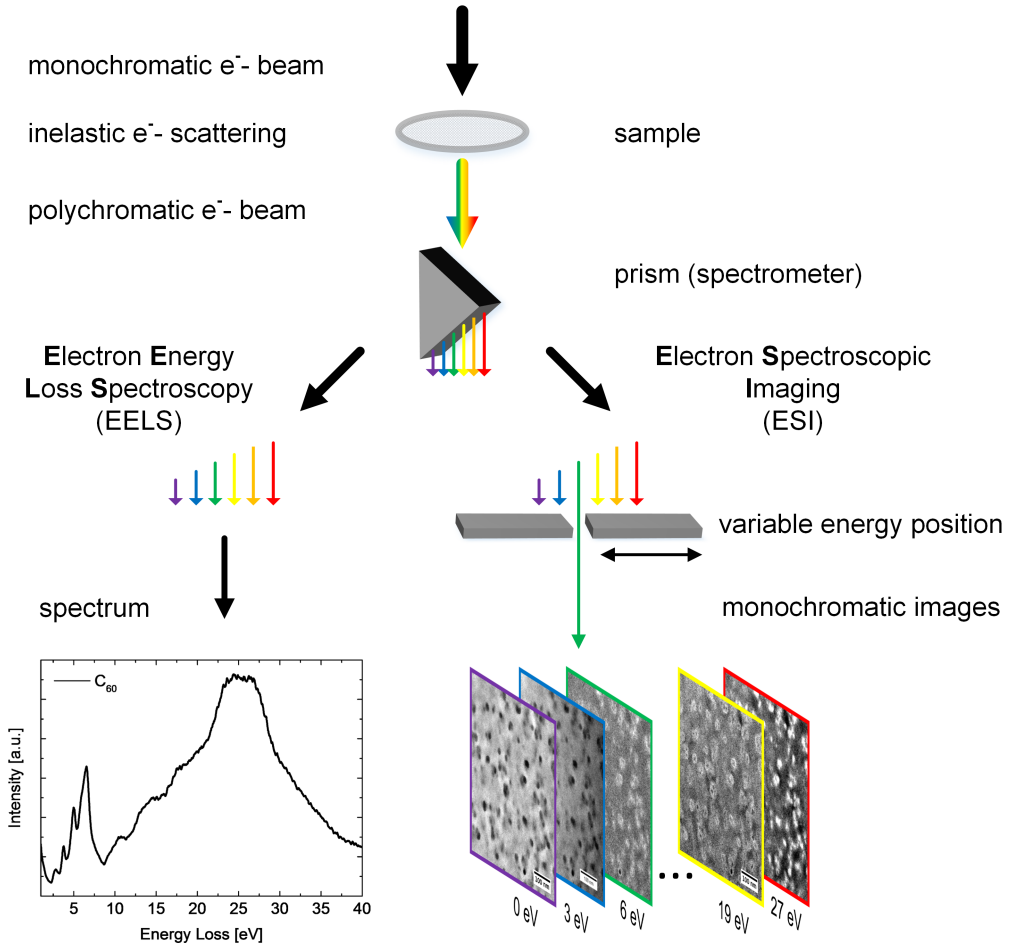

Figure 3.1: Schematic of analytical TEM based on [56]. Before the interaction with the sample the electron beam is monochromatic. After the interaction the electrons are scattered inelastically. The energy loss corresponds to electronic or plasmonic excitations and ionization of core electrons of the sample material. The measured EEL-spectrum represents the intensity of the polychromatic beam as a function of the energy loss of the electrons. Furthermore, it is possible to acquire a so called monochromatic image by detecting only electrons at a particular energy loss (ESI).

better visualization of the following excitations). In order to reduce noise an average of 5 spectra is acquired with a total electron dose of around $500\,\mathrm{e/nm^2}$. The low-loss regime between 0 eV and 60 eV involves electronic and plasmonic excitations. At around 1 eV −2 eV bandgap transitions are visible. Especially for organic materials $\pi - \pi^*$ and $\sigma - \sigma^*$ transitions below 10 eV are significant. These are usually followed by a collective excitation of the $\pi-$ and σ-electrons at around 20 eV, called plasmon excitation [41, 55]. At high energies the incident electrons can further ionize tightly bound core electrons. However, core-loss spectra are not of interest in the present work. The spectrum in figure 3.1 is only shown to facilitate the description of the course of an EEL-spectrum. A detailed assignment of the peaks and their position in the C_{60}-spectrum will be given in section 7.2.1. In order to understand the origin of the excitations an analyzing procedure of the spectra has to be conducted. The quantitative analysis of energy-loss data is explained in the following sections.

3.2.1.1. Deconvolution

So far only single-scattering events have been taken into account. However, especially for thicker specimens, multiple-scattering of electrons can occur. As a consequence individual peaks may not be visible in the spectrum. A widely used method to remove these effects is the deconvolution technique that uses a Fourier transformation [41]. The electron intensity I_n with inelastic scattering of order n follows a Poisson distribution:

$$I_n = I \cdot P^n = \left(\frac{I}{n!}\right)\left(\frac{t}{\lambda}\right)\exp\left(-t/\lambda\right), \tag{3.7}$$

where I is the total integrated intensity, P^n describes the probability of a scattering event, t the sample thickness and λ the mean free path of the electrons. If we assume that only elastic scattering occurs ($n = 0$), then the EEL-spectrum consists only of the zero-loss peak $Z(E) = I_0 R(E)$. Here $R(E)$ is the instrument response function with a FWHM corresponding to the energy resolution of the instrument. Given equation (3.7) for single scattering events with $n = 1$ the intensity distribution $S(E)$ satisfies:

$$\int_0^\infty S(E)dE = I_1 = I\left(\frac{t}{\lambda}\right)\exp(-t/\lambda) = I_0\left(\frac{t}{\lambda}\right). \tag{3.8}$$

Furthermore,

$$J^1(E) = R(E) * S(E), \tag{3.9}$$

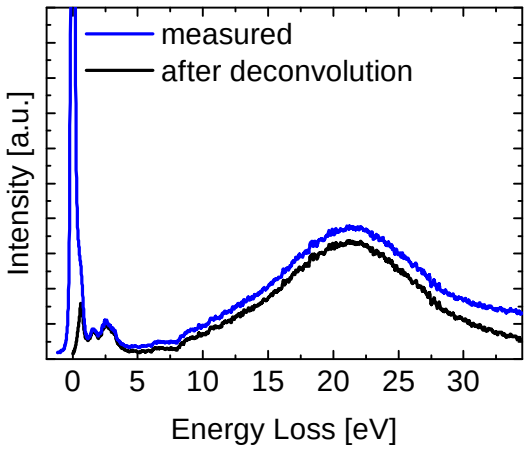

Figure 3.2: The measured EEL-spectrum (blue) includes the zero-loss peak and multi-scattering events. After deconvolution (black) the intensity of the spectrum is slightly lowered, as multi-scattering events are removed. Additionally, the ZL-peak is deconvolved, which is advantageous if the investigated material exhibits features in the energy range close to the ZL. As shown in the black spectrum, such features become visible after deconvolution.

where $J^{\mathrm{n}}(E)$ is a broadened distribution of the recorded spectrum $J(E)$. The recorded spectrum is limited by the instrument resolution:

$$J(E) = Z(E) + J^1(E) + J^2(E) + ... \tag{3.10}$$

The Fourier transformation of $J(E)$ is $j(\nu) = \int_{-\infty}^{\infty} J(E) \exp(2\pi \mathrm{i} \nu E) dE$ [41]. This leads to the following relationship:

$$j(\nu) = z(\nu) \exp[s(\nu)/I_0]. \tag{3.11}$$

The single-scattering distribution is calculated as described above by means of a MATLAB program provided by Egerton et al. [57]. As the ZL-peak is deconvolved with the measured spectra within this process, the ZL-peak is absent in the resulting spectrum. This is especially advantageous, if the investigated material exhibits strong excitations in the very low-loss region, which are usually superimposed by the ZL-peak. Figure 3.2 shows the effect of the deconvolution. In the measured EEL-spectrum of the charge transfer complex P3HT:F_4TCNQ a shoulder within the ZL-peak is clearly visible. After deconvolution it becomes obvious that the origin of the shoulder in the measured spectrum is an excitation peaking at 0.6 eV, which would not be visible without

data processing. Furthermore, the intensity of the deconvoluted spectrum is only slightly lower compared to the measured spectrum. This indicates that the impact of multiple-scattering on thin organic samples (40 nm −50 nm) is almost negligible with the present setup of our instrument. The spectrum from figure 3.2 will be explained in detail in section 6.5.

3.2.1.2. Kramers-Kronig-Relation

The optical properties of the investigated materials can be extracted from the energy-loss data. This is feasible, since, as shown in section 2.2 (equation (2.27)), the cross-section for inelastic scattering is related to the complex permittivity $\epsilon = \epsilon_1 + \mathrm{i}\epsilon_2$. As before, the contribution from multiple-scattering and the ZL-peak are removed by the deconvolution process explained in the previous section. The resulting single scattering spectrum $S(E)$ is described as follows [41]:

$$J^1(E) \approx S(E) = \frac{I_0 t}{\pi a_0 m_0 v^2} \mathrm{Im}\left[-\frac{1}{\epsilon(E)}\right] \ln\left[1 + (\frac{\beta}{\theta_\mathrm{E}})^2\right]. \tag{3.12}$$

I_0 is the zero-loss intensity, t the sample thickness, v the speed of the incident electron, θ_E the characteristic scattering angle for a particular energy loss and β the collection semi-angle. β denotes the angle under which electrons are collected in the spectrometer. In this work the angular distribution of the electrons is limited by the objective aperture. In order to enable comparability between the different measurements, all EEL-spectra were collected with the smallest possible objective aperture (30 µm). The resulting collection semi-angle β of 1.765 mrad was determined as described in [44]. As $\mathrm{Im}\left[-\frac{1}{\epsilon(E)}\right]$ is obtained by equation (3.12), $\mathrm{Re}\left[\frac{1}{\epsilon(E)}\right]$ can be derived from a Kramers-Kronig-relation [41]:

$$\mathrm{Re}\left[\frac{1}{\epsilon(E)}\right] = 1 - \frac{2}{\pi} P \int_0^\infty \mathrm{Im}\left[-\frac{1}{\epsilon(E')}\right] \frac{E' dE'}{E'^2 - E^2}, \tag{3.13}$$

where P is the Cauchy principal of the integral. For the calculations in this work the function is integrated over the measured energy range. Then, given $\mathrm{Im}\left[-\frac{1}{\epsilon(E)}\right]$ and $\mathrm{Re}\left[\frac{1}{\epsilon(E)}\right]$ one obtains the complex permittivity:

$$\epsilon(E) = \epsilon_1(E) + \mathrm{i}\epsilon_2(E) = \frac{\mathrm{Re}\left[\frac{1}{\epsilon(E)}\right] + \mathrm{iIm}\left[-\frac{1}{\epsilon(E)}\right]}{\left\{\mathrm{Re}\left[\frac{1}{\epsilon(E)}\right]\right\}^2 + \left\{\mathrm{Im}\left[-\frac{1}{\epsilon(E)}\right]\right\}^2}. \tag{3.14}$$

From the obtained dielectric functions $\epsilon_1(E)$ and $\epsilon_2(E)$ the real and imaginary part of the refractive index $n(E)$ and $k(E)$ can be determined:

$$n^2 = \frac{1}{2}\left(\sqrt{{\epsilon_1}^2 + {\epsilon_2}^2} + \epsilon_1\right), \tag{3.15}$$

$$k^2 = \frac{1}{2}\left(\sqrt{{\epsilon_1}^2 + {\epsilon_2}^2} - \epsilon_1\right). \tag{3.16}$$

The obtained results can be directly compared to the dielectric functions retrieved from optical measurements. Furthermore, if absorption is neglected for $E \to 0$ and the refractive index n is known, then equation (3.13) can be used to normalize the measured EEL-spectra to the refractive index. A detailed description of the normalization procedure can be found in the master thesis of Felix Schell [36].

The shape of the dielectric function allows an easier interpretation of the present excitations in the EEL-spectra. In conductors with quasi-free electrons the energy at which ϵ_1 is zero is taken as the collective excitation energy that corresponds to a plasmon peak in the energy-loss function. However, this does not apply for organic semiconductors, as the electrons are strongly bound. In this case the plasmon excitation can be described more precisely by an extended Drude model [55]:

$$\epsilon(E) = 1 - \hbar\omega_\mathrm{p}^2/(E^2 - E_\mathrm{b}^2 + \mathrm{i}E\Gamma),$$

where Γ is a damping constant, E_b the binding energy and ω_p the plasma frequency. The plasmon peak for organic compounds is broad due to strong damping. It typically occurs for $\epsilon_1 \approx \epsilon_2$ at low values for ϵ_2 at around 23 eV [55]. Figure 3.3 represents the results of a Kramers-Kronig analysis of measured EEL-spectra. Figure 3.3 a) shows the measured spectrum and the spectrum after deconvolution of an organic compound (F_4ZnPc, details will be explained in section 7.2.1). Figure 3.3 b) clearly shows that the shape of the energy-loss function $\mathrm{Im}\left[-\frac{1}{\epsilon(E)}\right]$ is proportionate to the measured spectrum and thus, in good agreement with the predictions of equation (3.12). In c) and d) the derived $\mathrm{Re}\left[\frac{1}{\epsilon(E)}\right]$, $\epsilon_1(E)$ and $\epsilon_2(E)$ are shown. As proposed by the extended Drude model the energy at $\epsilon_1 \approx \epsilon_2$, marked with black dashed lines at 23.6 eV in figure 3.3 d) is close to the measured plasmon maximum in a) at 22.2 eV (marked with blue dashed lines). The first crossing point of ϵ_1 and ϵ_2 at around 12 eV is not considered to be a plasmon as ϵ_2 exhibits a maximum at this energy. The peak is attributed to a single electron transition. The starting value for $\epsilon_1(E = 0)$ equals the squared refractive index (n^2) at energies well

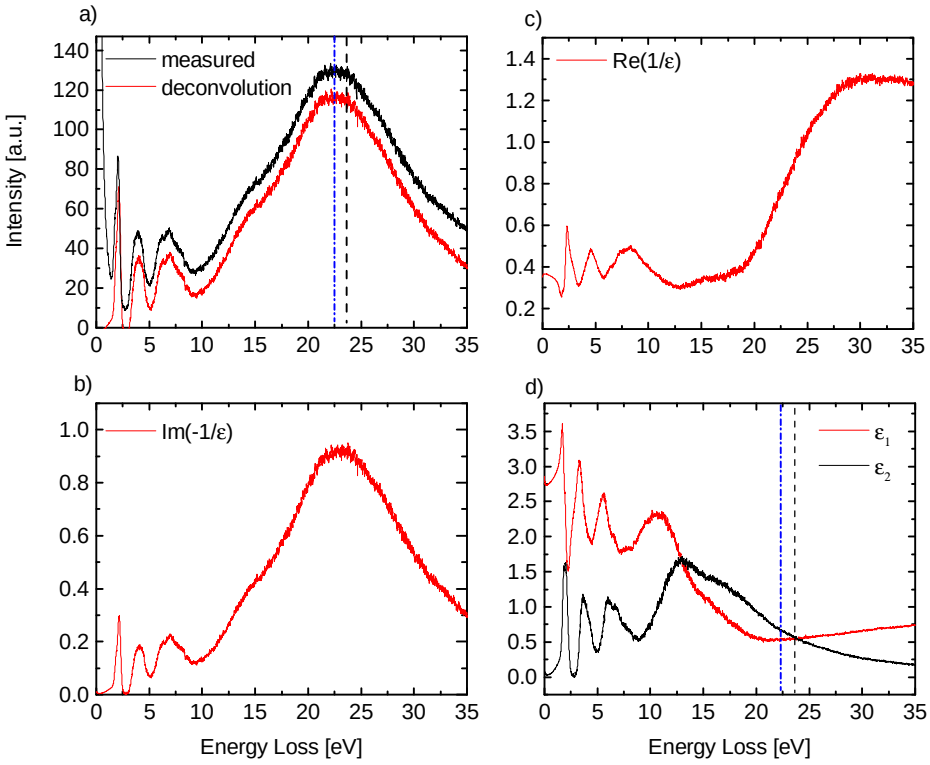

Figure 3.3: a) Prior to the Kramers-Kronig analysis, the ZL and multi-scattering events have to be removed by deconvolution (shown in red). b) The energy-loss function Im $\left[-\frac{1}{\epsilon(E)}\right]$ calculated from equation (3.12). The spectrum exhibits the same shape as the deconvolved spectrum from the measurement. c) The derived real part of the loss function Re $\left[\frac{1}{\epsilon(E)}\right]$ by means of the Kramers-Kronig relation. d) The resulting dielectric function. The energy at which $\epsilon_1 \approx \epsilon_2$ is satisfied, marked with black dashed lines (23.6 eV) in a) and d), is also close to the energy of the plasmon peak maximum (22.2 eV) in a) marked with blue dashed lines.

below the band gap of the material, which has to be determined by optical measurements prior to the analysis. It is one of the starting parameters along with the zero-loss integral, the incident-electron energy and the collection semi-angle beta that are necessary for the analysis. The refractive index is an important parameter as it determines if Cerenkov losses occur [58]. This is the case if the velocity of a charged particle in medium exceeds the speed of light. The emitted photons (Cerenkov radiation) lead to an additional energy loss of few eV especially for energies below the interband transitions [58]. This can falsify for example the determination of the band gap. However, as shown by Stöger-Pollach et al., for a refractive index below 2 and an electron accelerating voltage below 100 kV Cerenkov losses do not occur [58]. Hence, for the investigated materials in this work ($n \leq 2$) at 60 kV Cerenkov radiation is not considered. The Kramers-Kronig analysis in the present work was executed by means of a MATLAB program provided by Egerton et al. [57].

3.2.2. Electron Spectroscopic Imaging

In addition to the previous section, in which the entire spectroscopic range of the inelastically scattered electrons was of interest, a particular energy window can be selected. This is implemented by inserting a slit in the spectrometer plane. A schematic of the electron spectroscopic imaging (ESI), also known as energy filtered TEM (EFTEM) is shown in figure 3.1. The purpose of the slit is that only electrons that have lost a certain energy after specimen interaction contribute to the signal of the image. The resulting image is therefore also called monochromatic image. In this way features that appear bright in the image are assigned to the material in the sample that exhibits excitations at the chosen energy loss. As EEL features are characteristic, the energy filtered images enable the distinction of different compounds within the sample and reveal true material contrast [59]. A spatial resolution in the sub-nanometer range can be achieved especially for stable inorganic materials as demonstrated by Muller or Grogger et al. [60, 61]. This work focuses on EFTEM in the low-loss regime, as the cross-section for core-loss events is very low in organic materials and results in very weak image signals (see section 2.2).

Zero-loss images

For zero-loss images the energy filtering is applied in reverse. The slit selects a narrow window around the zero-loss peak in such a way that the the inelastically scattered electrons are filtered out and almost only the elastically scattered electrons contribute to the image. The slit leads to a better signal-to-noise

ratio, which in turn increases the contrast and the resolution. For this reason, all bright-field images in the present work were acquired with a zero-loss filter. The electron dose deposited on the sample during image acquisition at 89000 x magnification (0.21 nm/px), illumination step 14, and 500 ms exposure (if not indicated else) is about $5 \cdot 10^3$ e/nm^2.

3.2.2.1. ESI Series

One of the major advantages of EFTEM is that the distribution of different compounds can be resolved spatially due to their characteristic energy loss. This occurs, since inelastic scattering of electrons is a strongly localized process. However, especially for organic materials the loss spectra exhibit a strong overlap and very slight spectral differences. This hinders the classification of the pure materials in composites. Furthermore, thickness variations within the sample can increase the signal intensity. In order to overcome the mentioned issues an ESI series can be acquired [56, 62, 63]. In this case EFTEM images are collected successive over a broad energy range in steps. In this works series are acuired from 2 eV-35 eV in 1 eV steps if not indicated else. For an easier alignment (see 3.2.2.2) the ESI series starts with a ZL image and subsequently after every single inelastic image a further ZL-image is acquired. Additionally, in order to reduce noise, elastically scattered electrons at higher angles are filtered out by means of an objective aperture of 60 µm. As shown in figure 3.4, the profile of each pixel over the entire image stack represents an energy loss spectrum itself with a resolution corresponding to the energy step size and the inserted slit (for the present work around 2 eV due to the „broad" slit). By means of the available loss spectrum for every pixel and the known spectra of the pure materials present in the sample, each pixel can be assigned to one of the compounds. By comparing the plasmon peak positions for each pixel, Schaffer et al. demonstrated how to distinguish InAs quantum structures in a InP matrix [62]. A more detailed approach by multivariate statistical analysis (MSA) was introduced by Pfannmöller et al. for P3HT:PCBM organic solar cells [17, 56]. MSA is especially beneficial for organic materials that hardly differ in their spectral features. As both analysis procedures were applied in the present work, a short description will be given in the following. It has to be mentioned that the electron dose of 10^6 e/nm^2 for the settings used in this thesis (500 ms exposure for the ZL images, 5000 ms exposure for the energy filtered images, 89 kx magnification (0.21 nm/px), illumination step 14) deposited during the entire image series damages the sample. This is manifested in the disappearance of excitations in the loss spectrum. Yet the plasmon excitation, which is pivotal for the data analysis, is not affected.

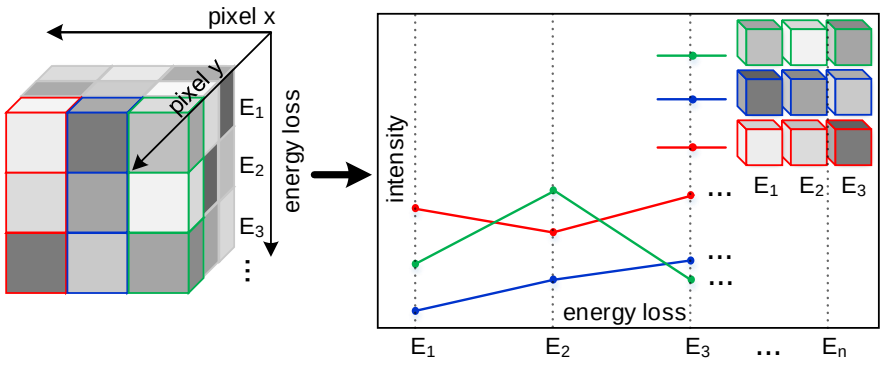

Figure 3.4: Schematic of the ESI series data stack. Every pixel from the first image over the entire series can be translated into an energy loss spectrum, with a resolution defined mainly by the energy steps.

Beam damage will be explained in detail in chapter 5.

3.2.2.2. Data Analysis

It is highly likely that there is a drift or film deformation during image series acquisition, especially if the sample is charged or damaged by the electron beam. Thus, an alignment of the image stack is crucial prior to data analysis. In this work an affine transformation is applied, which considers translation and rotation shifts as well as scaling factors and shearing effects. The procedure is applied to the ZL images from the ESI stack as they exhibit stronger contrast which facilitates the calculation of the alignment parameters. The latter are then applied to the energy filtered images. A detailed description of the alignment process is given in [56].

For a uniform illumination of the energy filtered images a further correction is needed. This is inevitable as a slight misalignment of the TEM can cause an illumination gradient in the images. For this purpose the plasmon peak position of each pixel in the stack is used as intensity value for the generation of a new image (plasmon peak map) [64]. By applying a very broad mean filter low frequencies in the plasmon map are suppressed and the resulting image reveals the magnitude of the illumination gradient. This gradient is then subtracted from the original images [62]. Further details on the correction of the so called non-isochromaticity are given by Felix Schell in his master thesis [36].

Plasmon Peak Mapping

One possible analysis method to reveal real material contrast from an ESI series is the plasmon peak mapping [65]. Especially if the investigated compounds exhibit a strong plasmon excitation peaking at distinct energies, like e.g. F_4ZnPc and C_{60} used in the present work, the plasmon map is a very convenient analysis method. As already explained in figure 3.4, each pixel in the acquired image stack represents a coarse energy loss spectrum. In order to determine the exact position of the plasmon peak maximum, a Gaussian fit is used. The plasmon map is generated with the peak positions from the fit taken as intensity values, the same way as it was done prior the isochromaticity correction. For the segmentation into two material classes, an Otsu threshold, which "maximizes the separability of the resultant classes in gray-levels" [66], is set. In this work, the chosen threshold for the maps maximizes the differences between the plasmon peak maxima of the two material classes.

Locally Linear Embedding

A more advanced statistical method for the data analysis of ESI series was introduced by Martin Pfannmöller [56]. In the following only a short overview of the locally linear embedding (LLE) [67] analysis is given. For an extensive explanation of the method and the used software ILASTIK [68], the author refers to the thesis of Martin Pfannmöller [56]. By applying LLE, pixels are segmented in statistically distinct classes resulting in well-separated data point clusters in the low-dimensional space. The normalized spectra of each pixel from the image stack represent a point in a space, with a dimension equivalent to the number of images in the series. For an easier handling of the data, the dimensionality of this space has to be reduced. For this purpose a set of pixels appearing bright at the characteristic energy loss of the different materials is chosen manually. For these pixels the local embedding can then be calculated by linear reconstruction of each data point from its neighbors with weight coefficients determined by a least-square fit. This coefficients are then used to determine the coordinates of all points that span the lower-dimension space. In a scatter plot the position of all pixels in the first three dimensions (in this thesis) of the new spanned space can be represented. This results in separated clusters, each corresponding to a different class. By means of a Random Forrest Classifier [69] the LLE components can be used for the classification of the pixels in the image stack. This leads to a two-dimensional projection, which represents a map that indicates the position of each class [56]. The advantage of this method is that the resulting number of classes is not chosen prior the

analysis manually, but is a statistical outcome.

3.3. Charge Carrier Mobility Measurements

For a comprehensive understanding of the charge transport properties in organic semiconductors two different techniques are applied in this thesis. In Charge Extraction by Linear Increasing Voltage (CELIV) the charge transport in diodes is measured throughout the whole organic layer perpendicular to the substrate between two electrodes. On the other hand, field-effect mobilities can be determined from the current-voltage characteristics of transistors. The advantage of applying two complementary methods is that the charge carrier mobilities are assessed from two different directions: along the substrate normal (CELIV) and parallel to the substrate along the dielectric interface (OFET). Therefore, anisotropic charge transport can be investigated.

3.3.1. Charge Extraction by Linear Increasing Voltage

In figure 3.5 the experimental technique is depicted schematically. The active layer (e.g. P3HT) in combination with the two electrodes forms a plate-capacitor structure. First, as visualized in figure 3.5, charges are generated after a short laser pulse (photo-CELIV) [70]. In order to trap the charges within the device an offset voltage V_{off} opposing the built-in-field is applied. Subsequently, a linearly increasing voltage ramp is applied and the current transient response is measured. The original rectangular shape of the current transient, which is characteristic for a capacitor, is superimposed by a peak caused by the extracted charges from the device. The exact peak position enables the calculation of charge carrier mobility and density [71]. Although the measurement setup is rather simple, the underlying theory and the assumptions necessary for the calculations are not trivial. Here, only the most important relationships are presented. For a detailed derivation the author refers to the master theses of Carsten Leinweber, Lars Müller, and further reading [72–78]. One important assumption is that for a sample with finite thickness d there is a blocking contact at $x = 0$. By applying a voltage all charge carriers at $x = l(t)$, where $0 < l(t) < d$, are extracted at a time t. In order to determine $l(t)$ the Poisson equation ($\nabla E = \frac{\rho(\mathrm{x})}{\epsilon_0 \epsilon_\mathrm{r}}$) and the continuity equation ($\frac{d\rho}{dt} + \mathrm{div}\boldsymbol{j} = 0$) are integrated from 0 to d and combined with:

$$j_\mathrm{d} = \sigma E(d,t) = en\mu E(d,t),$$

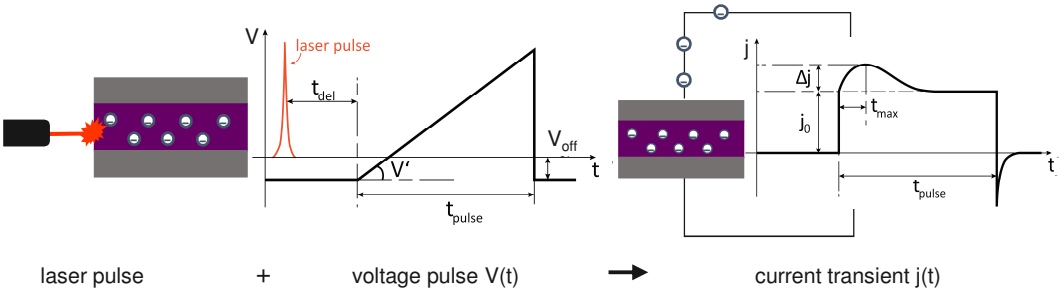

Figure 3.5: Schematic of the CELIV measurement technique. Charges in the sample are generated by a short laser pulse and extracted by a linear increasing voltage ramp. The mobility can be determined from the measured current transient. Based on [78]

resulting in a first-order differential equation:

$$\frac{dl(t)}{dt} + \frac{\sigma}{2d\epsilon_0\epsilon_r} l(t)^2 = \mu \frac{V't}{d}, \tag{3.17}$$

with $V't$ representing the linear voltage ramp. Lorrmann et al. solved analytically the Riccati-type equation (3.17), though leading to an expression with a dependence of the charge density n and charge mobility μ [77]. They derived the parametric equations:

$$\mu = \frac{d^2}{2V't_{\max}^2} \left(\frac{1}{6.2.(1 + 0.002\frac{\triangle j}{j_0})} + \frac{1}{(1 + 0.12\frac{\triangle j}{j_0})} \right)^2, \tag{3.18}$$

and

$$n = \frac{\epsilon_0\epsilon_r}{ed^2} \frac{V't_{\max}}{0.455} \frac{\triangle j}{j_0} \left(1 + 0.238\frac{\triangle j}{j_0} \right), \tag{3.19}$$

that can now be used for the calculation of the charge carrier mobilities and density.

3.3.2. Field-Effect Mobilities

In order to extract the charge carrier mobilities from the current voltage characteristics of a transistor within the saturation regime the MOSFET

(metal-oxide-semiconductor field-effect transistor) model is applied [79]:

$$I_{\mathrm{DS}} = \frac{1}{2}\mu_{\mathrm{sat}} C' \frac{W}{L}(V_{\mathrm{GS}} - V_{\mathrm{th}})^2,$$

where I_{DS} describes the drain-source current and C' the capacitance of the gate dielectric. W and L denote the width and length of the channel. V_{GS} describe the gate-source and V_{th} the threshold voltage. However, as the MOSFET model was originally developed for inorganic transistors it does not consider the often non-negligible contact resistance in organic transistors. In order to check the significance of the resistance for the calculated mobilities, the so called transmission line model (TLM) is applied [79] [79]:

$$R_{\mathrm{tot}} = R_{\mathrm{C}} + R_{\mathrm{CH}} = R_{\mathrm{C}} + \frac{L}{WC\mu(V_{\mathrm{GS}} - V_{\mathrm{DS}})}.$$

R_{tot} describes the total resistance of the transistor and R_{C} and R_{CH} the contact and channel resistance. L and W define the length and width of the channel, C the capacitance of the dielectric, V_{GS} the gate-source, and V_{DS} the drain-source voltage.

4. Organic Semiconductors and Sample Preparation

This chapter focuses on the details about materials and sample preparation, which are needed for a better understanding of the results in this work. After introducing the intrinsic material properties, the device fabrication of diodes, organic field-effect transistors and small molecule solar cells is explained. In the last part of this section two of the most common techniques for TEM sample preparation, floating and focused ion beam milling, are introduced.

4.1. Materials

The investigated organic materials in this work comprise polymers and small molecules. The materials are distinguished between p-type (donor) and n-type (acceptor) semiconductors.

Poly(3-hexylthiophen-2,5-diyl) (P3HT)

P3HT is a conjugated polymer with a monomer which consists of a thiophene ring and an alkyl chain. The determined energy levels from photoemission spectroscopy are $E_{\mathrm{HOMO}} = 4.65\,\mathrm{eV}$ and $E_{\mathrm{LUMO}} = 2.13\,\mathrm{eV}$ [81]. The structure is shown in figure 4.1. Due to the energy levels and the strong absorption between 400 nm and 600 nm, P3HT is often used as donor and absorber in bulk heterojunction solar cells with the fullerene derivative PCBM [82]. As a p-type semiconductor, P3HT is also used in organic field-effect transistors [83]. In polymers molecular weight (MW), polydispersity (PD) and regioregularity (RR) are decisive for the structure and ordering, as will be discussed in chapter 6. The P3HT used in this thesis is purchased from Merck KGaA (*lisicon*® SP001).

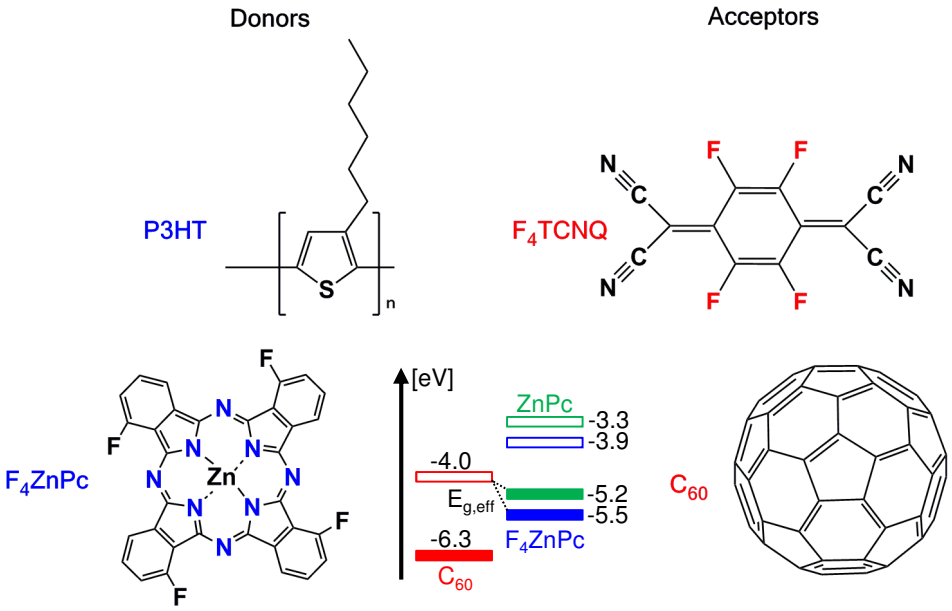

Figure 4.1: Chemical structures of the donor molecules P3HT and F_4ZnPc and acceptor molecules F_4TCNQ and C_{60} used in this work. The energy level diagram for ZnPc, F_4ZnPc, C_{60} indicate the effective band gap in a blend [36]. Values for ZnPc taken from [80].

2,3,5,6-Tetrafluoro-7,7,8,8-tetracynoquinodimethane (F_4TCNQ)

Due to the fluorination, F_4TCNQ is a strong acceptor with high electron affinity ($E_{LUMO} = 5.24\,eV$, $E_{HOMO} = 8.34\,eV$) and hence often used for p-type doping of evaporated or solution processed organic semiconductors [80, 84]. Moreover, F_4TCNQ is known to strongly interact with the donor molecules and to form charge transfer complexes [85, 86]. The structure is shown in the upper right corner in figure 4.1.

Buckminsterfullerene C_{60}

The chemical structure of C_{60}, also known as buckyball, is shown in figure 4.1 on the bottom right. C_{60} is one of the most used acceptors in organic solar cells, due to its relatively high electron mobility and crystalline texture [19, 87]. Additionally, the spherical symmetry is robust to twisting, which leads to a high electrical conductivity that is resistant to disorder [19]. The energy gap of C_{60} of 2.35 eV is determined by the energy levels $E_{HOMO} = 6.35\,eV$ and $E_{LUMO} = 4.0\,eV$ (from photoemission spectroscopy) [88]. C_{60} with purity $> 99.9\,\%$ was purchased from American Dye Source (ADS) and used as received.

Fluorinated Zinc Phtalocyanine (F_4ZnPc)

F_4ZnPc is the fluorinated derivative (only four hydrogen atoms are replaced by fluorine) of the well known planar molecule ZnPc, which is often used as donor material in small molecule solar cells. The chemical structure is shown in figure 4.1 on the bottom left. Fluorine is known to be a strong acceptor (see also F_4TCNQ) lowering the energy levels without significantly influencing the HOMO-LUMO gap, hence sustaining the good absorption properties of ZnPc [89, 90]. For this work F_4ZnPc is chosen over ZnPc as the lower energy levels ($E_{HOMO} = 5.46\,eV$ and $E_{LUMO} = 3.9\,eV$) increase the effective band gap ($E_{g,eff} = IP_{donor} - EA_{acceptor}$) when blended with C_{60}. This yields a higher open-circuit voltage in solar cells (see figure 4.1) [89]. Similar to other phtalocyanines, F_4ZnPc is expected to crystallize in different polymorphs [91]. F_4ZnPc for this work was provided by BASF SE and purified by sublimation before use.

4.2. Devices

In the following the fabrication processes for P3HT diodes, P3HT OFETs, and $F_4ZnPc:C_{60}$ BHJ solar cells are presented. All substrates (glass for OFETs, ITO-glass for diodes and solar cells) are cleaned prior use in an ultrasonic bath for 10 min in acetone and afterwards for 10 min in isopropanol. The ITO-glass is afterwards treated with oxygen plasma for 5 min, which increases the work function and hence facilitates injection of holes. Moreover, plasma treatment improves the surface wetting behavior of ITO for water-based solutions like PEDOT:PSS [92].

4.2.1. P3HT Diodes

The presented P3HT diodes in this thesis were fabricated and electrically characterized within the scope of the supervised master thesis of Lars Müller [78]. Structured ITO (indium tin oxide, resistivity 8.4Ω)[1] is used as anode for the P3HT diodes. PEDOT:PSS (Heraeus, *Clevios*^{TM}) is diluted with water in a 1:1 ratio, filtered with a 0.45 µm filter and spin coated in a two step procedure (step 1: acceleration 4300 rpm/min, velocity 1000 rpm for 10 s; step 2: 4300 rpm/min, 4300 rpm for 30 s) on top of the ITO. After annealing for 30 min at 140 °C in order to get rid of the water in PEDOT:PSS, the P3HT is spin coated (1500 rpm/min, 1000 rpm for 30 s) from a chlorobenze solution (40 mg/ml, stirred for 3 h at 80 °C). The resulting layer thickness is around 120 nm. As will be discussed in section 6, depending on the experiment, the sample is annealed after spin coating of P3HT. A 100 nm thick aluminum (Al) electrode is evaporated on top. A top and a side view of the device architecture is shown in figure 4.2 a) and b). The resulting active layer of 1 mm^2 is chosen due to the resulting low capacitance of the device, which is a requirement for the CELIV mobility measurements [74]. In order to avoid degradation as CELIV measurements are performed under ambient conditions, the active layer is encapsulated with a barrier foil (3M, FTB3-125a).

4.2.2. P3HT Transistors

The field-effect transistors shown in this work were produced and electrically characterized by Milan Alt (Karlsruhe Institute of Technology). The device architecture of the top gate P3HT transistor is shown in figure 4.2 c). First, Source and Drain electrodes out of 60 nm thick silver (Ag), with a sticking

[1] Structuring is carried out by photolithography. Details and parameters can be found in the master thesis of Lars Müller [78].

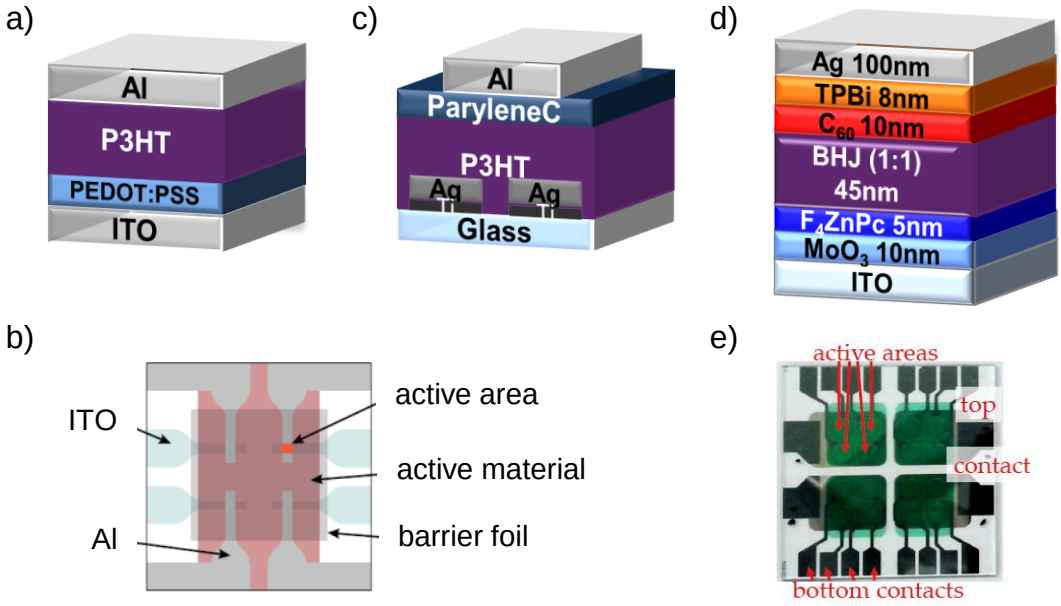

Figure 4.2: Device architectures used in this thesis. a) Side view of the P3HT diode. b) Top view of the diode. Image taken from [78]. c) Side view of the P3HT OFET. d) Side view of the F_4ZnPc:C_{60} BHJ indicating the layer thicknesses. e) Top view of the solar cell device structure. Image taken from [36].

layer of 5 nm to 10 nm thick titanium, were evaporated onto a glass substrate. Afterwards, P3HT is spin coated from the exact same solution as used for the diodes with the exact same parameters. After annealing in the glovebox (parameters discussed in section 6) the device is coated with 300 nm ParyleneC, which at the same time acts as dielectric and encapsulation in the transistor. Subsequently, 100 nm of Al are evaporated as a gate electrode on top.

4.2.3. Small Molecule Solar Cells

Fabrication and I-V characterization of the small molecule F_4ZnPc:C_{60} solar cells is carried out by Michael Scherer within the scope of the co-supervised master thesis of Felix Schell [36]. The used device layout along with side view of the stack with indicated layer thicknesses are shown in figure 4.2 d) and e). The circular solar cells exhibit an active area of 4 mm^2. Contact with the ITO is realized through metal rings surrounding the active area and connected to a small panel. All layers are deposited by thermal evaporation in the integrated vacuum system *Clustertool* at a pressure of about 10^{-7} mbar. Evaporation rates are monitored via quartz crystal microbalances. The tooling factor is

determined from thickness measurements by means of ellipsometry. After deposition of MoO_3 and F_4ZnPc, the BHJ is deposited by co-evaporating F_4ZnPc and C_{60} in a 1:1 volume ratio. For the heated devices the substrate is heated to 100°C ± 10°C during co-evaporation. For this purpose an infrared Elstein SFH4 heater was integrated in the vacuum chamber (for details see [36]). After the samples have cooled down, the hole blocking layer TPBi[2] and the Ag top contact are evaporated. Eventually, the solar cells are characterized with a solar simulator (LOT-Quantum Design) under a AM 1.5 illumination in the glovebox. The I-V curves are recorded by means of a Keithley 2601B SYSTEM Source Meter. The contacting for this setup via alligator clips can lead to uncertainties regarding the short circuit current.

4.3. TEM Sample Preparation

In this section the preparation techniques of TEM specimens will be explained. The most common method, used as well for the samples in this work, is floating. A more advanced technique is the milling of a TEM lamella by a focused ion beam. Both methods have advantages as well as drawbacks which are discussed in the following.

4.3.1. Floating

Floating is a very fast and convenient technique for TEM sample preparation and widely accepted in the TEM community. In order for the floating process to be successful, a water soluble layer has to be deposited prior the actual film. The stack is slowly dived into deionized water and when the underlying layer is dissolved, the layer of interest swims on the water surface. It is picked up by a TEM grid and then mounted in the TEM holder. The floating process is described in figure 4.3 a). The used grids in this work, Quantifoil®, 3 mm in diameter, consist of a copper grid covered with a carbon holey film, as depicted in figure 4.3 b). The grids are cleaned with a 10 s oxygen plasma before use, such that they are hydrophilic afterwards. In this work PEDOT:PSS is used as the water soluble layer, which is spin coated on top of ITO glass in a two step process in order to obtain homogenous layers (step 1: acceleration 4300 rpm/min, velocity 1000 rpm for 10 s; step 2: 4300 rpm/min, 4300 rpm for 30 s; annealing for 30 min at 140 ℃). Using PEDOT:PSS is an advantage as it is often used as hole transport layer on top of ITO. In that way the film growth conditions of the layer are the same as in devices. Subsequently, the

[2] 2,2',2"-(1,3,5-Benzinetriyl)-tris(1-phenyl-1-H-benzimidazole)

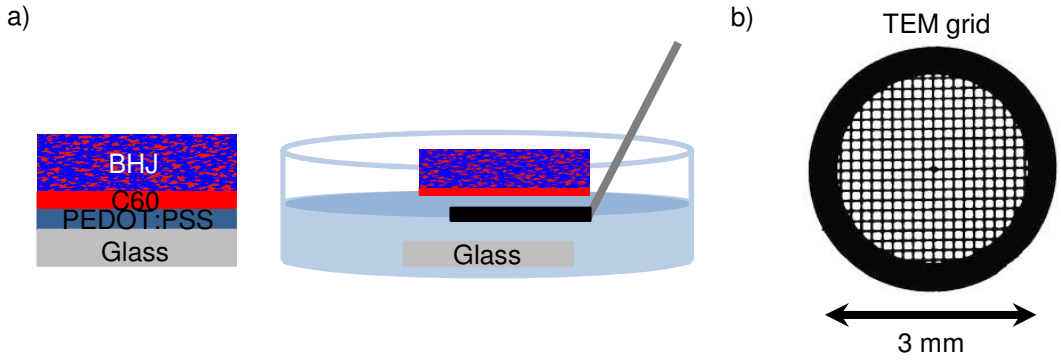

Figure 4.3: a) Illustration of the floating process. The investigated stack consisting of a BHJ and a transport layer (e.g. C_{60}) is floated off the substrate as PEDOT:PSS dissolves in water and is picked up by a TEM grid. b) The structure of a copper TEM grid.

active layer is deposited on top (typically 40nm to 50nm for transmission measurements). As the active layer of the investigated F_4ZnPc:C_{60} devices in this work is 45 nm the same thickness is used for the TEM samples in order to achieve maximal comparability between the device and TEM measurements. However, the underlying layer used in these kind of devices is different than PEDOT:PSS. Here, F_4ZnPc is used as underlying layer in non inverted and C_{60} in inverted F_4ZnPc:C_{60} BHJ solar cells. Therefore, the appropriate transport layer is deposited on top of PEDOT:PSS followed by the BHJ. The whole stack, consisting of the transport layer and the BHJ is floated off the substrate and picked up with the TEM grid (see figure 4.3). As usually transport layers are about 5 nm the signal arising from the layer is superimposed by the signal of the BHJ and does not disturb the measurement. In such way, process conditions are kept exactly the same as in the device, which is very important for substrate dependent thin film growth. One drawback is that at least one of the layers is in contact with water. However, from a comparison of a floated and a directly evaporated BHJ layer on a TEM grid (see appendix A), it can be concluded that the water has no impact on the morphology.

4.3.2. Cross-Sections by Focused Ion Beam Milling

A further TEM sample preparation technique is the focused ion beam (FIB) milling of TEM lamellas. This technique has the advantage that the morphology of vertical devices, such as solar cells or OLEDs, can be investigated in the cross-section prepared from a fully working device. Furthermore, it enables imaging

of interfaces between transport and active layers. For inorganic materials TEM lamella preparation is one of the standard procedures, however for organic materials there are very few successful examples. The main challenge to overcome is the amorphization of the organic materials from the milling with Ga^+- ions [93, 94]. Due to their higher mass than electrons, the ions have a very high momentum and penetrate the layers easily. Under direct exposure it is even possible to electronically dope the treated material, as was shown by Saive et al. for pentacene field effect transistors [95].

Within this work a technique had to be developed for the preparation of TEM lamellas from organic devices by means of a Carl Zeiss Crossbeam® Workstation AURIGA™ . Figure 4.4 indicates each step of TEM lamella processing. To protect the active layer from the Ga^+- ions, a 0.9 µm thick platinum layer is deposited from the gas injection system (GIS). Afterwards a slice is milled into the sample (figure 4.4a)) with a high current of 2 nA at 30 kV. This slice is cut off at both sides and at the bottom and is then lifted out from the sample by a micromanipulator (figure 4.4b)), which is attached to the slice by a platinum deposition. After lift out, the lamella is attached to a TEM grid, shown in 4.4c) and d), again by a platinum deposition [96]. Few measuring windows are polished down to approximately 100 nm thickness (figure 4.4e)) starting with a current of 5 pA and going down to 2 pA. At the end the whole lamella is "showered" with 20 pA at 5 kV to remove the first few nm at the surface, penetrated by the Ga^+- ions. This is necessary, as the penetration depth depends on the primary energy of the ions and the atomic number Z of the penetrated medium [97]. The incident ion beam is perpendicular to the top of the sample, thus the sidewalls of the lamella, which are of interest, are not penetrated directly by the ions. It has been reported that the penetration depth in silicon is reduced from around 22 nm at 30 kV to 2.5 nm at 5 kV acceleration voltage, compared to more than 100 nm penetration depth if the incident beam is perpendicular to the sample surface [93]. However, as the atomic number of silicon is higher than for carbon, it is estimated that damage in organic materials occurs deeper than 20 nm even after polishing with 5 kV.

The described method was used for lamella preparation from organic BHJs (P3HT:PCBM, F_4ZnPc:C_{60}), but TEM measurements did not reveal material contrast on the length scale of typical domain sizes $\sim$ 20 nm due to amorphization of the organic layers. The TEM lamella preparation technique was applied successfully for differently processed P3HT/PCBM bilayers to study the interdiffusion at the interface, as the required lateral resolution is lower. In energy filtered TEM images it could clearly be distinguished between the two materials. The interface is clearly visible and the difference between a laminated bilayer stack and a spin coated one from orthogonal solvents is

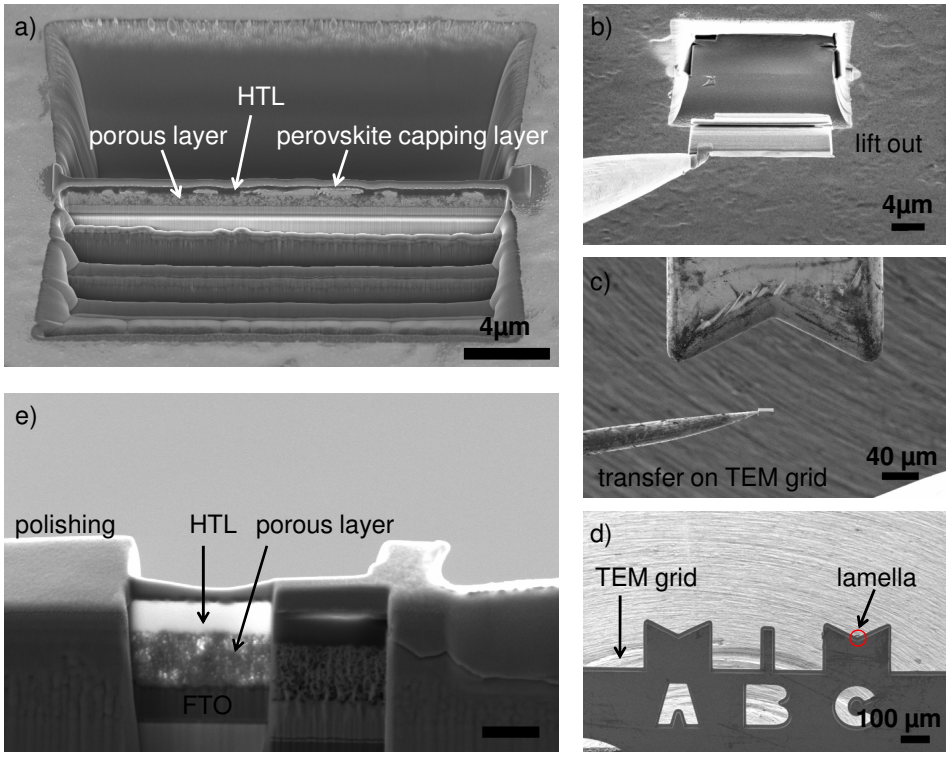

Figure 4.4: TEM lamella fabrication process. a) Milled slice in a perovskite solar cell. b) Lift out using a micromanipulator. c) Attachment to a TEM grid. d) Overview of a lamella attached to a TEM grid. e) Polished measuring window.

obvious (images shown in appendix A). Furthermore, the lamella preparation method was successfully applied for hybrid solar cells, consisting of a TiO_2 mesoporous scaffold, filled with $CH_3NH_3PbI_{3-x}Cl_x$ (perovskite) and an organic hole transport material on top. The TiO_2 scaffold provided high stability for the entire stack during the milling process, such that reproducible cross-sections were fabricated. Morphology differences visible in the cross-sections were correlated to varying device performance, which demonstrated that TEM lamella preparation is a very powerful technique. As this topic is beyond the scope of the present work, further details can be found in my publication [98].

5. Preparatory Study on Beam Damage: Polymers vs. Small Molecules

In this chapter an extensive study on electron beam damage of the investigated materials is presented. For this purpose, EEL-spectra, which describe the characteristic signature of compounds, were collected sequentially after illumination with a certain electron dose [99]. The electron dose was determined by measuring the beam intensity in vacuum on the CCD camera in e/nm^2s . The entire dose is derived from the illumination time. The impact of beam damage is important for ESI series acquisition, as the series requires a high dose of $10^6\,e/nm^2$. Especially the development of the plasmon peak with increasing electron dose is monitored, since the distinction of different materials in blends is based on energy filtered images at the plasmon energy loss. In the following, the behavior of C_{60} and PCBM under illumination is described. Beam stability of polymers and small molecules is discussed and compared with their stability within composites. For better visualization, the spectra were smoothed over 31 data points, which corresponds to 0.1 eV. Here, the spectra are described qualitatively. A detailed description of all features and their origin is presented in chapters 6 and 7.

PCBM vs. C_{60}

In figure 5.1 EEL-spectra of C_{60} and its derivative PCBM[1] are shown. The first recorded spectrum is displayed in black, followed by several spectra after sequential illumination. The spectrum in red is the last recorded spectrum after an illumination of 4 min for C_{60} and 3 min for PCBM in total.

[1] PCBM ([6,6]-phenyl-C61-butyric acid methyl ester) is introduced in this chapter for a better understanding of beam damage mechanisms in C_{60}. PCBM will not find further mention in the remaining chapters.

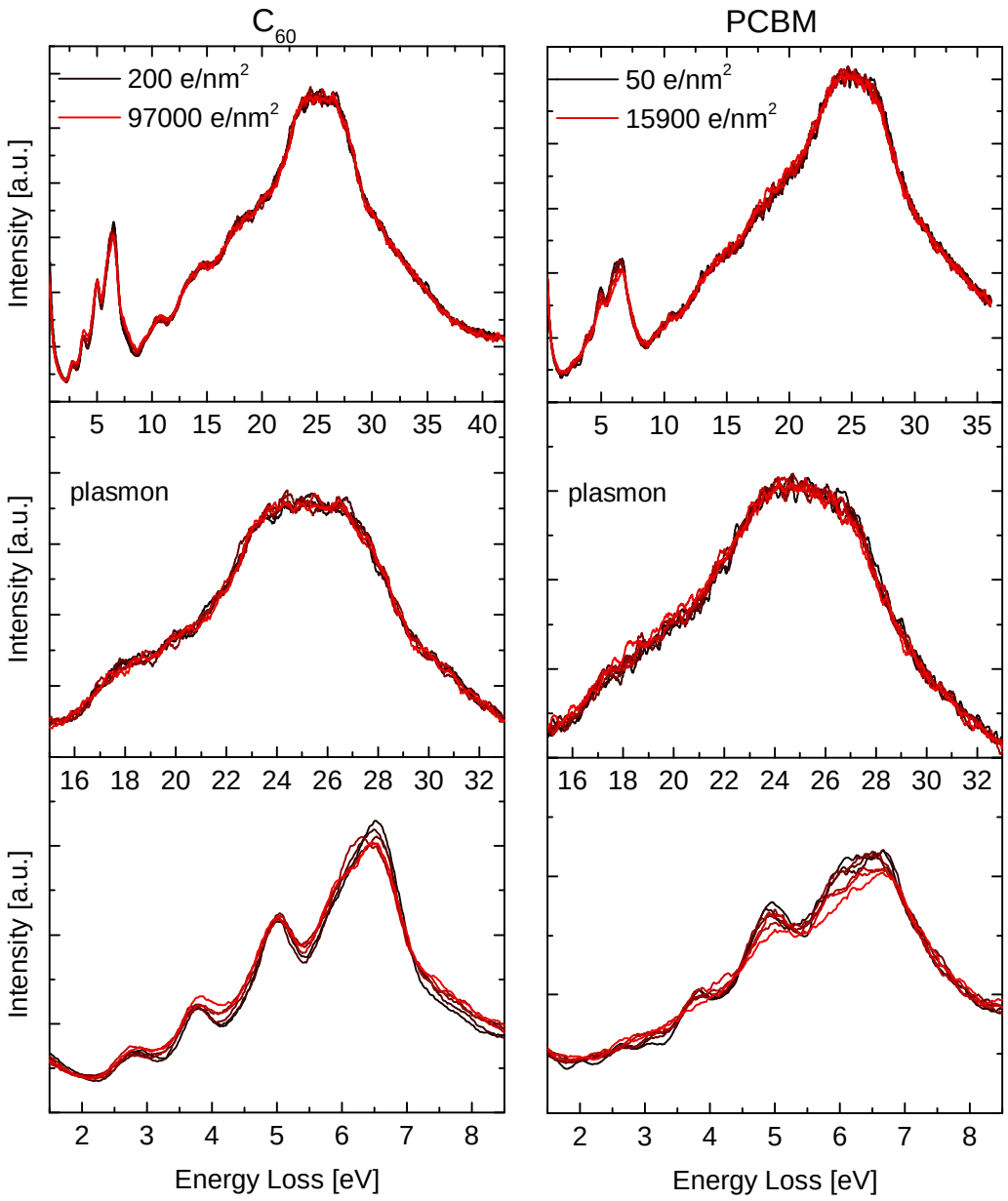

Figure 5.1: EEL spectra before (black) and after (red) illumination of (left) C_{60} illuminated for 4 min and (right) of PCBM illuminated fro 3 min in total. The top spectrum is a survey spectrum. The middle part of the plot shows a zoom on the plasmon peak. The bottom spectrum represents the very low loss region.

The spectra on top in figure 5.1 represent the energy loss over a wide energy range. C_{60} exhibits sharp peaks in the lower energy loss and a characteristic shape of the plasmon excitation at around 25 eV. Due to the side group on the fullerene the spectral shape of PCBM is different. The features between 2 eV and 8 eV are not as sharp as for C_{60} and the plasmon is broadened. However, as can be seen in the spectra in the middle part, in both cases the plasmon excitation is not affected by beam damage in the investigated dose range. This is beneficial for ESI series as will be shown later on. In the low energy loss region on the bottom of figure 5.1 it is observed that the features of PCBM smear out at a lower electron dose compared to C_{60} where no change of the peaks is observed up to almost 10^6 e/nm^2. PCBM is not investigated up to this electron dose as it will not be used for further measurements in this thesis. The C_{60} derivative is understood to be more sensitive than C_{60} in the electron beam as the side chain makes the molecule susceptible to faster damage.

F_4ZnPc vs. P3HT

In figure 5.2 the behavior of F_4ZnPc and P3HT under the electron beam is compared. The first recorded spectrum is shown in black. Four spectra after sequential illumination are shown in dark red and with dashed lines. The last recorded spectrum after the highest dose is shown in red. In both cases the loss spectra over a wide energy range shown on top in figure 5.2 seem to change. The zoom on the plasmon peak in the middle reveals instability for P3HT already at a lower electron dose of 10^3 e/nm^2 compared to the plasmon of F_4ZnPc which does not change significantly. It seems that beam damage occurs faster in polymers. A possible explanation is that the electrons from the beam are dissipated faster by the F_4ZnPc molecule. This is likely, as F_4ZnPc is a planar molecule. Due to the planarity, the overlap of the π-orbitals is very strong which leads to strong delocalization. In comparison, the polymer chains in P3HT are not planar as they tend to twist. Therefore, the overlap is not as high as in planar molecules or even interrupted, which results in a weaker delocalization [100]. Hence, the electrons cannot be dissipated fast enough away from the polymer, which is likely to cause damage. Beam damage can induce changes in the plasmon energy as the plasmon represents a collective excitation of $\pi-$ and σ- electrons. In figure 5.2 (middle) a slight shift (~ 1 eV) of the P3HT plasmon towards higher energies and a decrease of the intensity is observed. The decrease of the intensity points to a decrease of the film thickness. This is possible in case the polymer is heated by the electron beam. The HOMO-LUMO transition of P3HT at 2.6 eV (figure 5.2 bottom) is

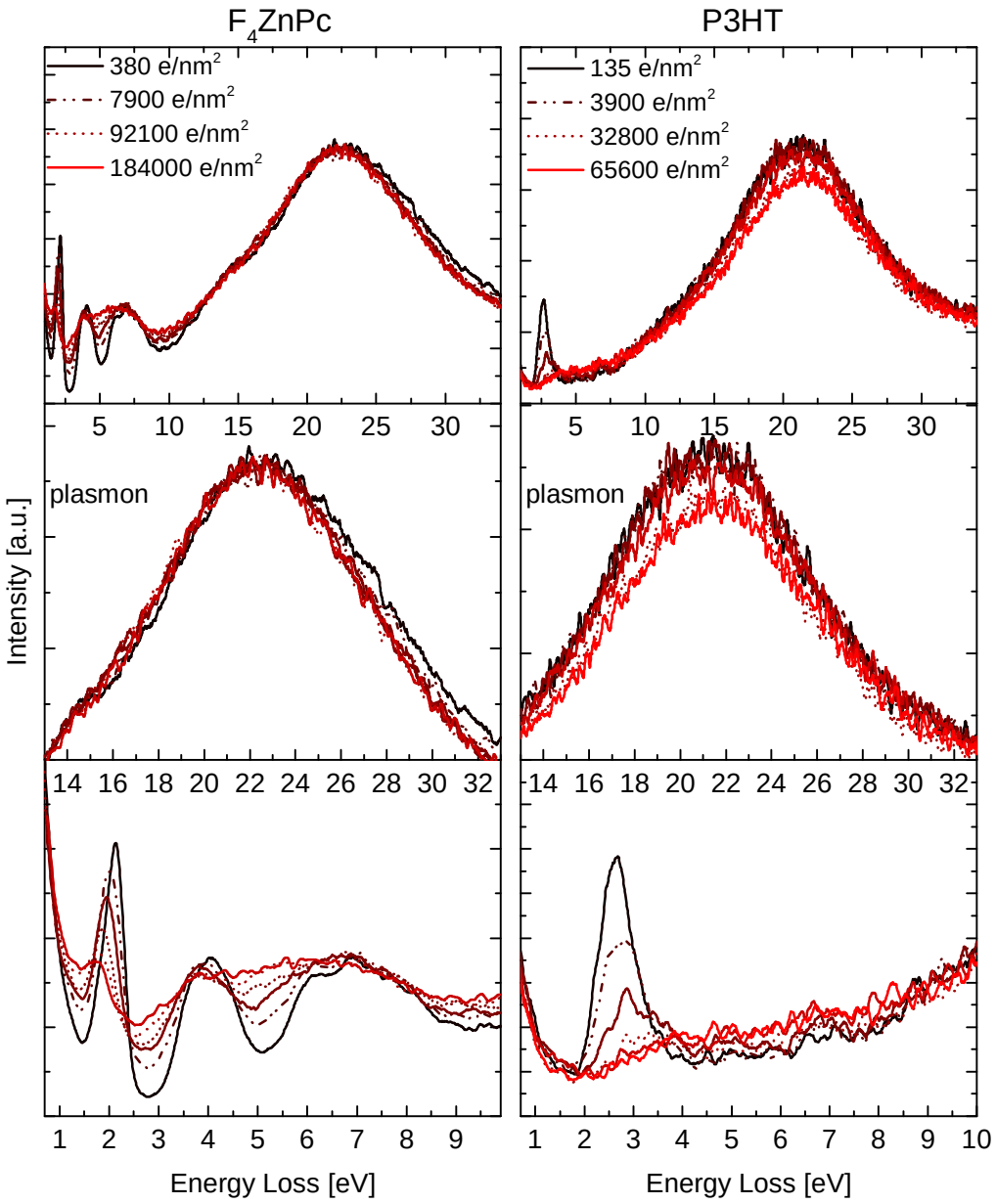

Figure 5.2: EEL spectra of (left) P3HT and (right) F_4ZnPc before illumination (black). Four spectra after sequential illumination are shown in dark red and with dashed lines. The last spectrum (highest dose) is shown in red. In the energy region of HOMO-LUMO transitions (bottom) significant beam damage is observed for both materials.

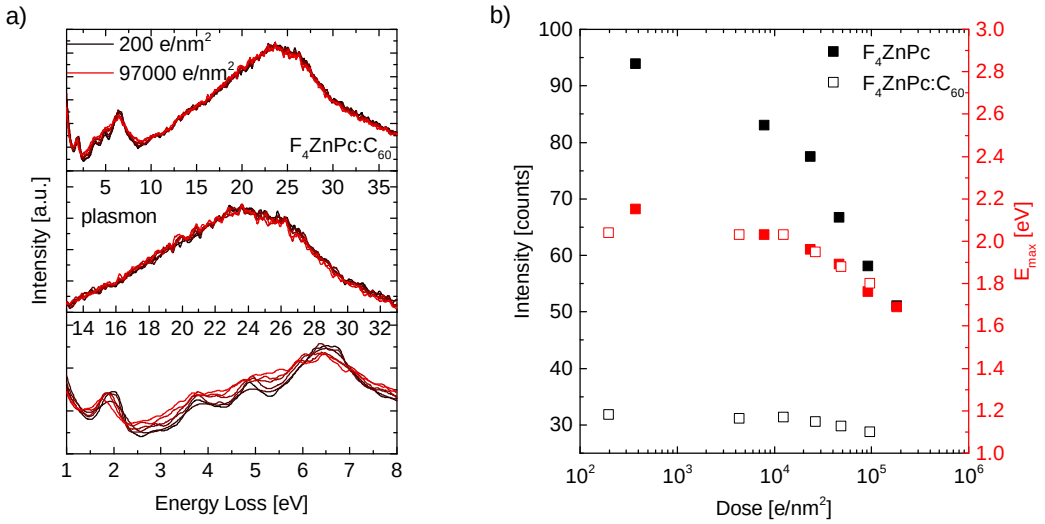

Figure 5.3: a) EEL spectra of a $F_4ZnPc:C_{60}$ blend before (black) and after (red) electron beam exposure. b) Correlation between the electron dose, the intensity and the energy position of the HOMO-LUMO transition of F_4ZnPc in a pristine and blended layer. Pure F_4ZnPc is more sensitive to beam damage than in a blend.

completely destroyed after 30 s of electron beam exposure, whereas for F_4ZnPc an energy shift towards smaller frequencies and a drop of intensity can be observed. The HOMO-LUMO gap is a result of conjugation in the organic molecules. The conjugation is strongly affected by the electron beam. In both cases it is clear that energy filtered images will not reveal material contrast in the low loss regime as excitations are shifted or destroyed already for an electron dose lower than required for EFTEM.

Bulk Heterojunctions

In the following, the impact of electron beam damage on BHJs will be discussed. In figure 5.3 a) (top) the whole range of the EEL-spectrum of a $F_4ZnPc:C_{60}$ blend is shown. The shape of the spectrum appears as a superposition of the spectra of the pure materials (will be explained in detail in 7.2.3). In the plasmon region shown in the middle part of figure 5.3 changes of the spectra are not observed. Hence, the composite is resistant against beam damage. A very interesting effect can be observed in the bottom spectra in 5.3 a). First of all, the transitions of the C_{60} between 3 eV and 7 eV are smeared out and decrease in intensity, which was not the case for the pure compound.

A similar effect has been observed for polymer solar cells with the fullerene derivative PCBM [101–103]. It is reported that the interfacial charge transfer (CT) state in the blend partially recombines in the polymer triplet state [101]. The remaining excited CT states trigger electron transfer to contaminants and thus generating reactive species. As this process is mainly driven by the interfacial states in a blend, this would explain the stability of the pure fullerene [104]. Additionally, the intensity of the excitation at 2.6 eV decreases very slightly and the peak maximum is not shifted towards smaller energies as was the case for pure F_4ZnPc. In the literature it is reported that PCBM can mediate stabilization of polymers [102]. This is owed to the fact that the degradation process happens through the acceptor, such that the polymer (donor) is not oxidized. The analogy to the considered materials here can elucidate the stabilization of F_4ZnPc in a F_4ZnPc:C_{60} blend. A further aspect leading to the stabilization of the donor material by adding an acceptor (e.g. PCBM or C_{60}) is the excited-state quenching, which reduces the reactivity of the donor [104–107]. Figure 5.3 a) (bottom) reveals quenching of the HOMO-LUMO transition of F_4ZnPc at around 2.6 eV as the relative intensity between the HOMO-LUMO and the plasmon peak is reduced compared to the relative intensities in the spectrum of pure F_4ZnPc in figure 5.2. Hence, the beam damage measurements are in agreement with the literature reports that degradation of the blend under light exposure is triggered by the fullerene and the stability of the donor increases.

In figure 5.3 b) the relationship between the intensity and the energy shift of the HOMO-LUMO transition of pure and blended F_4ZnPc and the electron dose is shown. For the pure material a decrease of around 40 % in intensity and a shift of $\triangle E = 0.4$ eV of the excitation energy is observed, whereas no change in intensity and only a slight shift of $\triangle E = 0.2$ eV is noted for the blend. F_4ZnPc is stabilized in the BHJ. This is the opposite effect compared to C_{60}, which is less stable in the blend.

A further study is carried out for BHJs deposited on pure F_4ZnPc or C_{60}, which are normally used as transport layers for this type of BHJs. Figure 5.4 shows the lower energy loss region for both cases. In the BHJ deposited on C_{60} (a) the transitions of C_{60} between 3 eV and 7 eV can be clearly distinguished from each other even after a high dose of 10^5 e/nm^2. This is not the case for the BHJ on F_4ZnPc shown in b). Moreover, the intensity of the HOMO-LUMO transition of F_4ZnPc in the blend deposited on pure F_4ZnPc decreases faster than for the blend on C_{60}. The instability of the excitations of C_{60} and F_4ZnPC in b) compared to a) is influenced by the underlayer. C_{60} is known to be a good electron transporter. The electrons from the beam are therefore dissipated faster away from the sample to the holder and cannot cause as much

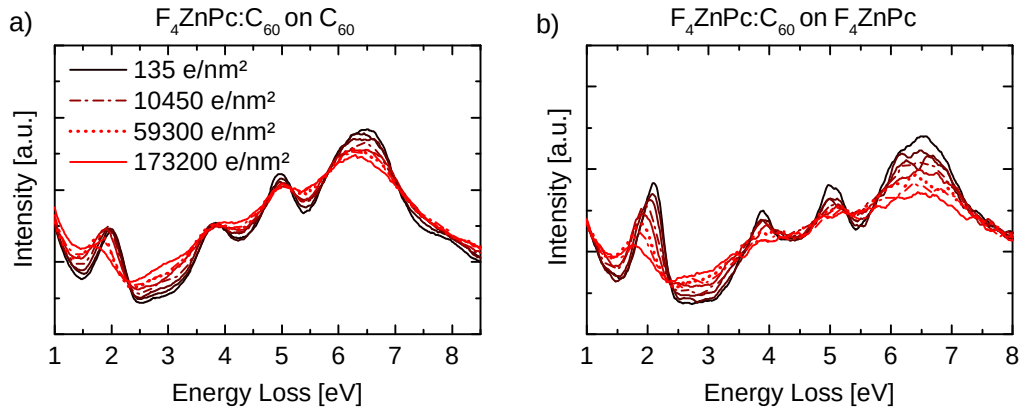

Figure 5.4: EEL spectra in the very low loss regime of a) a F_4ZnPc:C_{60} blend deposited on pure C_{60} and b) a F_4ZnPc:C_{60} blend deposited on pure F_4ZnPc. The blend on C_{60} is more stable against beam damage.

damage as it is the case for a not purely electron conducting layer like F_4ZnPc. A similar observation is made for samples deposited on graphene or highly conductive titanium-silicon films [108, 109]. Less beam damage is observed for sensitive biological samples, explained by the fast electron transport of the conductive underlayers away from the specimen [108, 109].

Conclusion

The preparatory study on beam damage revealed stability of the collective plasmon excitation for all investigated materials up to a high dose of 10^6 e/nm^2. Hence, classification of materials by their spectroscopic properties in further EFTEM measurements in this work is justified. The HOMO-LUMO transition of F_4ZnPc and especially P3HT is damaged quickly, which impedes imaging of these materials within a compound at this particular energy loss. On the other hand, C_{60} and its derivative PCBM were found to be robust. Interestingly, the stability of the donors increases and the stability of the acceptors decreases in a BHJ. This effect is also observed in the literature and is explained by the different degradation mechanisms, which are material depended [101, 102, 104, 106, 110]. Besides, the EEL-spectra confirmed the impact of an electron transport layer underneath the investigated films on their beam sensitivity.

6. Correlation between Structural and Electronic Properties of P3HT Thin Films

One very important material class of organic semiconductors are polymers. As they exhibit a rather complicated structure, which is strongly influenced by the molecular chain length or the processing conditions, a high impact of the morphology on the charge transport properties is expected. The following chapter starts with a summary of significant state of the art TEM investigations of polymers and especially P3HT. Bright-field images and electron diffraction measurements of P3HT annealed at different temperatures are presented. Additionally, the impact of the molecular weight on crystallinity is discussed. Charge transport in P3HT-diodes and field effect transistors is studied and correlated to the structural properties from TEM. In the last part of this chapter, the results from analytical TEM measurements on doped P3HT are presented. The findings are supplemented by infrared spectroscopy for the determination of the charge transfer in doped films. At the end of this chapter, the influence of crystallinity on charge transfer characteristics is discussed.

6.1. State of the Art

P3HT is one of the most studied organic semiconductors in the past twenty years. However, its complex structure-function relationship is by far not fully understood yet. Bao et al. were the first to introduce an organic field effect transistor using solution cast regioregular P3HT exhibiting mobilities of up to $0.01\,\mathrm{cm}^2/\mathrm{Vs}$ with an on/off ratio exceeding 10^3 [83]. These values strongly depend on the solvent and the annealing conditions. It became clear very quickly that an ordered morphology is crucial for the field-effect mobility. Besides the processing conditions, it was found that also the intrinsic material properties such as molecular weight and regioregularity play a key role for an

increased crystallinity of P3HT [111–114].

Beyond applications in OFETs, additionally P3HT gained more and more the interest of the organic photovoltaic community for applications in BHJs. Yang Yang was the first to introduce P3HT:PCBM solar cells with efficiencies above 3 % triggering innumerous publications on this topic [82]. However, the findings from OFETs on the factors influencing the P3HT mobility cannot be transferred one-to-one to BHJs as the fundamental charge transport mechanisms are distinct. Especially, as P3HT is found to exhibit anisotropic charge transport [111, 115–117]. In OFETs field assisted charge transport occurs parallel to the substrate, whereas in BHJs the transport is along domains perpendicular to the electrodes. For this purpose, the CELIV (charge exctraction by linear increasing voltage) technique, which was originally used for the characterization of inorganic materials [118], is introduced for organic semiconductors [70]. CELIV enables the determination of charge carrier mobilities normal to the substrate in the actual device without the need of artificially thick layers as used for example in time-of-flight measurements [70, 119]. The CELIV technique was newly established at the InnovationLab within this work with the help of two supervised master theses by Carsten Leinweber and Lars Müller [74, 78]. For the understanding of the electrical properties gained from the new technique and their correlation to the spectroscopic properties from EELS and the structural properties from electron diffraction, the model system P3HT is eligible. The unique feature of the following chapter is that the entire set of measurements are performed on identically processed samples. There are very few reports on TEM measurements of P3HT that are directly correlated to device performance of OFETs and diodes. Recently, a 3D-reconstruction of the P3HT lamellar structure in different solvents by means of cryo-TEM[1] has been presented, however without showing any device data [120].

By now, the trend in OFETs goes mainly in the direction of laterally controlled crystallization. A method for a controlled nucleation of spherulitic structures in P3HT by carbon disulphide vapor annealing has been demonstrated [121]. The spherulitic structure exhibits a sufficiently high diameter such that an entire transistor channel can be placed within the well-oriented domain. The transistor exhibits mobilities of $0.07\,\mathrm{cm^2/Vs}$ parallel and $0.2\,\mathrm{cm^2/Vs}$ perpendicular to the radial spherulite growth direction [121]. Hartmann et al. present state of the art high resolution TEM images and electron diffraction of highly edge-on oriented P3HT layers treated by mechanical rubbing, however without investigating its relevance in actual devices [122].

A further common way to improve the charge properties of organic semi-

[1] Cooling prevents beam damage of the crystal structure during image acquisition

conductors for transistors or for hole- or electron-injecting layers is by doping [123, 124]. In this work, p-type solution doping of P3HT with F_4TCNQ is addressed, which is reported to lead to conductivities of up to 100 S/cm [85]. There are few attempts to understand typical doping-phenomena such as the complex conductivity-doping-ratio relationship of this material system, however there are not many reports on the structural properties [84, 125–127]. There is only one reported TEM measurement on P3HT:F_4TCNQ by Deschler et al. [125]. The authors claim that the dopant agglomerates in the P3HT matrix, however without giving a clear evidence from their TEM measurements [125]. As was shown by Donhauser et. al, dopant agglomeration can play a significant role for the doping efficiency in organic semiconductors [128]. Therefore, the correlation between the morphology from TEM measurements and the underlying doping mechanism in solution-doped P3HT with F_4TCNQ is investigated in the following chapter.

6.2. Structural Properties of Pure P3HT Layers from TEM Measurements

As already discussed in the literature overview, the P3HT nanostructure depends on the intrinsic properties (e.g. molecular weight or regioregularity) and the process conditions such as solvents, casting techniques, and annealing temperatures. In order to narrow the set of parameters, the regioregularity, the solvent, and the casting technique for all samples were kept constant. Therefore, all samples were spin coated from a chlorobenzene solution. First, the optimum annealing temperature, leading to the highest order of the films, was determined. The established fabrication technique was then used for the film processing of P3HT with varying molecular weight. The structural properties are deduced from bright-field and electron diffraction measurements. For every sample and every TEM mode (bright-field, diffraction, EELS) measurements were acquired from at least 5 different spots all over the sample.

6.2.1. Annealing

P3HT (24320 g/mol) films were spin coated from a chlorobenzene solution as described in chapter 4. One sample was kept without heating treatment (not annealed). The other two samples were annealed for 10 min at 80 °C or 120 °C. In the literature annealing temperatures range mostly between 50 °C and 150 °C, going up to the melting point at 205 °C [129–132]. However, the optimum temperature for the process and material conditions used in this work, have not

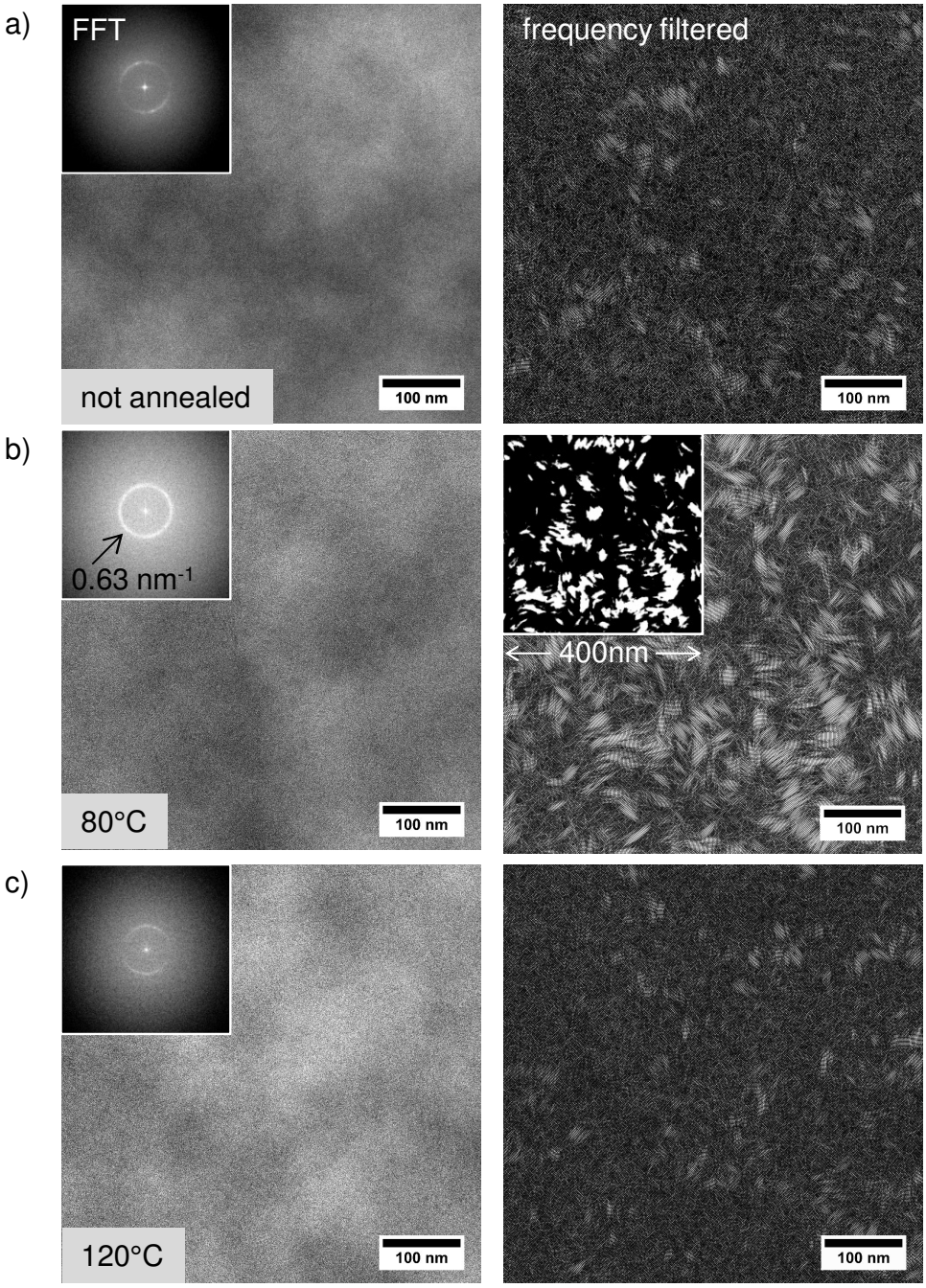

Figure 6.1: Bright-field images, FFTs and frequency filtered images of P3HT films spin coated from a chlorobenzene solution a) not annealed b) annealed for 10 min at 80 °C and c) annealed for 10 min at 120 °C.

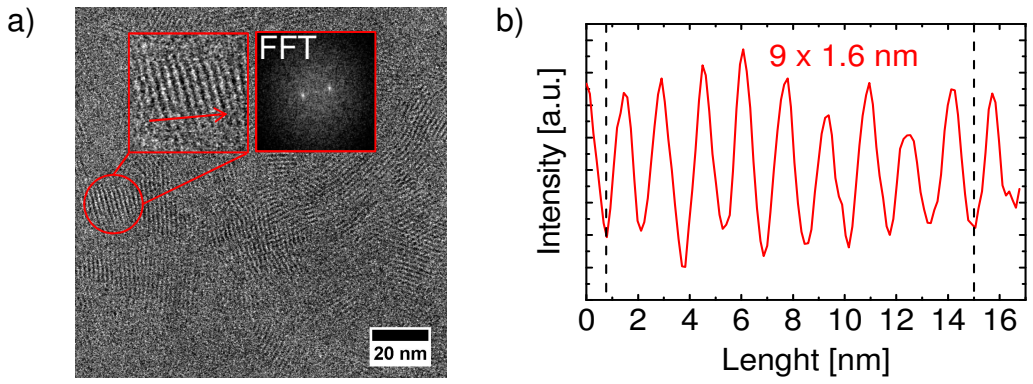

Figure 6.2: P3HT annealed at 80 ℃. a) Zoom of a BFTEM image with the corresponding FFT indicating the orientation of the domain. b) A radial profile along the lamellar stacking showing 1.6 nm spacing.

been reported. Figure 6.1 shows bright-field TEM (BFTEM) images (left-hand side) for three different P3HT samples with the corresponding Fast Fourier Transform (FFT) of the image in the upper-left corner and frequency filtered images on the right-hand side. All layers exhibit a smooth and homogenous texture. The FFTs of the images (upper left corner) indicate a very pronounced repeating frequency at $0.63\,\mathrm{nm}^{-1}$, which corresponds to a spacing of 1.6 nm. Lattice fringes with this spacing are visible in the BFTEM images. For a better perceptibility a narrow ($\triangle f = 0.02\,\mathrm{nm}^{-1}$) angular frequency filter around $0.63\,\mathrm{nm}^{-1}$ is applied, cutting off the remaining frequencies. The frequency filtered image is shown on the right-hand side. Domains exhibiting lattice fringes with this spacing appear white and are clearly visible. Additionally, an interconnected network consisting of small, elongated structures is observed in all samples. The FFT of the film annealed at 80 ℃ exhibits a coherent and distinct ring. Therefore, the frequency filtered image on the right-hand side shows large ordered domains. A zoom of the BFTEM image of the 80 ℃-sample is presented in figure 6.2 a). The FFT shows two distinct spots, indicating the orientation of the domain. The discussed lattice fringes with 1.6 nm spacing are determined from the radial profile over the domain shown in b).

Qualitatively, it is obvious that the other two samples have a similar texture and significantly less lattice fringes with this particular spacing. One possible way to determine the degree of crystallinity is by converting the filtered image into a binary black and white image (see inset in figure 6.1 b) on the right-hand side) and then calculating the fraction of ordered domains including their typical size. For the sample annealed at 80 ℃ the average domain size is calculated to be 51 nm with a fraction of 16 % crystalline material in an

area of $400\,\mathrm{x}\,400\,\mathrm{nm}^2$. For the other two samples the quantitative analysis is not feasible. Only about 2 % oriented domains and an average domain size of about 7 nm −12 nm are estimated. It is striking that the preferential orientation decreases with increasing temperature above 80 ℃. However, this does not imply that the overall crystallinity of the 120 ℃-film is lower. As the bright field image is a projection through the whole bulk, it is also possible that superposition of signals hinders the imaging. A way to resolve crystal orientation that is not visible in the bright field images is electron diffraction.

In figure 6.3 a) the radial profiles from the diffraction measurements of all three samples are depicted. Two very pronounced peaks are visible in all samples. As marked in the diagram, the peaks are indexed to the (100)-orientation and (010)-orientation of P3HT [126]. The small bump between the peaks is attributed to (001)-orientation. The corresponding spacings ($1.64\,\mathrm{nm} \pm 0.04\,\mathrm{nm}$, $0.83\,\mathrm{nm} \pm 0.05\,\mathrm{nm}$, $0.378\,\mathrm{nm} \pm 0.03\,\mathrm{nm}$) are in very good agreement with the lattice parameters a=1.618 nm, b=0.772 nm, c=0.789 nm (γ=86.5°, α=β=90°) of the monoclinic unit cell reported in literature from measurements and molecular dynamics simulations [113, 117, 133–136]. The vectors and the unit cell are shown in figure 6.3 b). It is important to note that this kind of space group ($P2_1c$) needs a crystal basis with stacked dimers. This explains why the stacking period of $b/2$, which corresponds to π-stacking of the chains, is measured in the diffraction [117, 133]. The a-axis indicates the interlamellar spacing, whereas c is related to the orientation along the conjugated backbone [113]. P3HT is known to be polymorphic, meaning that a different crystal structure is adopted depending on the annealing temperature. Poelking et al. reported on two existing polymorph forms for P3HT with one being metastable (I') and a thermodynamically stable polymorph (I) with a transition that occurs between 300 K and 425 K [117]. As the π-stacking is observed to increase to 0.40 nm for polymorph I' it is assumed that in this work the investigated P3HT is present in polymorph (I) form (0.38 nm) [117].

Comparing the radial profiles of the three samples significant differences are not observed. The relative intensity between the (100)- and (010)-peak is only slightly higher for the 80 ℃-sample (1.22) compared to the the 120 ℃-sample (1.16) and the unannealed sample (1.12). This means that the orientation along the a-axis is slightly more pronounced after 80 ℃ annealing. A further technique to study quantitative differences in crystallinity is determining the Full Width at Hall Maximum (FWHM) of the diffraction peaks. This is usually used for XRD data analysis as the Scherrer equation directly relates the FWHM of the peaks to the crystal size [113, 137, 138]. Different models exist for the fit of the peaks, including the Lorentzian or PseudoVoigt analytical function, which worked best for the data in this thesis [139]. The fit is shown

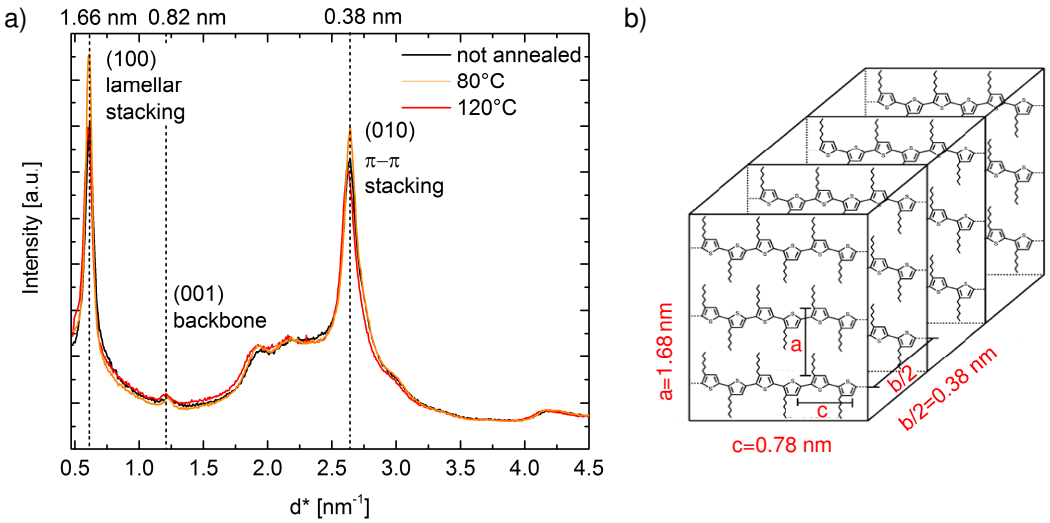

Figure 6.3: a) Radial profiles of the not annealed (black), 80 ℃ (orange) and 120 ℃ (red) annealed sample. The main peaks are indexed and correspond well to the monoclinic unit cell of P3HT. b) The reported unit cell of P3HT with lattice parameters a, b and c. Unit cell taken from [113].

in figure 6.4 a). After background subtraction the FWHM is measured for the two pronounced peaks by means of the curve fitting program *Fityk* [140]. The results are shown in figure 6.4 b) with errors calculated from the "goodness-of-the-fit" (R^2). The crystal sizes for regions oriented along the lamellar stacking in the 80 ℃-sample appear larger than for the other two samples, whereas all samples exhibit similar sizes for crytstallites oriented along the $b/2$-axis. However, it must be considered that the Scherrer equation assumes ideal crystals. As the present crystals are not "ideal" the absolute values are of limited significance and only the relative deviations are considered. In conclusion, the 80 ℃ annealing temperature is appropriate for the processing of semicrystalline layers.

The diffraction pattern of the 80 ℃-sample is shown in figure 6.4 c). Corresponding to the three peaks from the radial profile, two very strong, (100) and (010), and one rather faint ring (001) are clearly visible. The occurrence of rings in the diffraction pattern points out that the crystalline domains are ordered randomly and do not exhibit a preferential growth direction. The absence of distinct speckles is a sign for the presence of rather small crystalline structures. In the case of P3HT and in general for polymers the concept of semicrystallinity is often introduced, as molecular chain folding usually disrupts lamellar crystals [141]. This means that ordered domains are often separated

a)

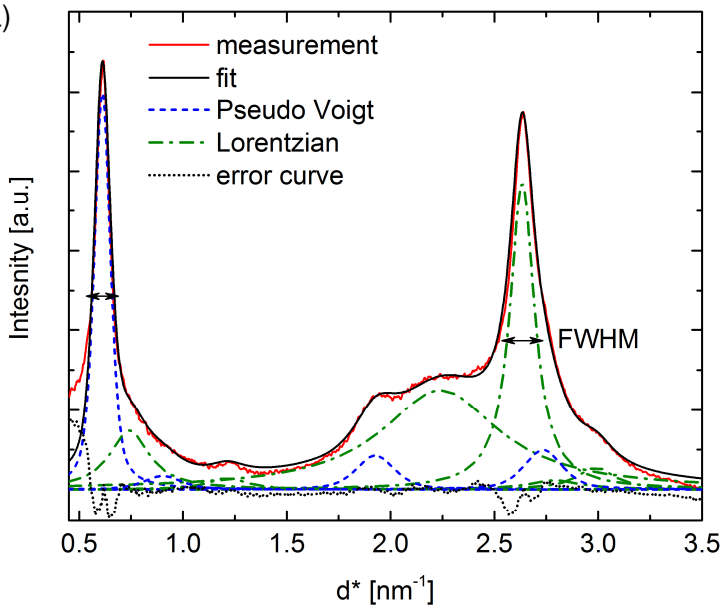

b)

	a [nm]	b/2 [nm]
non annealed	11.11 ± 0.12	7.14 ± 0.12
80°C	14.28 ± 0.04	7.14 ± 0.07
120°C	11.11 ± 0.18	6.66 ± 0.03

c)

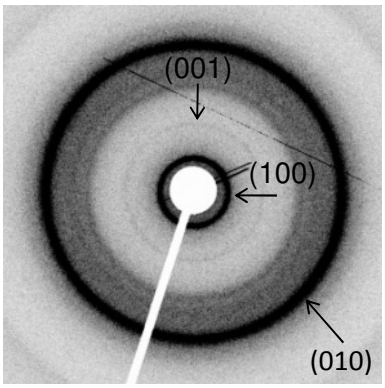

Figure 6.4: a) Fit function (black) shown exemplary for the radial profile of the unannealed sample (red). Pseudo Voigt (blue) or Lorentzian (green) analytical functions used for the fit. The error curve represents the good agreement between the measurement and the fit (black dashed line). b) Calculated typical crystal size from the FWHM of the two main peaks (a- and $b/2$- axes) after background subtraction and fit. c) A Typical diffraction pattern of the 80 °C annealed sample showing three distinct rings corresponding to the unit cell spacings.

	Molecular Weight	Regioregularity	Polydispersity
Abbreviation	MW [g/mol]	RR [%]	PD
14k	14160	> 91	1.18
24k	24320	93.7	2.10
31k	31264	93.6	2.00
54k	54233	94.2	2.30

Table 6.1: Material characteristics of the used P3HT. The 14k material is provided by a cooperation partner, thus the exact RR is unknown.

by amorphous regions. In general, one has to be careful with the definition of "crystal" for polymers, as they are soft materials and material properties such as regioregularity have a strong impact on the degree of positional disorder (paracrystallinity) [117].

6.2.2. Molecular Weight Dependence

In the following, the structure is studied for P3HT with different molecular weights. The material parameters are summarized in table 6.1[2]. All samples are annealed for 10 min at 80 °C. It is important that the materials exhibit similar regioregularity (RR) values preferentially $> 90\,\%$ as it is shown in the literature that the RR influences the structural and electronic properties [111, 117]. Unfortunately, the exact value for the 14k is not known, which has to be kept in mind. The polydispersity (PD), which describes the distribution of molecular mass in the polymer, is comparable for the commercial P3HT and even significantly lower for the 14k material. BFTEM images of all samples with the corresponding FFT (lower left corner) and frequency filtered images are shown in figure 6.5. The overall texture for all samples is homogenous. Only the 24k and the 54k samples exhibit pronounced repeating frequencies, which correspond to 1.65 nm lattice fringes as indicated in the inset. The frequency filtered images confirm the lack of oriented domains with 1.65 nm lattice spacing for the 14k and 31k samples (only very few small domains are found) as can be seen on the right-hand side in a) and c). Typical domain sizes in the 54k sample reach about 5 nm to 10 nm and 2 % crystallinity on a $360 \times 360\,\mathrm{nm}^2$ area. The 24k as well exhibits only about 2 % crystalline domains and domain sizes range between 10 nm and 15 nm, which is significantly lower compared to the sample from the annealing series in figure 6.1. This is surprising as the

[2]The 14k material was synthesized by the group of Prof. Christine Luscombe, University of Washington, and was used as received, without further treatment.

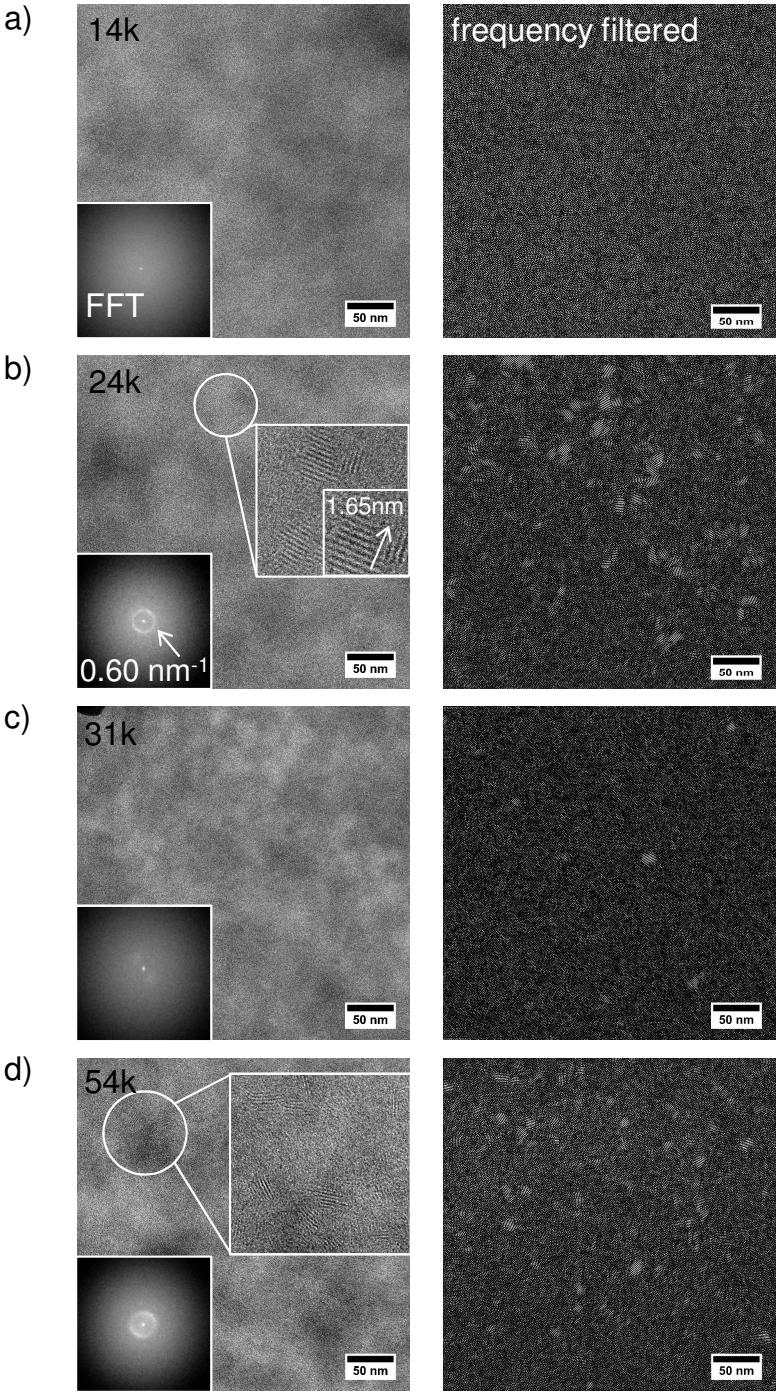

Figure 6.5: Bright-field images, FFTs and frequency filtered images of different molecular weights of P3HT a) 14k b) 24k c) 31k and d) 54k.

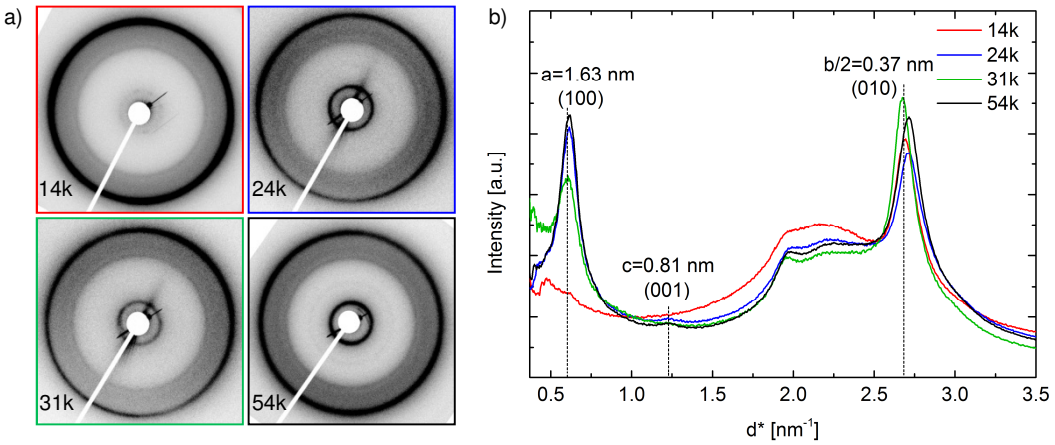

Figure 6.6: Electron diffraction of P3HT with different molecular weights. a) Diffraction patterns showing mainly two pronounced rings except for the 14k sample. b) Radial profile with indicated peaks corresponding to the lattice parameters of crystalline P3HT.

same P3HT material batch was used for both samples. It is not clear why the highly crystalline texture could not be reproduced, as process conditions were kept exactly the same. It is possible that the solvent was slightly contaminated or the glovebox parameters such as humidity, oxygen level or temperature were higher during processing. This issue emphasizes the difficulty of reproducing the crystallinity of P3HT.

For a detailed description of the crystal structure the results from electron diffraction are shown in figure 6.6. The diffraction patterns in a) clearly reflect differences between the samples. The innermost ring is only faintly visible for the 31k sample and not visible at all in the 14k image. The remaining two samples resolve two distinct and sharp rings. The rings and the lack of speckles again point out the existence of randomly distributed crystallites. In b) the radial profiles of the diffraction patterns are presented. All peaks are assigned to the a, b or c lattice parameters as discussed in the previous section. No further hint is found in the literature describing the origin of the plateau between c and b. It is probably caused by amorphous material. The intermolecular lamellar stacking at 1.63 nm is, as expected from the patterns, not visible for the 14k sample, indicating its lack of orientation along the a-axis. This is surprising, as one would assume that shorter molecular chains are more mobile and can arrange easily when heated. For this sample there is obviously no lamellar stacking or backbone chain order (no peak visible for the c-spacing). Lamellar stacking for the 31k sample is not as pronounced as for

spacing	a (lamellar stacks)	$b/2$ ($\pi-\pi$- stacks)
	[nm]	[nm]
14k	-	7.14±0.12
24k	4.99±0.03	6.25±0.18
31k	4.54±0.06	4.99±0.08
54k	6.25±0.5	4.545±0.007

Table 6.2: Calculated crystal size for the two most pronounced orientations from the peak width in the radial profile of P3HT with varying molecular weight.

24k and 54k P3HT but is still clearly visible. A very faint peak is attributed to the c-spacing at 0.81 nm. The latter is induced by an increased order in the backbone chain of the 24k, 31k and 54k polymer. π-π stacking is observed in all four samples with a sharp peak at 0.37 nm in excellent agreement with published work [113, 117, 133–136]. A slight shift towards larger spacings is noted for the 14k and 31k sample. However, the shift of about Δd^*=0.005 nm^{-1} is within the error margin of the instrument calibration and is not considered to be significant.

In the literature, a preferential edge-on (normal to the (100)-axis) or face-on (normal to the (010)-axis) orientation of the polymer chains with respect to the substrate is often observed [6, 111, 142–145]. The edge-on orientation is considered as thermodynamically favored and is usually obtained under conditions close to the equilibrium from slow casting methods like e.g. drop casting [111, 146, 147]. Spin coating is only considered as a slow casting technique if carried out with high-boiling point solvents, which is the case for the solvent used in this thesis (chlorobenzene) [148].

Furthermore, high regioregularity ($> 95\,\%$) is beneficial for a preferential edge-on orientation. However, as shown by Liu and co-workers, preferentially oriented P3HT generates distinct spots and higher-orders (e.g. (200) and (300)) in electron diffraction [149]. Here, only rings up to the first order are observed, leading to the conclusion that crystalline domains are present in all samples, but randomly oriented. It is not clear if the random crystallite orientation is caused by the intrinsic material properties (regioregularity of $93-94\,\%$) or the process conditions. In order to estimate the size of the domains, the already introduced FWHM method is applied [114]. The results are summarized in table 6.2. For the lamellar stacking the 24k and 54k samples exhibit an equal peak width corresponding to a crystal size of about 5 nm −6 nm. About 4 nm are determined for the 31k sample. With preferential π-stacking the largest domains are measured surprisingly for the 14k sample (7 nm) and about

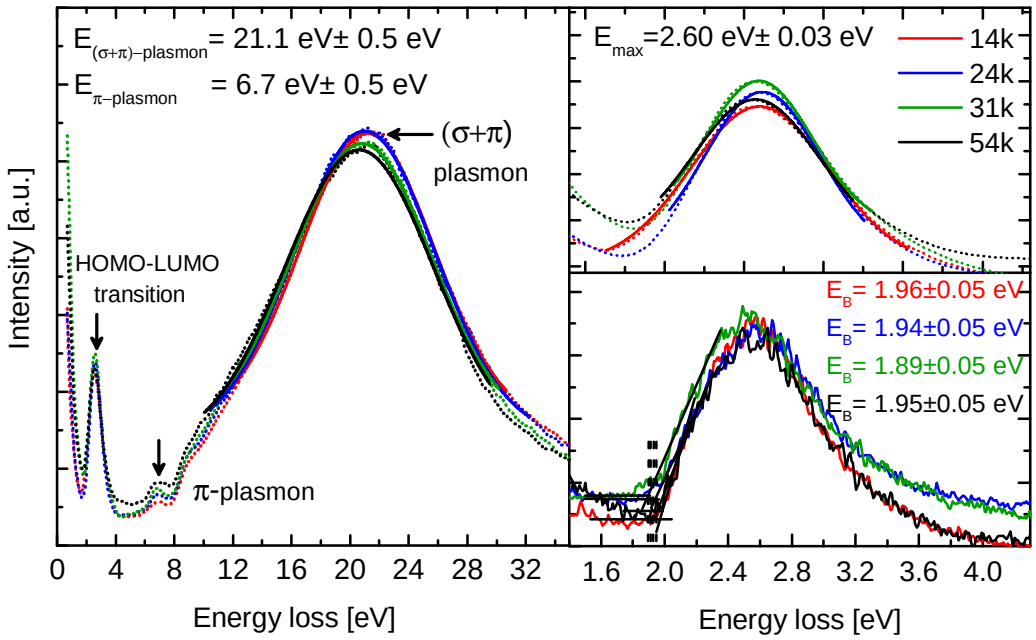

Figure 6.7: EEL spectra of P3HT for four different molecular weights: 14k (red), 24k (blue), 31k (green) and 54k (black). On the left-hand side a survey spectrum is shown indicating three pronounced features. The energy positions are determined from a Gaussian fit. On the ride-hand side a zoom of the low loss regime (1.5 eV −4.5 eV) is shown. The maximum energy is determined from a Gaussian fit on the HOMO-LUMO transition peak and the band gap is derived from a linear extrapolation of the peak onset.

4 nm −6 nm are determined for the other three samples.

Electron energy loss spectra and the assignment of the band gap for all samples are shown in figure 6.7. For a more clear representation, the spectra are normalized over the integrated area and smoothed over 20 points (0.17 eV). Three pronounced features for all samples are observed in the survey spectrum on the left-hand side. The first peak is attributed to single electron transitions from the HOMO to the LUMO, followed by a collective excitation of the π-electrons at 6.7 eV ±0.5 eV [56]. The π-plasmon excitation is expected to appear as the P3HT backbone consists of sp^2-hybridized electrons. The broad peak at 21.1 eV ±0.5 eV (position determined by a Gaussian fit) is assigned to a collective excitation of the σ- and π-electrons, which is typical for organic

compounds and also known as plasmon excitation [55, 56]. The maximum energy of the single-electron excitation at 2.60 eV ±0.03 eV (Gaussian fit) is shown on the right-hand side (top) in figure 6.7. The band gap is determined from a linear extrapolation at the onset of the peak [150]. The determined values (1.95 eV ±0.05 eV) are in good agreement with the optical band gap of P3HT at around 1.9 eV, which is determined from UV-VIS absorption spectra [151]. The considerable agreement with data from non-invasive optical measurements demonstrates that the used instrument settings do not induce significant beam damage in the films. The HOMO-LUMO gap of P3HT is determined from photoemission spectroscopy to be 2.52 eV [81]. Here, we measure a significantly lower value for the band gap in analogy to the optical band gap from UV-VIS measurements. This leads to the conclusion that in EELS the measured energy loss of the electrons is reduced by the binding energy of the exciton, which is relatively high in organic compounds [152].

There are no changes of the spectral features for the different molecular weights. It is reported that significant changes in the absorption behavior of P3HT with different molecular weights is not expected except for a blue-shift for very low molecular weights (<4k) [114, 129]. Hence, the structural differences from the diffraction measurements have no impact on the EEL spectra as there are no spectral differences noted for P3HT with varying molecular weights. Furthermore, the HOMO-LUMO transition and the collective plasmon excitations seem to be independent of the polymer chain length. A Kramers-Kronig analysis for the calculation of the dielectric functions of P3HT will be carried out in section 6.5 as it is of greater interest for doped films.

6.2.3. Conclusion: P3HT Structure

The presented TEM measurements on different P3HT films lead to the following conclusions for the structural properties:

- In all investigated P3HT samples order assigned to $\pi - \pi$-stacking of the polymers is observed independent of the annealing temperature or the molecular weight.
- A slight increase of the overall crystallinity and larger ordered domains are noted for P3HT annealed at 80°C.
- A preferential edge-on or face-on orientation is not observed in any of the samples. Hence, the orientation of the ordered domains is random. The crystalline domains are mostly surrounded by amorphous material.

- For the chosen process conditions and intrinsic material properties P3HT adopts semicrystalline texture.
- Lamellar stacking is surprisingly not observed for the lowest molecular weight (14k), however the structures exhibiting π-π-stacking are relatively large (7 nm).
- Significant differences in the EEL spectra for the distinct molecular weights are not noted. The determined band gap is in good agreement with reported values from optical measurements. Thus, the intrinsic material properties are not influenced by the electron beam.

6.3. Electrical Characterization of P3HT Devices

For a comprehensive understanding of the charge transport properties in polymers the charge carrier mobilities in P3HT with varying molecular weights were studied by means of two different techniques. A schematic of both device architectures with indicated charge transport directions is shown in figure 6.8. In Charge Extraction by Linear Increasing Voltage (CELIV) the charge transport in P3HT diodes is measured throughout the whole organic layer perpendicular to the substrate and between the two electrodes (see a)). Additionally, field-effect mobilities are determined from bottom-contact, top-gate P3HT transistors (see b)). The methods are chosen in such way that both charge carrier mobilities along the substrate normal (CELIV) and parallel to the substrate along the dielectric interface (OFET) are considered. Consequently, anisotropic charge transport, caused by the polymer crystallinity, is studied.

6.3.1. Mobilities Extracted from CELIV Measurements

The four different molecular weights from the previous section (14k, 24k, 31k and 54k) are used for the fabrication of P3HT diodes (architecture shown in figure 6.8 a)). The detailed device preparation is explained in chapter 4. Photo-CELIV measurements were performed on all samples within the scope of the master thesis of Lars Müller [78].

The measurements for the 24k, 31k and 54k samples are performed with a voltage ramp of 0.3 V/µs and with $V_{\text{off}} = 0$ (see section 3.3.1). The delay time between the laser pulse and the applied voltage ramp is varied between

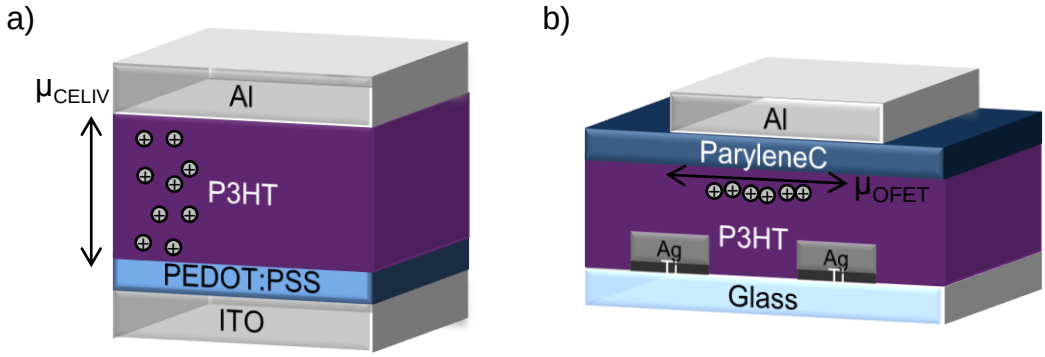

Figure 6.8: Schematic of the devices used for mobility measurements in a) diodes (CELIV) and b) OFETs.

2 µs and 500 µs. The resulting mobilities for the different delay times are averaged such that the standard deviation is added to the error of a single measurement. The calculated mobilities and charge densities from equations (3.18) and (3.19) as well as values from the literature determined by time of flight (TOF) measurements are plotted in figure 6.9 a) [153]. The CELIV measurements presented here are novel and can therefore only be compared with TOF measurements. However, the comparison with TOF-mobilities is meaningful for several reasons. In TOF the mobilities are derived from the measured time for the charge carriers to travel through the whole bulk vertically from one electrode to the other. Hence, the charge transport direction is the same as in CELIV. From both measurements a negative electric-field dependence of the mobilities as an intrinsic feature of P3HT is observed and attributed to large positional disorder. The TOF results by Ballantyne et al. presented in figure 6.9 a) are acquired from similarly processed P3HT samples (spin coated from a heated chlorobenzene solution), which can also influence the charge properties and are important for a reliable comparability of mobilities [153].

As shown in figure 6.9 a) the CELIV mobility decreases with increasing molecular weight. The values are similar for the 14k and 24k sample, drop significantly from 10^{-3} cm^2/Vs to 4.10^{-4} cm^2/Vs for 31k molecular weight and continue to decrease for 54k. The overall trend of the TOF-mobilities is in good agreement, with absolute values being lower, as well showing a huge drop between 20k and 30k. In both measurements the drop of the mobility between the lowest and the highest molecular weight is one order of magnitude.

The resulting charge carrier densities are shown in figure 6.9 a) in red (right y-axis). As the charge density decreases for all molecular weights with

increasing delay time due to recombination, n is determined for a fixed t_{del} of 10 µs. A significant increase of the density is observed between the 14k and 24k sample, which then remains more or less constant for the other samples. One possible explanation for this trend are the lower mobilities of the higher molecular weight samples. Hence, the charge carriers are kept longer within the bulk as they are not so mobile. This leads to an enhanced charge density. Furthermore, lower mobility leads to less recombination, if it is assumed that Langevin recombination, which is mobility dependent, is the dominating recombination process in disordered organic semiconductors [35]. It must be considered that the measured signal in photo-CELIV is not from the intrinsic properties of the material but is caused by the generated charge carriers from the laser pulse. Therefore, varying charge densities can also be attributed to a different absorption behavior of the samples with higher molecular weight. Moreover, the higher electron density in longer molecular chains is also expected to lead to a higher density of the extracted charges. Trap states, on the other hand, can hinder the extraction of charges, which decreases the overall measured density.

For a deeper understanding of the underlying charge transport processes field effect mobilities of the same materials are investigated in the following section.

6.3.2. Field-Effect Mobilities

The OFETs in this section were fabricated and evaluated by Milan Alt (Karlsruhe Institute of Technology). The devices (architecture shown in figure 6.8 b)) are prepared from the exactly same solution as the devices from the previous section in three different variations: not annealed and annealed for 10 min or 60 min at 80 °C. For the investigated P3HT transistors the transmission line method (see [78]) indicated a contact resistance in the same order of magnitude for all samples, thus its effect on the relative mobility values is neglected. Calculated mobilities for all samples are shown in figure 6.9 b). For all molecular weights the mobility increases after annealing. Especially for the 31k sample, the mobility increases further with longer annealing times, whereas no difference is observed for the 14k and the 54k sample after 60 min annealing and only a slight variation is observed for 24k. An increase of the mobility in P3HT transistors after annealing is often attributed in the literature to a release of oxygen out of the active layer, which usually dopes the polymer and degrades the on/off ratio [154]. As the 31k sample exhibits overall the highest mobility a continuous rise of the mobility with increasing molecular weight is not noted. The second highest value of 0.08 $\mathrm{cm}^2/\mathrm{Vs}$ is obtained for

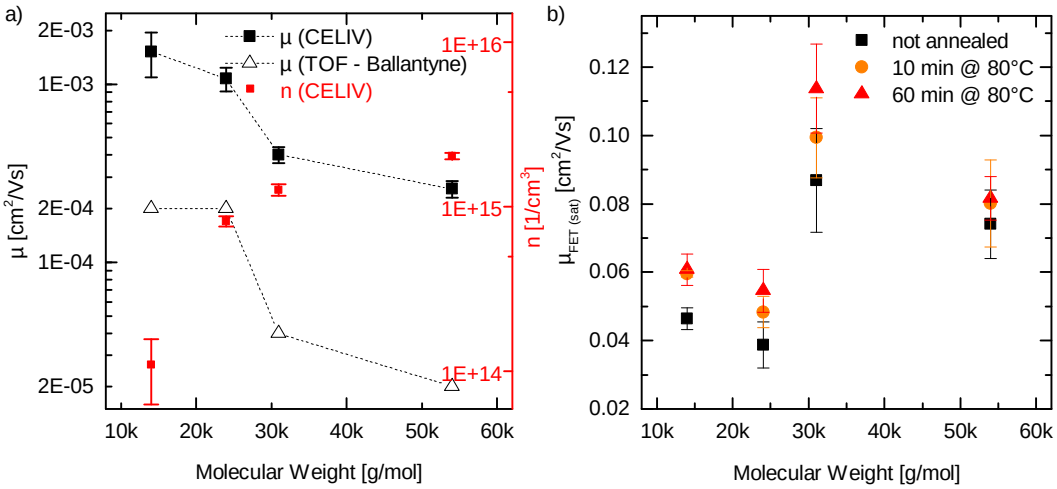

Figure 6.9: Calculated mobilities for different molecular weights of P3HT. a) Mobilities calculated from CELIV measurements are presented by black squares. Open black triangles indicate TOF measurements by Ballantyne et al. [153]. Charge carrier densities derived from the CELIV mobilities are plotted with red squares with respect to the right axis. b) OFET mobilities for varying molecular weights of not annealed samples (black) and samples annealed at 80°C for 10 min (orange) and 60 min (red).

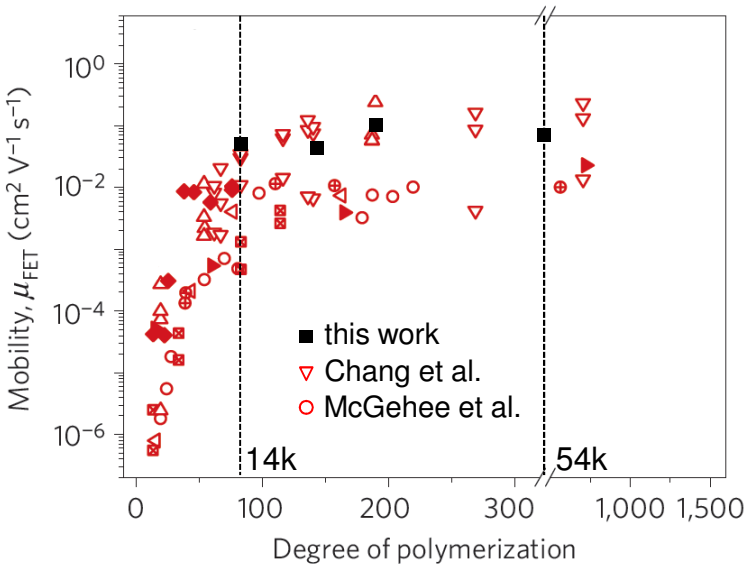

Figure 6.10: Summary of the field-effect mobility vs. the degree of polymerization from over 30 different publications taken and modified from [78, 155]. The degree of polymerization indicates the quantity of monomers. The dashed lines locate the range of molecular weights investigated in this work. The black squares indicate the mobilities determined in this work, which are in a comparable range with mobilities e.g. determined by Chang et al. and McGehee et al. [112, 156].

the 54k sample followed by 14k and 24k at around 0.06 cm^2/Vs. The 14k and 24k samples exhibit the same mobility values within the error margin for the longer annealing time.

There are many publications dealing with the impact of molecular weight on charge carrier mobilities in P3HT OFETs [114, 142, 155–158]. In most of the studies a saturation for the mobilities with increasing molecular weight is observed. The mobility increases over several orders of magnitude (from 10^{-6} cm^2/Vs to about 10^{-2} cm^2/Vs) for molecular weights up to 10000 g/mol and remains more or less constant between 10k and 30k. This is in agreement with the results from this thesis. Here, the mobility varies between 0.05 cm^2/Vs and 0.1 cm^2/Vs for the annealed samples, which is the same order of magnitude as reported [155].

A summary of the field-effect mobility in dependence on the degree of polymerization[3] from over 30 publications given by Noriega et al. [155] is

[3]The degree of polymerization indicates the quantity of monomers and is accordingly calculated by dividing the molecular weight of the polymer (e.g. 14160 g/mol) by the molecular weight of a monomer (166.28 g/mol).

represented in figure 6.10. The results from this work are indicated with black squares and are in very good agreement with the published values. However, for a direct comparison it has to be considered that processing conditions can have a significant impact on the charge carrier mobility. Chang et al. investigated the dependence of field-effect mobilities in P3HT on the preparation technique. Values are marked with reversed red triangles in figure 6.10. For drop casted devices from a chloroform solution the mobility increases from $10^{-3}\,\mathrm{cm}^2/\mathrm{Vs}$ (15.4k and 20k) to $10^{-1}\,\mathrm{cm}^2/\mathrm{Vs}$ (52k) with increasing molecular weight. However, they do not observe a systematic dependence of the mobility on the molecular weight for spin coated devices from 15k to 270k (range between $10^{-3}\,\mathrm{cm}^2/\mathrm{Vs}$ and $10^{-2}\,\mathrm{cm}^2/\mathrm{Vs}$) [156]. A similar report is given by McGehee et al., as they observed for spin coated devices from chloroform solution a mobility increase of three to four orders of magnitude for molecular weights up to 15k and an increase of maximum one order above 15k [112]. The results are indicated with open red circles in figure 6.10. This effect is attributed to the rapid film formation (spin coating), which leads to a more disordered structure compared to the highly crystalline films from slow film formation (drop casting) [112]. The same observations were made by Bao et al. by comparing mobilities for devices from different solvents which influence the film formation [146]. Spin coated devices from chlorobenzene solution are reported to have about one order of magnitude lower mobilities than the devices in this thesis, though for bottom-gate transistors, which possibly explains the difference. Here, a top-gate[4] architecture is used such that the important interface for the charge transport is formed between the first few top monolayers of P3HT and the dielectric. In bottom-gate transistors the crucial interface is between the dielectric and the first few monolayers at the bottom of the P3HT layer [159]. It is observed that the structure of P3HT at the bottom of the layer can be distinct from the structure on top [160, 161]. Oosterbaan et al. demonstrate an increase of the mobility in a bottom-gate transistor if the active layer is flipped after spin-coating such that the former polymer/air interface is placed at the dielectric [160]. It seems that this morphology is more favorable for the charge transport and would confirm the higher mobilities in the top-gate configuration presented in this work. A similar effect can be achieved by reducing the surface energy of the dielectric surface by treatment with self-assembling monolayers, which can improve the edge-on orientation of the polymer and thus the mobility [142]. As the structure has an impact on the charge transport, it can be assumed that even if devices are processed in

[4]The top-gate architecture is chosen as it is more common for applications in flexible electronics.

the same way however in a top- or bottom-gate architecture, the extracted mobilities are distinct. This makes the general comparability between organic devices, however built from the "same" material, very challenging.

6.3.3. Conclusion: Charge Carrier Mobilities

Based on the findings from the mobility measurements the following conclusions can be drawn:

- The charge carrier mobility in the bulk determined by CELIV measurements decreases with the molecular weight of the polymer by almost over one order of magnitude.
- A clear trend for the field-effect mobilities in top-gate transistors is not observed. Samples with higher molecular weights (31k, 54k) exhibit in general slightly higher mobilities, whereas for low molecular weights (14k, 24k) an almost constant mobility is noted.

Depending on the molecular weight the trend observed for the CELIV and OFET mobilities is different. This is attributed to the distinct underlaying fundamental processes defining the charge transport. As already mentioned, the charge transport in OFETs occurs in the very few monolayers between the organic semiconductor and the dielectric parallel to the substrate and is determined by the structure at the interface. In CELIV, charge transport is measured through the whole bulk along the substrate normal. Here, the overall film order is crucial. Anisotropic charge transport has been reported for P3HT, but mostly from theoretical calculations [115,117,121]. The findings from this section underline the importance of CELIV mobility measurements for the investigation of anisotropic charge transport. In order to understand if the anisotropic charge transport is triggered by structural differences in the P3HT devices in this work, in the following the electrical measurements are correlated to the TEM investigations from the previous section.

6.4. Discussion: Crystallinity Impact on Charge Carrier Mobilities

Summarizing most findings from the literature a general trend for decreasing crystallinity with increasing molecular weight along with an increasing mobility in OFETs is noted [6]. This leads to the conclusion that the well-ordered crystalline domains with a typical size of few nanometers, seen in the TEM

measurements in this work, do not have a direct impact on the charge transport occurring at a length scale of few micrometers. The fact that the 14k sample, which does not show ordered domains with the intermolecular spacing of 1.6 nm, exhibits almost the same field-effect mobility as the more ordered 24k sample, confirms this statement. It also confirms the reported anisotropy for which the charge transport along the lamellar stacking is found to be the slowest one and has obviously no significant impact [115, 116]. The slightly higher mobility of the 31k and 54k sample, which have a similar texture as the 24k sample in terms of crystallinity, is attributed to a better connectivity. It is assumed that in semicrystalline films, the long polymer chains connect the ordered regions leading to improved charge transport [155]. This is further assisted by the transport along the backbone of the longer polymer chains, which from other experiments as well as theoretical calculations is considered to be the fastest transport mechanism in P3HT [111, 115, 116]. It is likely that the amorphous regions do not participate in the charge transport and that in low molecular weight samples there are less bridges between the well-ordered regions, which results in an overall lower mobility [115]. Crossing points, which are usually more present in films with smaller ordered regions can additionally hinder the charge transport [115]. The paracrystallinity of P3HT, reported by Noriega et al. [155], is directly connected to deep traps in the density of states and increases with molecular weight. Thus, a saturation for the mobility is achieved as the optimal morphology for charge transport is a trade-off between high connectivity through long polymer chains (high molecular weight) and structural disorder [155]. Additionally, the transport along the backbone is also limited to the grain boundaries of the ordered domains. As already shown in figure 6.10, the investigated molecular weights in this thesis (marked in black) lie in the plateau where the mobility is limited by the discussed effects. This explains the only very small deviation of the mobility values for the different samples. Furthermore, the results from this work are in good agreement with theoretical calculations predicting OFET mobilities between $10^{-1}\,\mathrm{cm}^2/\mathrm{Vs}$ and $10^{-2}\,\mathrm{cm}^2/\mathrm{Vs}$ [115, 117, 155]. Strikingly, the published experimental results and the simulations assume a preferential edge-on orientation in order to achieve these values with charge transport in two dimensions: along the backbone and the π-π- stacks. In the TEM measurements in this work a preferential edge-on orientation is not observed, but still mobilities of the same order of magnitude, as assumed for edge-on orientation, are measured.

In addition, there is a further hint that the here investigated films have a preferential orientation. The derived mobilities perpendicular to the substrates from CELIV measurements are about two orders of magnitude lower than in the field-effect transistors along the interface with the dielectric. From

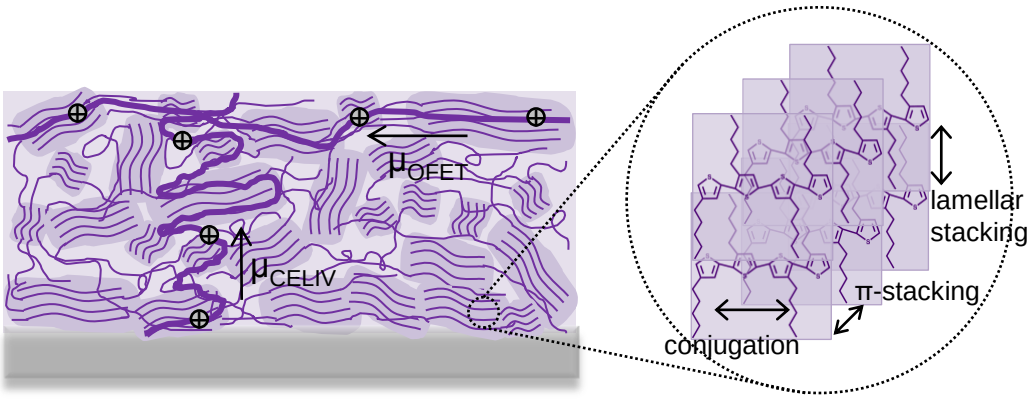

Figure 6.11: Simplified schematic of the P3HT layer structure based on the findings from this chapter with exemplary charge transport paths. The figure is based on [155].

the charge transport anisotropy it becomes clear that the orientation of the ordered regions cannot be completely random. Otherwise, if the morphology is the same in all directions of the film, the mobilities in the normal and parallel direction should be similar. The high mobilities in the OFET structure imply that at least at the interface between P3HT and the dielectric there are ordered domains preferentially edge on with π-π- stacking parallel to the dielectric. Although they are still surrounded by amorphous material, the domains are also connected through the molecular chains, which provide fast charge transport. On the other hand, this kind of orientation leads to a preferential lamellar stacking along the direction of the charge transport paths perpendicular to the substrate, measured in CELIV. Hence, the low CELIV mobilities are expected, as transport along the lamellar stacks is less efficient ($10^{-4}\,\mathrm{cm}^2/\mathrm{Vs}$ [117]). As there is still a huge amount of randomly oriented domains within the whole bulk, it is not surprising that the 14k exhibits the highest CELIV mobility although it does not show any lamellar stacking. The high connectivity between the domains by the long polymer chains along the substrate seem to hinder the charge transport to the substrate normal, explaining the decreasing CELIV mobility with increasing molecular weight. A conclusive schematic of the findings from this section unifying the anisotropic charge transport with the molecular order in P3HT is shown in figure 6.11.

The lessons learned from this chapter underline the importance of the correlation between electronic and structural properties derived from measurements of identically prepared samples. The TEM measurements exclusively would

not lead to a clear understanding of the material properties. One of the main reasons are the distinct length scales. Charge transport in OFETs happens only in the first few layers at the interface between the semiconductor and the dielectric, which cannot be directly assessed by TEM. Although the mobility in CELIV is measured through the whole bulk as in TEM, the active area of the diode ($1\,\mathrm{mm}^2$) exceeds the area that is measured in TEM ($\sim 1\,\mu\mathrm{m}^2$). Hence, TEM is only a snap-shot of a small part from the active area. The fundamental charge transport mechanisms happen on a significantly larger scale, which is not directly accessible. Only in combination with the electrical measurements of the mobility a comprehensive understanding of the polymers functionality is attained.

6.5. Structural Properties of P3HT Doped with F_4TCNQ from TEM Measurements

In the following section the effect of p-type doping of P3HT with the small molecule F_4TCNQ on the structural and electronic properties is investigated. The impact of doping on the crystal structure of P3HT is measured by means of electron diffraction. The spectroscopic features from EELS and infrared spectroscopy enable the determination of the degree of charge transfer from the donor to the acceptor molecule. Due to rather low reproducibility of the film quality, the shown results were collected from only one batch of samples. All investigated samples were prepared by Dr. Patrick Pingel (now at Fraunhofer Institute for Applied Polymer Research IAP, Potsdam) within a cooperation with Prof. Dieter Neher at the University of Potsdam and shipped over to Heidelberg for TEM and FTIR (Fourier transform infrared) measurements. The FTIR measurements were carried out by Dr. Tobias Glaser and compared with calculations of the F_4TCNQ molecule, performed by Dr. Christian Krekeler, TU Braunschweig. For the calculations the density functional theory (DFT) method was used with the BP86 functional (composed of the Becke 1988 exchange functional and the Perdew 86 correlation functional) and a DZP (double-zeta polarized) basis set.

6.5.1. Electron Diffraction

Electron diffraction measurements were performed on pure and doped P3HT (1:10 molar ratio). Diffraction patterns from 12 spots randomly distributed over the film were acquired from the doped sample and from 4 spots for the pure P3HT. Representative diffraction patterns of both samples are shown in

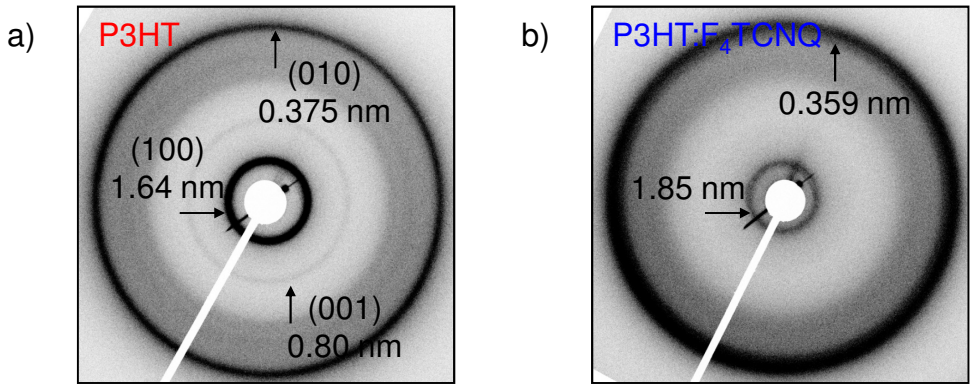

Figure 6.12: Diffraction pattern of a) neat P3HT and b) P3HT doped with F_4TCNQ in a 1:10 molar ratio. A significant change of the (100) and (010) ring diameters is noted.

figure 6.12 a) for the pure P3HT and b) P3HT:F_4TCNQ. As already introduced in the previous section, three distinct rings are clearly visible for P3HT and assigned to lamellar stacking (100), orientation along the backbone (001) and π-π- stacking. The sharpness of the rings indicates the presence of large crystalline domains, but without preferential orientation as there are no distinct diffraction spots. In the diffraction pattern of the doped sample in 6.12 b) the innermost ring (100) shrinks significantly in diameter and intensity. No order along the backbone of P3HT (001) is observed. The outside ring (010) is obviously broadened compared to the ring of pure P3HT, implying a decrease of the crystallinity.

The corresponding radial profiles are shown in figure 6.13 in red for P3HT and blue for the doped sample. As already assumed from the diffraction patterns, the peak attributed to the a-spacing at 1.64 nm shrinks. It is clearly broader and shifts to a larger spacing of 1.85 nm. The typical crystal size determined from the FWHM analysis decreases from 12 nm to about 5 nm. A similar change is observed for the π-stacking, however with the inverse effect that the peak shifts to smaller spacings from 0.375 nm to 0.359 nm. Furthermore, the peak exhibits a shoulder at the position of the π-stacking of the neat film at 0.38 nm determined from the Lorentzian fit as shown in figure 6.13. The radial profile of the doped film hints to the formation of a new semicrystalline phase. In the new crystal structure the dopant is incorporated into ordered P3HT domains. However, from the shoulder in the $b/2$- spacing, it is assumed that neutral P3HT is still present. In the literature the distance of 0.353 nm, which is in good agreement with the measured peak here at 0.359 nm, is calculated from DFT to be optimal between the F_4TCNQ and four thiophene

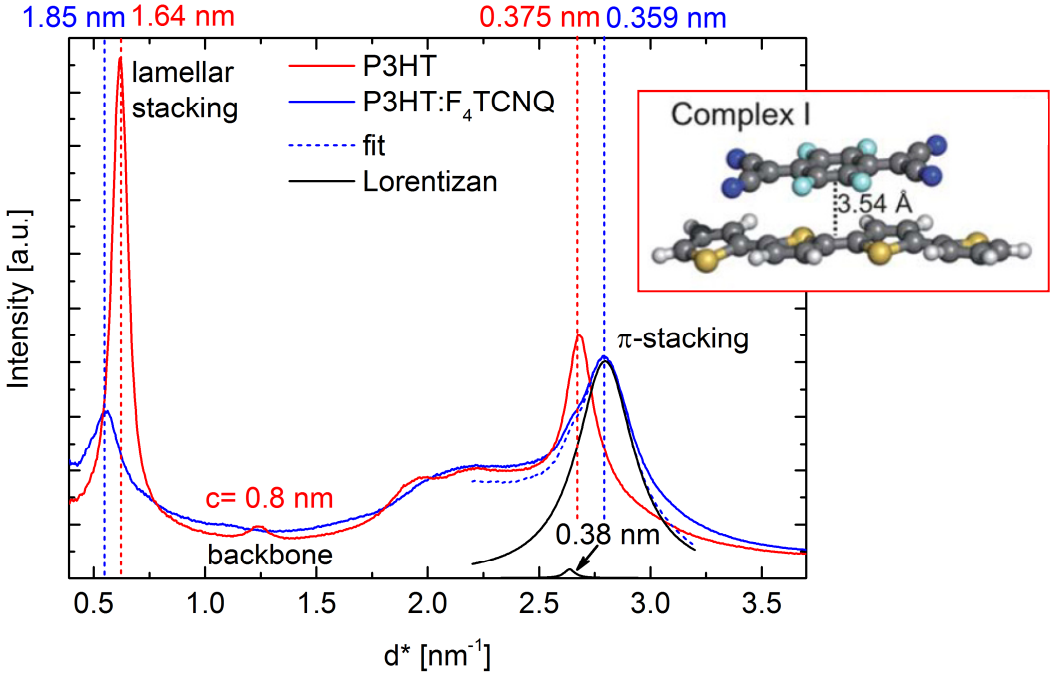

Figure 6.13: Radial profiles with indicated peak positions (in nm) of pure P3HT (red) and doped P3HT (blue). The position of the shoulder in the π-stacking peak is determined by a Lorentzian fit. It points out the presence of pure P3HT. The calculated charge transfer stack by Gao et al. between F_4TCNQ and four thiophene rings with 0.354 nm spacing is depicted [127].

monomers [85]. The spacing is consistent not only with the calculations but also with GIXD measurements (0.359 nm) by Duong et al. [126]. For this type of "high" doping concentration as in this work they suggest that the ionized F_4TCNQ is localized at the crystalline P3HT domains. Hence, doping reduces the $\pi-$stacking. These domains are surrounded by mostly amorphous P3HT. This model is consistent with the here presented TEM measurements. Further calculations additionally revealed that the four thiophene monomers, which originally exist in a non-planar geometry, are planarized after the formation of a charge transfer complex in a stack with F_4TCNQ [127]. The proposed stack by Gao et al. is shown in figure 6.13 [127]. The calculated spacing predicts considerably well the determined spacing from the radial profile. An increased planarity of the polymer backbone is expected to reduce the amount of shallow traps and thus enhance charge transport [127].

6.5.2. EELS and Energy Filtered TEM

EEL spectra are acquired in order to investigate the electronic properties of doped P3HT. From the determined excitations the eligible energy loss for energy filtered images is specified in order to examine the doped films for possible dopant agglomeration. The EEL spectra of neat F_4TCNQ, neat P3HT and doped P3HT are shown in figure 6.14. Normalized survey spectra of all three samples are shown in a). F_4TCNQ (shown in black) turned out to be very unstable in the electron beam. The intensity of the peak at 3.1 eV and of the plasmon at 21 eV decreases very strongly after the first spectrum acquisition. Therefore, it is not possible to show averaged and less noisy spectra. The onset at 2.6 eV of the marked peak at 3.1 eV is consistent with the calculated HOMO-LUMO transition from the S_0 to the S_2 state (transitions into S_1 are forbidden) for F_4TCNQ at 2.88 eV [86]. No further features are noted for F_4TCNQ.

The spectrum of pristine P3HT (red) exhibits the same shape as presented in the previous section and consists basically of the HOMO-LUMO transition at 2.6 eV and the collective π- and $(\sigma + \pi)$-electron plasmon excitation at 6 eV and 21 eV. The peak at 2.6 eV is in good agreement with the calculated (DFT) lowest electronic transition $S_0 \rightarrow S_1$ for four thiophene rings [86]. Interestingly, the spectrum of the doped compound (blue) resembles the shape of neat P3HT except for a peak between 1 eV and 2 eV and a slight increase of the plasmon intensity at 30 eV. This increase probably originates from the broad plasmon of F_4TCNQ.

In order to understand the origin of the excitations in the very low loss regime the spectra of P3HT and P3HT:F_4TCNQ are deconvoluted (explained in chapter 3.2.1.1)[5]. The results are shown in figure 6.14 b). In this case it is obvious that the zero-loss peak has superimposed features that are only visible after deconvolution. Two additional pronounced peaks with a maximum at 0.6 eV and 1.5 eV are clearly visible, which cannot be assigned to any of the pure species as they do not exhibit excitations in this energy range. The origin of the 0.6 eV will be discussed later on in detail. The peak at 1.5 eV is assumed to be a product of the formation of a charge transfer complex. This assumption is consistent with DFT calculations performed by Zhu et al. which predict peaks at 1.48 eV and 1.87 eV upon the formation of a charge transfer complex between F_4TCNQ and four thiophene rings [86]. The peaks are assigned to intermolecular transitions into the S_1 state from the donor HOMO to the acceptor LUMO (1.48 eV) and to a S_2 transition from the HOMO-1 of the donor to the LUMO of the acceptor (1.87 eV). Zhu et al. compare their calculations

[5]Deconvolution of the F_4TCNQ spectrum could not be carried out due to the strong noise.

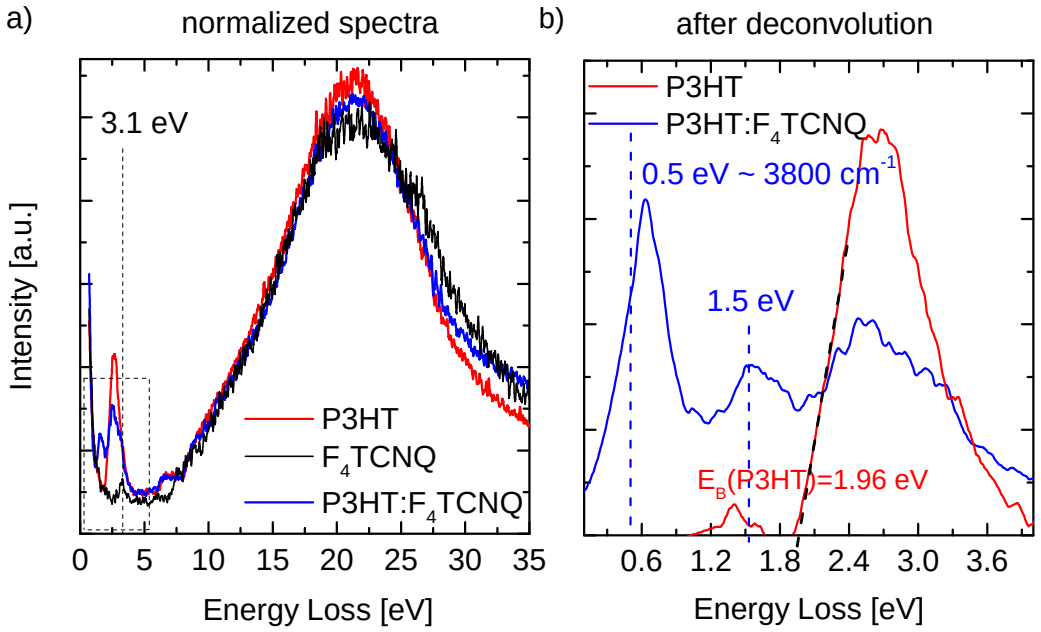

Figure 6.14: EEL spectra of F_4TCNQ (black), P3HT (red) and doped P3HT (blue) a) from 0 eV to 35 eV and b) after deconvolution in the very low energy loss region. Two new peaks for the doped P3HT, that cannot be assigned to the pristine species, are observed.

as well with experimental data from optical absorption measurements showing peaks at 1.55 eV and 1.61 eV, which are consistent with the 1.5 eV peak in the EEL spectrum in figure 6.14 b) [86]. The deviation between the experimental values and the calculation is explained by the assumption of only four thiophene rings in the calculation [86]. With increasing chain length the energy gap between HOMO and HOMO-1 is narrowed which explains the energy difference of only $\Delta E = 0.06$ eV in the experiment compared to $\Delta E = 0.39$ eV from DFT. In EELS, though, a superposition of both peaks is measured at 1.5 eV appearing as one broad peak limited by the resolution of the instrument which is usually about 80 meV. On the other hand, absorption peaks at 1.43 eV and 1.6 eV are also observed in experiments by Duong et al. and Pingel et al., but are attributed to sub-band absorptions of the negatively ionized F_4TCNQ, also known as a polaron absorption [84, 126]. Both models, the charge transfer complex transition as well as the polaron absorption, deliver a possible explanation for the observed peak at 1.5 eV in the EEL spectrum.

Moreover, the peak of the doped compound at 2.6 eV appears to be slightly

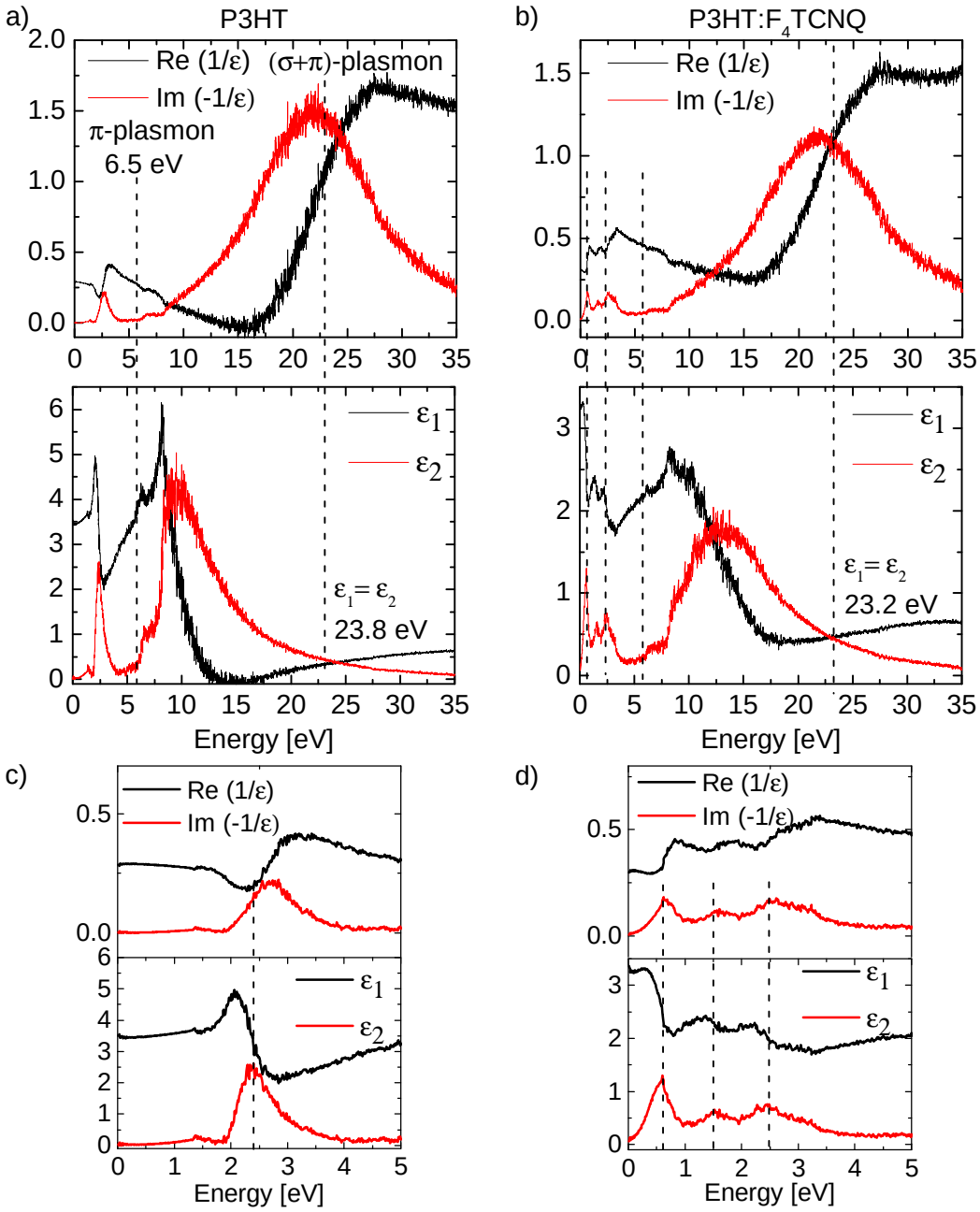

Figure 6.15: Im $\left[-\frac{1}{\epsilon(E)}\right]$ (red), Re $\left[\frac{1}{\epsilon(E)}\right]$(black), $\epsilon_1(E)$ (black) and $\epsilon_2(E)$ (red) calculated for a) P3HT and b) P3HT:F_4TCNQ in a 1:10 molar ratio. Characteristic features are marked with dashed lines. The range between 0 eV and 5 eV is shown in c) for P3HT and d) for P3HT:F_4TCNQ.

shifted towards smaller energies with respect to the peak of the neat P3HT. This is also consistent with the theoretical calculations. Its origin is suggested to be the intramolecular HOMO-LUMO transitions of the pristine molecules [86]. The origin of the strongest peak at 0.6 eV is discussed and correlated to IR measurements in the following section 6.6.

In order to study the nature of the new excitations in the doped sample more in detail a Kramers-Kronig analysis is implemented on the EEL spectra of pure and doped P3HT. For the analysis a refractive index of $n = 1.9$ is assumed for both samples[6] [162]. Im $\left[-\frac{1}{\epsilon(E)}\right]$ and Re $\left[\frac{1}{\epsilon(E)}\right]$ together with the corresponding dielectric functions are derived as explained in section 3.2.1.2 and plotted in figure 6.15 for a) P3HT and b) P3HT:F_4TCNQ. As the EEL-spectrum is proportional to the loss-function, Im $\left[-\frac{1}{\epsilon(E)}\right]$ (red) in a) and b) is in good agreement with the measured P3HT and P3HT:F_4TCNQ spectrum. Re $\left[\frac{1}{\epsilon(E)}\right]$ (black) resembles the differential of Im $\left[-\frac{1}{\epsilon(E)}\right]$ as expected from the mathematical relationship. The corresponding dielectric functions are presented in figure 6.15 (bottom) a) and b). The conditions for a plasmon excitation are fulfilled if $\epsilon_1 \approx \epsilon_2$ in the region where the dielectric functions do not exhibit any peaks. In this measurement this condition is valid at 6.5 eV and 23.8 eV for P3HT a) and at 23.2 eV for P3HT:F_4TCNQ. The positions are marked with dashed lines. The energies are in accordance with the plasmon peak maxima in the EEL-spectra. In 6.15 c) and d) a close up of the functions between 0 eV and 5 eV is shown. Pronounced peaks are observed in the dielectric function of doped P3HT in d) at 0.6 eV and 1.5 eV. Therefore, it is concluded that the new excitations in the doped film, which cannot be attributed to the pure materials, represent single-electron transitions. In this case, a collective electron excitation is excluded, as the conditions for a plasmon are not fulfilled.

Bright-field images of pristine and doped P3HT with 1:10 molar ratio are shown in figure 6.16. The zero-loss filtered images of pure P3HT in a) and doped P3HT in b) exhibit similar textures. Lattice fringes with 1.6 nm and 1.8 nm spacing are noted and marked with red and blue arrows. Dark appearing regions can be recognized in the doped sample, however in order to reveal true material contrast further energy-filtered images were acquired. From the EEL spectra it is clear that P3HT and F_4TCNQ cannot be distinguished by means of the plasmon excitation in the blend, as both plasmons peak at the same energy. The strongest spectral difference is given by the band gap transition of P3HT at 2.6 eV. An energy filtered image at 2.6 eV energy loss is shown in figure 6.16 c). The image does not reveal any pronounced features

[6] The refractive index of the doped samples is assumed to be the same as of P3HT.

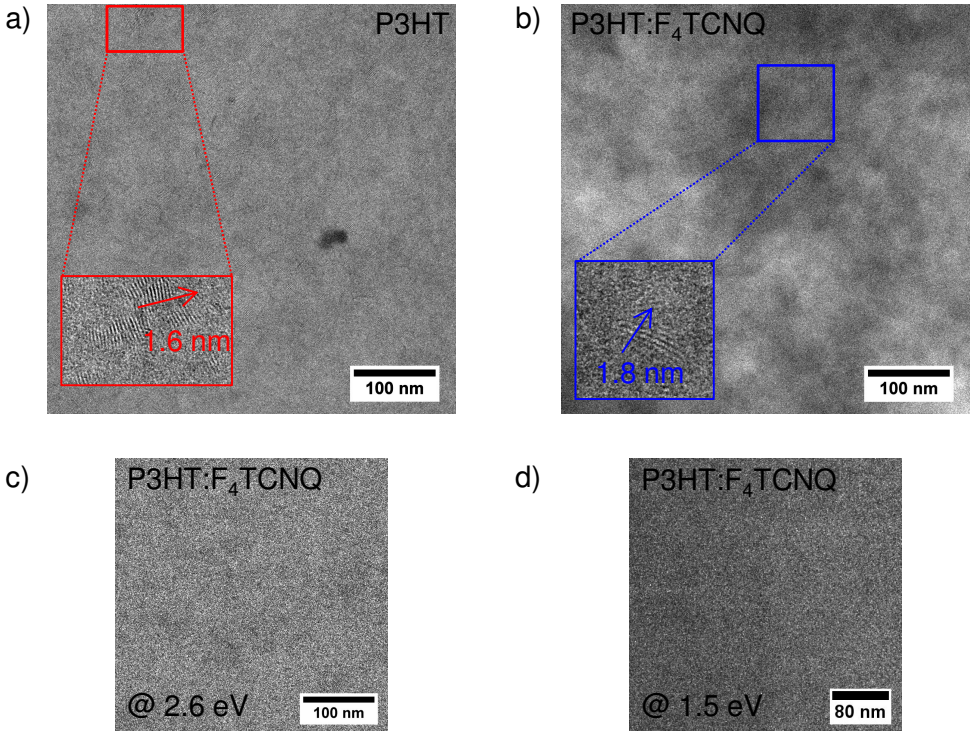

Figure 6.16: Bright-field images of a) P3HT, b) doped P3HT, c) at 2.6 eV energy loss of the doped sample and d) at 1.5 eV of the doped sample.

and exhibits mostly white noise. This points out a probably homogenous distribution of the dopant or at least excludes larger clusters. Further EFTEM images from 0 eV to 40 eV could neither reveal any specific material contrast. Due to the low cross-section of fluorine the acquisition of core-loss images at the fluorine energy edge could not be carried out in order to localize possible donor agglomerates [163]. In agreement with the TEM measurements, the formation of isolated acceptor clusters is ruled out by Pingel et al., who as well prepared the samples for this work, as they do not see any presence of neutral F_4TCNQ from UV-VIS-NIR absorption measurements [84, 164]. A further publication states agglomeration of F_4TCNQ in a P3HT matrix, however a clear evidence from experiments is not presented [125].

Beyond the P3HT features, the peak at 1.5 eV would offer the possibility to localize the charge transfer complex in an EFTEM image. The image at 1.5 eV energy loss is shown in figure 6.16 d). Unfortunately, a large part of the image is slightly superimposed by the intensity of the zero-loss signal as the energy selecting slit is not narrow enough (width around 1.5 eV). Additionally, as the

signal from the features is very weak, the image in figure 6.16 d) exhibits mostly noise. Further experiments to image the charge transfer complex could not be carried out within the scope of this work as the alignment of the instrument deteriorated and did not allow high-resolution energy filtered measurements. Furthermore, the sample batch could not be reproduced in its layer quality so far.

6.5.3. Conclusion: TEM Measurements

The findings from the TEM measurements on P3HT doped with F_4TCNQ can be summarized as follows:

- The formation of a new crystal structure with a π-stacking between P3HT and F_4TCNQ of 0.359 nm is derived from electron diffraction. A small fraction of the crystal structure of pristine P3HT is preserved.
- EELS reveals the existence of two new peaks upon doping of P3HT at 0.6 eV and 1.5 eV. So far it is not specified whether the peaks are caused by transitions within the energy levels of the charge transfer complex or by polaron absorption of ionized P3HT or F_4TCNQ. The dielectric functions point to a single-electron transition and exclude a collective excitation.
- Bright-field and energy filtered TEM images suggest a homogenous distribution of the dopant within the P3HT matrix.

6.6. Charge Transfer Determined by Infrared Spectroscopy

FTIR (Fourier transform infrared) measurements were performed on the same batch of samples as presented in the previous section. However, as the measurements were carried out in transmission mode, one important requirement for the substrates is transparency in the infrared regime. Therefore, all samples were spin coated on silicon (SiO_x) substrates. The infrared (IR) spectrum of neutral F_4TCNQ along with the DFT calculated spectrum are shown in figure 6.17 a). A very good agreement is noted as the shapes of the spectra are very similar. Even small features, for example the rather weak band at lower wavenumbers next to the strong asymmetric C-C-stretching mode at 1574 cm^{-1} is represented as a pronounced shoulder in the calculation. Shifts of about 10 cm^{-1} between the calculated and measured absolute position

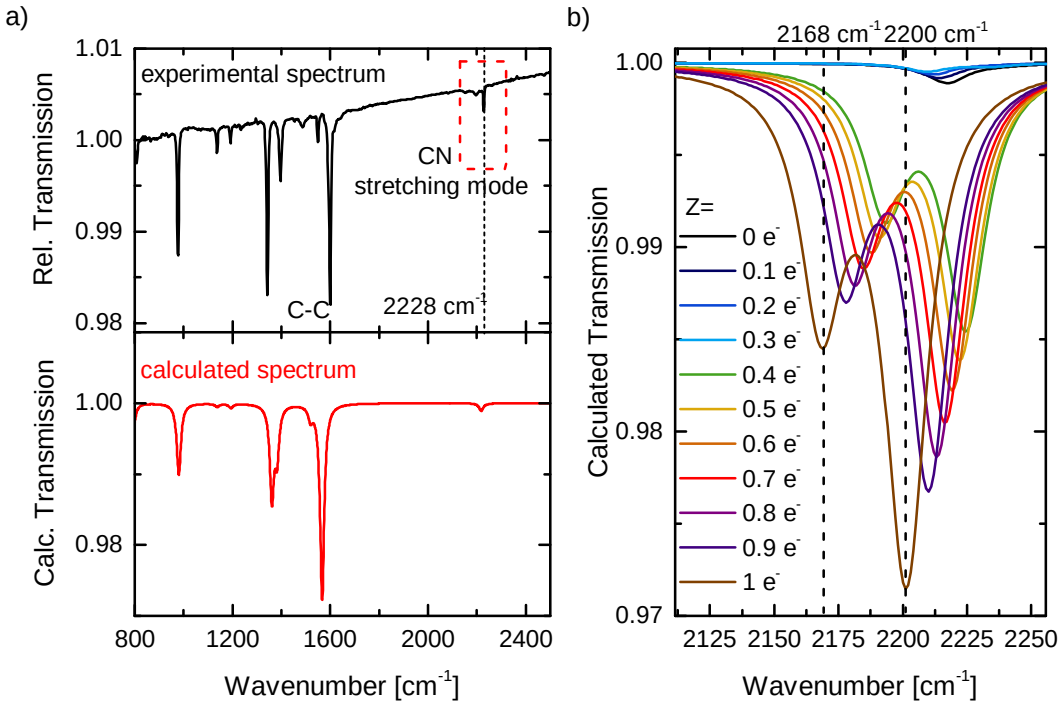

Figure 6.17: IR spectra of F_4TCNQ. a) Comparison between a measured and a calculated spectrum of neutral F_4TCNQ. b) The calculated frequency shift of the CN-stretching mode of F_4TCNQ with increasing partial charge transfer.

of the modes are within the error margin of this calculation method with the chosen basis set [86, 100].

The following measurements, however, mainly focus on the CN-stretching mode at 2228 cm^{-1} marked in figure 6.17 a) (a zoom on the mode will be shown later on). The CN-mode is known to be very sensitive to electronic changes in the molecule [165,166]. If a charge is transferred from the HOMO of the donor into the LUMO of the acceptor, the CN-bond length increases. The bond is weakened as the LUMO of F_4TCNQ is antibonding with respect to the CN-bond. Hence, if charge transfer occurs and the LUMO of the acceptor is occupied, the CN-mode is shifted towards lower frequencies. Therefore, the CN-stretching mode can be used as an indicator for charge transfer between donor and acceptor molecules. Additionally, it has been observed for the non-fluorinated TCNQ, that there is a linear relationship between the degree of charge transfer and the frequency shift of the CN-mode [165, 166]. The degree of charge transfer (Z) basically describes the probability to find the transferred

electron at the donor HOMO or acceptor LUMO. Thus, by monitoring the CN-stretching mode in the IR-spectrum of P3HT doped with F_4TCNQ, the degree of charge transfer can be estimated.

The calculated frequency shift with respect to the charge transfer is shown in figure 6.17 b). For the calculation 0.1...1.0 electrons (e^-) are added successively to the LUMO of the acceptor and the geometry of the molecule in the gasphase is optimized accordingly. For partial charge transfer up to $0.4\,e^-$ the frequency of the CN-mode decreases linearly starting at $2217\,\mathrm{cm}^{-1}$. For Z higher than $0.4\,e^-$ a second vibration, which surfaced only as a small shoulder before, appears very pronounced at $2227\,\mathrm{cm}^{-1}$. Now both vibrations shift linearly to lower frequencies with increasing Z. The same effect has been reported for TCNQ [165]. It is assumed that with increasing negative partial charge on the dicyanomethine group of TCNQ the local dipole moment increases causing the higher IR-activity of the second mode [165]. The linear relationship between the frequency shift of the CN-mode and the charge transfer for F_4TCNQ is shown in figure 6.18. A discontinuity is observed between $0.3\,e^-$ and $0.4\,e^-$, which is an artefact of the calculation method[7].

The calculated possible symmetries of the CN-modes of neutral F_4TCNQ, four in total, are depicted on the right-hand side in figure 6.18. The red vectors indicate the oscillation direction. The first two stretching modes with b_{3g} and b_{2u} symmetry exhibit the highest intensity. Hence, the strongest mode from the experiment at $2228\,\mathrm{cm}^{-1}$ is attributed to a joint oscillation of the b_{3g} and b_{2u} mode. This is also in good agreement with published calculations for the same symmetries by Zhu et al. at $2219.64\,\mathrm{cm}^{-1}$ [86]. As already mentioned, the discrepancy between the calculated $2217\,\mathrm{cm}^{-1}$ and the measured $2228\,\mathrm{cm}^{-1}$ is within the error margin of the calculation method. In the presented calculations the a_g mode is not IR-active and not present in the measurement. The b_{1u} mode exhibits a much lower intensity than b_{3g} and b_{2u} and is excited at higher wavenumbers. This mode is not visible in the measured spectrum of the neutral acceptor. However, for the charged F_4TCNQ the IR-activity of the b_{1u} mode increases strongly and even exceeds the intensity of b_{3g} and b_{2u} as already presented in figure 6.17 b).

At this point, it has to be mentioned that the assignment of the symmetries is not explicit and needs to be considered carefully. The assignment is based on calculations which assume the gasphase of the molecule. Though, as shown by Zhu et al., the calculated spectrum of a F_4TCNQ crystal can be distinct [86]. In

[7] For $Z < 0.4\,e^-$ the LUMO of neutral F_4TCNQ is filled successively with partial charges, whereas for $Z > 0.4\,e^-$ partial charges are removed from the ionized acceptor causing the slight discrepancy in the values for the absolute wavenumber [100].

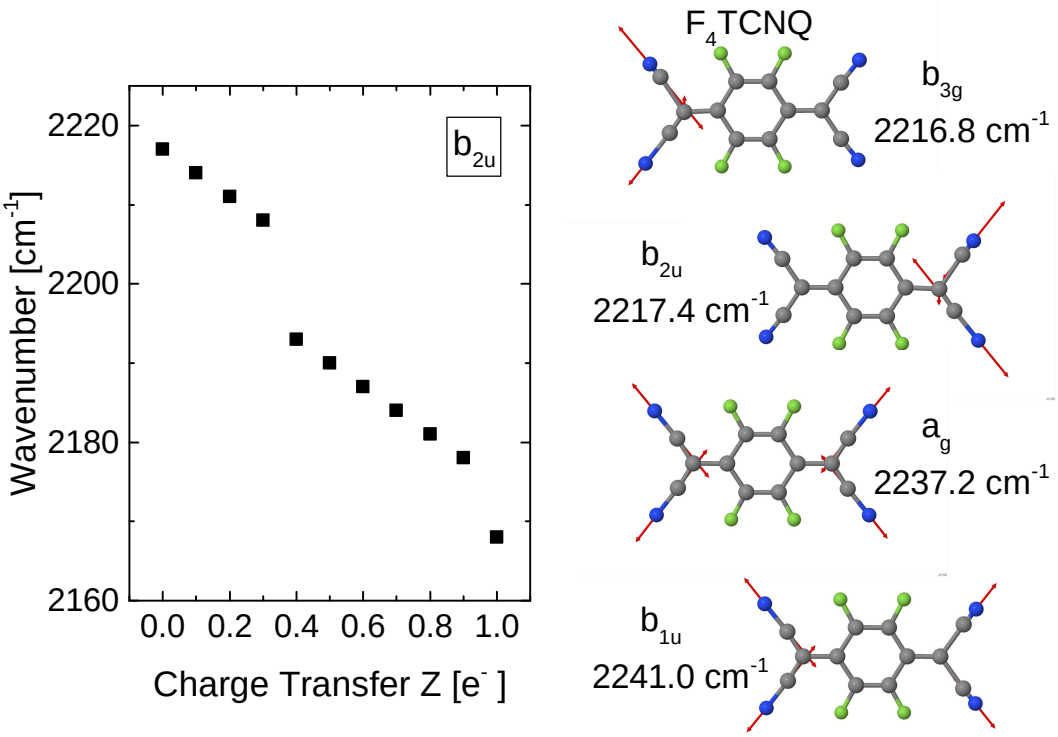

Figure 6.18: The linear relationship between the calculated frequency shift of the CN-stretching mode of F_4TCNQ and the degree of charge transfer Z. The four calculated symmetries b_{3g}, b_{2u}, a_g and b_{1u} of the CN-mode with the corresponding oscillation vectors (red arrows) are shown on the right-hand side.

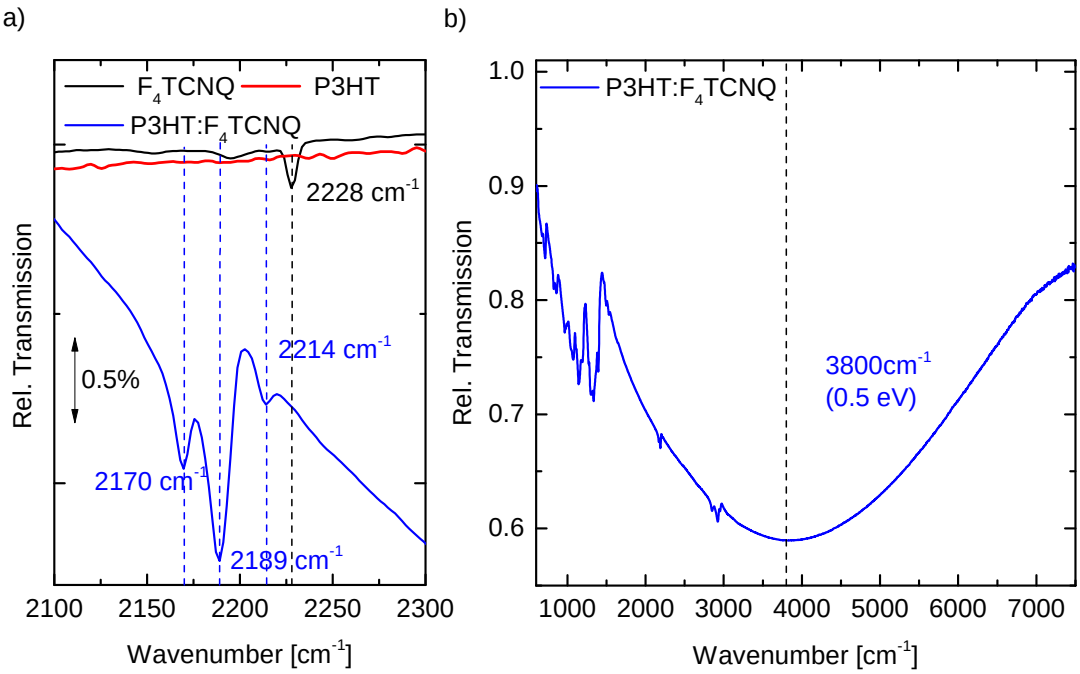

Figure 6.19: Measured IR spectra of a) F_4TCNQ (black), P3HT (red) and P3HT:F_4TCNQ (blue) with marked mode positions. b) NIR spectrum of P3HT:F_4TCNQ exhibiting a broad absorption at $3800\,cm^{-1}$.

this case the b_{1u} mode exhibits the highest intensity at the highest wavenumber followed by a very weak b_{3g}/b_{2u} mode at lower wavenumbers. Hence, the measured vibration at $2228\,cm^{-1}$ exhibits a b_{1u} symmetry in the crystalline phase. As shown in the TEM measurements, the F_4TCNQ doped sample is polycrystalline. Therefore, it is likely that the calculations for the crystal by Zhu et al. are more suitable for the description of the measurements in this thesis. However, both calculation methods agree on the shift towards lower frequencies upon charge transfer.

The measured vibrational spectrum of neutral P3HT, F_4TCNQ and doped P3HT (1:10 molar ratio) is shown in figure 6.19 a). Pure P3HT (red) does not show any features in this spectral range. As expected from the DFT calculations, the neutral F_4TCNQ (black) exhibits one CN-stretching mode at $2228\,cm^{-1}$. In the doped sample (blue), the CN-mode exhibits a red shift to $2189\,cm^{-1}$ and a second vibration at $2170\,cm^{-1}$ has appeared as predicted from the calculation. A third vibration is observed at $2214\,cm^{-1}$, which is attributed by Pingel et al. and Zhu et al. to one of the CN-modes in neutral

F_4TCNQ [86, 164]. It is possible that the mode at $2214\,cm^{-1}$ is too weak to be resolved for the neutral F_4TCNQ in this measurement. However, it is not clear if neutral F_4TCNQ is still present in the charge transfer complex, why the mode at $2228\,cm^{-1}$, which is also attributed to the neutral acceptor, is not observed in figure 6.19 a). It is striking, that the resulting degree of charge transfer of $1.25\,e^-$, which corresponds to the frequency shift of the CN-stretching mode, exceeds integer charge transfer. This has not been reported so far. However, the agreement with the calculated red shift from figure 6.17 b) is very convincing. Pingel et al. assume an integer charge transfer from their measurements [164].

Moreover, an overall strong decrease of the transmission is observed in figure 6.19 a) towards higher wavenumbers. This is elucidated by a further measurement in the near infrared range shown in figure 6.19 b). Here, a very broad and strong absorption is spotted with an absorption minimum at $3800\,cm^{-1}$, which correspond to 0.5 eV. In the EEL spectrum from the previous section a pronounced peak was observed at 0.6 eV, which seems to be associated with the NIR absorption. Based on the diffraction measurements, which revealed a new crystal structure of P3HT doped with F_4TCNQ, it is possible that the measured absorption at $3800\,cm^{-1}$ represents an electronic excitation of a charge transfer state. Broad absorption bands with this kind of shape at a similar frequency have been observed in other organic material systems [165, 167]. Glaser et al. attribute a wide band at around $5000\,cm^{-1}$ in doped CBP to a transition between charge transfer states [167]. The charge transfer complex DBTTF:TCNQ as well is reported to exhibit a pronounced absorption of the charge transfer state [165]. On the other hand, a polaron absorption of charged P3HT in e.g. iodine doped films is often observed at around 0.4 eV and a bipolaron absorption of the doubly charged polaron is reported at 0.5 eV [84, 168–170]. This leads to the conclusion, that the origin of the wide absorption band measured here might be also a polaron absorption of P3HT. The fact that the absorption is observed in P3HT doped with other compounds than F_4TCNQ implies that this is more likely a property of P3HT than an excitation of the charge transfer complex P3HT:F_4TCNQ.

6.6.1. Conclusion: Infrared Spectroscopy

From the presented results of the FTIR measurements on P3HT doped with F_4TCNQ it is concluded:

- From the frequency shift of the CN-stretching mode a degree of charge transfer higher than $1\,e^-$ is determined for P3HT:F_4TCNQ in a 1:10

molar ratio.

- There is no clear evidence for the presence of neutral F_4TCNQ in the doped film.
- A broad absorption is observed at 0.5 eV, which might be induced by transitions of the charge transfer state. However, polaron absorptions of the charged P3HT, usually excited at a similar energy range, cannot be excluded.

6.7. Discussion: Crystallinity Impact on Charge Transfer

A very interesting result from this section is the charge transfer exceeding 1 e^- for P3HT doped with F_4TCNQ in a 1:10 molar ratio. The crystallinity of the film might play a key role for the degree of charge transfer. In the electron diffraction measurements two very distinct spacings at 1.85 nm and 0.359 nm are observed confirming the existence of a new crystal structure. The formation of this crystalline structure is possibly triggered by the formation of a charge transfer complex between P3HT and F_4TCNQ. From the rings in the diffraction pattern it is clear that the film is polycrystalline. In ordered domains the delocalization of electrons is very strong and extended on a large scale. It is likely that the polymer offers more than one electron to the acceptor as the electrons of the polymer are delocalized over a large range. One possible way to investigate the impact of crystallinity on the charge transfer is by intentional decrease of the film crystallinity. A lower degree of charge transfer is expected in that case for the approval of the proposed hypothesis. For this purpose, two different batches of spin coated samples out of a chlorobenzene (expected to decrease the order within the film) instead of a chloroform solution were prepared and investigated along with a reference sample prepared as in the first batch (1:10, chloroform). Preliminary results indicate lower ordering and an integer charge transfer for the doped sample spin coated from the chlorobenzene solution, which strengthens the hypothesis. However, the reference samples in the second batch did not show any signature of doped P3HT. It is possible that degradation of the samples has occurred during the long transport period from Potsdam to Heidelberg. This is likely to happen, as F_4TCNQ is known to be very volatile already at low temperatures of 50°C - 60°C, which might cause diffusion of the dopant out of the P3HT matrix. In order to exclude degradation effects the samples have to be prepared

the same day as measured, which is a future project and beyond the scope of this work. Additionally, further doping concentrations are of high relevance for the comprehensive understanding of the impact on charge transfer and the underlying doping mechanism in solution processed organic systems.

The chapter on pure and doped P3HT clarified some of the challenges for advanced analytical measurements on solution processed samples: reproducibility. Results have to be considered critically on their universality especially when compared with other works. The set of variable processing parameters is very large and hard to control. In vacuum-deposited small molecule films, which are investigated in the next chapter, the set of variable processing conditions is smaller, which is promising for a more controllable morphology.

7. The Decisive Role of Active Layer Morphology for Solar Cell Performance

At the beginning of this chapter a review of the present state of the art investigations on the structure-function-relationship of small molecule organic cells is presented. Following this section the results achieved in this thesis are shown, focusing on EELS, EFTEM and electron diffraction measurements on pristine organic layers and blends (BHJs). Moreover, IV-characteristics of small molecule BHJ solar cells are presented. In the last part of this chapter a comprehensive discussion and a conclusion on the impact of morphology on device performance is given.

7.1. State of the Art

The influence of the active layer morphology on organic solar cell performance has been widely discussed in the literature for the past years. Tang was the first to introduce the organic solar cell with a simple bilayer structure [3]. Later, it was discovered by Heeger et al. that an interpenetrating donor-acceptor network (bulk heterojunction) is needed for more efficient charge separation at the interfaces of the two materials [26]. Therefore, the morphology of the active layer became more complex [26, 171–173]. This is especially true for solution-processing of BHJs that enables a large number of parameters like molecular weight of the materials [130], varying solvents and additives [174–176], thermal annealing [177], solvent annealing [178] etc.. These parameters directly drive crystallization processes and phase separation in the active layer [179–182]. The numerous publications on the processing conditions already demonstrate that controlling and understanding the exact morphology, which is the key for high performance devices, is a challenge. Additionally, the variance of the different fabrication approaches leads to a lack of reproducibility (see chapter 6).

In contrast, vacuum-deposited small molecule solar cells, which are investigated in this chapter, offer a smaller set of processing parameters, such as evaporation rate, composite ratio, substrate, and substrate temperature during material deposition [12, 183–185]. A correlation between substrate temperature during co-evaporation of the blend and device efficiency is observed for various small molecule blends with C_{60} as acceptor [183, 185]. For example in DCV4T:C_{60} blends deposited on heated substrates, the device efficiency decreases, which is attributed to a decrease in light absorption arising from changes in the crystal orientation [185]. Phase separation for the blend on heated substrates is derived from photo-luminescence measurements, but seems not be beneficial for device performance. The contrary effect is demonstrated for DCV6T:C_{60} blends [183]. Here, device performance increases from 1.6 % to 3.8 % for blends deposited at elevated substrate temperatures, which is explained by improved demixing and larger structures observed in AFM measurements. Contradictory findings exist also for ZnPc:C_{60} BHJs. Leo et al. deduce from AFM and GIXRD measurements phase separation and polycrystalline growth for co-evaporated blends deposited at heated substrates, which leads to well connected percolation paths for the charge carriers and thus improved device performance [12, 13, 184]. Others point out that already unheated ZnPc:C_{60} blends form separate domains of ZnPc and C_{60}, but heating enhances the crystallinity of C_{60}, whereas ZnPc remains disordered [13]. The performance improvement in these cells, though, is not significant and mainly attributed to the segregation of the materials and not to the crystallinity. On the other hand, Schindler et al. did not observe a significant increase in efficiency for ZnPc:C_{60} devices on substrates heated to 90°C, although they demonstrate clear phase separation from TEM measurements [186].

More studies exist on only molecular orientation, crystallinity and phase separation of C_{60} blends with different donor materials without the connection to actual devices [15, 187–193]. Banerjee et al. observed that column-like crystallites grow in segregated species in a DIP:C_{60} blend, with the crystallite domain size depending on the film thickness, which was monitored by in situ GIXRD [187]. Further measurements of grazing incidence small angle scattering and x-ray reflectivity indicated that the distance of the separated islands depends on the mixing ratio of DIP:C_{60}. This result needs to be kept in mind, as column crystal growth can induce anisotropic charge transport, which must be considered for device architecture [128].

For F_4ZnPc:C_{60} (the fluorinated version of ZnPc), which is used in this thesis, an increased fill factor, higher short circuit current and improved efficiency from 3.6 % to 4.6 %, due to substrate heating (104 °C), is observed [89]. Meiss et al. attribute this effect to larger structure sizes from AFM and SEM

measurements and probably better connection of the charge carrier percolation paths. The authors neglect effects arising from the crystallinity of the layers, as XRD does not reveal peaks that can be assigned to crystalline F_4ZnPc or C_{60}. In conclusion, the results from the substantial literature do not present a clear correlation between morphology and device performance. So far, morphology investigations focused mainly on phase separation. Its connection to possible key factors like preferential orientation of the donor or acceptor molecules, crystallinity and column growth, remain undefined. The overall good performance of F_4ZnPc:C_{60} solar cells and the unresolved origin of their significant efficiency improvement when deposited on heated substrates, makes this material combination a promising candidate for this thesis.

TEM Studies

TEM measurements allow a good understanding of the active layer morphology. The advantage over other structural probing methods like XRD or AFM is the possibility to spatially resolve domains with true material contrast (EFTEM) combined with crystallinity deduced from electron diffraction. Very few TEM measurements on small molecule blends covering all aspects exist [12, 64, 65]. Pfuetzner et al. performed bright-field TEM on ZnPc:C_{60} indicating crystalline ZnPc domains from the spacings in the Fourier-transformation [12]. An overall overview on orientation from electron diffraction or domain assignment from EFTEM measurements is not given. Schindler et al. reported on the investigation of phase separation in ZnPc:C_{60} blends by plasmonic contrast from EFTEM images at the characteristic energy loss of the fullerene [64]. The presented plasmon peak map reveals temperature induced C_{60} agglomeration for samples deposited at 90°C , but diffraction profiles and the impact on devices are not shown. The work by Gilchrist and co-workers presents a new, less damaging, cross-section preparation technique by FIB milling preserving the crystalline nature of CuPc and C_{60}, but also without further correlation to actual solar cells [194].

The TEM measurements in this chapter mainly address the crystallization processes as an additional and important aspect to morphology in pure and blended F_4ZnPc and C_{60} layers deposited at room temperature and on substrates heated to 100 °C during layer deposition. For a successful distinction between the donor and the acceptor, the study is completed by acquisition and classification of ESI series, as introduced by Pfannmöller et al. (and also explained in chapter 3.2.2) [17]. The segmentation of the image series by plasmon peak mapping [65] or multivariate statistical analysis is expected to spatially resolve F_4ZnPc and C_{60} rich domains [17]. Typical domain size and

crystallinity is directly correlated to device performance, in order to get an extensive understanding of the material system, which is, given the already discussed literature, the unique feature of this thesis.

7.2. TEM Measurements on Small Molecule OPV Cells: F_4ZnPc:C_{60}

For a successful and profound structural analysis of BHJs by TEM, the properties of the pristine layers must be studied first. The electronic properties, such as electronic transitions, collective excitations or the dielectric function are determined from EELS and correlated to optical measurements. The overall appearance of the layers on heated and non-heated substrates, including crystalline domains, are imaged by means of the TEM bright-field mode. The exact lattice spacings are deduced from electron diffraction patterns. Subsequently, the spectroscopic properties of F_4ZnPc:C_{60} blends deposited at different substrate temperatures are probed. The comparison with the features of the pristine layers provides a deeper understanding of the electronic interaction between the compounds and their absorption behavior. From the diffraction patterns the crystallization processes upon co-evaporation of the pure materials on varying substrates at different temperatures are examined. The overall structural properties of the OPV blend are completed by the energy filtered TEM measurements exploring for phase separation and agglomeration in the films.

The entire set of measurements was performed with the same TEM settings on the exactly same samples. All films were evaporated with $1.0 - 1.5\,\mathrm{nm/min}$ and exhibit the same thickness of $45\,\mathrm{nm} \pm 5\,\mathrm{nm}$ in order to ensure the comparability between the measurements. Additionally, the film thickness was chosen to correspond to the thickness of active layers in devices, which justifies the relevance of the results. The spot size on the sample (illuminated area) was about 100 nm in diameter for EELS, and $905 \times 905\,\mathrm{nm}^2$ for BFTEM and diffraction. If not indicated otherwise, all layers for the TEM measurements were deposited on ITO/PEDOT:PSS and floated off the substrate as described in 4.3.1. The different TEM measuring modes were applied to samples deposited on substrates at room temperature (RT) and on heated substrates at $100 \pm 10°\mathrm{C}$. The chosen temperature is reported to be optimal for the best device performance [89, 184]. For a more convenient readability of the chapter, the samples deposited on substrates at RT or 100 °C will be abbreviated RT-sample and 100 °C-sample, respectively.

7.2.1. Pristine F_4ZnPc Layers Grown at Different Temperatures

The complete sequence of TEM measurements described above was applied to the pure donor F_4ZnPc deposited at RT and at 100 °C. Each type of measurement (BFTEM, EELS and diffraction) was acquired from four different spots chosen randomly from each sample. The reproducibility, compared to the previously discussed polymers, is very high. Variations of the spectroscopic and structural properties within one sample were not noted. In the following, for each sample the results from one representative measuring spot are shown. A compilation of all measurements is presented in the appendix A.

TEM Spectroscopy

The EEL-spectra measured on F_4ZnPc are shown in figure 7.1. The spectrum acquired from the RT-sample is indicated in black, the 100 °C-sample in red (figure 7.1 top). It is considerable that both spectra are in excellent agreement, indicating that the probed electronic properties do not change upon heating. The numbers in the spectrum marked 1 through 5 correspond to the five commonly seen peaks. As widely shown in the literature from optical absorption measurements and valence effective Hamiltonian calculations, absorption spectra of metal-phtalocyanines exhibit one intense band in the visible region, the so called Q band, and one in the UV spectral range, the B band (also known as the Soret band) [195–202]. Both bands are assigned to $\pi-\pi^*$ transitions from the HOMO to the LUMO. The Q band at 1.9 eV and the B band at 3.4 eV for ZnPc are in good agreement with peaks 1 (2.1 eV) and 2 (3.9 eV) from the measured F_4ZnPc EEL-spectrum in figure 7.1 (top) [197,198]. The slight deviations are not surprising as the reported values are derived from rather broad absorptions. Due to the similar shape of peak 3 it is assumed that latter corresponds as well to a $\pi-\pi^*$ transition. EEL-spectra in the literature do not resolve peaks 1-3, as the ZL-peak is very broadened by the used electron accelerating voltage of 200 kV (compared to 60 kV in this work) and the lack of a narrow monochromator [65]. Beside a small shoulder (4), the collective plasmon excitation (5) of the $\pi-$ and σ-electrons features the typical broad shape for organic compounds (see 3.2.1). The peak maximum at 22.9 eV (determined by a Gaussian fit), is in good agreement with the 23 eV measured by Schindler et al. for the non fluoridated ZnPc [65].

Im $\left[-\frac{1}{\epsilon(E)}\right]$ and Re $\left[\frac{1}{\epsilon(E)}\right]$ are derived from the Kramers-Kronig-Relation as explained in section 3.2.1.2 and plotted in figure 7.1 (middle). Due to the proportionality of the measured EEL-spectrum to the loss-function Im $\left[-\frac{1}{\epsilon(E)}\right]$

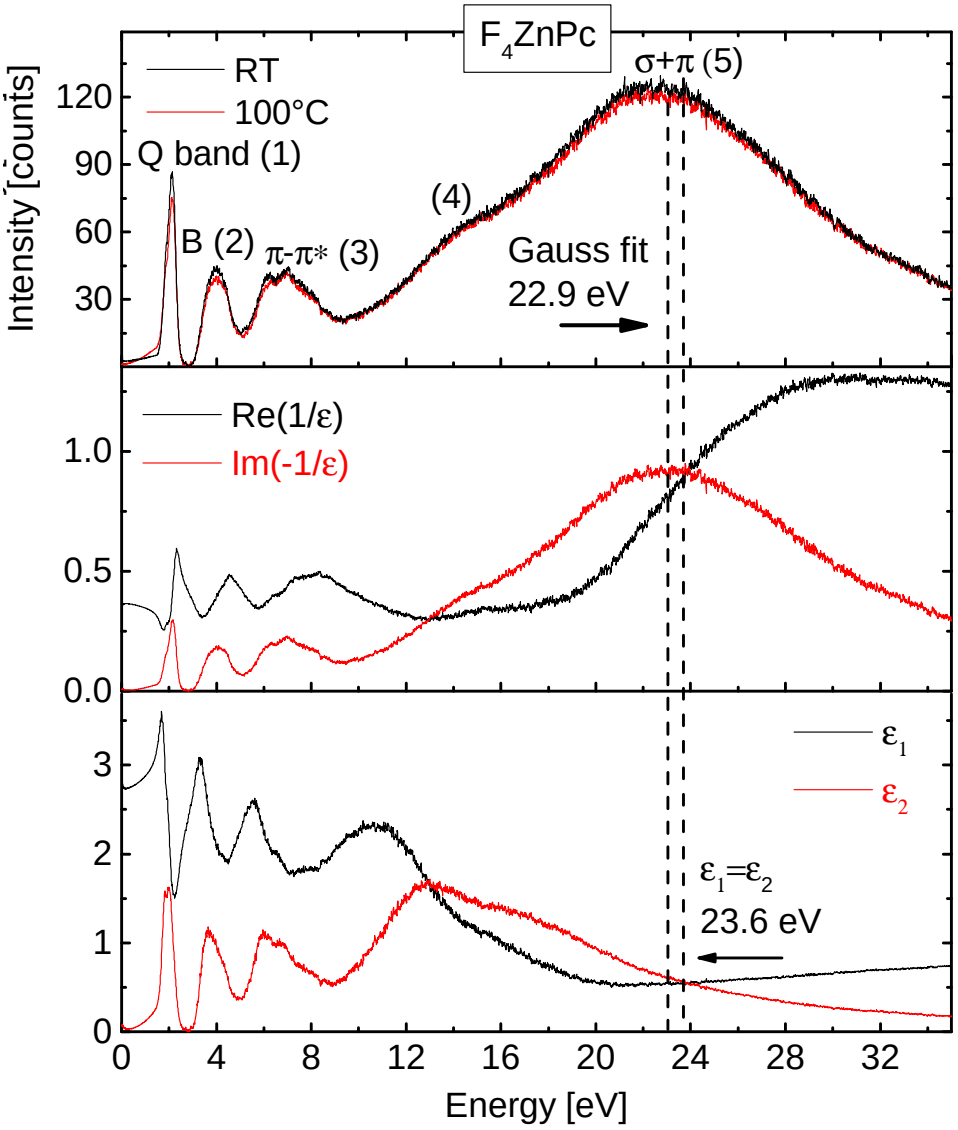

Figure 7.1: (top) Measured EEL-spectra of F_4ZnPc deposited at RT and at 100 °C. The spectra do not show significant differences. Pronounced peaks are numbered. The plasmon peak position (Gauss fit) is marked. (middle) Im $\left[-\frac{1}{\epsilon(E)}\right]$ and Re $\left[\frac{1}{\epsilon(E)}\right]$ derived from the Kramers-Kronig-relation. Im $\left[-\frac{1}{\epsilon(E)}\right]$ exhibits the same shape as the EEL-spectrum. (bottom) The calculated dielectric functions. The dashed line marks the position at $\epsilon_1 \approx \epsilon_2$, which is attributed to the plasmon excitation.

(red), both spectra are in excellent agreement. Re $\left[\frac{1}{\epsilon(E)}\right]$ (black) resembles the differential of Im $\left[-\frac{1}{\epsilon(E)}\right]$, which is expected from the mathematical relationship. The calculated dielectric functions are presented in figure 7.1 (bottom). The conditions for a plasmon excitation are fulfilled if $\epsilon_1 \approx \epsilon_2$ in the region where ϵ_2 does not indicate excitation peaks - in this measurement at 23.6 eV as marked with a dashed line. The lack of zero-crossing for ϵ_1 is due to the high electron binding energy in molecular materials (compared to quasi-free electrons in metals) as discussed in section 3.2.1.2 for the extended Drude-model. The energy is in accordance with the plasmon peak maximum at 22.9 eV deduced from the EEL-spectrum. For the implementation of the described calculations a refractive index of $n = 1.7$ at low energies is assumed. This value is taken from ellipsometry measurements performed by Felix Schell (not shown in this work) and also confirmed in the literature [15, 36, 202]. As discussed in the cited literature, the refractive index can change slightly depending on the orientation angle of the molecules. Simultaneous measurements on F_4ZnPc by Johannes Zimmermann (master thesis) revealed a substrate and temperature dependence of the orientation angle [203]. However, as shown in the master thesis of Felix Schell, changes up to $\triangle n$ =0.4 have no significant impact on the calculations from EELS measurements [36].

In the next step the real and imaginary part of the refractive index $n(E)$ and $k(E)$ are calculated (see equations (3.15) and (3.16)) and depicted in red in figure 7.2 a)-c) in addition to Im $\left[-\frac{1}{\epsilon(E)}\right]$. n and k determined from optical measurements on ZnPc taken from [202] are shown in black. It is striking that the peak positions and shape of Im $\left[-\frac{1}{\epsilon(E)}\right]$ and the real and imaginary part of the refractive index determined from EELS and optical measurements (literature) are in good agreement. This is surprising, given the two completely different measuring techniques. Only slight differences in the overall intensity are visible. It needs to be considered that for the calculation of n and k from optical measurements the exact film thickness has to be determined as it contributes inversely proportional to the absorption coefficient which in turn is proportional to k (and inverse to n): $\alpha = 2\omega k/c$. Hence, an over- or underestimation of the film thickness has a direct impact on the intensity of k. The uncertainty of the sample thickness in the measurements by Schechtman et al. is 25 % [202]. This explains the intensity deviations from the EELS measurements. The first two $\pi - \pi^*$ transitions (Q and B band) in the visible and near ultraviolet regime, denoted in 7.2 b), are followed by four other transitions. The last transition at around 10 eV is broadened and marks the onset of the collective $\pi-$ and σ-electron transition (plasmon). As pointed out by Schechtman et al., optical measurements covering such a wide spectral

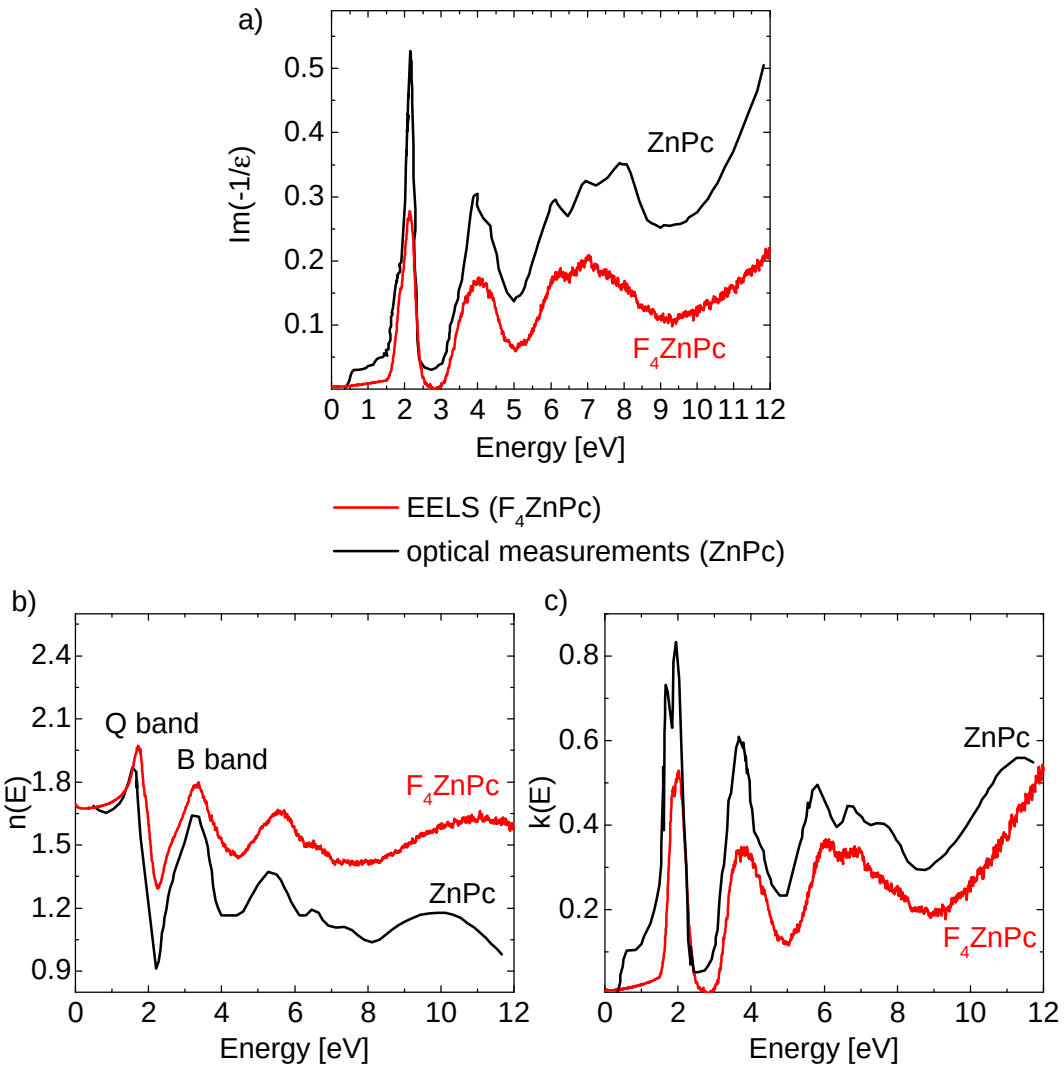

Figure 7.2: Comparison between the optical properties of F_4ZnPc deposited at 100 °C from EELS (red) and the optical properties of ZnPc (black) measured by Schechtman et al. [202]. a) The calculated Im $\left[-\frac{1}{\epsilon(E)}\right]$ from both measurements. b) The Real part of the refractive index $n(E)$ and c) the imaginary part $k(E)$. The overall agreement of both techniques is good, except for slight intensity deviations which are attributed to the uncertain film thickness in the optical measurements from the literature.

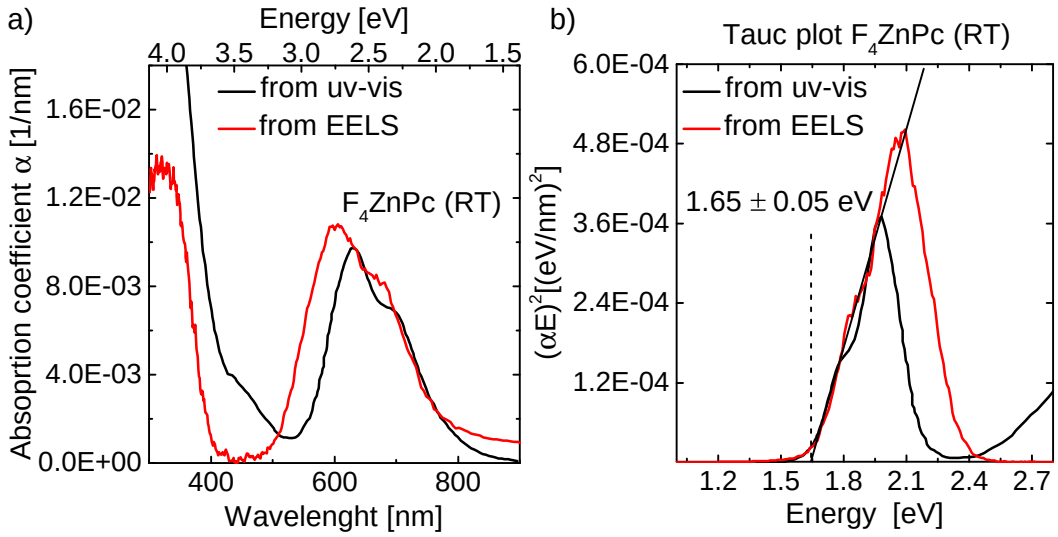

Figure 7.3: a) UV-VIS absorption (Meisst et al. [89]) compared to absorption calculated from EELS of F_4ZnPc deposited at RT indicating the characteristic Q and B bands. b) Band gap determined from EELS (red) and from optical absorption (black) data by means of a Tauc plot.

range are hard to perform due to technical difficulties of vacuum ultraviolet measurements [202]. Taking figure 7.2 into account, it becomes clear that EELS measurements can facilitate the determination of the optical constants. These are usually needed for the full understanding and description of optical and certain electronic properties of materials. Furthermore, the refractive index represents a true material property, which would immediately reveal changes due to degradation. Hence, it can be concluded that F_4ZnPc has not been significantly damaged by the electron beam, as the deduced optical properties are the same as the properties from the non-invasive optical measurements.

A further parameter that is derived from EELS and compared to optical absorption measurements is the absorption coefficient (α) and the band gap. The absorption measurement performed on F_4ZnPc by Meiss et al. along with the coefficient calculated from EELS are shown in figure 7.3 a) [89]. As already discussed, strong absorption over a wide range of the solar spectrum with the Q (between 500 and 800 nm) and B (between 200 and 400 nm) absorption bands is visible in both measurements [89]. The Q band consists of a wide peak and a red-shifted shoulder. In the literature, this feature is assigned to Davidov splitting, usually arising from degenerated excited states in molecular crystals as in the solid state of ZnPc [197, 204]. For F_4ZnPc it is more a shoulder than a splitting, which is explained by modified intermolecular interactions caused

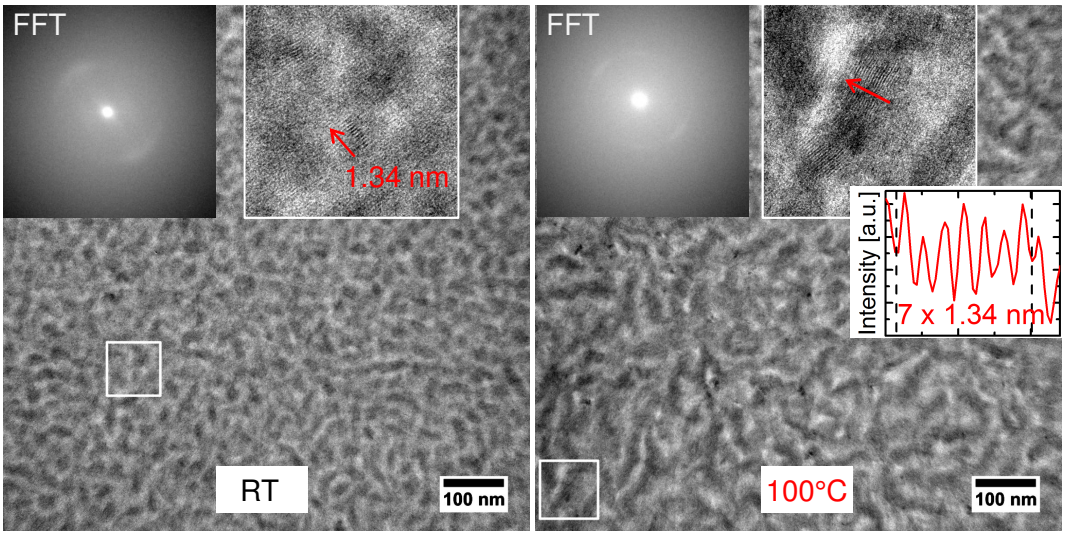

Figure 7.4: BFTEM images of a RT-sample (left) and a 100 °C-sample (right). The FFTs (upper left inset of each panel) indicate features corresponding to crystalline domains with a spacing of 1.34 nm (shown in the upper right) which is attributed to a (010) orientation [89, 206].

by the additional fluorine atoms [89]. In figure 7.3 b) the band gap derived from EELS and respectively from the optical absorption measurement in a Tauc plot is shown. The Tauc plot is introduced, since the absorption of direct, amorphous semiconductors can be approximated by $\alpha(E) \propto E^{-1/2}$ [205]. The value of the band gap is calculated to be 1.65 ± 0.05 eV from the linear fit to the low energy onset of the absorption deduced from the Tauc plot ($(\alpha E)^2$). It is in good agreement with the band gap of 1.6 eV reported in the literature [89]. Further, this indicates that the electronic properties have not changed during electron beam exposure.

Zero-loss filtered bright-field TEM images (BFTEM)

BFTEM images of a RT- and 100 °C-sample are presented in figure 7.4. Both samples exhibit elongated structures, similar to ZnPc [91], with typical structure sizes being larger for the 100 °C-sample. The FFT of each image is shown in the upper left corner. In both cases repeating frequencies at $0.75\,\mathrm{nm}^{-1}$ can be observed, which correspond to 1.34 nm spacing of fringes, as shown in the insets. For the 100 °C-sample the radial profile of a crystalline domain is shown. Both samples exhibit such domains, indicating an overall preferential

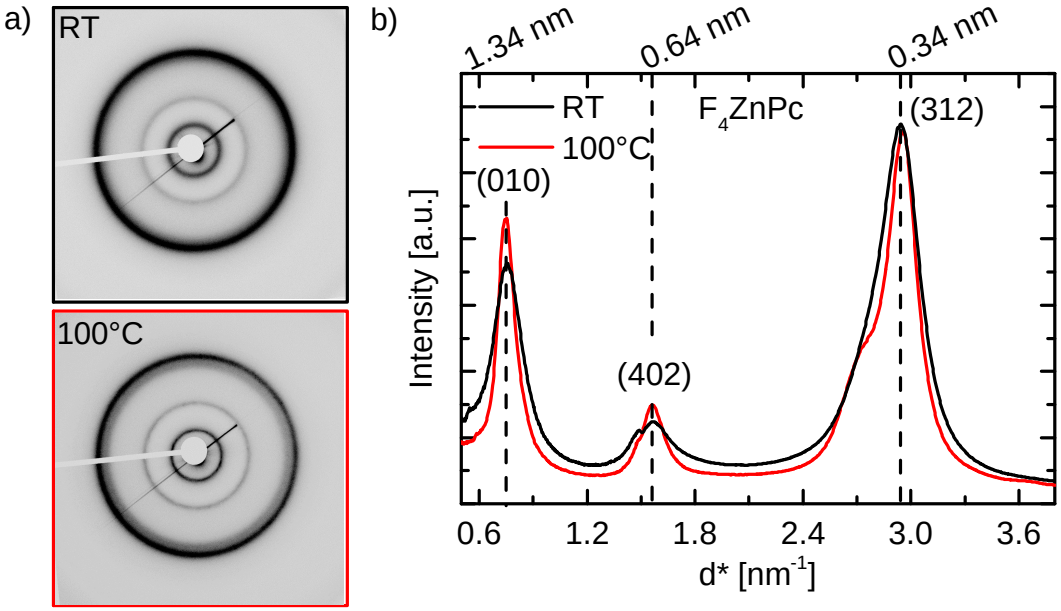

Figure 7.5: Electron diffraction measurements on F_4ZnPc deposited at RT and 100°C. a) Diffraction patterns of the unheated (black frame) and heated (red frame) samples showing distinct rings. b) The corresponding radial profiles with indicated peak positions converted in nm. [87, 89].

orientation in the films, which is slightly more pronounced for the heated sample.

Electron diffraction of F_4ZnPc

The diffraction patterns and the corresponding radial profiles of the same samples introduced for the BFTEM images are shown in figure 7.5. Both patterns reveal three rings as can be seen in a). The rings of the heated sample are slightly sharper and speckled with distinct reflection spots indicating a higher degree of crystallinity. The corresponding three peaks are shown in the radial profile in figure 7.5 b). All peaks appear broadened, with an additional shoulder arising for the heated sample at the peak at $2.94\,nm^{-1}$ (corresponding to 0.34 nm). The position of the first peak at $0.74\,nm^{-1}$ (corresponding to 1.34 nm) is in excellent agreement with the XRD measured distance at 6.6° by Meiss et al. [89]. The appearance of the peak is attributed to a (010)-orientation in analogy to the diffraction peak of α-ZnPc (triclinic unit cell) at 6.8° [206]. The slight shift for the fluorinated ZnPc is explained by the change of the intermolecular distance, which is known to occur when adding additional

side groups to the phthalocyanine [207]. All peaks for F_4ZnPc are as well present in ZnPc structures at 1.27 nm, 0.57 nm and 0.33 nm as reported by Maennig et al. from TEM measurements but are slightly shifted, as expected, due to the fluorination of the molecule [87]. The corresponding lattice planes (010), (402) and (312) are indicated in the radial profile in figure 7.5 b). The origin of the shoulder in the (312) peak of the heated sample remains unclear.

In conclusion, F_4ZnPc layers deposited at elevated substrate temperatures compared to substrates kept at RT do not show significant changes of the electronic and structural properties. EELS and optical measurements reveal permanent spectral features. BFTEM and diffraction images indicate an increase of the typical structure sizes and a small enhancement of the crystallinity for the 100 ℃-sample.

7.2.2. Pristine C_{60} Layers Grown at Different Temperatures

TEM measurements were performed on the pure acceptor material C_{60} deposited at RT and 100 ℃. On each sample EELS was measured at seven different spots, BFTEM and diffraction on four distinct areas of the films. Deviations of the measurements within one sample are not observed. A summary of all measurements is given in the appendix A. Here, only one measurement for each TEM mode is shown.

TEM spectroscopy

Figure 7.6 (top) shows EELS measurements on C_{60} deposited at RT and at 100 ℃ substrate temperature. Pronounced peaks are labeled with numbers from 1 to 8. Significant spectral differences between the two samples are not observed. The measured spectra are in accordance with previous EELS measurements on C_{60} [208–210]. Peak 1 at 2.5 eV corresponds to a transition across the fundamental gap between the HOMO and the LUMO at 2.15 eV [209]. Peaks 2, 3 and 4 at 3.6 eV, 4.8 eV, and 6.2 eV are in good agreement with optical absorption measurements and calculated values at 3.6 eV, 4.7 eV, and 5.6 eV [211, 212]. Peak 2 and 3 are attributed to single-electron $\pi - \pi^*$ transitions, whereas peak 4 is assumed to be a collective oscillation of the π-electron system, which is caused by the one-electron transitions at 4.5 eV (peak 3). π-plasmons provoked by single-electron transitions are also observed in graphite [208]. The shoulders 5, 6 and 7 are interpreted as bonding-antibonding $\sigma - \sigma^*$ and mixed $\pi - \sigma^*$, $\sigma - \pi^*$ transitions [209]. The plasmon peak at 25.1 eV (Gaussian fit) includes the collective resonance of all valence electrons ($\sigma + \pi$)

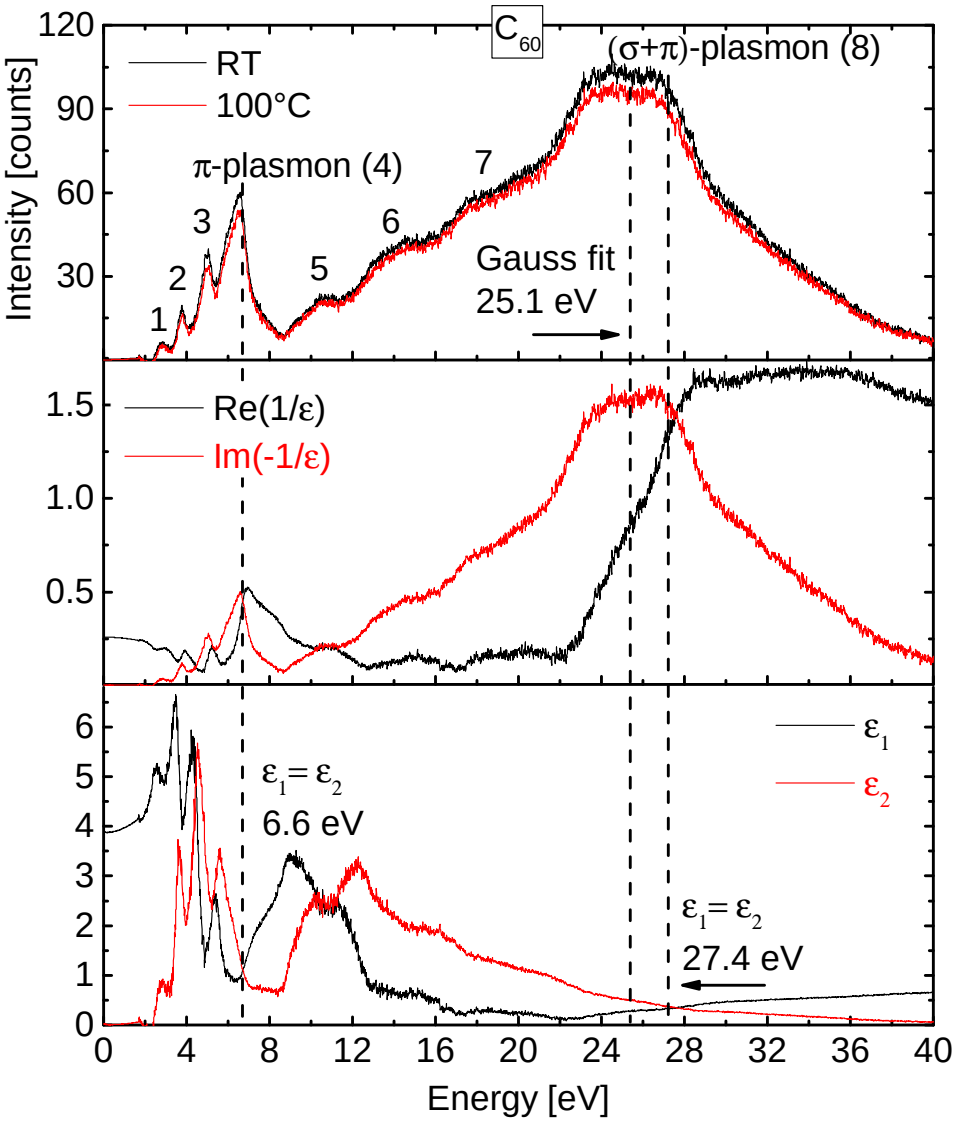

Figure 7.6: (top) EELS measurements on C_{60} deposited at RT- and 100 °C. The shape of both spectra is similar. The main spectral features are numbered. The plasmon peak position, determined from a Gaussian fit, is indicated. (middle) The determined real and imaginary part of the loss-function from EELS. (bottom) Dielectric functions ϵ_1 and ϵ_2. The crossing points of ϵ_1 and ϵ_2 are marked with dashed lines and are in agreement with the two plasmon excitations indicated from EELS.

and is in agreement with the measured 27 eV by Sohmen at al. [209]. It is also similar to the known plasmon peak for graphite [209]. In C_{60} the electrons are confined to a volume of closely packed fullerenes [210, 213]. The good correlation to graphite is expected under the assumption that the electron density, which determines the plasmon energy, is similar for both materials.

In figure 7.6 (middle) the derived [1] Im $\left[-\frac{1}{\epsilon(E)}\right]$ and Re $\left[\frac{1}{\epsilon(E)}\right]$ are presented, with Im $\left[-\frac{1}{\epsilon(E)}\right]$ again showing the same shape as the EEL-spectrum and Re $\left[\frac{1}{\epsilon(E)}\right]$ being its differential. The above described transitions are all visible in the dielectric function ϵ_2 as shown in figure 7.6 (bottom). ϵ_2 exhibits a sharp absorption edge at 8 eV followed by a broad range of transitions, as was also reported by Sohmen et al. from a Kramers-Kronig-analysis of EELS on C_{60} [209]. One also recognizes ϵ_1 crossing ϵ_2 nearly at the energies that were assigned to the collective π and $(\sigma + \pi)$ oscillations at ~ 6 eV and ~ 26 eV as marked with dashed lines in figure 7.6.

The calculated Im $\left[-\frac{1}{\epsilon(E)}\right]$, $n(E)$ and $k(E)$ are shown in figure 7.7 a)-c) (red). As was already the case for F_4ZnPc, the agreement between values from the literature [214] and calculated values from EELS is remarkably high, despite very slight energy and intensity shifts. The variation in peak intensity in the optical measurements is usually caused by an uncertainty of the film thickness. The first four single-electron transitions between 2 eV and 6 eV are recognized in all plots a)-c).

The Optical absorption of C_{60} deposited at room temperature [2] is shown in figure 7.8 a). A relatively sharp peak is observed at around 330 nm followed by a broad peak with a plateau around 500 nm in the visible range. This is in agreement with literature [208, 212]. The band gap determined by the two complementary methods in figure 7.8 b) EELS (red), optical absorption (black) reveal slightly different values. Faiman et al. reported that the optical band gap of fullerenes adjusts to the degree of crystallinity: 1.3 eV-1.6 eV for crystalline films and 2.4 eV-2.6 eV for amorphous films [215]. The values, determined in figure 7.8 of 2.17 ± 0.05 eV and 2.46 ± 0.05 eV, lie in between, indicating the presence of an amorphous and a crystalline phase in the investigated C_{60} films.

Zero-loss filtered BFTEM images

Figure 7.9 presents zero-loss bright field images of a RT-sample (left) and a 100 ℃-sample (right). Both samples exhibit round features, but the typical

[1] $n = 2$ assumed as reported in [209] and measured by ellipsometry.
[2] Spectrum of the 100 ℃-sample exactly the same, therefore not shown.

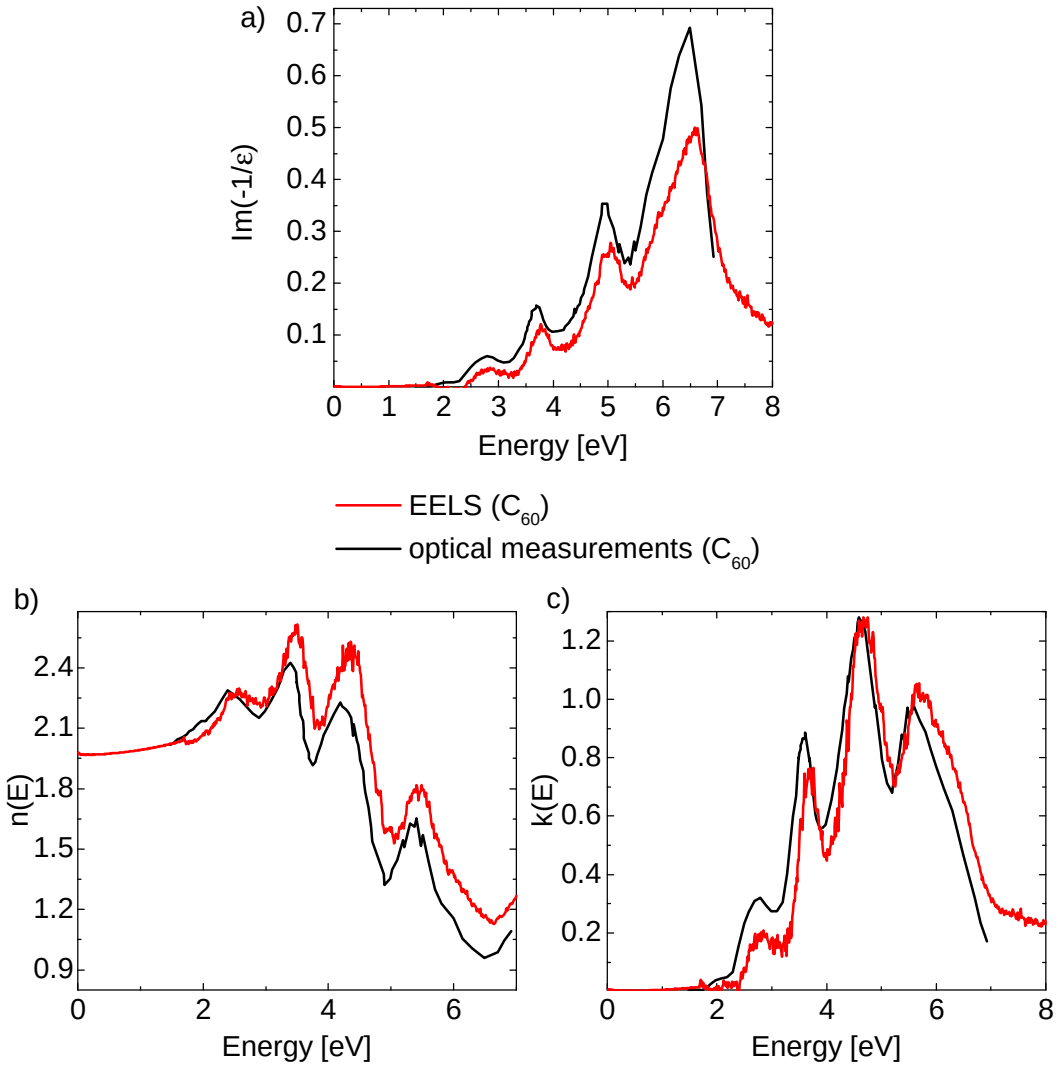

Figure 7.7: Comparison between a) Im $\left[-\frac{1}{\epsilon(E)}\right]$, b) the real part $n(E)$ and c) the imaginary part of the refractive index $k(E)$ derived from optical absorption measurements from the literature (black) [214] and from EELS (red). All results show a very good agreement between the two measuring techniques.

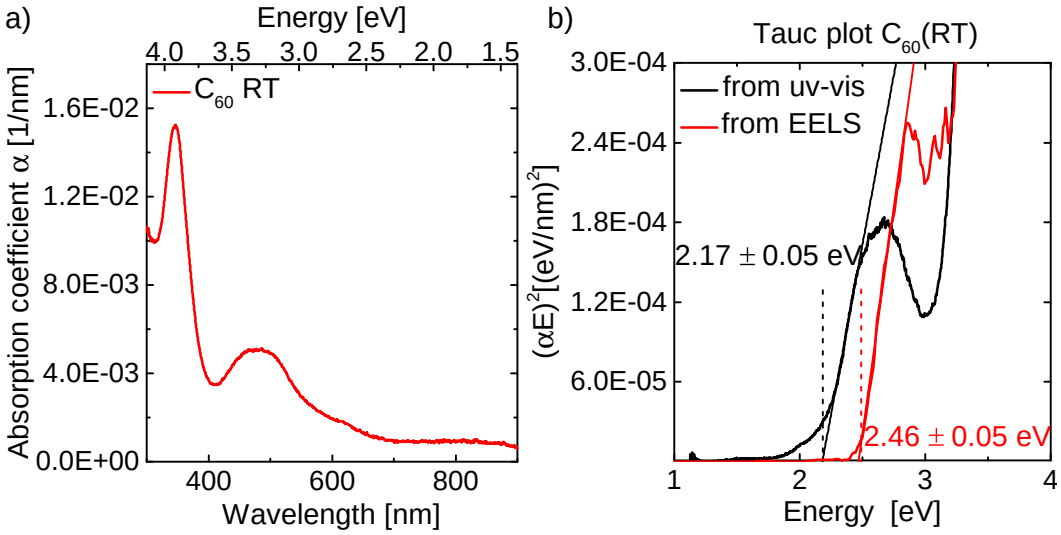

Figure 7.8: a) UV-VIS spectrum of C_{60} RT-sample indicating two characteristic features in the ultraviolet and visible region. b) Derived band gap from EELS (red) and optical absorption (black) in a Tauc plot.

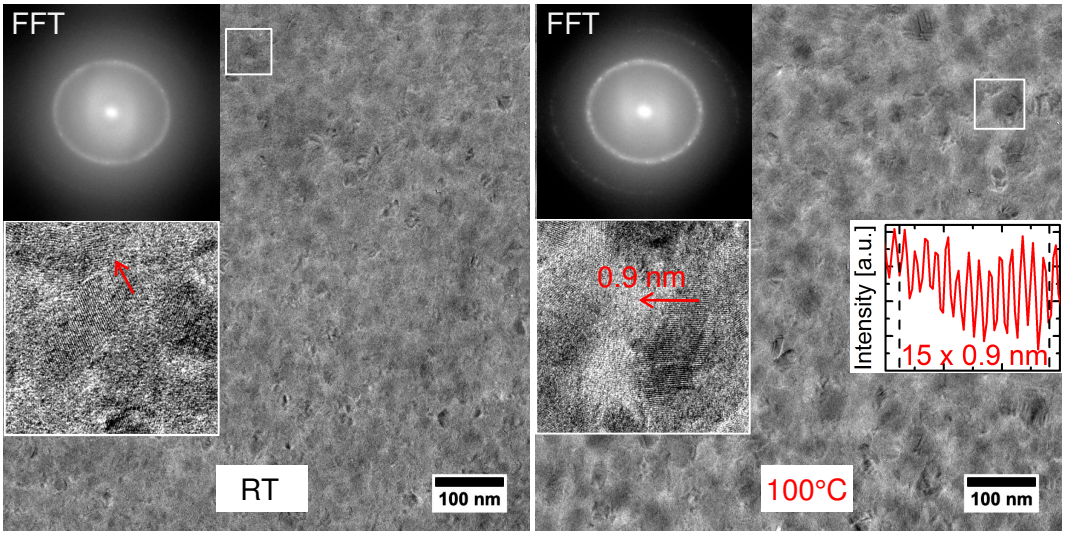

Figure 7.9: BFTEM images of C_{60} deposited at RT (left) and 100°C (right). In the FFTs of the images (upper left corner) one pronounced ring is observed in each sample indicating the polycrystalline structure of the samples. A close up of the region marked with white squares is shown below the FFTs. The orientation of the crystalline domains is marked with a red arrow. The 0.9 nm spacing derived from a profile taken across the domain is attributed to a (111) orientation [87].

structure size for the heated sample appears to be larger. Crystalline domains are observed in both images, which is confirmed by the FFTs shown in the upper left corner. Sharp rings are visible in both FFTs at a frequency of $1.15\,\mathrm{nm}^{-1}$, but the ring of the heated sample is more pronounced with distinct spots indicating a larger number of ordered fringes in the film. The spatial frequency corresponds to a spacing of 0.87 nm, which can be seen in the insets in figure 7.9. A profile taken across a crystalline domain in the 100 ℃-sample is shown, indicating the repeating fringe distance of 0.9 nm. Typical domain sizes vary between $10 - 40\,\mathrm{nm}$. The determined roughness from AFM is comparable for both films ($\mathrm{RMS_{RT}} = 1.5\,\mathrm{nm}$; $\mathrm{RMS_{100°C}} = 1.8\,\mathrm{nm}$).

Electron diffraction of C_{60}

The C_{60} diffraction patterns and radial profiles obtained via electron diffraction can be seen in figure 7.10 where results from both heated and RT samples are plotted alongside. The images in a), b) and the corresponding radial profiles in c) of both samples exhibit four major features. In both diffraction patterns distinct spots (speckles) are visible within the rings, confirming the polycrystallinity of the films. However, the 100 ℃-sample indicates a larger amount of pronounced speckles especially within the double ring. Speckles usually arise from diffraction on larger crystallites [44], implying that larger crystalline domains are present in the heated sample in a higher density. The peak positions are indicated in nanometer units on top of the graph in figure 7.10 c). The first peak at $1.17\,\mathrm{nm}^{-1}$ (0.85 nm) corresponds to the spacing visible in the BFTEM images. The double-peak at $1.96\,\mathrm{nm}^{-1}$ and $2.27\,\mathrm{nm}^{-1}$ (corresponding to 0.51 nm and 0.44 nm) appears sharper for the RT-sample. The peak at $3.12\,\mathrm{nm}^{-1}$ (0.32 nm) is followed by two smaller peaks exhibiting small intensity in both profiles. As indicated in the radial profile in figure 7.10 c) in blue, five peaks correspond very well to the (111), (220), (311), (331) and (402) lattice planes from a simulation of the electron diffraction pattern for the used microscopy setup. The small shift between the simulation and the measurements to higher reciprocal distances for all peaks is probably caused by minor deviations of the pixel per nm^{-1} calibration. The simulation is based on the crystal structure from neutron powder diffraction measurements and is carried out by means of the software $JEMS$[3] [217]. Electron diffraction measurements (0.818 nm, 0.504 nm, 0.43 nm, 0.319 nm) from the literature are in good agreement with the determined lattice planes [87, 194, 216].

Similar to F_4ZnPc, only slight differences are noted between the RT and the

[3] cimewww.epfl.ch/people/stadelmann/home.htm

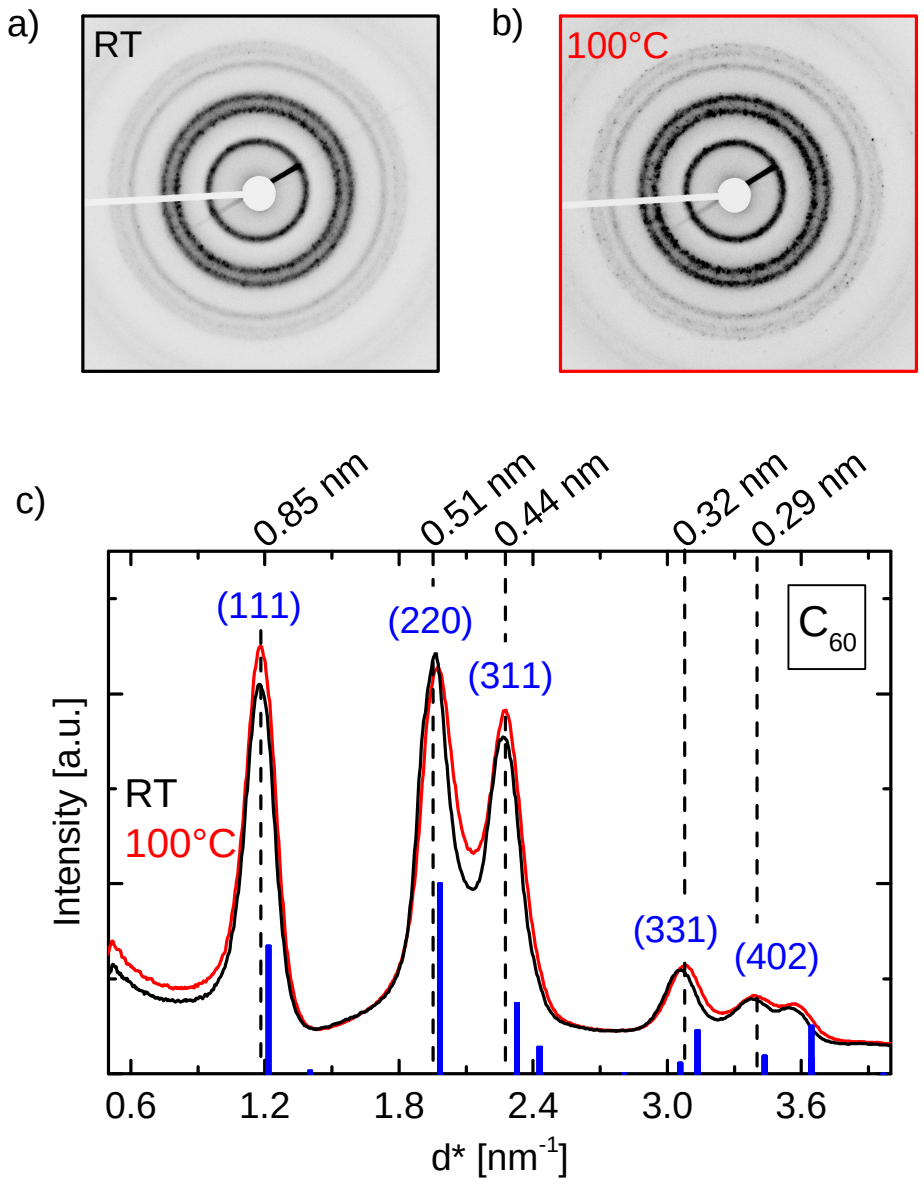

Figure 7.10: Electron diffraction of C_{60} at RT and 100°C. Diffraction patterns of a) the RT-sample and b) the 100 °C-sample. Speckles caused by scattering on larger crystallites are recognized in both patterns, but are present to a greater extend in the heated sample. c) The Corresponding radial profiles do not change significantly with substrate heating. Peak positions in the corresponding nanometer units are indicated on top and are in good agreement with the literature and simulation [87, 216]. The simulated electron diffraction peaks are indicated in blue.

heated films of C_{60} . Both samples are polycrystalline, with larger structure sizes for the heated sample. The optical and electronic properties assessed by UV-VIS and EELS measurements are not affected by the substrate temperature. The similarity between the two complementary experimental techniques again demonstrates that the films have not suffered beam damage during EELS acquisition.

7.2.3. $F_4ZnPc:C_{60}$ Blends Deposited on Different Substrates at Varied Temperatures

In this section $F_4ZnPc:C_{60}$ blends (BHJs) are investigated extensively by means of analytical TEM. As in the previous sections, the optical and electronic properties are assessed by UV-VIS and EELS followed by structural properties from EFTEM and electron diffraction. The main focus of this study is to understand what impact temperature and substrate have on the results. The donor and acceptor are co-evaporated in a 1:1 ratio on substrates at RT or at 100°C. As with the TEM samples, PEDOT:PSS coated ITO-glass is used as the substrate, if not indicated otherwise. Furthermore, to better mimic the actual device stack, the influence of 5 nm pristine C_{60} or F_4 ZnPc layers underneath the blend, as used in inverted and non-inverted devices, is analyzed. Each measurement (EELS, BFTEM, diffraction) is acquired from at least five different spots from one sample for the RT-samples (on PEDOT:PSS, on F_4ZnPC and on C_{60}) and from two different samples prepared on different days for the 100 ℃- samples with considerable reproducibility. It is important to note, that the pure C_{60} or F_4 ZnPc underlayers are deposited at RT. When afterwards the substrate is heated to 100°C during the deposition of the blend, this effectively leads to a post-annealing of the pure layers. However, as demonstrated in the previous section, heating does not have a great impact on the properties of the pristine materials. Additionally, the impact on the blend structure of a slower evaporation rate such as 0.3 nm/min compared to the usual $1.0 - 1.5$ nm/min is examined. The correlations between all mentioned factors is discussed at the end of this section.

7.2.3.1. EELS

EELS was performed on a BHJ (on PEDOT:PSS) deposited at RT. The loss spectrum is shown in figure 7.11 (orange). For a comparison, the spectra of pure C_{60} (red) and F_4ZnPc (blue) are depicted. An important remark at this point is the obvious shift between the plasmon energy of both materials. The plasmon intensity of F_4ZnPc dominates the total signal over the intensity of

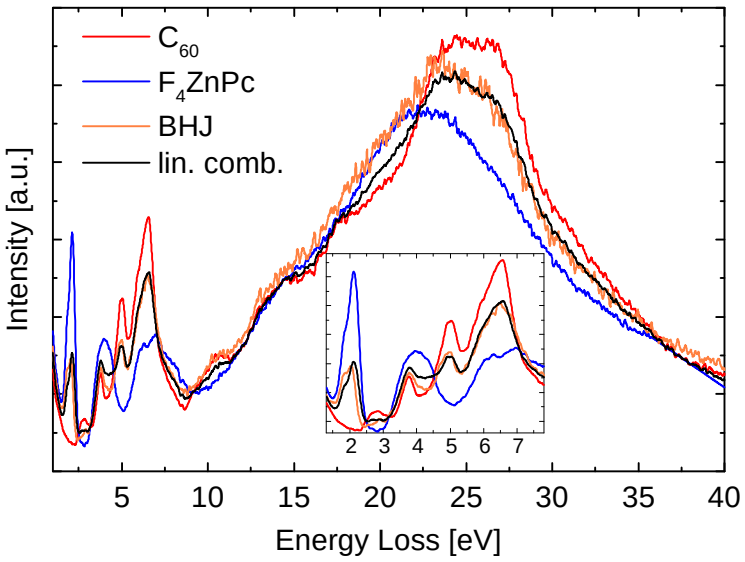

Figure 7.11: EEL spectra of RT samples of C_{60} (red), F_4ZnPc (blue) and a F_4ZnPc:C_{60} blend (orange). The inset represents a zoom of the spectrum between 1 eV and 8 eV. The linear combination of the spectra of pristine materials is shown in black. A good agreement is recognized between the linear combination and the measured BHJ spectrum.

C_{60} between $15 - 18$ eV reversing to a stronger C_{60} signal at around 20 eV. This intensity inversion corresponds to a contrast inversion in EFTEM images, which is beneficial for the distinction of the materials in a blend and will be discussed in the next section.

If considered qualitatively, the blend spectrum appears as a superposition of the pristine spectra. The single-electron transitions of the donor and acceptor between 1 eV -6 eV (see inset in figure 7.11) remain unaffected in the BHJ spectrum, except for the first transition of F_4ZnPc (~ 2 eV) which is quenched. Quenching is expected to happen, as already discussed in chapter 5. The π-plasmon excitation of C_{60} at around 6 eV is lowered in its intensity and broadened in the blend as it is superimposed on the broad excitation of F_4ZnPc at the same energy. A quantitative analysis is implemented by representing the BHJ spectrum as a linear combination of the EEL spectra of the pure materials:

$$(a \cdot EELS(F_4ZnPc) + b \cdot EELS(C_{60})) - EELS(BHJ) = min.$$

The coefficients a and b are optimized such that the deviation between the linear combination and the measured blend spectrum is minimized (least square fit). The determined linear combination with $a = 0.43$ and $b = 0.57$ is illustrated in black in figure 7.11. The coefficients match the 1:1 co-evaporation ratio with a deviation of 12%. The uncertainty of the evaporation rates monitored by means of a quartz microbalance is estimated to about 10 %. Therefore, it is likely that the concentration in the film does not correspond exactly to 1:1. From the resulting coefficients of the linear combination the real concentration can be estimated, pointing out a slight surplus of C_{60} in the presented sample. It is considerable that the peaks between 1 eV and 8 eV (see inset in figure 7.11) and the complex shape of the plasmon peak are described very well by the fit. As has been shown for P3HT:PCBM blends by Pfannmoeller et al., a convincing description of the plasmon by the linear combination is not always the case [17]. For P3HT:PCBM this result leads to the assumption, that a new electronic state is formed by the donor-acceptor (D-A) interaction. The so called charge transfer state in P3HT:PCBM was additionally confirmed by the appearance of a new vibrational band in a measured IR-spectrum [218].

However in the investigated $F_4ZnPc:C_{60}$ blend in this work, the linear combination of spectra from the pure compounds correlates well with the measured BHJ spectrum, leading to the conclusion that the donor and acceptor do not interact in the blend. Electronic interactions, in terms of formation of charge transfer states due to electron exchange between the donor and acceptor would otherwise cause new transitions or energy shifts, which is clearly not the case. The materials are not expected to interact when mixed due to the high energetic barrier between the ionization potential of F_4ZnPc (IP = 5.46 eV) and the electron affinity of C_{60} (EA = 4 eV) [89]. A high energetic difference at the D-A interface leads to a higher effective band gap and is favored for an increased open circuit voltage in solar cells [219, 220]. Besides, the lack of D-A electronic interaction in $F_4ZnPc:C_{60}$ blends is confirmed by IR-spectroscopy measurements performed by Johannes Zimmerman within his master thesis [203]. No additional vibrational modes or shifted bands were observed in the IR spectra.

Now, EEL spectra of blends on different substrates (PEDOT:PSS (top), F_4ZnPc (middle), C_{60} (bottom)) deposited at RT and 100°C are compared in figure 7.12 a)[4]. In all three cases there are no spectral changes between the heated and the non-heated sample, which in not surprising as the spectra of

[4]EEL spectrum of the BHJ evaporated with a lower rate (0.3 nm/min) can be found in the appendix A.6.

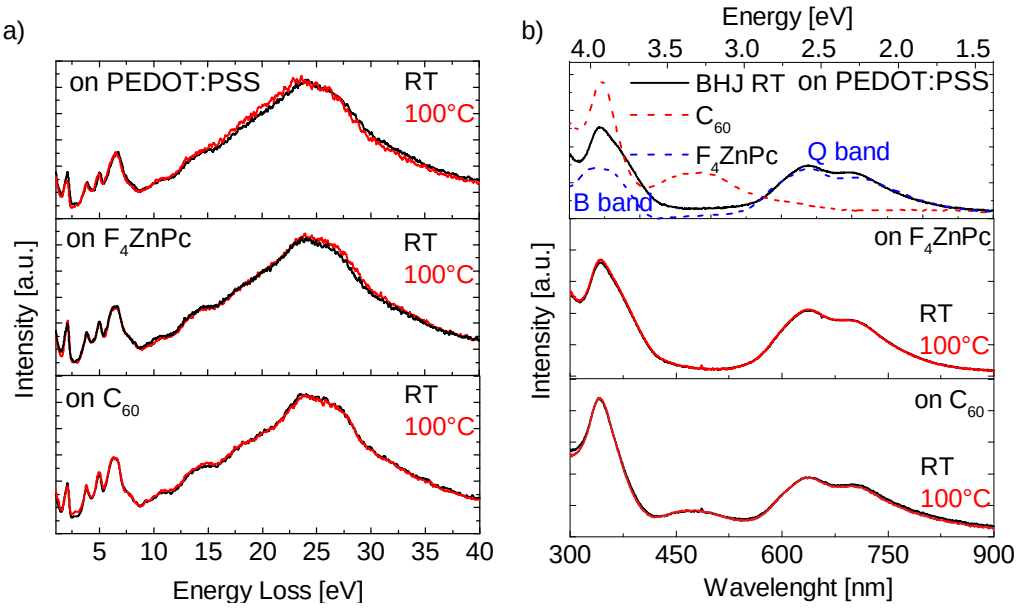

Figure 7.12: a) EEL spectra of BHJs on PEDOT:PSS (top), on F_4ZnPc (middle), on C_{60} (bottom) deposited at RT (black) and 100°C (red), all exhibiting the same features. b) UV-VIS spectra of BHJs on F_4ZnPc and C_{60}. The appearance of new features or shifts is not observed in the EELS and absorption spectra. All features can be assigned to the pure materials.

pristine layers are also unaffected by the substrate temperature. Hence, even if there are changes of the blend crystallinity caused by the underlying layer, they are not reflected in the energy loss spectra. The 5 nm pure F_4ZnPc or C_{60} substrate seems additionally not to have a significant impact on the spectral features, as the main signal is from the BHJ itself, reinforcing the significance of the measurements on different substrates. The EEL spectra of BHJs on F_4ZnPc or C_{60} can - analogously to the sample from figure 7.11 a) on PEDOT:PSS - be represented as a linear superposition of the pristine donor and acceptor (see appendix A.6), indicating the lack of electronic interaction between the two species. This statement is strengthened by the optical absorption spectra of the BHJs in figure 7.11 b). In the top panel UV-VIS spectra of F_4ZnPc[5] (blue), C_{60} (red) and F_4ZnPc:C_{60} deposited on PEDOT:PSS at RT (black) are shown. The main absorption features of the pure materials are present in the blend, with the exception of the broad band of C_{60} at around 500 nm. The same features are as well visible in the BHJ on F_4ZnPc (middle) and in the

[5]The low intensity of the F_4ZnPc UV-VIS spectrum is probably caused by misalignment of the instrument, which was observed to lead to fluctuations of the intensities.

BHJ on C_{60} (bottom). In the BHJ spectrum on C_{60} (bottom) a small hump at around 450 nm is visible, which is attributed to pure C_{60} probably from the substrate. In conclusion, the absorption of the blends does not change upon heating and is independent of the substrate.

7.2.3.2. Energy Filtered TEM

After the characterization of the electronic and optical properties of the blends the structural properties are addressed. A series of energy filtered TEM (EFTEM) images were acquired for BHJs deposited with slow (0.3 nm/min, only on PEDOT:PSS) and fast deposition rates ($1.0 - 1.5$ nm/min) at RT and elevated temperatures on the three different substrates already discussed in the previous section. In figure 7.13 EFTEM images of all RT-samples are displayed: a) on PEDOT:PSS, b) slow evaporation rate on PEDOT:PSS, c) on F_4ZnPc and d) on C_{60}. For each sample the zero-loss image, acquired only with elastically scattered electrons, is shown first (left column), followed by energy filtered images at 18 eV (middle) and 27 eV (right). Here, only two energy selected images from the whole EFTEM series are shown[6]. These energies are chosen such that given the EEL spectra from figure 7.11, the strongest contrast inversion is expected, with F_4ZnPc-rich domains appearing bright at 18 eV and dark at 27 eV and vice versa for C_{60}-rich domains.

As already mentioned in chapter 3.2, contrast differences in zero-loss images are more often caused by thickness variations or crystalline domains than by the distinct materials in the blend [41, 44]. Thus, structures in the ZL-images in figure 7.13 a)-d) do not reveal any information on the donor-acceptor distribution in the mixed phase. The ZL-image of the BHJ on C_{60} exhibits less structures and appears more homogenous and smoother compared to the other films. The EFTEM images at 18 eV and 27 eV in figure 7.13 a)-d) show mostly noise. Only very faint structures, if any, and no contrast inversion can be observed. There are no visible features neither for the energy loss at which F_4ZnPc exhibits high intensity in the EEL spectrum (18 eV) nor at the characteristic energy loss of C_{60} (27 eV), exhibiting predominant intensity in the spectrum.

The only exception is observed in the EFTEM images in figure 7.13 d) for the blend on C_{60}. Especially in the 27 eV image brighter, round structures appear faintly. However, the analysis of the entire EFTEM image stack and the generation of a plasmon peak map (see appendix A.8) revealed a very small spectral separation of the features indicating still a predominant mixing

[6] Pre-processing in this section includes only lateral translation alignment of the image stack.

rather than segregation (see master thesis of Felix Schell for details [36]). Due to the strong random noise and the featureless appearance of the films, further data analysis methods like plasmon peak mapping or LLE, as introduced in 3.2.2.2, were not carried out.

Consequently, as no clear phase separation of the donor and acceptor is noted, the investigated RT-samples seem to be homogeneously intermixed independently of the substrate. This result is in agreement with published TEM measurements on related material systems. ZnPc:C_{60} blends deposited at room temperature (Schindler et al.), as well as cross-sections of CuPc:C_{60} blends deposited on pristine CuPc at RT (Glichrist et al.) do not indicate phase separation or specific features at all [65, 194].

EFTEM images of samples prepared under the exactly same conditions as the RT-samples, except for the elevated substrate temperature of 100°C, are presented in figure 7.14 a)-d). In contrast to the RT-samples, all films exhibit a very pronounced and complex structure in the zero-loss filtered image.

The black, round structures in the ZL-image of the PEDOT:PSS-sample in a) are about 10 nm to 20 nm in diameter. They are underlaid by a network of dark and bright features. The black spots remain at 18 eV energy loss, but are framed by white domains. At this energy loss structures appearing bright or even white are expected to be F_4ZnPc enriched. The rest of the features appear uniformly gray and cannot be assigned. In the image at 27 eV the reverse effect can be observed. The black spots surrounded by dark domains from the ZL-image are white and framed by bright features, whereas the white domains have turned black. As already known from EELS, the highlighted features at this energy loss are attributed to C_{60}-rich domains. Comparing both EFTEM images it is apparent that the contrast inversion is not clearly defined, as larger bright domains in the 27 eV image appear rather gray than dark for 18 eV energy loss. Thus, the images in figure 7.14 a) so far only suggest a possible agglomeration of C_{60} that still needs to be proven.

As can be assessed from the images in figure 7.14 b), a lower deposition rate has a strong impact on the film structure. A very coarse structure and high contrast variations are observed in the ZL-image. Black dots are surrounded by dark domains with sharp boundaries. Some of the white regions appear black in the 18 eV as well as in the 27 eV image, indicating possible holes in the film. These holes are framed in white in the 18 eV image showing potential accumulation of the donor. The black spots remain unchanged, whereas the residual domains appear gray. In the following image at 27 eV energy loss all dark regions from the ZL-image are turned bright, speckled with white spots, which correspond to the former black ones. Thus, the C_{60}-rich agglomerates dominate the film structure. It seems that the strong phase

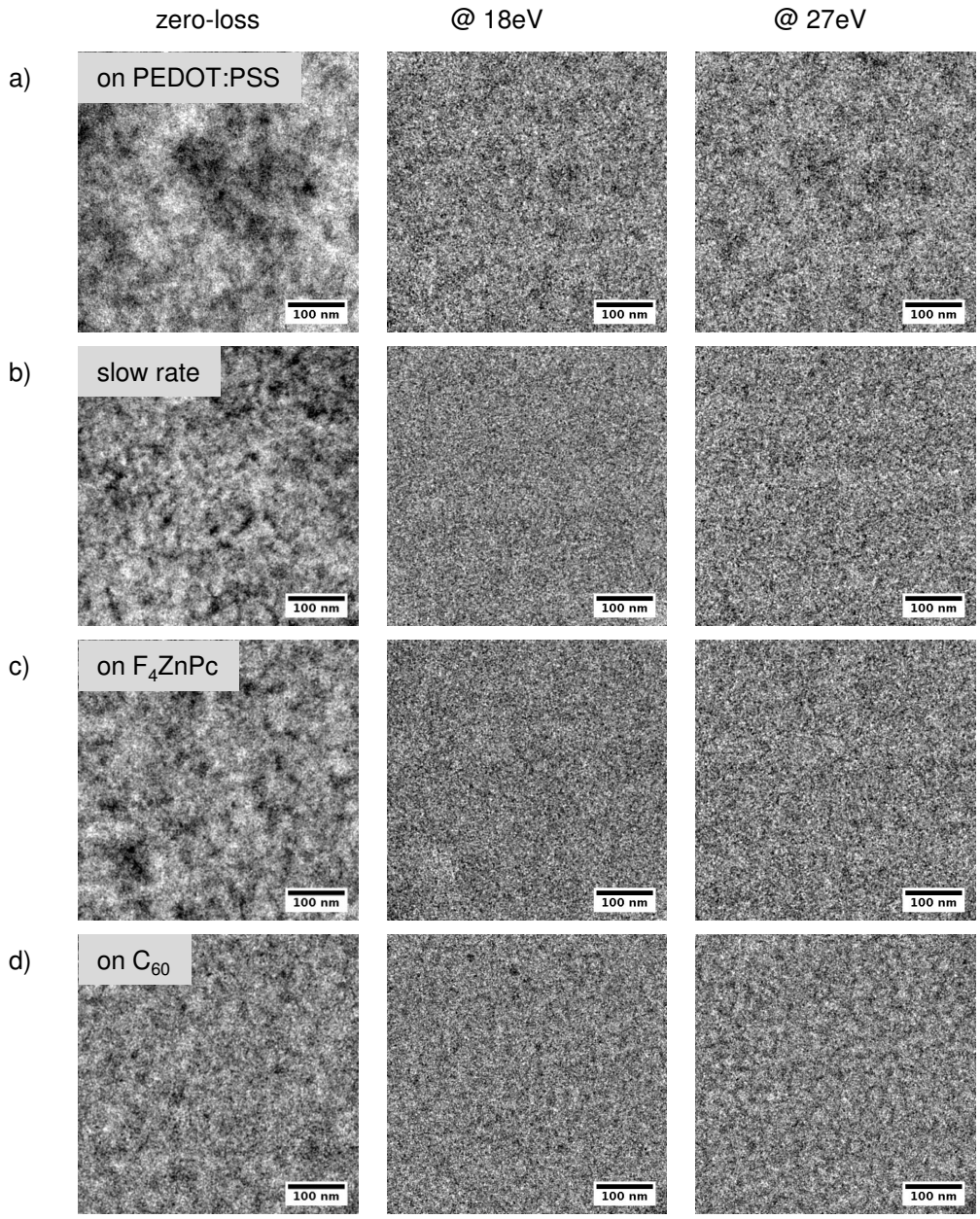

Figure 7.13: Filtered images at zero energy loss, 18 eV and 27 eV of BHJs deposited at room temperature on a) PEDOT:PSS, b) PEDOT:PSS (slow rate), c) F_4ZnPc and d) C_{60}. The images at the characteristic energy loss of F_4ZnPc and C_{60} do not exhibit clear features. All blends appear homogeneously mixed independent of the underlying layer.

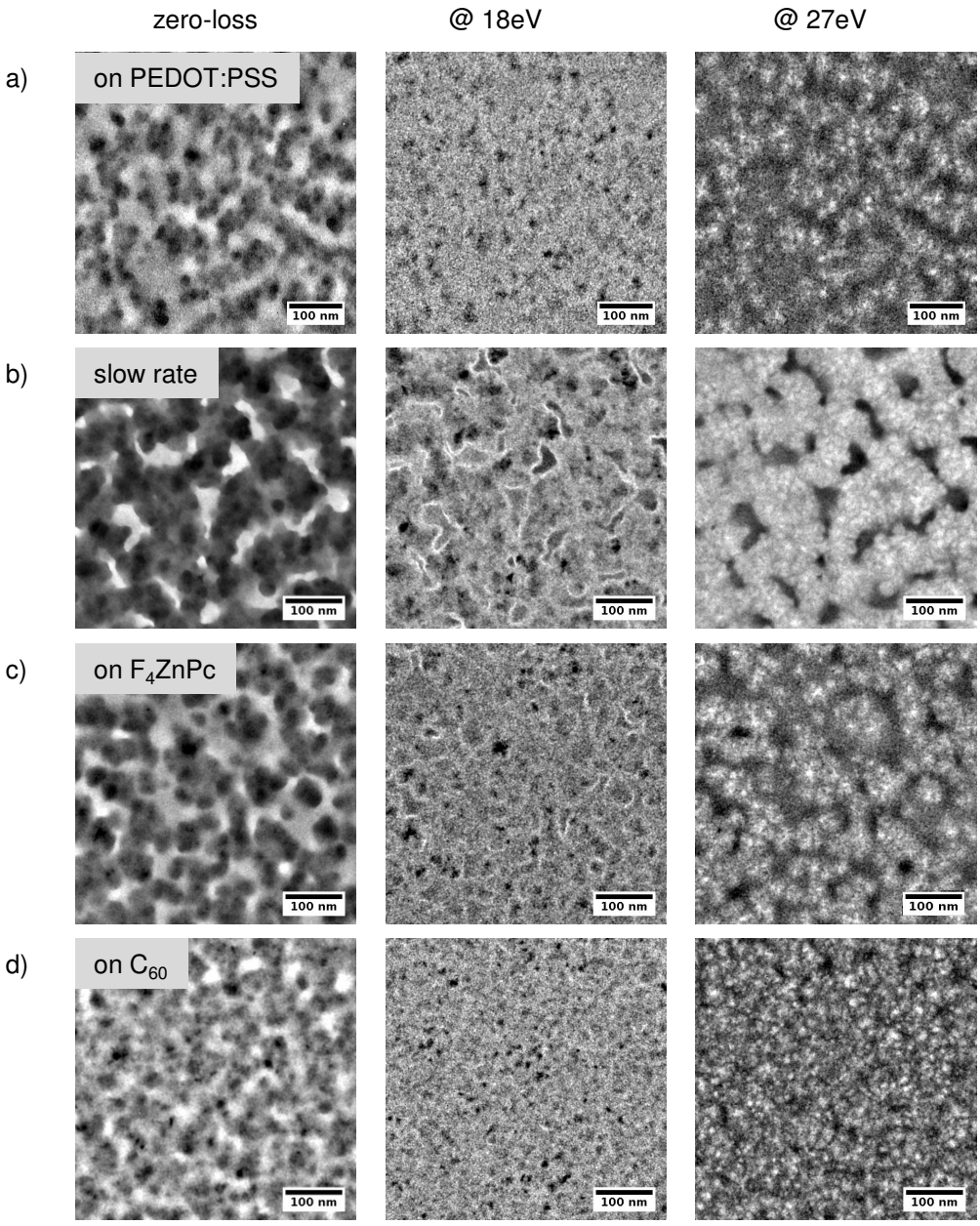

Figure 7.14: Filtered images at zero energy loss, 18 eV and 27 eV of BHJs deposited at 100°C on a) PEDOT:PSS, b) PEDOT:PSS (slow rate), c) F_4ZnPc and d) C_{60}. All samples exhibit strong phase separation. The distinct white structures in the 27 eV images indicate C_{60} agglomeration in the films independent of the substrate.

separation has caused contraction of the film leading to a holey texture and high roughness[7]. Latter, however, is rather adverse for device functionality, as very rough surfaces usually cause a lot of short circuits in the solar cell.

Figure 7.14 c) shows EFTEM images of a blend evaporated on 5 nm pure F_4ZnPc. The images resemble the texture of the PEDOT:PSS sample in a), however with better defined structures. The black spots embedded in dark domains appear bright in the 27 eV image again indicating C_{60} agglomeration, as well as bright features and white edges defining possible F_4ZnPc accumulation in the 18 eV image.

The last set of images of the BHJ on C_{60} in figure 7.14 d) reveal finer grained structures compared to the previous samples. The black spots from the ZL-image appear as very pronounced and distinct white spots at 27 eV, but as was also the case for the previous images, the contrast inversion is not very clear.

In summary, all images from 7.14 suggest possible C_{60} agglomeration in blends deposited on heated substrates independent of the layer underneath, in contrast to the homogeneously mixed RT-samples. Especially the slowly evaporated BHJ exhibits strong phase separation in combination with very high film roughness leading to a holey texture, which is not beneficial in the active layer of solar cells as the holes will cause shortcuts in the device. C_{60} agglomeration (in blends with DIP and ZnPc) is also observed in the literature [65, 187]. Banerjee et al. observed column-like growth of C_{60}, which in a 2D TEM image, as it is a projection of the entire stack, is expected to appear as round agglomerates as well [187]. Whether the agglomerates are actual columns in the present blend can only be assessed by electron tomography [128]. Preliminary 3D reconstructions of blends from tomography will be discussed in the outlook of this thesis.

Due to the unclear contrast inversion, the interpretation of the images is not explicit. It also needs to be considered that the presented images are not normalized, such that thickness variations can also influence the contrast in EFTEM images. For a more specific understanding of the agglomeration and typical domain sizes, the full spectral range of the entire EFTEM image series will be analyzed in the following section.

7.2.3.3. ESI Series

One of the presented data analysis methods in chapter 3.2.2.2 for ESI-series is the LLE decomposition. In LLE analysis the entire image stack, after alignment,

[7]Surface RMS=12.9 nm, determined by AFM (see appendix A.7).

normalization and isochromaticity correction, is used for the determination of the present spectral components, as each pixel from the series represents a coarse energy loss spectrum itself. For P3HT:PCBM such LLE decomposition yielded three, distinct spectral components, the third one being attributed to a new phase of the blend [56]. This assumption is supported by the fact that the energy loss spectrum of the third phase extracted from the ESI-series is not a linear superposition of the P3HT and PCBM spectrum. Here, the LLE analysis for F_4ZnPc:C_{60} blends revealed a different result. The findings for a BHJ deposited on 5 nm C_{60} are shown in figure 7.15 a)-d). In the scatter plot (a) of the first three dimensions in LLE space three well separated clusters of data points are depicted. The points represent the pixels that were assigned to C_{60} (red), F_4ZnPc (blue) or a mixture[8] (green) by the algorithm. Given the very clear separation of the data point clusters, a segmentation into three-classes is justified.

The extracted energy loss spectra for each pixel class are shown in b). As shown in the inset, the plasmon energies of C_{60} and F_4ZnPc are shifted towards each other in the right way, peaking at a higher energy for C_{60}. However, the shift is slightly lower ($\Delta E = 3\,\mathrm{eV}$) than it was the case for the measured EEL spectra of the pristine materials ($\Delta E = 4\,\mathrm{eV}$), with the exact plasmon peak position of C_{60} being at a lower energy. The shift of the plasmon energy to an average value for both materials is not surprising due to the fact that the determined donor- and acceptor-rich phases are not pure, containing a certain amount of mixed material. Additionally, it is important to consider that the measurement corresponds to a projection throughout the entire bulk, which is responsible for a background of mixed signals. The background is expected to cause a shift in the plasmon peak energy. The spectrum of the assigned mixed phase (green) in figure 7.15 b) is a linear combination (not shown) of the C_{60} and F_4ZnPc spectra. Thus, the indicated third phase in this case is not based on the electronic interaction between the materials, but is probably caused by the superposition of signals from the pure materials in the projection. It is also possible that the third phase represents homogeneously intermixed regions. The deduced 2D three-class segmentation is illustrated in figure 7.15 c) with C_{60}-rich domains in red and F_4ZnPc-rich areas in blue. The mixed phase in green separates the other two phases indicating the transition between the donor- and acceptor-enriched domains. Typical C_{60} domain sizes fluctuate between $5\,\mathrm{nm} - 30\,\mathrm{nm}$, which will be discussed in detail in the following section in comparison to other BHJs. Moreover, the structures appear rather fine grained and not well interconnected. An overlay of the semi-transparent

[8] Pixel that could not be assigned neither to C_{60} nor F_4ZnPc.

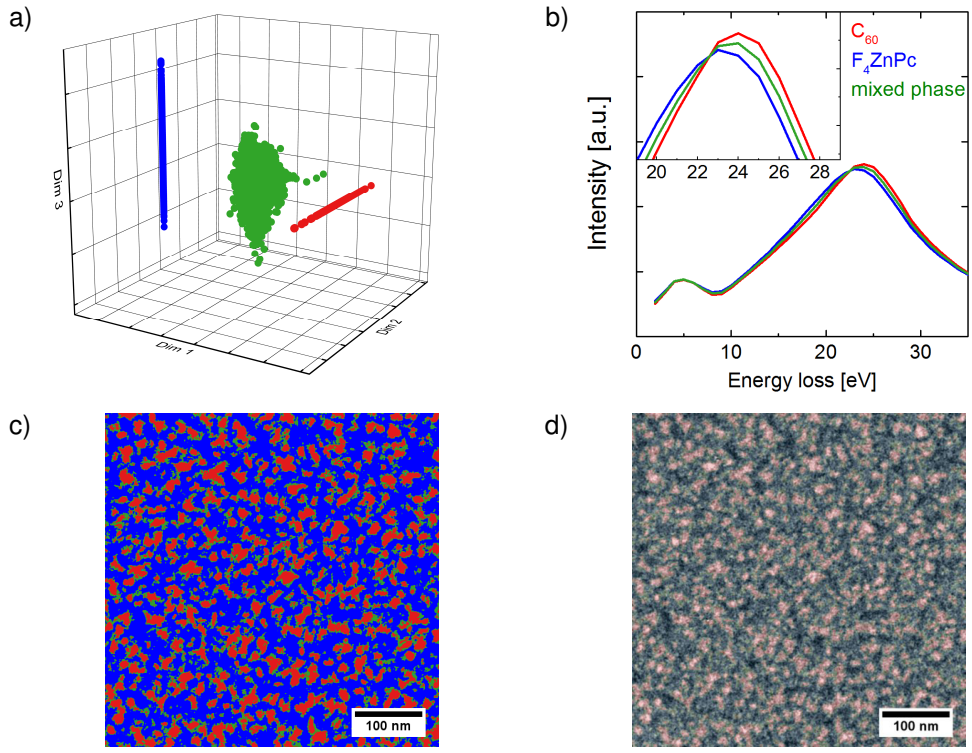

Figure 7.15: LLE analysis of the blend deposited on C_{60} at 100 °C. a) Scatter plot of the first three LLE components. The data points represent the classified pixel from the 2D segmentation. b) Energy loss spectra extracted from the entire image stack correspond to the three-phase-segmentation. The spectrum of the mixed phase can be represented as linear superposition by the pure spectra. c) 2D classification indicating the phase separation of C_{60} - rich (red) and F_4ZnPc-rich (blue) domains. The mixed phase (green) is understood as the superposition of the pure phases. d) Normalized image at 27 eV energy loss superposed by the semi-transparent segmentation shown in c). The C_{60} - rich (red) domains are in good agreement with the bright features in the EFTEM image.

segmentation on the normalized EFTEM image at 27 eV energy loss is shown in d). As assumed, the C_{60} domains, colored in red, correspond very well to the bright spots in the EFTEM image. In addition, the dark regions, that were previously assigned to F_4ZnPc, agree with the domains depicted in blue. The grey regions in the EFTEM image are assigned to F_4ZnPc, but they probably contain a fraction of mixed materials.

In summary, the LLE analysis clearly confirmed the agglomeration of C_{60} in the 100 ℃-sample on C_{60}. By means of LLE components a 2D segmentation was compiled indicating the phase separation between the donor and acceptor and very few intermixed regions being mostly assigned to be F_4ZnPc enriched domains. It is assumed that the C_{60} agglomeration triggers the phase segregation. A third phase representing the electronic interaction of the materials was not found. As a consequence, the less time consuming plasmon peak mapping evaluation was conducted and compared to the results from LLE. For details on the comparison and the entire LLE evaluation of the remaining 100 ℃-samples, the author refers to the master thesis of Felix Schell [36]. In the strict sense, LLE did not lead to any further perceptions that cannot be derived from plasmon peak mapping, such as degree of segregation and domain sizes. Hence, only the analysis by means of plasmon peak mapping for the remaining 100 ℃-samples will be addressed in the following.

7.2.3.4. Plasmon Peak Map

Prior to the plasmon peak mapping, a further, rather simple, analysis is conducted for the characterization of the EFTEM images. First of all, the images from the entire ESI-series are normalized in order to remove contrast variations caused by thickness effects. The normalization is carried out by dividing each pixel's intensity by the integrated intensity of the whole ESI-spectrum. Normalized images for a 100 ℃-BHJ on 5 nm F_4ZnPc at 18 eV and 27 eV energy loss are shown in figure 7.16 a) and b). Whereas the image in b) looks almost like the non-normalized one from figure 7.14 c), the 18 eV image exhibits much more pronounced structures. Compared to the non-normalized image, bright domains are confined clearly and do not appear uniformly gray. Additionally, the white edges, surrounding dark regions, have vanished.

Given the entire ESI-series from 2 eV to 35 eV, the resulting coarse loss spectra from a group of 10 pixels (1 px $\sim$ 0.22 nm) can be compared with the measured EEL spectra of pristine materials, shown in red (C_{60}) and blue (F_4ZnPc) in figure 7.16 c). Colored arrows in a) and b) mark the position from which the spectra in c) are extracted over all energy losses. The orange and red arrows mark black spots in a) and respectively white spots in b). As can be

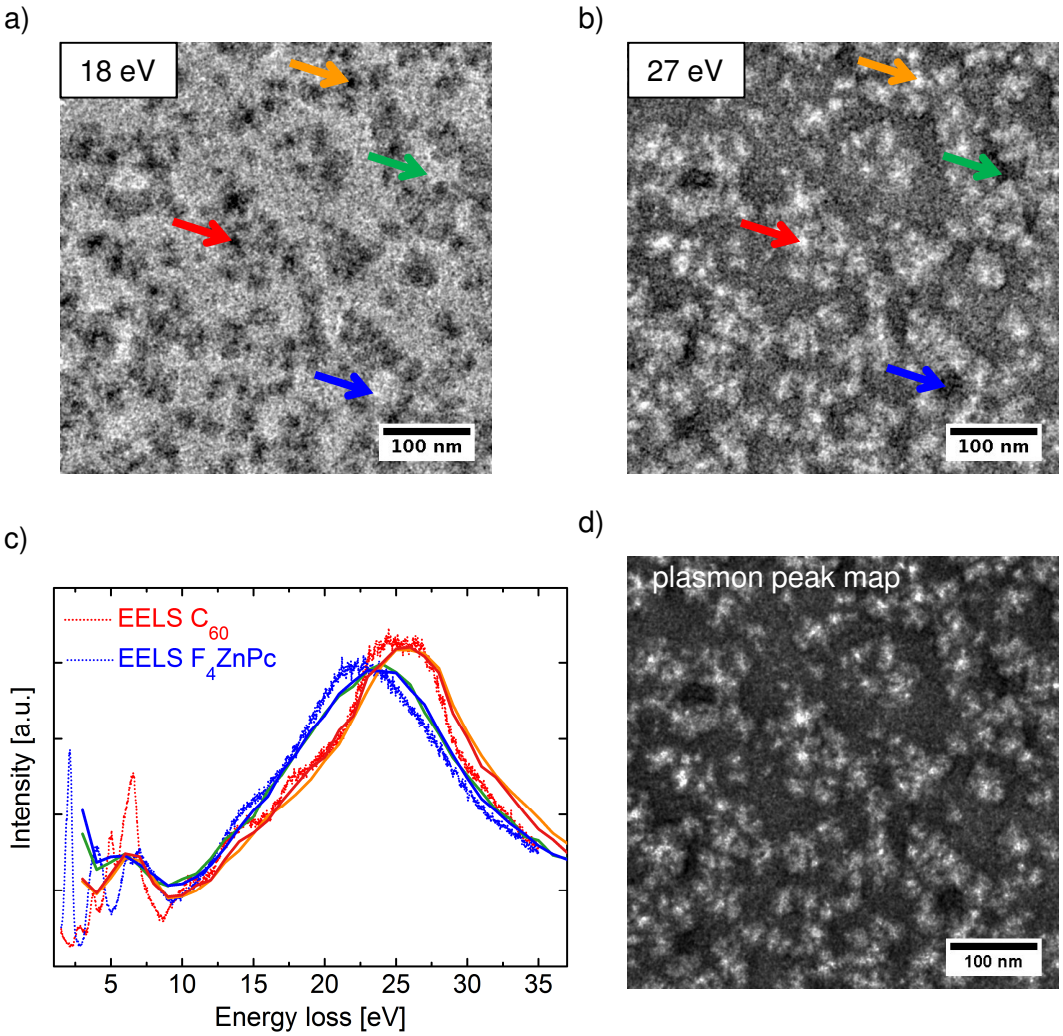

Figure 7.16: Normalized EFTEM images of the blend deposited on F_4ZnPc at 100 °C at a) 18 eV and b) 27 eV energy loss. The arrows indicate the areas for the extracted loss spectra. c) Extracted energy loss spectra from ESI-series compared with measured EEL spectra. An excellent agreement is observed. d) Plasmon peak map deduced from the ESI-series. The bright features are in accordance with the C_{60} agglomerates in the 27 eV EFTEM image.

seen in c), the resulting spectra are in excellent agreement with the measured C_{60}-spectrum. It is striking that even the rather complex form of the plasmon is reproduced precisely. Also the π - plasmon at 6 eV is represented very well in the loss spectrum from the ESI-series, however with a much lower resolution, as the images are acquired in 1 eV energy loss steps. Accordingly, the blue and green spectra are chosen from white areas at 18 eV, which correlate to black areas at 27 eV. Again, the overlap with the measured F_4ZnPc spectrum (blue) is surprisingly high, including the HOMO-LUMO transition at 2 eV, which is noted at the beginning of the spectrum.

Spectra from the exact same group of pixels from the non-normalized images look the same and only differ in their intensity. Hence, the normalization enhances mainly the contrast and the visibility of the domains by removing effects caused by thickness variations. Pixels chosen from an area with intermediate contrast (gray) in the shown images exhibit spectra that lie in between the F_4ZnPc and C_{60} spectra indicating the existence of intermixed phases. Vertically stacked pure donor and acceptor components can of course also cause this kind of mixed signal.

In conclusion, the results shown in figure 7.16 a)-c) reinforce the statements from the previous sections. From the extracted spectra it becomes clear that the nicely separated black spots at 18 eV (white at 27 eV) consist of almost pure C_{60}. The fact that pure F_4ZnPc-domains are mainly found next to pure acceptor domains substantiates the proposed interpretation that the phase separation process is driven by C_{60}.

In figure 7.16 d) the derived plasmon peak map from the image stack is presented. The intensities in the map are generated from the plasmon peak position for each pixel location [65]. The latter is determined by a Gaussian fit. This approach is justified as the plasmon is the pivotal attribute for distinguishing between the donor and acceptor material. The plasmon peak map in d) looks very much like the EFTEM image at 27 eV in b) with better defined structures. There are no features in the map that can be attributed to obvious F_4ZnPc-areas, which is a further proof for the C_{60} agglomeration being the driving force for the donor-acceptor demixing.

For a better illustration of the results, an Otsu threshold is applied such that the differential between the plasmon peaks of both materials is maximal [66]. The resulting two-phase classification for BHJs deposited on the heated substrates PEDOT:PSS (left), F_4ZnPc (middle) and C_{60} (right) are shown in figure 7.17 a)[9]. In the LLE section, all segmentations are dominated by

[9] As of now, results of the slowly evaporated BHJ are omitted as it has no relevance for devices (see appendix A.9 for results).

the C_{60} agglomerates (red). Additionally, the revealed domain shapes are the same as for LLE (e.g. compare figure 7.15 a) and 7.17 a)), with the exception that there is no third phase surrounding the acceptor domains. However, as the third phase does not describe a physical material property, the two-phase separation in figure 7.17 is sufficient for the description of the domain structures. At first glance, the domain distribution and the typical structure sizes for the samples on PEDOT:PSS and F_4ZnPc appear identical. However, the blend deposited on C_{60} exhibits a finer grained structure resulting in smaller and less cohesive C_{60}-rich domains. These observations confirm the overall impression from the EFTEM images at 27 eV energy loss in figure 7.14. A factor that can be calculated from the segmentations is the fraction of the two components as indicated in figure 7.18 a) on top of the images. As already qualitatively assumed from the segmentations, the samples on PEDOT:PSS and F_4ZnPc exhibit the same ratios, supporting their similarity in domain appearance. However, it is important to remark that all blends should exhibit approximately a 1:1 ratio in terms of processing. Strikingly, for all films the fraction of C_{60} (25.8 %, 25.4 % and 30.5 %) is significantly lower than for F_4ZnPc (74.2 %, 74.6 % and 69.5 %). Hence, the assigned C_{60} regions probably consist predominantly of very pure C_{60}, whereas the F_4ZnPc rich domains still hold a significant amount of C_{60}. The calculated amount for C_{60} from the three class LLE segmentations (11.8 % (on PEDOT:PSS), 14.9 % (on F_4ZnPc), 22.9 % (on C_{60}), see appendix A.9 for details) is even lower, as it is partly assigned to a mixed phase. Both segmentation methods seem to recognize only pure phases of C_{60} and F_4ZnPc-rich areas intermixed with the remaining amount of C_{60}. Moreover, based on both analyses, it seems that the blend on C_{60} contains a larger amount of pure domains than the other two blends.

In order to understand the correlation between the two-phase-segmentation and the zero loss images of the blends, the classified C_{60}-rich domains are overlaid with the equivalent TEM image. The results are shown in figure 7.17 b). In fact, the dark appearing regions from the ZL image are mostly covered by the resulting C_{60} segmentation. Consequential, as also stated in the previous sections, the dark and black spots in the zero loss filtered TEM image are pure or C_{60} enriched. As the structures are much smaller, the overlap for the blend on C_{60} is not as clear as for the other two samples.

A degree for the complexity of a certain pattern can be specified by its so-called fractal dimension [221]. The fractal dimension of a two-phase image can be determined by means of fractal box counting, which in this work was carried out by the analyzing tool „Fractal Box Count" in *Fiji*. Results are summarized in a table in figure 7.17 c). The counts indicate how many boxes of

a) on PEDOT:PSS on F_4ZnPc on C_{60}

25.8%(C_{60});74.2%(F_4ZnPc) 25.4% ; 74.6% 30.5% ; 69.5%

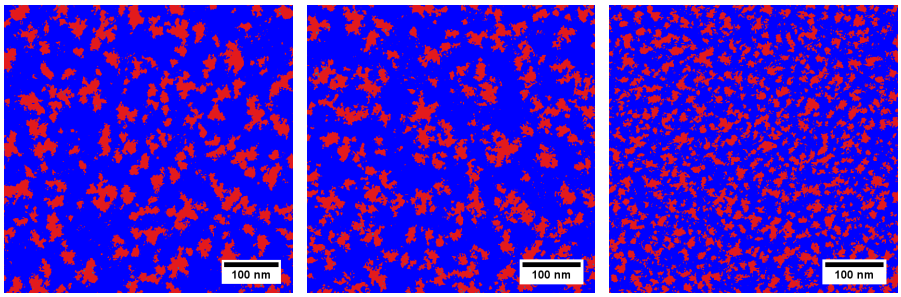

b)

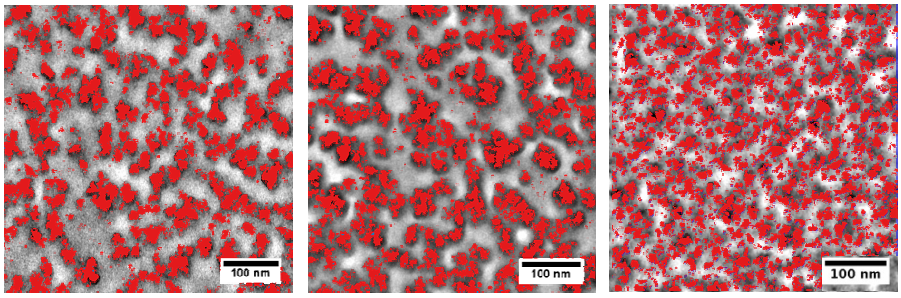

c)

Fractal box counting			
box size [nm]	on pedot [counts]	on F_4ZnPc [counts]	on C_{60} [counts]
2.4	28103	28317	36366
4.9	9302	9575	13120
fractal dimension	1.56	1.56	1.65

Figure 7.17: a) Two-phase segmentation of plasmon peak maps of heated blends deposited on PEDOT:PSS, F_4ZnPc and C_{60} by means of Otsu thresholding. The values indicate the fractions of both donor- and acceptor-rich domains. b) C_{60} segmentation superimposed with ZL images. Dark and black regions in the TEM image are covered almost completely by the classified C_{60}-rich domains. c) Results from fractal box counting for two different box sizes. The determined values for the complexity of the domain textures is higher for the blend on C_{60}.

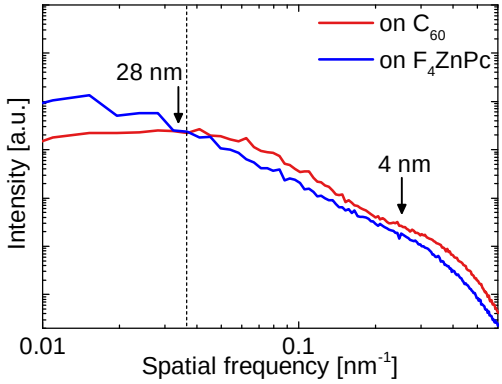

Figure 7.18: Power spectral density of blends deposited at 100 °C on C_{60} (red) and on F_4ZnPc (blue). The red profile exhibits a maximum for a typical domain size of 28 nm and a bump starting at 4 nm.

a particular size (here 2.4 nm or 4.8 nm) are needed to describe the interfaces of the domains. The higher the counts the higher the complexity of the interface. Thus, as the counts for the blend on C_{60} with two different box sizes are significantly higher than for the other blends, the domain texture is more detailed. This confirms the overall fine grained structure of the blend. The similarity of the domain texture of the blends on PEDOT:PSS and F_4ZnPc is reflected in the resemblance of the count values and the fractal dimension.

For a further quantitative analysis of the two-phase segmentations the power spectral density (PSD) of the blends on C_{60} and F_4ZnPc is determined (figure 7.18). A PSD is a logarithmic representation of the FFT's radial profile calculated from an image[10]. It describes the distribution of the power of a signal over different frequencies. Thus, typical structure sizes and domain distances can be deduced from the relation of the calculated PSD's of different samples [222]. As shown in figure 7.18, the profiles of the blends cross at a spatial frequency which corresponds to 28 nm. For frequencies below this value the intensity of the BHJ on C_{60} is higher, and for frequencies above 28 nm, the intensity is lower. Hence, structures smaller than 28 nm appear more often in blends on C_{60}, whereas structures with a size or distance between each other larger than this value are abundant in blends on F_4ZnPc. At a frequency of around 0.25 nm^{-1}, marked in figure 7.18, the onset of a bump is visible for the blend on C_{60} indicating a significant amount of features of 4 nm or smaller.

A possible explanation for the distinct C_{60} agglomerate sizes depending on the underlayer can be presented based on literature findings. McAfee et al.

[10]Calculated by means of the „Raw Power Spectrum" function in the software *Fiji*.

observed strong dewetting of C_{60} evaporated on top of CuPc and annealed at 105 °C [223]. They attribute this effect to the distinct surface energies of the compounds (CuPc: $35 \cdot 10^{-3}\,\mathrm{Jm}^{-2}$ [224], C_{60}: $48 \cdot 10^{-3}\,\mathrm{Jm}^{-2}$ [225]). The high surface energy of the fullerene implies a large ratio of the volume to surface area [223]. This leads to preferentially large clusters and is additionally supported by the lower surface energy of CuPc. Thereby, the overall free energy of the system is minimized [223]. In conclusion, high surface diffusion of C_{60} on a CuPc layer is triggered already at low temperatures (105 °C). Furthermore, Bommel et al. reported a high energy barrier for surface diffusion of C_{60} molecules deposited on an ordered C_{60} film, due to a short attractive interaction range between the molecules [226]. The short range makes the particle less mobile. The consideration of both references leads to the conclusion that C_{60} has a longer diffusion range on a F_4ZnPc layer (assuming the analogy to CuPc[11]) than on a C_{60} layer. This behavior elucidates why the fullerene agglomerates in the blend evaporated on C_{60} are smaller than in the blend on F_4ZnPc.

From the results presented in the preceding section, one can conclude that absolute values from three- or two-phase segmentations (independently from the data analysis method LLE or Otsu) are not explicit. On the other hand, for the relative comparison of resembling samples with slight differences in processing like in the present work, the classification provides a descriptive image of typical domain shapes and sizes.

Further analysis of zero loss filtered images

As has been shown in figure 7.17 b) the dark spots in the zero loss images correspond to C_{60}-rich domains. Usually, high-contrast regions appear when electrons scatter strongly on objects with a high mass density. However, from the comparison of the atomic numbers of both compounds the zinc containing F_4ZnPc is expected to provide a higher contrast. From the previously shown normalized images (see figure 7.16) it is also clear that C_{60}-rich domains are not significantly thicker as thickness variations occur throughout the entire sample, including also F_4ZnPc-rich areas. One possible explanation for the elevated contrast in the ZL images is the presence of crystalline C_{60} domains. Electron channeling, a widely discussed effect in the literature, occurs when crystalline domains are oriented towards the incident beam in such a way that electrons can pass through the lattice planes without being scattered [227, 228]. This effect causes features to appear bright. The opposite of this effect is the

[11] The surface energy of F_4ZnPc: $39 \cdot 10^{-3}\,\mathrm{Jm}^{-2}$, measured by Michael Scherer, TU Braunschweig, is also lower than for C_{60}.

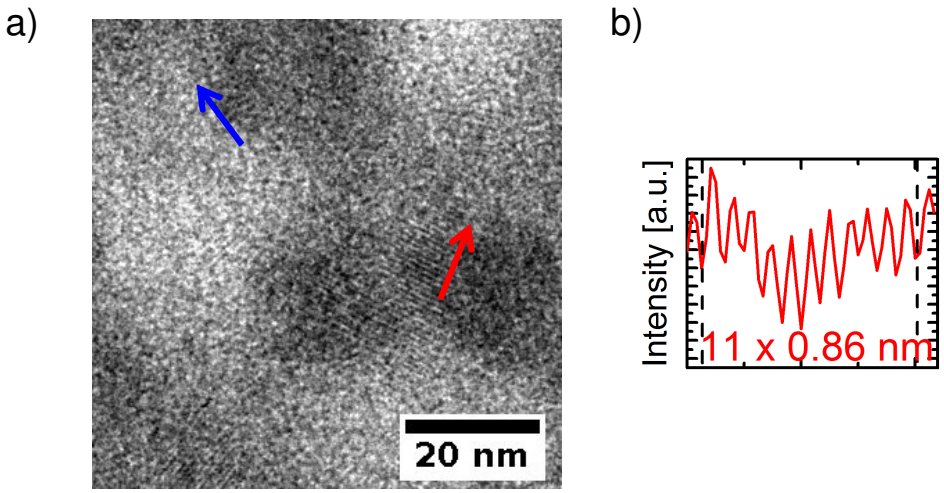

Figure 7.19: a) Dark spots in the blend on C_{60} exhibit lattice fringes that can be attributed to crystalline F_4ZnPc (blue) and C_{60} (red). b) Radial profile along the red arrow from the BFTEM image, indicating the (111) spacing (0.86 nm) of C_{60}.

case in which the orientation of the lattice planes is not preferable for the electrons to propagate without deflection. This causes strong scattering under a wide angle. Thus, the electrons do not reach the CCD camera, leading to dark regions in the image.

This effect is observed, for example, in the BHJs deposited on F_4ZnPc and C_{60} (and not on PEDOT:PSS) as shown representative for one of the agglomerates in figure 7.19 a) in a blend on C_{60}. Periodic lattice fringes are recognized within dark C_{60} regions. From the radial profile (shown in b)) a spacing of 0.86 nm is measured which corresponds to the (111) reflection of C_{60} (see 7.2.2). At the interface of the C_{60} agglomerate, fringes corresponding to F_4ZnPc lattice spacing (1.2 nm) are observed (marked in blue). Crystalline domains within bright domains are not found. It is striking that F_4ZnPc lattice fringes, indicating the presence of pure material, preferentially occur at the acceptor interface. This supports the conclusion that donor and acceptor crystallization is mainly triggered by the C_{60} agglomeration. The contraction of pure C_{60} clusters out of the blend leads to pure F_4ZnPc regions at the interface. These observations however, describe crystallinity only on a very small scale. For an understanding of the average orientation over a wider physical range in the films electron diffraction measurements are necessary.

7.2.3.5. Electron Diffraction

Electron diffraction is performed on the previously mentioned blends deposited at RT and at 100°C on PEDOT:PSS, F_4ZnPc and C_{60}. The diffraction patterns and the corresponding radial profiles are shown in figure 7.20 a) and b). Measurements on RT-samples are indicated in black and respectively in red for the 100 ℃-samples.

All RT-samples exhibit three diffuse, broadened rings in the diffraction pattern in a) revealing the amorphous nature of the blends. The absence of distinct diffraction spots affirms this assumption.

In figure 7.20 b) (top) the radial profile of the RT-blend on PEDOT:PSS is shown in black. As expected from the diffraction pattern, three broad peaks are identified. For a better comparability the diffraction profiles of pristine C_{60} (green dashed line) and F_4ZnPc (blue dashed line) are depicted. The first peak in the blend is dominated by the (111) at $1.17\,nm^{-1}$ corresponding to the 0.85 nm spacing of pure C_{60} with an asymmetry caused by the (010) peak of F_4ZnPc at $0.74\,nm^{-1}$ (corresponding to 1.34 nm). The double peak of pristine C_{60} is represented by one broad peak at $2.08\,nm^{-1}$ (0.48 nm) in the BHJ. The last peak at $2.94\,nm^{-1}$ (0.34 nm) is associated with both materials. As the relative intensity of the last peak in the blend lies in between the peaks of the pure compounds, it is likely that the pristine materials contribute equally. Maenning et al. observed only the broad C_{60} peak (0.48 nm) at a similar position (0.46 nm) for ZnPc:C_{60} blends by electron diffraction [87]. As the peaks of crystalline C_{60} are less pronounced in the blend (and disappear in some of their measurements), they state that the blend is largely amorphous.

For the RT-sample on F_4ZnPc, the same radial profile is noted (figure 7.20 b) (middle)), with the only exception that the asymmetry of the first peak is now a clear shoulder at $0.74\,nm^{-1}$ (1.34 nm). The enhancement of this feature is probably caused by the pristine underlayer, as the shoulder is clearly assigned to the (010) peak of F_4ZnPc. However the major three features are still dominated by C_{60}. Similar observations were also made by Glichrist et al. for CuPc:C_{60} deposited on CuPc [194]. In the diffraction pattern of the blend they observed faint, and broadened rings, speckled with very few distinct spots, which are attributed to C_{60}. Furthermore, Glichrist also observed few C_{60} lattice fringes in the HRTEM images of the cross-section of the BHJ on CuPc [194].

In b) (bottom) the radial profile of the BHJ evaporated at RT on C_{60} is shown. Here, the shoulder in the first peak is again reduced confirming the assumption that in the previous sample it was caused by the F_4ZnPc underlayer. The following peak exhibits an asymmetry towards the higher

feature of the double peak of C_{60}, which is probably caused by the pristine C_{60} substrate.

In fact, all peaks in the RT-samples are assigned to one of the two compounds indicating the coexistence of crystalline and mostly amorphous donor and acceptor domains. This leads to an overall short-range order. Formation of a new crystalline structure from donor-acceptor interactions does not occur. As all radial profiles look very similar, the substrate seems not to have a high impact on the blend crystallinity. Although the F_4ZnPc and C_{60} underlayers exhibit high crystallinity, as was demonstrated from the radial profiles of the pristine samples, their features surface in the blend radial profiles very faintly. This result is consistent with the observations from the EFTEM images, which revealed homogenous films without phase separation for all RT-samples.

Now, turning to the diffraction patterns of the 100 ℃-samples in figure 7.20 a) it is immediately apparent that the rings are sharper. For the BHJ on F_4ZnPc and especially on C_{60}, speckles within the rings become visible, already indicating the presence of larger crystalline domains. The amount of speckles in the pattern of the blend on C_{60} is significantly higher than for the blend on F_4ZnPc implying a higher degree of crystallinity. Besides, in the diffraction pattern of the blend on C_{60} a double ring is visible in the middle feature. This confirms the increased order in the sample when deposited on a heated substrate.

The corresponding radial profiles are shown in red in figure 7.20 b). For the sample on PEDOT:PSS (top) it is striking that although the EFTEM images revealed strong phase separation for the 100 ℃-sample, the radial profiles almost look alike. The only difference is noted in the shoulder arising at $0.74\,\mathrm{nm}^{-1}$ (corresponding to 1.34 nm) indicating slight F_4ZnPc stacking. Obviously the phase separation does not induce significant crystallization, which also explains the absence of lattice fringes in the ZL images.

In the radial profile of the blend on F_4ZnPc (middle) a pronounced peak instead of a shoulder is visible in the first feature. As this was not clearly visible in the RT-sample, it is not a feature from the substrate. The shoulder might be caused by stacking of pure F_4ZnPc within the blend triggered by the heated underlayer. The peak at $2.08\,\mathrm{nm}^{-1}$ has decreased in intensity and exhibits an asymmetry, whereas the third peak has slightly increased. However, an overall strong increase of the crystallinity is not noted.

A significant change is observed in the radial profile of the BHJ deposited on C_{60} (bottom). All peaks of crystalline, pristine C_{60} appear very pronounced in the blend. Whereas the F_4ZnPc shoulder in the first peak increases only slightly, the feature at $1.17\,\mathrm{nm}^{-1}$ is strongly enhanced, well-separated, and in perfect agreement with the (111) peak in pure C_{60}. Additionally, the

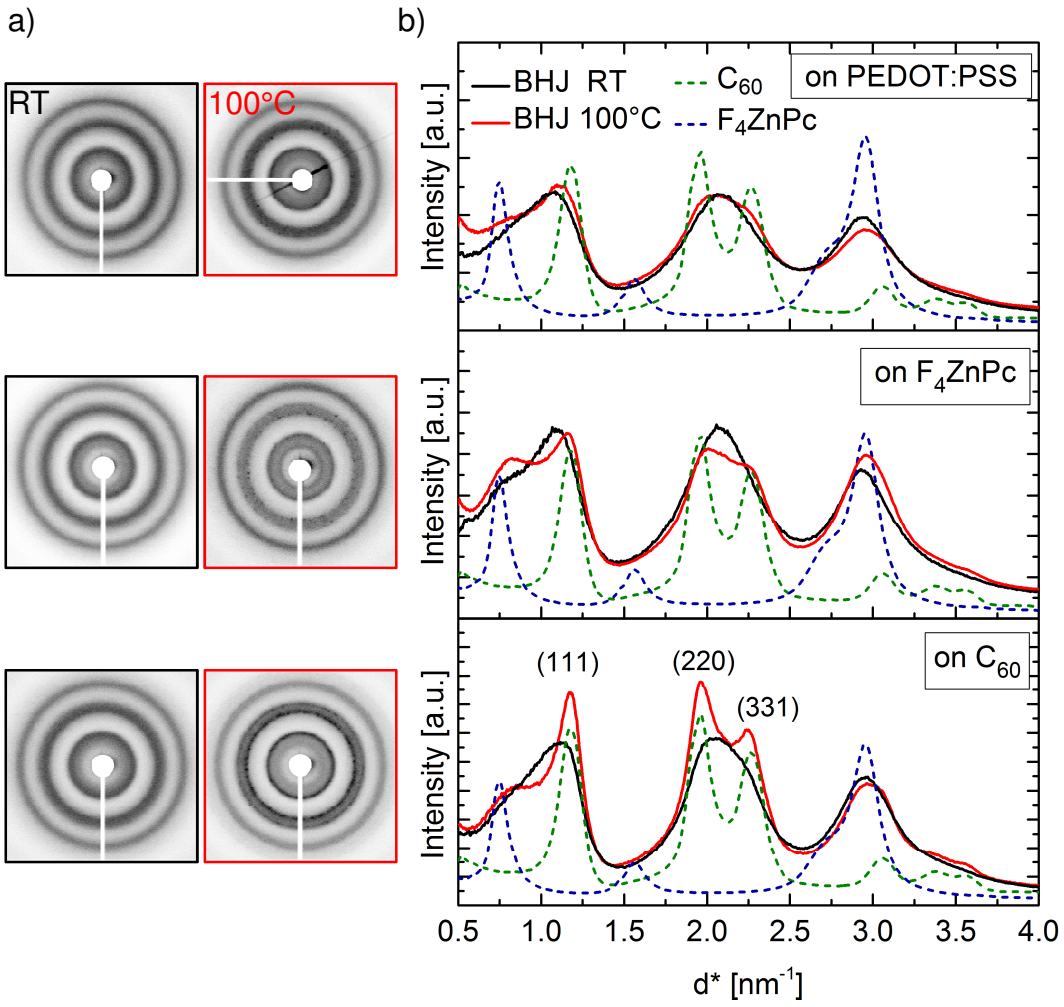

Figure 7.20: a) Diffraction patterns of RT- (black frame) and heated (red frame) samples. b) Corresponding radial profiles of BHJs on PEDOT:PSS (top), F_4ZnPc (middle) and C_{60} (bottom). The dashed green and blue lines indicate the profiles of pristine C_{60} and F_4ZnPc. The profiles in black (RT) look very similar for all samples, whereas the profiles of 100 ℃-samples (red) exhibit significant differences.

double peak structure of the pristine material at $1.96\,\mathrm{nm}^{-1}$ (220) and 2.27 nm (311) along with the small features at $3.5\,\mathrm{nm}^{-1}$ are clearly discernible. The peak $2.94\,\mathrm{nm}^{-1}$, which is mos likely dominated by F_4ZnPc stacking, on the other hand remains unaffected by the heated substrate. One can conclude that the features of crystalline C_{60} in the blend arise from the C_{60} substrate as otherwise they should have also been visible in the RT-sample deposited on the same underlayer. This was not the case. Further, it is ruled out that post-annealing of C_{60} could cause such features, as the radial profile of the pristine material does not exhibit any changes after heating (see 7.2.2). Thus, the peaks in figure 7.20 b) in the BHJ on C_{60} are attributed to the strong crystallization of C_{60} within the blend. It is highly likely that the C_{60} underlayer contains crystallization seeds for the subsequent co-evaporated C_{60} in the blend. However, the seeds contained in the substrate are not enough to trigger the crystallization process as crystalline C_{60} is not observed in the RT-sample on C_{60} (compare radial profile in black). Obviously, the crystallization process is provoked only if accompanied by additional activation energy from the heated substrate. The elevated thermal energy of the system enables diffusion of the molecules. Hence, the crystallization seeds contained in the substrate in combination with the thermal activation of the acceptor molecules cause the crystallization of C_{60} in the blend. Taking the demonstrated phase separation from the previous section into account, it can be assumed that the agglomerates mainly consist of crystalline C_{60}.

The above discussed results can be strengthened by considering the distinct surface energies of the molecules (F_4ZnPc: $39 \cdot 10^{-3}\,\mathrm{Jm}^{-2}$, C_{60}: $48 \cdot 10^{-3}\,\mathrm{Jm}^{-2}$ [225]). It is reported for CuPc:C_{60} blends that due to the distinct surface energies of the molecules, vertical phase separation is energetically favorable upon thermal annealing [193, 229]. As CuPc exhibits a lower surface energy than C_{60} [224, 225], it accumulates preferentially at the air interface, whereas C_{60} accumulates at the substrate, reducing the overall energy of the system. Assuming that this effect is also valid for F_4ZnPc:C_{60} blends, C_{60} is expected to accumulate close to the pristine C_{60} substrate. Hence, the C_{60} in the blend is very susceptible for crystallization seeds offered by the pure layer. This explains the presence of crystalline C_{60} , which is clearly pronounced in the radial profile.

7.2.4. Conclusion: TEM Measurements

From the discussed TEM measurements (EELS, bright-field TEM, energy filtered TEM, electron diffraction) in the important results are:

- Pristine F_4ZnPc and C_{60} exhibit preferential stacking when deposited at temperatures as low as room temperature. Heated substrates do not have a significant impact on crystallinity, however they increase the average structure size.
- Electronic interaction between the donor and acceptor is not observed in the blend. Substrate choice and heating does not influence the spectral features of the materials.
- Blends deposited at room temperature exhibit homogenous film growth and do not demonstrate phase separation independently of the substrate.
- All BHJs deposited at 100°C show clear phase separation including pronounced C_{60} agglomeration.
- Three- and two-phase segmentation revealed typical C_{60}-rich domain sizes of around 30 nm −50 nm for BHJs deposited on heated PEDOT:PSS and F_4ZnPc. Finer grained structures of 5 nm −30 nm are observed for the blend on heated C_{60}. Moreover, the species ratios from the segmentations hint at a higher amount of pure C_{60} in the blend deposited on C_{60}.
- The radial profiles of BHJs deposited at RT indicate an amorphous phase of the films independent of the substrate.
- Crystallinity of the blend on PEDOT:PSS does not increase with heating. For the BHJ on F_4ZnPc only a slight impact on order is noted due to possible stacking of F_4ZnPc within the blend.
- A considerable change in the radial profile of the heated blend on C_{60} is observed. Clear crystallization of C_{60} in the BHJ is noted. The crystallization process is possibly triggered by crystallization seeds in the substrate accompanied by molecular diffusion, which is provoked by the elevated temperature of the system.

7.2.5. Correlation to Structural Properties Obtained by Infrared Spectroscopy

Simultaneously to this work in-situ FTIR (Fourier transform infrared) measurements were performed on the pristine and blended materials F_4ZnPc and C_{60} by Johannes Zimmermann [203]. In order to ensure a better comparability between the measurements in this work and the infrared (IR) measurements, the samples were processed under the same conditions (rate, temperature etc.).

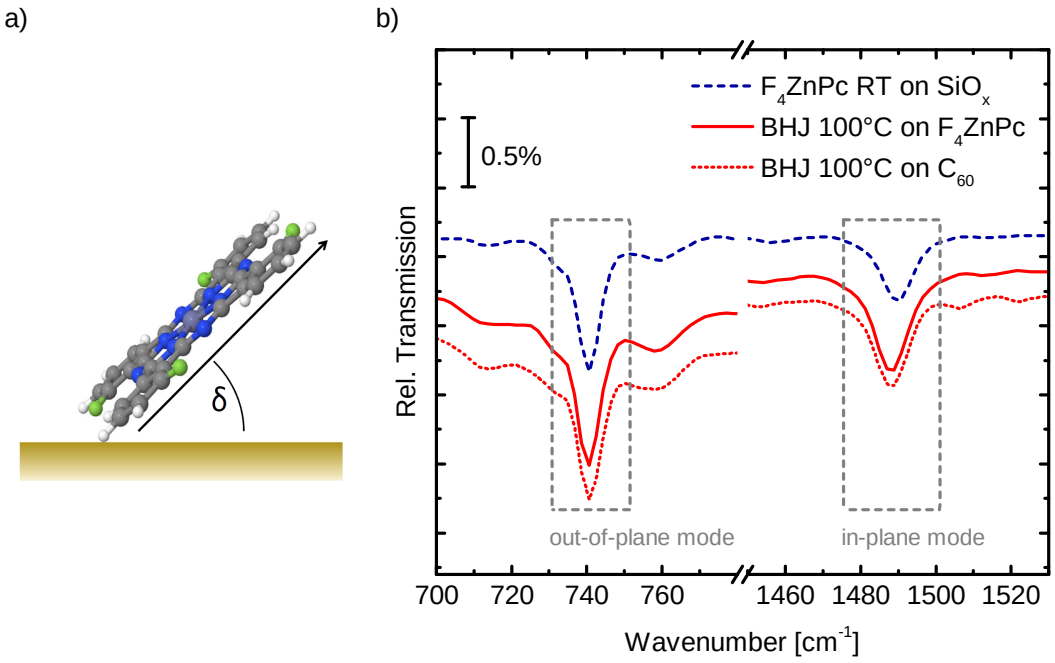

Figure 7.21: a) Graphic representation of the orientation angle δ of the F_4ZnPc molecule with respect to the substrate taken from [203]. b) IR spectrum of pristine F_4ZnPc deposited at RT on Si (blue). The out-of-plane (oop) and in-plane (ip) modes are indicated. The IR spectra of BHJs on F_4ZnPc (solid line) and on C_{60}(dashed line) deposited at 100 ℃ are shown in red. The intensity ratio of the oop to ip mode is identical for the spectra of both BHJs. The spectra taken from [203].

FTIR spectroscopy is a powerful technique, which enables the determination of the orientation angle of molecules with respect to the substrate. Therefore, FTIR measurements can elucidate a possible orientation of the F_4ZnPc molecules, which is not assessed from diffraction measurements.

For this purpose, IR spectra under different angles of incidence are acquired in transmission geometry and compared with simulations. In the case of normal transmission only molecular vibrations with a transition dipole moment parallel to the substrate can be excited. In particular, for the almost planar molecule F_4ZnPc this means that the more upright the molecules are standing on the substrate, the stronger the intensity of out-of-plane modes (oop) increases. Respectively, the intensity of the in-plane (ip) modes is expected to decrease. The resultant intensity ratio of the oop and ip modes can be used as a measure for the average orientation of the molecules in the layer.

It is also possible to calculate an approximate orientation angle from vari-

ations of the relative mode intensities of the thin film spectrum compared to the intensities of the isotropic powder[12] IR spectrum of the corresponding molecule [203, 230]. The orientation angle δ describes the angle of the molecule with respect to the substrate as illustrated in figure 7.21 a).

In figure 7.21 b) the IR spectrum of a pure F_4ZnPc layer deposited at RT on silicon (Si) with a native SiO_x layer is shown (blue dashed line). In the presented frequency range the two strongest absorption bands are assigned to an oop and an ip mode of the molecule. The assignment was realized by making use of DFT-calculations of F_4ZnPc [203]. From the comparison of measurements under varying angles of incidence with simulations, Zimmermann demonstrated in his work that F_4ZnPc exhibits a preferred upright orientation when deposited as a pure layer on Si at RT [203]. Accordingly, the shown spectrum in figure 7.21 b) is attributed to an orientation angle of F_4ZnPc of $75° \pm 5°$ [203]. A similar orientation angle was also determined for F_4ZnPc deposited on a heated (100 °C) Si substrate [203]. These findings are in agreement with recent X-ray diffraction measurements, which showed a preferential orientation of F_4ZnPc evaporated at room temperature on pure C_{60} [231].

Furthermore, the IR spectra of a F_4ZnPc:C_{60} BHJ deposited on F_4ZnPc and C_{60} at 100 °C are shown in figure 7.21 b) in red (solid and dashed line respectively). The intensity ratio of the oop to ip mode in both spectra is identical. Hence, the average orientation of the F_4ZnPc molecules in the BHJ deposited on heated substrates does not dependent on the underlying layer. The intensity ratio of the modes in the BHJs is slightly lower as for the pristine molecule on Si. Therefore, the preferred orientation is probably less than $75° \pm 5°$, but an upright orientation of the F_4ZnPc molecules is still present in both BHJs. For further details on sample preparation, the IR measurements and the data analysis the author refers to Zimmermann's master thesis [203].

7.3. I-V Characteristics of F_4ZnPc:C_{60} Solar Cells

As discussed in the introduction of this chapter, in various publications, blend morphology is proposed to have a significant impact on device performance. From the results obtained in the previous section it becomes clear that heated substrates, which induce strong phase separation, might play a key role for devices. However, as was also demonstrated by the electron diffraction measurements, the substrate induces crystallization processes that also need to

[12]The powder from the pristine material is embedded in a KBr pellet.

be considered for device architecture. For this purpose, non-inverted (F_4ZnPc under the BHJ) and inverted (C_{60} under the BHJ) F_4ZnPc:C_{60} solar cells are presented. As the inverted device architecture requires n- and p-doping of the electron- and hole- transport layers respectively, which could not be conducted in this thesis, the author will refer to results from the literature for the inverted solar cells.

7.3.1. Non-inverted vs. Inverted Devices

The device stack used in this work, which was found to perform best and reproducibly, is shown in figure 7.22 a)[13]. Starting from the transparent ITO/glass substrate 10 nm of MoO_3 are evaporated increasing the work function and acting as a hole-extraction layer [232]. For a better electron-blocking contact a 5 nm F_4ZnPc layer is evaporated on top. This layer must be kept thin as F_4ZnPc is known to exhibit rather low hole mobilities [89]. It is followed by a 45 nm BHJ in a 1:1 ratio and the substrate is kept at RT or heated at 100°C . The next 10 nm C_{60} layer smooths the BHJ and acts as a good electron transporting interlayer. It is followed by a 8 nm hole blocking layer of TPBi [233]. Silver is chosen as the top electrode. The optimized, inverted stack used by Meiss et al. is shown in figure 7.22 b) [89]. The first layer is an electron transport layer of n-doped C_{60}, followed by a hole-blocking layer of 10 nm pristine C_{60}. After a 65 nm blend, a p-doped layer is deposited, which exhibits good hole-transport properties. The top electrode consists of aluminum.

In figure 7.22 c) I-V-Characteristics of non-inverted solar cells on non-heated and heated substrates under 1-sun illumination are shown. The indicated average characteristics with a standard deviation of eight devices are taken from two different substrates with four cells each [14]. Compared with the characteristics of inverted devices (active layer 65 nm) by Meiss et al., shown in figure 7.22 d), the determined values for the RT solar cell deviate only by about 10 %. This demonstrates that the non-inverted devices match the performance of inverted state of the art solar cells [89]. For a 45 nm thick BHJ Meiss et al. even present devices with the short circuit current of $j_{sc} = 9.2 \pm 0.1\,\mathrm{mA/cm^2}$ being as high as for the presented devices here ($j_{sc} = 9.1 \pm 0.1\,\mathrm{mA/cm^2}$), indicating

[13] Further device architectures including bilayer solar cells, inverted and non-inverted BHJs with different interlayers and varying thicknesses were tested within the master thesis of Felix Schell [36]. Device data of inverted solar cells indicated mainly problems at the contacts (s-shaped I-V curves) overruling morphology effects. As the performance was rather unstable and not reproducible they will not find further mention in this thesis.

[14] Among 16 devices variation is less than 10 %.

a) non-inverted device

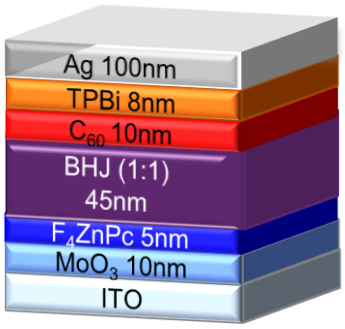

b) inverted device (Meiss et al.)

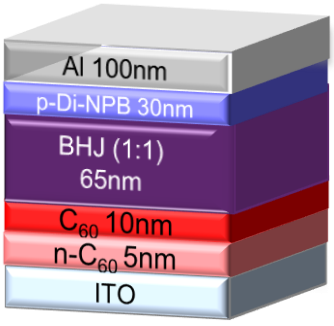

c)

	RT	100°C
V_{oc} [mV]	628±9	639±9
J_{sc} [mA/cm²]	9.1±0.1	9.0±0.1
FF [%]	50.2±2.2	48±0.6
η [%]	2.9±0.1	2.8±0.1

d)

Meiss et al.	RT	100°C
V_{oc} [mV]	730	690
J_{sc} [mA/cm²]	10.6± 0.2	12.1± 0.2
FF [%]	45	55
η [%]	3.6±0.1	4.6±0.1

e)

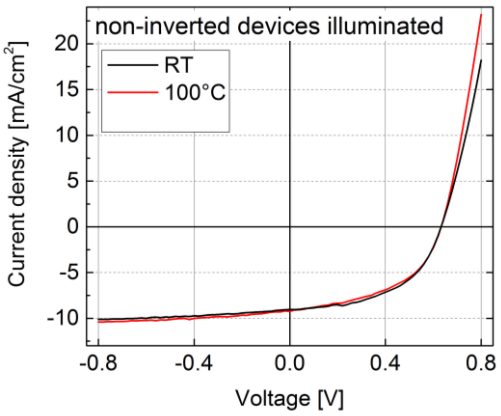

f)

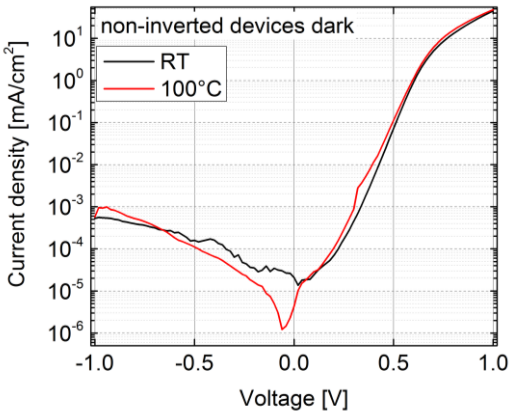

Figure 7.22: Device stacks of the a) non-inverted solar cell used in this thesis and of b) inverted solar cells used by Meiss et al. [89]. c) Average characteristics for eight non-inverted devices at RT (black) and heated (red). d) Parameters averaged for fifteen inverted devices [89]. An increase of the efficiency for the heated non-inverted device is not observed. I-V curves of the best performing non-inverted RT (black) and heated (red) devices e) illuminated and f) dark, indicating equal performance.

the same efficient charge generation. As expected from the higher ionization potential of the fluorinated material, the open circuit voltage $V_{oc} = 628 \pm 9\,\text{mV}$ is higher as for ZnPc:C_{60} solar cells with $V_{oc} \approx 500\,\text{mV}$ [12, 234]. The overall performance of the RT devices with a resulting efficiency of 2.9 % and a fill factor of 48 % is acceptable. Surprisingly, the efficiency for the heated solar cell (7.22 c) red) has not increased and is on average even slightly lower (2.8 %) compared to the RT device. The V_{oc} has not changed significantly. In the inverted devices of Meiss (see d, red) even a slight decrease in the V_{oc} is observed after heating. It is suggested that ground state interactions of the donor and acceptor, such as dipole formation, are induced by the additional thermal energy in the system. This can influence the recombination dynamics and subsequently the open circuit voltage [89]. Meiss observes an increase of the fill factor and the short circuit current leading as well to a significant increase of the efficiency to 4.6 %. This effect is attributed to a well-formed network, healed charge carrier percolation paths and less dead ends, all triggered by the changed morphology upon heating [89]. An increase of FF and j_{sc} , though, is not observed for the non-inverted devices as presented in figure 7.22 c). The FF has even decreased. I-V curves under illumination of the best performing non-inverted BHJs are depicted in figure 7.22 e) in black (RT) and in red (heated). It is clear, that there is no difference in the performance of the two cells. Figure 7.22 f) shows the corresponding dark curves. A relatively low current at reverse bias is noted, indicating high series resistance, which does not alter the properties of the heated device. The leakage currents are two orders of magnitude lower than for the inverted device of Meiss, showing that the overall performance of the non-inverted devices is satisfactory and not overruled by other effects such as bad contacts.

7.3.2. Conclusion: Device Characteristics

From the I-V-characteristics of non-inverted F_4ZnPc:C_{60} solar cells deposited on heated or unheated devices in combination with the characteristics of inverted F_4ZnPc:C_{60} devices from the literature (Meiss et al. [89]) the following conclusions are drawn:

- F_4ZnPc:C_{60} BHJs deposited at RT perform similarly independent whether the non-inverted or inverted device architecture is implemented.
- An increase of efficiency of the non-inverted, heated device compared to the RT solar cell is not noted. None of the significant factors for improvement - such as fill factor or short circuit current - change notably with heating.

- In the literature, a significant increase of the FF and the j_{sc} in inverted $F_4ZnPc:C_{60}$ devices is observed, attributed to a well-constructed percolation path network, which improves the device efficiency [89].

7.4. Discussion: Structure-Function-Relationship

At the beginning of this chapter, based on findings from the literature, it became clear that an unified model for the morphology impact on small molecule solar cell devices does not exist. The presented results for $F_4ZnPc:C_{60}$ blends from the previous sections propose a completely new and extensive interpretation than previously made by Meiss et al. on the same material system. The main findings of this thesis are summarized in figure 7.23. For an inverted device architecture, meaning that the blend is deposited on pure C_{60}, a 15 % efficiency increase of the solar cell is observed if the substrate is heated during co-evaporation of the blend [89]. In the mentioned publication, it was assumed that the improvement is caused by morphology changes, however, without specifying the key factors. Here, we find that the heated substrate during co-evaporation induces strong phase separation mainly represented by C_{60} agglomeration, irrespective of the underlayer. This confirms the assumption of Meiss, that heating enhances the connectivity of the domain network and reduces dead ends which usually cause recombination losses. Better connectivity eventually leads to higher short circuit currents and increased efficiencies. However, although strong phase separation does occur in blends deposited on F_4ZnPc, an efficiency improvement of non-inverted solar cell devices (with F_4ZnPc as underlayer) is not noted. It might be argued that enhanced device performance is not visible in the heated, non-inverted device because the positive morphology effects are counterbalanced by other factors such as not optimized selective contacts with high resistance or higher surface roughness causing short cuts. Both factors would hinder efficiency improvement. As the non-heated device performs similar to the inverted, optimized stack by Meiss et al., effects from the contacts are assumed to be negligible. Optical absorption properties do not indicate any discrepancies as well. Blend layers in the heated and unheated non-inverted devices exhibit similar roughness, which is deduced from AFM (see appendix A.7). Therefore, an increased surface roughness in the heated layer, causing shorts, can be excluded.

Summarizing the results from the literature, a pattern becomes very striking. In analogy to the results in this work, improvement of small molecule solar

cells (e.g. CuPc:C_{60} and ZnPc:C_{60}) upon substrate heating is only observed in the inverted device architecture in which the blend is deposited on a pristine C_{60} layer [12, 184, 235]. If the blends are deposited on a pure CuPc layer or a pure ZnPc layer, respectively, in non-inverted solar cells, the heated and unheated devices perform equally [14, 64, 186].

Surprisingly, although the morphologies of the heated and unheated films are so different, the greater phase separation is not sufficient for improved functionality. Obviously, there are additional key factors that play a significant role, which brings us to the major difference between inverted and non-inverted devices - the blend underlayer. For the non-inverted device the blend is usually deposited on the electron-blocking donor, the phtalocyanine, and accordingly on the hole-blocking acceptor, the fullerene, for the inverted architecture, drawing the attention to the significant discrepancies between the two blend morphologies.

Based on the IR measurements, which revealed the same average orientation of the F_4ZnPc molecule in both BHJs, the change of relative donor/acceptor orientation [15, 16] in the BHJ is excluded as main cause for the improved efficiency of the inverted device.

One of the differences, elaborated in the previous sections, is the typical domain sizes, which are observed to be smaller for the BHJ deposited on C_{60} (5 nm −30 nm), compared to 30 nm −50 nm for the BHJ on F_4ZnPc. It can be concluded that domains are significantly larger and phase separation is rather coarse in the blend on F_4ZnPc. This is possibly adverse for device performance. It is feasible, that as the domain size exceeds the exciton diffusion lengths ($L_{\mathrm{diff,C_{60}}} = 40 \pm 5$ nm; $L_{\mathrm{diff,ZnPc}} = 30 \pm 10$ nm [25]), the dissociation efficiency is lowered for the device on F_4ZnPc. The lower dissociation rate counteracts the enhanced charge transport and the lower recombination rates in the larger and continuous domains. This perhaps leads to an overall lower efficiency. Good device functionality is known to be a tradeoff between domain size and well-connected percolation paths, which is not necessarily the case for the BHJ deposited on F_4ZnPc [187]. Another peculiarity is the distance between the C_{60} agglomerates, being larger for the blend on F_4ZnPc and possibly interrupting the charge carrier paths. As reported by Banerjee et al., island size and distances are likely to depend on mixing ratio indicating that the ratio in one of the blends might deviate from 1:1. This could also have an impact on device performance [187].

There is still one major difference in the structural properties of the two blends left, that might deliver a more evident reason for the improvement of the inverted, heated device. From the diffraction measurements in section 7.2.3.5 it became clear that the heated BHJ on C_{60} is the only one to exhibit

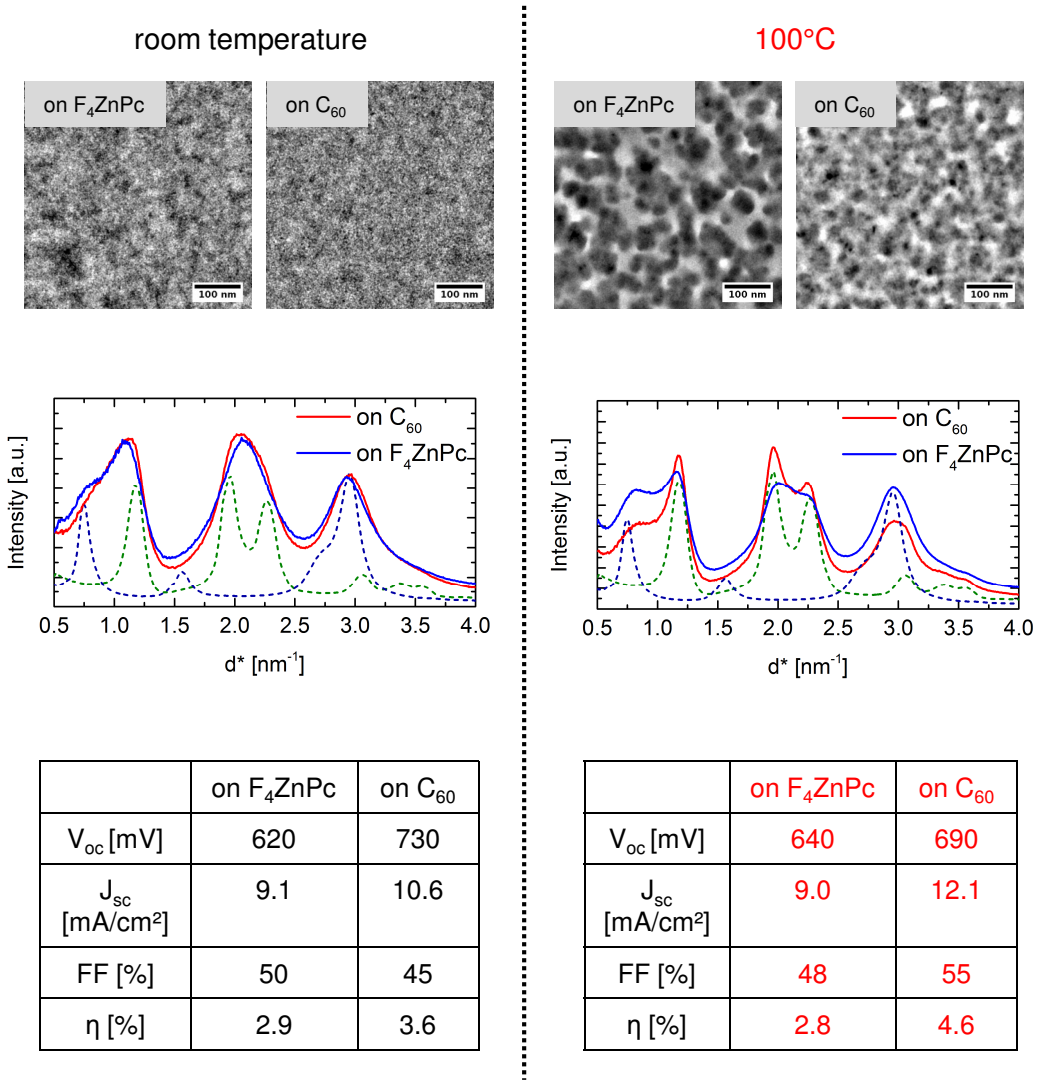

	on F_4ZnPc	on C_{60}
V_{oc} [mV]	620	730
J_{sc} [mA/cm²]	9.1	10.6
FF [%]	50	45
η [%]	2.9	3.6

	on F_4ZnPc	on C_{60}
V_{oc} [mV]	640	690
J_{sc} [mA/cm²]	9.0	12.1
FF [%]	48	55
η [%]	2.8	4.6

Figure 7.23: Summary of the main findings from this chapter focusing on the difference in morphology, crystallinity and device performance between unheated and heated devices deposited on F_4ZnPc or C_{60}.

pronounced crystallinity of C_{60} in the blend. The crucial question now is why do crystalline acceptor domains improve device performance?

The impact of ordered fullerene domains on charge transport properties has been recently a topic of interest in the literature [18–20, 27, 236]. Bartelt et al. determined by means of time-resolved terahertz spectroscopy that photoconductivity in ZnPc:C_{60} blends increases with domain size and crystallinity of C_{60} [236]. They attribute this effect to an enhanced separation of the charge transfer (CT) states due to strong charge delocalization. This is accompanied by higher electron mobilities in crystalline fullerene and follows the Onsager-Braun-Model [32], which considers dissociation to be mobility and field dependent [27]. However, as discussed by Nayak et al., the electric field does not dominate the charge separation in fullerene blends, counter to Onsager-Braun [27]. Crystalline C_{60} exhibits high-energy delocalized states, accessible for the charges after photoinduced CT, which triggers exciton dissociation directly into free electrons and holes [27]. If charge separation is efficient than the direct exciton dissociation is independent of the applied voltage. To this end, the fill factor of the solar cells with crystalline C_{60} is expected to increase. This was the case for the heated, inverted F_4ZnPc:C_{60} blends discussed in this work [89]. Savoie et al. confirm the crucial existence of delocalized states in ordered fullerene by electronic structure calculations and ultrafast transient measurements [19]. They state a resonant coupling of excitons to high-energy states in the fullerene leading to efficient charge generation. As the density of the available charge-separated states (unbound CT states) is high, the free charge carriers bypass inefficient, localized CT states, which usually lead to recombination losses [19]. Additionally, the necessary C_{60} crystallite size for the formation of these band-like, delocalized CT states, which decay on a sub-picosecond scale, is found to be $\sim 4\,\mathrm{nm}$ [18]. With increasing crystallite size the polarizability of the CT states is observed to increase as well, which leads to a stronger delocalization [18].

With the discussed results from the literature a more distinct explanation for the performance of the devices can be given. It is clear that the delocalized CT states, which are crucial for charge generation, are only provided in blends with C_{60} crystallites of at least 4 nm in size. This is actually only the case for the heated BHJ deposited on C_{60} (as in the better performing, inverted device). For the latter, plasmon peak maps from TEM measurements revealed pure and crystalline C_{60} domains to a greater extend compared to the BHJ deposited on F_4ZnPc as in the non-inverted device. The C_{60} domains in the heated blend on F_4ZnPc are too disordered, as crystalline C_{60} signature is not observed in the radial profile. The F_4ZnPc underlayer is probably not favorable for C_{60} crystallization due to the lack of crystallization seeds. Therefore, a

high number of excitons couple with the predominantly localized CT-states. These states lead to recombination, limiting the device efficiency in the same way as for the unheated devices, where the lack of delocalized CT states is attributed to the absence of phase separated, crystalline C_{60} domains.

The higher crystallinity of C_{60} in the BHJ deposited on C_{60} at 100 °C possibly causes the decrease of the V_{oc} in the inverted devices. Under the assumption that the stack is optimized [89], the V_{oc} is mainly determined by the effective band gap of the materials (see 2.1.2). As already mentioned in section 7.2.2, the band gap of C_{60} decreases with increasing degree of crystallinity [215]. This might explain the lower V_{oc} in the heated BHJ compared to the unheated one in the inverted device architecture and is a fruther evidence for the presence of crystalline C_{60}.

There is still an open question that cannot be answered from the present results and requires further measurements: the vertical phase separation. As already mentioned, TEM measurements represent the projection of the entire bulk. Hence, the exact position of crystallites and domains in the film with respect to the surface and substrate is not determined. However, vertical segregation might also play a crucial role for device performance. As discussed in section 7.2.3.5, there are references proposing accumulation of the fullerene preferentially at the substrate due to its higher surface energy [225] compared to the surface energy of phtalocyanine molecules [193, 229, 237]. In the inverted device structure this effect implies assembly of the electron-transport material (the C_{60}) at the electron-collecting electrode (pristine C_{60} on ITO) resulting in a more efficient charge extraction at the contact and an overall enhanced functionality of the device [237]. The direct imaging of such a diffusion-induced gradient would acknowledge and subsequently expand the results of this thesis. Basically, there are two ways to approach vertical information by TEM measurements: (i) electron tomography (ii) examination of focused ion beam (FIB) milled cross-sections. FIB-milling turned out not to be possible (as discussed in chapter 4.3.2) in the framework of this thesis. Due to strong amorphization of the organic layers by the FIB, domains and structures within the cross-section of a F_4ZnPc:C_{60} blend could not be resolved. Further development of the preparation technique needs to be carried out in order to reduce FIB damage, which is beyond the scope of this work.

As was shown by Donhauser et al., electron tomography is an eligible method for the investigation of the three-dimensional structure of organic thin films [128]. From the tilt series of TEM bright-filed images in the cited work, the 3D volume of doped organic films is reconstructed, revealing that the initially proposed doping agglomerates from the projection in a conventional TEM image are in fact filamentous, column-like structures. A thickness dependent

growth of elongated donor and acceptor islands was as well observed for DIP-C_{60} blends [187]. If these columnar structures are available for direct percolation paths through the device, the anisotropic charge transport might improve the solar cell. In order to study if the C_{60} agglomerates exhibit column-like growth in the blend, electron tomography was carried out on a heated F_4ZnPc:C_{60} blend deposited on PEDOT:PSS towards the end of this work. The reconstruction shows rather round, than column-like structures, however the result is not explicit. Further reconstruction algorithms need to be tested and implemented on the more relevant blends deposited on pristine donor or acceptor layers, which exceeds the framework of this thesis.

7.5. Proposed Model for the Solar Cell Functionality Based on Structural and Electronic Properties

The main findings of this chapter reveal for the first time a consistent picture for the structure-function-relationship of small molecule solar cells:

- Strong phase separation, mainly driven by agglomeration of the fullerene, occurs only if the substrate is heated (100°C) during co-evaporation of the donor and acceptor molecules.
- Phase separation is not a sufficient prerequisite for improved device performance, as no difference in the efficiency of non-inverted, heated or unheated, devices was observed.
- The key factor for enhanced device performance are crystalline C_{60} domains, which provide delocalized, band-like CT states. These high-energy electronic states of the fullerene are crucial for efficient exciton dissociation into free charge carriers.
- Pronounced crystalline fullerene domains are only observed in blends deposited on heated, pure C_{60}, as the pristine layer is assumed to provide crystallization seeds for the acceptor. This leads for the first time to the conclusion that significant improvement in the solar cell performance is only achieved for devices in an inverted architecture.

A conclusive schematic of the results from this thesis on F_4ZnPc:C_{60} solar cells is given in figure 7.24.

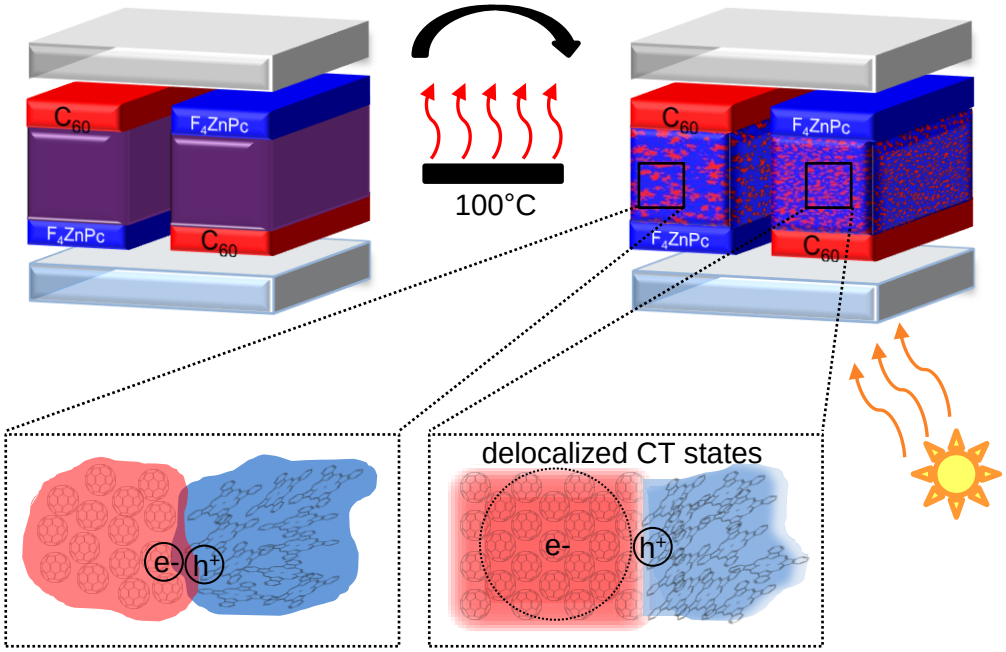

Figure 7.24: Graphical abstract based on the findings from this chapter.

8. Conclusion and Outlook

Within the scope of this work a novel correlation between the structural and electronic properties of organic semiconductors was presented. The crystallinity and absorption behavior of the films from TEM/EELS measurements were directly compared with the functionality of different types of devices.

In a preparatory study on the impact of beam damage on the material properties, the investigated polymers and small molecules were found to be sufficiently stable for energy filtered TEM image series, which require a high electron dose of up to $10^6\,\mathrm{e/nm^2}$. Especially, the collective plasmon excitation, which is mostly used for the discrimination of different organic compounds, did not exhibit any changes in shape and intensity upon beam exposure. Furthermore, it was shown that the dielectric function and the band gap derived from EELS are in good agreement with optical measurements from the literature, which is an additional proof for the sustained intrinsic properties of the materials in the TEM. Finally, it could be also demonstrated that EELS is a suitable technique for the determination of optical constants up to a high energy range.

As P3HT is a well known and widely used model system, at the beginning of this thesis TEM measurements on solution processed P3HT layers were carried out with the aim to establish new experimental techniques. It was found that the amount of ordered domains in the films depends on the annealing temperature and the molecular weight of the polymer, which however does not affect the spectroscopic properties measured with EELS. Furthermore, electron diffraction measurements showed that ordered domains are surrounded by amorphous material. Mobility measurements along the substrate and perpendicular to the substrate in two different setups (CELIV and OFET) indicated anisotropic charge transport in agreement with theoretical calculations from the literature. The TEM measurements could not unravel completely the direct impact of film morphology on the charge transport as P3HT exhibits a locally dependent and strongly varying morphology due to the mixture of crystalline and amorphous domains. These results point out the relevance of controlling the long-range order in high performance materials. Therefore, ongoing research focuses on single crystalline structures yielding fast charge transport of e.g. up to $8.6\,\mathrm{cm^2/Vs}$, as recently reported for air stable n-type

OFETs [238]. However, polymorphism effects, which have a great impact on the charge transport properties in organic thin films, make single crystal growth in the individual pure phase still very challenging [238]. Hence, a simple processing technique for organic single crystal growth is still a matter of interest [239, 240].

Moreover, P3HT doped with F_4TCNQ was investigated by means of TEM and IR spectroscopy. Electron diffraction measurements revealed a novel crystal structure of P3HT upon doping, that points at the formation of a charge transfer complex. This conjecture was supported by high resolution EEL spectra that indicated additional peaks at low energy losses such as 0.6 eV and 1.5 eV, which cannot be assigned to the pristine compounds. IR measurements confirmed the existence of a wide absorption band in doped P3HT at 0.5 eV, which can be attributed to an excitation of the charge transfer complex or to a polaron absorption of P3HT. Furthermore, it was found from DFT calculations that the vibration frequency of the CN-stretching mode in F_4TCNQ shifts linearly with the degree of charge transfer. The shift determined from IR measurements hinted at a charge transfer exceeding one electron per acceptor molecule, which was attributed to the crystalline texture of P3HT from the TEM measurements. This was reported for the first time. The high order might enable a charge transfer to the acceptor of more than one electron. Due to the low reproducibility of P3HT films, the influence on the degree of charge transfer with varying degree of crystallinity and distinct doping concentration could not be further studied. The morphology of the supposed model system P3HT turned out to be difficult to control. Hence, the structure-function relationship is not completely clear. Controlling the crystallinity in solution processed films will remain a matter of concern. Especially, solution doping is of great interest for highly conductive layers in possible applications such as printed devices and circuits [164, 241, 242]. Additionally, as there is still a lack of comprehensive understanding of some of the underlying processes, molecular doping is of high relevance in ongoing fundamental research [243].

In the last part of this thesis the influence of the active layer morphology on the solar cell performance of F_4ZnPc:C_{60} small molecule bulk heterojunctions (BHJ) was investigated. The aim of the measurements was to address the question often discussed in the literature whether substrate heating during evaporation enhances the device efficiency. It was found that the pristine donor and acceptor exhibit a polycrystalline structure, which is not significantly affected by substrate heating. The determined excitations from the EEL spectra of the pure materials are distinct. Especially the shift between the maximum plasmon energy of F_4ZnPc and C_{60} turned out to be pivotal for the distinction of the materials in blends from energy filtered TEM (EFTEM)

images. To ensure comparability between the structural and device properties, the BHJs for TEM were evaporated on a pristine F_4ZnPc and C_{60} layer as also used in devices with non-inverted (on F_4ZnPc) and inverted (on C_{60}) device architecture. For both types of blends EFTEM measurements indicated homogenous mixing when evaporated on substrates at room temperature and pronounced phase separation on heated substrates. The non-inverted devices in this thesis, however, did not show any improvement in the device performance when processed on heated substrates. It was demonstrated that the effect of substrate heating on the efficiency of small molecule solar cells is more subtle than previously believed: higher molecular diffusion at elevated temperature promotes phase separation in the BHJ, but does not necessarily lead to an enhanced efficiency. A two-phase segmentation in F_4ZnPc- and C_{60}-rich domains from a detailed analysis of the EFTEM image stacks revealed smaller but probably more pure C_{60} agglomerates in the blend on C_{60}.

The large, segregated domains in the blend on F_4ZnPc were found to exceed the reported exciton diffusion lengths for the investigated materials [25], which might be a reason for the lack of improvement of the heated device. As TEM measurements represent a projection of the entire bulk, electron tomography will help in future experiments for the 3D reconstruction and the exact domain distribution in the blends. Additionally, it was observed that the phase separated areas are still largely amorphous if the BHJ is grown on F_4ZnPc. If grown on a pristine C_{60} layer, as it is typically the case for inverted devices, the blend exhibits substrate-induced local fullerene ordering. These highly pure and ordered fullerene domains improve free charge carrier generation and hence device efficiency. Based on the findings from this thesis, it is explained for the first time why record efficiencies of 8.3 % in single junction cells are only achieved in inverted device architecture [8]. Moreover, these results clarify why literature reports on the effect of substrate heating on the efficiency of small molecule BHJs with fullerene as acceptor show mixed results. The underlayer used in the actual devices, which is proven to be essential by this thesis, has not been considered in any reports on the structural properties of small molecule BHJs so far. This underlines the unique feature of this work, in which TEM measurements were performed on the actual device structures and compared with complementary measurements on identically processed samples.

In addition, the findings from F_4ZnPc:C_{60} blends might point to a new direction in organic photovoltaic development. A device architecture and material combination that allows not only the acceptor, but also the donor in the BHJ to form highly ordered domains, would partially overcome the disorder related loss in the open circuit voltage in organic solar cells [244]. However, it is important that the band gap does not decrease with increasing

order. This is the case for C_{60} and might also lead to a lower V_{oc}.

Recently, it was reported on covalent organic frameworks, which represent open lattice structures and allow the integration of donor-acceptor heterojunctions into periodic columnar arrays in thin films [245]. Such structures meet the requirement for ordered donor and acceptor domains and will possibly find soon application in organic solar cells.

A further approach for improving the device performance is replacing the fullerene. Fullerene is relatively expensive in production and limits the photocurrent generation due to its rather low absorption of the solar spectrum. Cnops et al. presented a non-fullerene small molecule solar cell based on two acceptors, subphtalocyanine and subnaphtalocyanine, and α-6T as donor [246]. The three layer device architecture enables a two-step exciton dissociation process, such that excitons generated in the first acceptor layer (wide-bandgap) are transferred to the second acceptor layer with a smaller band gap (Förster energy transfer) [246]. Subsequently, the exciton dissociation occurs at the donor interface. The presented solar cell architecture exhibits a record efficiency of 8.4 % and demonstrates an important alternative to the conventional devices investigated in this thesis [246]. However, it is not clear to what extend the morphology is involved in the functionality of this type of devices. The investigation of the layer crystallinity is fundamental as ordered domains could possibly lead to even higher device efficiencies.

In conclusion, the present work highlights the potential of analytical TEM for unraveling the nanoscale morphology in organic thin films. As demonstrated in this thesis, the morphology and especially crystallinity has a great impact on the performance of any type of organic devices. To enable a direct correlation to the electrical properties, it is important that TEM measurements are performed on the actual device structures. Combined with electrical characterization, analytical TEM is a very powerful technique for the investigation of the structure-function relationship in devices. It will hopefully contribute to a better understanding of the fundamental processes in organic semiconductors, which will help to fully exploit the potential of organic electronic devices.

A. Appendix

Comparison between floated and evaporated samples

In figure A.1 BFTEM images of pristine F_4ZnPc deposited at 100 °C, floated (a) and deposited directly on a TEM grid (b), are shown. The films exhibit similar texture. Due to a slight drift during image acquisition of the floated sample (a) the features are blurry. In the EEL spectra shown in c) both samples exhibit the same features. The spectrum of the evaporated sample (red) exhibits less pronounced features because (i) the sample is probably thinner due to shadowing effects during evaporation on the grid (ii) the amorphous grid layer causes a stronger background.

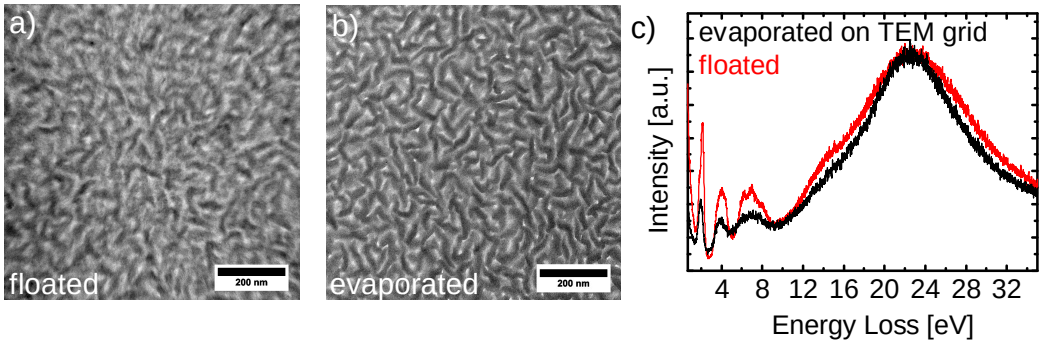

Figure A.1: BFTEM images of pristine F_4ZnPc deposited at 100 °C a) on PEDOT:PSS and floated off the substrate and b) deposited directly onto a SiN TEM grid. c) EEL spectra of the evaporated (black) and floated (red) sample.

Focused Ion Beam (FIB) milled cross sections

In figure A.2 a)-c) the EFTEM images at 28 eV energy loss (high plasmon intensity of PCBM) show cross sections of differently prepared P3HT/PCBM bilayers. In all samples the two layers are clearly distinguishable.

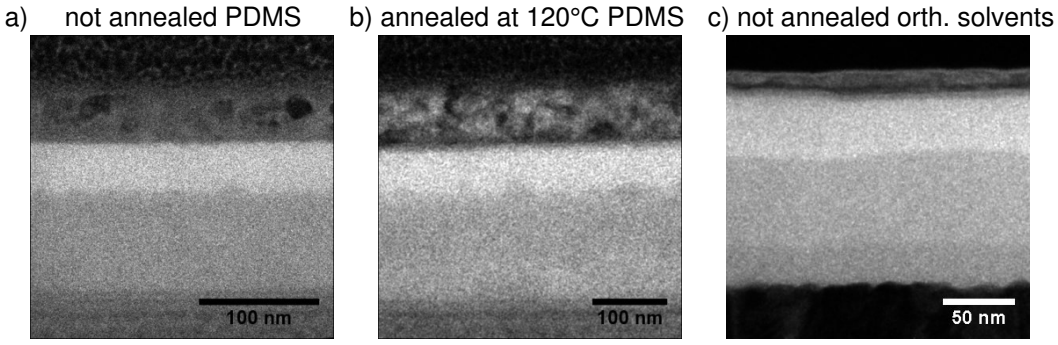

Figure A.2: EFTEM images at 28 eV energy loss of FIB milled cross sections of P3HT/PCBM bilayers. a) PCBM stamped (by a PDMS stamp) on top of P3HT and not annealed. b) PCBM stamped on top of P3HT and annealed at 120 °C for 10 min. c) PCBM spin coated on top of P3HT from a dichlormethane solution. The PCBM layer appears bright as the plasmon excitation of PCBM exhibits high intensity at 28 eV energy loss. Due to annealing the interface in b) is soaked.

Reproducibility of F_4ZnPc:C_{60} samples

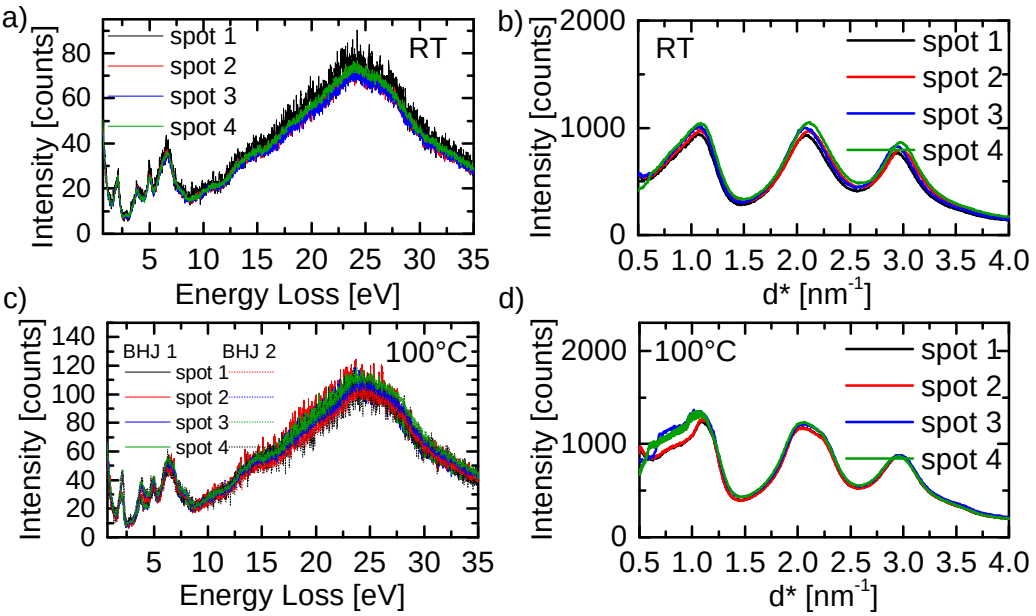

Figure A.3: EELS and electron diffraction measured on different spots of a blend deposited on PEDOT:PSS at RT (a and b) and at 100 °C (c and d).

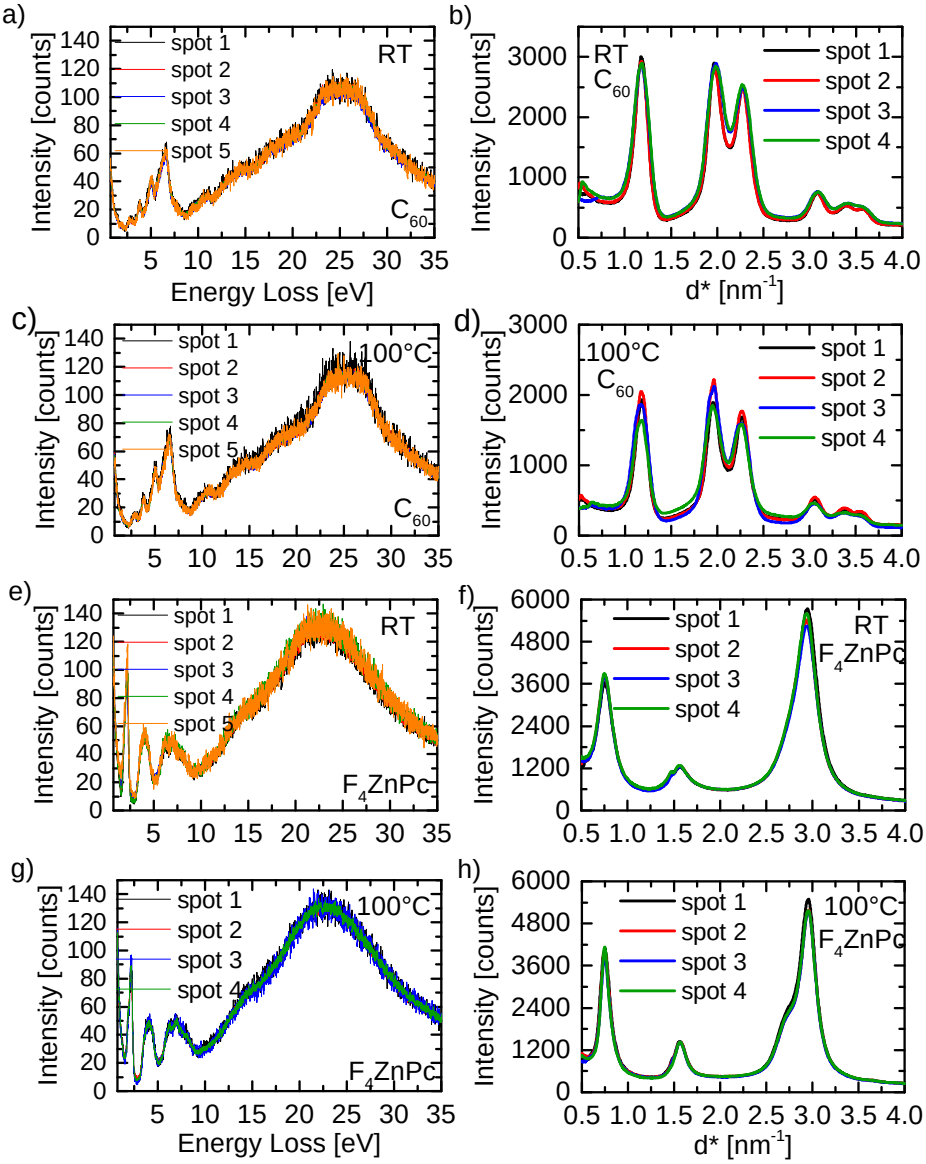

Figure A.4: EELS and electron diffraction measured on different spots of a pristine C_{60} layer deposited at RT (a and b), at 100 °C (c and d) and of a pristine F_4ZnPc layer deposited at RT (e and f) and at 100 °C (g and h).

Linear combination of EEL spectra

A good agreement between the linear combination (black) and the measured BHJ spectrum (orange) is noted for all samples in figure A.6 a)-c). In d) the results from diffraction measurements on the slow evaporated BHJ are shown.

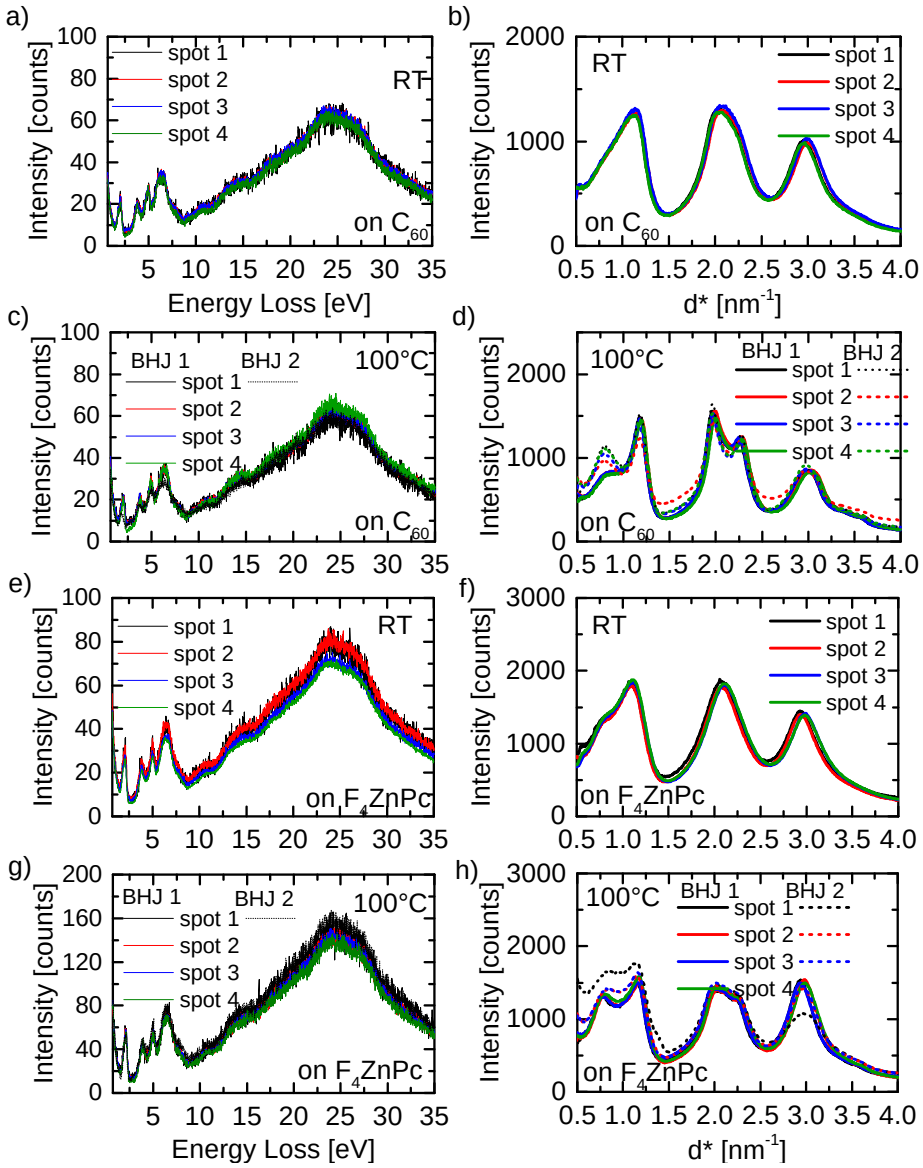

Figure A.5: EELS and electron diffraction measured on different spots of a blend deposited on C_{60} at RT (a and b), at 100 °C (c and d) and of a blend deposited on F_4ZnPc at RT (e and f) and at 100 °C (g and h).

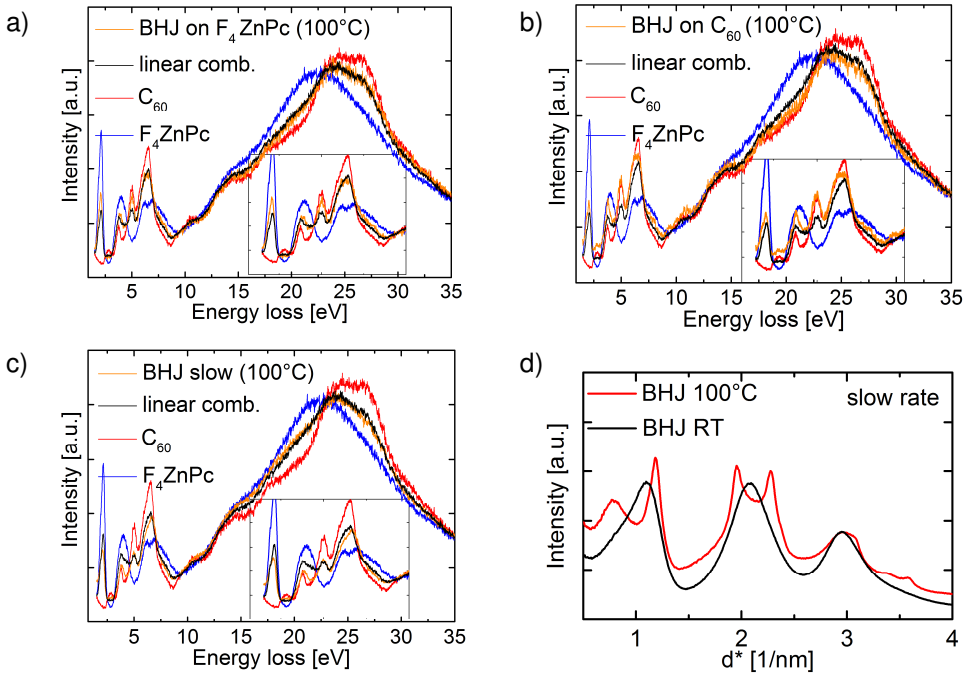

Figure A.6: EEL spectra of BHJs deposited at 100 °C (orange) and the linear combination (black) of pristine F_4ZnPc (blue) and C_{60}(red) spectra for BHJs deposited a) on F_4ZnPc, b) on C_{60} and c) on PEDOT:PSS (slow). The inset shows the low loss regime between 0 eV and 10 eV. c) Radial profiles of the slowly evaporated BHJ on PEDOT:PSS at RT (black) and 100 °C (red). Due to the strong phase separation, the heated sample exhibits high crystallinity.

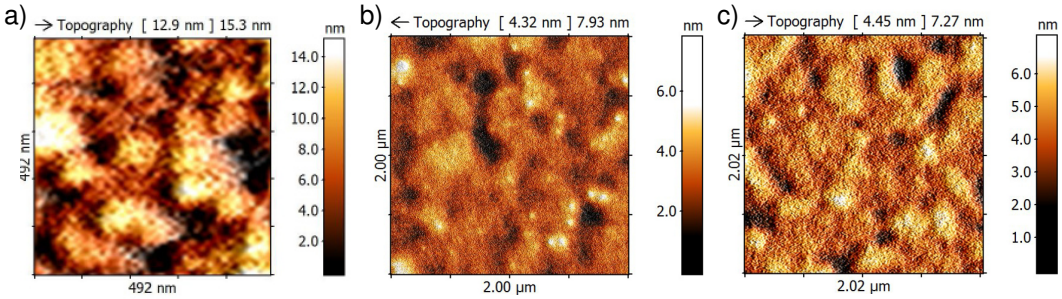

Figure A.7: AFM images of a) BHJ deposited with a slow evaporation rate on PEDOT:PSS indicating a rough surface, b) a BHJ deposited on F_4ZnPc at RT and c) a BHJ deposited on F_4ZnPc at 100 °C. Both BHJs on F_4ZnPc show a comparable surface roughness.

Segmentations from ESI series

Figure A.8 a) shows the plasmon peak map of the blend deposited on C_{60} at RT. As can be seen from the spectra in b) there is no hint for phase separated domains. LLE segmentations of heated blends are shown in figure A.9.

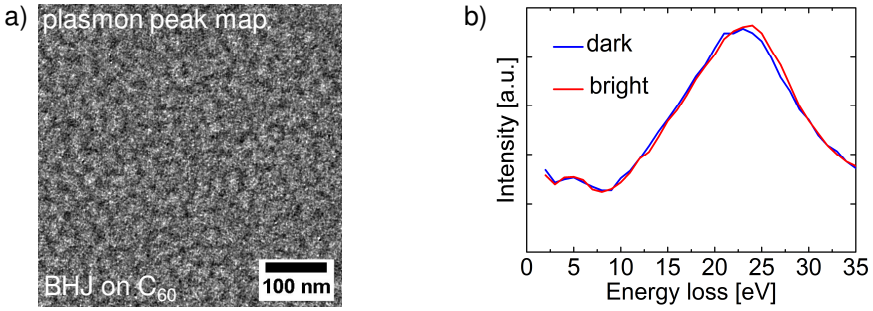

Figure A.8: a) Plasmon peak map extracted from the ESI series of the BHJ deposited on C_{60} at RT. b) Energy loss spectra from bright and dark appearing regions. The spectra are not clearly distinguishable, hence there is no phase separation in the BHJ.

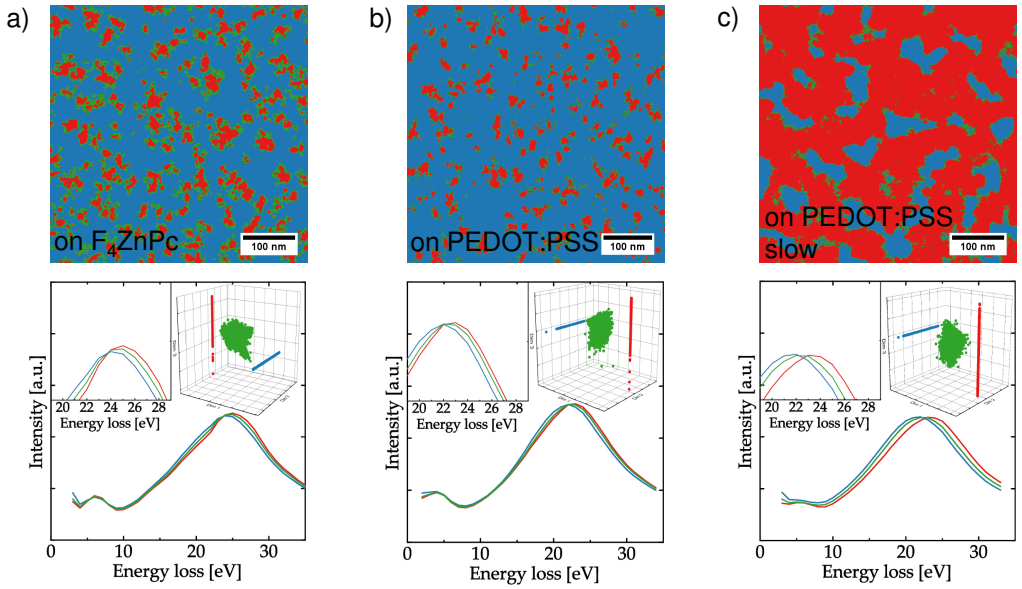

Figure A.9: LLE segmentations of blends deposited at 100 °C on different substrates. a) BHJ on F_4ZnPc with ratios: C_{60} (red) 14.9 % , F_4ZnPc (blue) 66.5 %, mixed (green) 18.6 %. b) BHJ on PEDOT:PSS: C_{60} (red) 11.8 % , F_4ZnPc (blue) 81.4 %, mixed (green) 6.8 %. c) BHJ on PEDOT:PSS (slow evaporation rate): C_{60} (red) 74.6 % , F_4ZnPc (blue) 18.6 %, mixed (green) 6.8 %.

Bibliography

[1] M. Pope, H. P. Kallmann, and P. Magnante. Electroluminescence in organic crystals. *The Journal of Chemical Physics*, 38(8), 1963.

[2] Hideki Shirakawa, Edwin J. Louis, Alan G. MacDiarmid, Chwan K. Chiang, and Alan J. Heeger. Synthesis of electrically conducting organic polymers: halogen derivatives of polyacetylene, (ch). *J. Chem. Soc., Chem. Commun.*, pages 578–580, 1977.

[3] C. W. Tang. Two-layer organic photovoltaic cell. *Applied Physics Letters*, 48(2):183–185, January 1986.

[4] Ching W Tang and SA VanSlyke. Organic electroluminescent diodes. *Applied physics letters*, 51(12):913–915, 1987.

[5] WK Kwak, KH Lee, CY Oh, HJ Lee, SA Yang, HE Shin, and HK Chung. 9.2: A 5.0-in wvga amoled display for pdas. In *SID Symposium Digest of Technical Papers*, volume 34, pages 100–103. Wiley Online Library, 2003.

[6] Sabine Ludwigs. *P3HT Revisited – From Molecular Scale to Solar Cell Devices*. Springer, November 2014.

[7] Pabitra K Nayak and David Cahen. Updated assessment of possibilities and limits for solar cells. *Advanced Materials*, 26(10):1622–1628, 2014.

[8] Rico Meerheim, Christian Koerner, and Karl Leo. Highly efficient organic multi-junction solar cells with a thiophene based donor material. *Applied Physics Letters*, 105(6):–, 2014.

[9] Masahiro Hiramoto, Hiroshi Fujiwara, and Masaaki Yokoyama. Three-layered organic solar cell with a photoactive interlayer of codeposited pigments. *Applied physics letters*, 58(10):1062–1064, 1991.

[10] Peter Peumans, Soichi Uchida, and Stephen R. Forrest. Efficient bulk heterojunction photovoltaic cells using small-molecular-weight organic thin films. *Nature*, 425(6954):158–162, September 2003.

[11] Kerstin Schulze, Christian Uhrich, Rico Schüppel, Karl Leo, Martin Pfeiffer, Eduard Brier, Egon Reinold, and Peter Baeuerle. Efficient vacuum-deposited organic solar cells based on a new low-bandgap oligothiophene and fullerene c60. *Advanced Materials*, 18(21):2872–2875, 2006.

[12] Steffen Pfuetzner, Christine Mickel, Jens Jankowski, Moritz Hein, Jan Meiss, Christoph Schuenemann, Chris Elschner, Alexandr A. Levin, Bernd Rellinghaus, Karl Leo, and Moritz Riede. The influence of substrate heating on morphology and layer growth in c60:ZnPc bulk heterojunction solar cells. *Organic Electronics*, 12(3):435–441, March 2011.

[13] Christoph Schünemann, David Wynands, Lutz Wilde, Moritz Hein, Steffen Pfützner, Chris Elschner, Klaus-Jochen Eichhorn, Karl Leo, and Moritz Riede. Phase separation analysis of bulk heterojunctions in small-molecule organic solar cells using zinc-phthalocyanine and c60. *Physical Review B*, 85(24):245314, June 2012.

[14] S. Ouro Djobo, L. Cattin, M. Morsli, A. Godoy, F. R. Diaz, M. A. del Valle, J. C. Bernede, P. Predeep, Mrinal Thakur, and M. K. Ravi Varma. Effect of the substrate temperature on the performance of small molecule organic solar cells. pages 251–253, 2011.

[15] Barry P. Rand, David Cheyns, Karolien Vasseur, Noel C. Giebink, Sébastien Mothy, Yuanping Yi, Veaceslav Coropceanu, David Beljonne, Jérôme Cornil, Jean-Luc Brédas, and Jan Genoe. The impact of molecular orientation on the photovoltaic properties of a phthalocyanine/fullerene heterojunction. *Advanced Functional Materials*, 22(14):2987–2995, 2012.

[16] Antti Ojala, Andreas Petersen, Andreas Fuchs, Robert Lovrincic, Carl Pölking, Jens Trollmann, Jaehyung Hwang, Christian Lennartz, Helmut Reichelt, Hans Wolfgang Höffken, et al. Merocyanine/c60 planar heterojunction solar cells: effect of dye orientation on exciton dissociation and solar cell performance. *Advanced Functional Materials*, 22(1):86–96, 2012.

[17] Martin Pfannmöller, Harald Flügge, Gerd Benner, Irene Wacker, Christoph Sommer, Michael Hanselmann, Stephan Schmale, Hans Schmidt, Fred A. Hamprecht, Torsten Rabe, Wolfgang Kowalsky, and Rasmus R. Schröder. Visualizing a homogeneous blend in bulk heterojunction polymer solar cells by analytical electron microscopy. *Nano Letters*, 11(8):3099–3107, August 2011.

[18] B. Bernardo, D. Cheyns, B. Verreet, R. D. Schaller, B. P. Rand, and N. C. Giebink. Delocalization and dielectric screening of charge transfer states in organic photovoltaic cells. *Nature Communications*, 5, February 2014.

[19] Brett M. Savoie, Akshay Rao, Artem A. Bakulin, Simon Gelinas, Bijan Movaghar, Richard H. Friend, Tobin J. Marks, and Mark A. Ratner. Unequal partnership: Asymmetric roles of polymeric donor and fullerene acceptor in generating free charge. *Journal of the American Chemical Society*, 136(7):2876–2884, 2014.

[20] Simon Gélinas, Akshay Rao, Abhishek Kumar, Samuel L. Smith, Alex W. Chin, Jenny Clark, Tom S. van der Poll, Guillermo C. Bazan, and Richard H. Friend. Ultrafast long-range charge separation in organic semiconductor photovoltaic diodes. *Science*, 343(6170):512–516, January 2014.

[21] W. Demtröder. *Atome, Moleküle und Festkörper*. Springer-Verlag, Berlin Heidelberg, 2005.

[22] W. Brütting. *Physics of Organic Semiconductors*. Wiley VCH Verlag, 2005.

[23] J. Frenkel. On the transformation of light into heat in solids. i. *Phys. Rev.*, 37:17–44, Jan 1931.

[24] Letian Dou, Jingbi You, Ziruo Hong, Zheng Xu, Gang Li, Robert A. Street, and Yang Yang. 25th anniversary article: A decade of organic/polymeric photovoltaic research. *Advanced Materials*, 25(46):6642–6671, 2013.

[25] Peter Peumans, Aharon Yakimov, and Stephen R. Forrest. Small molecular weight organic thin-film photodetectors and solar cells. *Journal of Applied Physics*, 93(7):3693, 2003.

[26] G. Yu, J. Gao, J. C. Hummelen, F. Wudl, and A. J. Heeger. Polymer photovoltaic cells: Enhanced efficiencies via a network of internal donor-acceptor heterojunctions. *Science*, 270(5243):1789–1791, December 1995.

[27] Pabitra K. Nayak, K. L. Narasimhan, and David Cahen. Separating charges at organic interfaces: Effects of disorder, hot states, and electric field. *The Journal of Physical Chemistry Letters*, 4(10):1707–1717, 2013.

[28] Harald Hoppe and Niyazi Serdar Sariciftci. Organic solar cells: An overview. *Journal of Materials Research*, 19(07):1924–1945, 2004.

[29] Y. Zhou, C. Fuentes-Hernandez, J. Shim, J. Meyer, A. J. Giordano, H. Li, P. Winget, T. Papadopoulos, H. Cheun, J. Kim, M. Fenoll, A. Dindar, W. Haske, E. Najafabadi, T. M. Khan, H. Sojoudi, S. Barlow, S. Graham, J.-L. Bredas, S. R. Marder, A. Kahn, and B. Kippelen. A universal method to produce low-work function electrodes for organic electronics. *Science*, 336(6079):327–332, April 2012.

[30] Christian Koerner. Oligothiophene materials for organic solar cells, photophysics and device properties, 2012.

[31] Dirk Veldman, Stefan C. J. Meskers, and Rene A. J. Janssen. The energy of charge-transfer states in electron donor acceptor blends: Insight into the energy losses in organic solar cells. *Advanced Functional Materials*, 19(12):1939–1948, 2009.

[32] Charles L. Braun. Electric field assisted dissociation of charge transfer states as a mechanism of photocarrier production. *The Journal of Chemical Physics*, 80(9):4157–4161, May 1984.

[33] Chengmei Zhong, Hyosung Choi, Jin Young Kim, Han Young Woo, Thanh Luan Nguyen, Fei Huang, Yong Cao, and Alan J. Heeger. Ultrafast charge transfer in operating bulk heterojunction solar cells. *Advanced Materials*, pages n/a–n/a, 2015.

[34] Artem A Bakulin, Akshay Rao, Vlad G Pavelyev, Paul HM van Loosdrecht, Maxim S Pshenichnikov, Dorota Niedzialek, Jérôme Cornil, David Beljonne, and Richard H Friend. The role of driving energy and delocalized states for charge separation in organic semiconductors. *Science*, 335(6074):1340–1344, 2012.

[35] Carsten Deibel and Vladimir Dyakonov. Polymer–fullerene bulk heterojunction solar cells. *Reports on Progress in Physics*, 73(9):096401, September 2010.

[36] Felix Schell. Morphology of small molecule organic solar cells from transmission electron microscopy, 2014.

[37] Pabitra K Nayak, Germà Garcia-Belmonte, Antoine Kahn, Juan Bisquert, and David Cahen. Photovoltaic efficiency limits and material disorder. *Energy & Environmental Science*, 5(3):6022–6039, 2012.

[38] James C Blakesley and Dieter Neher. Relationship between energetic disorder and open-circuit voltage in bulk heterojunction organic solar cells. *Physical Review B*, 84(7):075210, 2011.

[39] H. Baessler. Charge transport in disordered organic photoconductors a monte carlo simulation study. *physica status solidi (b)*, 175(1):15–56, 1993.

[40] Alexander Hinderhofer and Frank Schreiber. Organic organic heterostructures: Concepts and applications. *ChemPhysChem*, 13(3):628–643, February 2012.

[41] Ray F. Egerton. *Electron Energy-Loss Spectroscopy in the Electron Microscope*. Springer Science+Business Media, New York, Dodrecht, Heidelberg, London, third edition edition, 1996.

[42] JP Langmore, J Wall, and MS Isaacson. Collection of scattered electrons in dark field electron-microscopy. 1. elastic-scattering. *Optik*, 38(4):335–350, 1973.

[43] Siegfried Hunklinger. *Festkörperphysik*. Oldenbourg Verlag, 2007.

[44] David B Williams and C. Barry Carter. *Transmission Electron Microscopy*. Springer Science+Business Media, New York, 2009.

[45] RH Ritchie. Plasma losses by fast electrons in thin films. *Physical Review*, 106(5):874, 1957.

[46] L. Reimer and H. Kohl. *Transmission Electron Microscopy*. New York:Springer, 2008.

[47] Isabel Angert, Christoph Burmester, Christoph Dinges, Harald Rose, and Rasmus R. Schröder. Elastic and inelastic scattering cross-sections of amorphous layers of carbon and vitrified ice. *Ultramicroscopy*, 63(3):181–192, July 1996.

[48] R. H. Wade. A brief look at imaging and contrast transfer. *Ultramicroscopy*, 46(1):145–156, October 1992.

[49] O. Scherzer. Über einige fehler von elektronenlinsen. *Zeitschrift für Physik*, 101(9-10):593–603, September 1936.

[50] www.ceos-gmbh.de/literature.

[51] David J. Smith. Development of aberration-corrected electron microscopy. *Microscopy and Microanalysis*, 14(01):2–15, February 2008.

[52] Christoph Weißbäcker and Harald Rose. Electrostatic correction of the chromatic and of the spherical aberration of charged-particle lenses. *Journal of Electron Microscopy*, 50(5):383–390, January 2001.

[53] Nicole Frindt, Marco Oster, Simon Hettler, Björn Gamm, Levin Dieterle, Wolfgang Kowalsky, Dagmar Gerthsen, and Rasmus R. Schröder. In-focus electrostatic zach phase plate imaging for transmission electron microscopy with tunable phase contrast of frozen hydrated biological samples. *Microscopy and Microanalysis*, 20(01):175–183, February 2014.

[54] Katrin Schultheiss, Joachim Zach, Bjoern Gamm, Manuel Dries, Nicole Frindt, Rasmus R. Schröder, and Dagmar Gerthsen. New electrostatic phase plate for phase-contrast transmission electron microscopy and its application for wave-function reconstruction. *Microscopy and Microanalysis*, 16(06):785–794, December 2010.

[55] R. F. Egerton. Electron energy-loss spectroscopy in the TEM. *Reports on Progress in Physics*, 72(1):016502, January 2009.

[56] Martin Pfannmöller. *Visualisierung von Nanostrukturen in organischen, photoaktiven Mischsystemen durch dreidimensionale analytische Elektronenmikroskopie*. PhD thesis, Cuvillier, E, Göttingen, September 2013.

[57] Matlab programs from EELS in the electron microscope 3rd edition, March 2012.

[58] M. Stoeger-Pollach, H. Franco, P. Schattschneider, S. Lazar, B. Schaffer, W. Grogger, and H.W. Zandbergen. Cerenkov losses: A limit for bandgap determination and kramers kronig analysis. *Micron*, 37(5):396 – 402, 2006. Proceedings of the International Workshop on Enhanced Data Generated with Electrons (EDGE).

[59] L. Reimer. Energy-filtering transmission electron microscopy. In Peter W. Hawkes, editor, *Advances in Electronics and Electron Physics*, volume Volume 81, pages 43–126. Academic Press, 1991.

[60] D. A. Muller and J. Silcox. Delocalization in inelastic scattering. *Ultramicroscopy*, 59(1–4):195–213, July 1995.

[61] Werner Grogger, Maria Varela, Roger Ristau, Bernhard Schaffer, Ferdinand Hofer, and Kannan M. Krishnan. Energy-filtering transmission electron microscopy on the nanometer length scale. *Journal of Electron Spectroscopy and Related Phenomena*, 143(2–3):139–147, May 2005.

[62] Bernhard Schaffer, Gerald Kothleitner, and Werner Grogger. EFTEM spectrum imaging at high-energy resolution. *Ultramicroscopy*, 106(11–12):1129–1138, October 2006.

[63] Bernhard Schaffer, Werner Grogger, Gerald Kothleitner, and Ferdinand Hofer. Application of high-resolution EFTEM SI in an AEM. *Analytical and Bioanalytical Chemistry*, 390(6):1439–1445, March 2008.

[64] Wolfram Schindler. *TEM-Plasmonenkartierung des Donator-Akzeptor-Heterokontakts in organischen Solarzellen*. PhD thesis, FU Berlin, August 2012.

[65] Wolfram Schindler, Markus Wollgarten, and Konstantinos Fostiropoulos. Revealing nanoscale phase separation in small-molecule photovoltaic blends by plasmonic contrast in the TEM. *Organic Electronics*, 13(6):1100–1104, June 2012.

[66] A threshold selection method from gray-level histograms. *IEEE Transactions on Systems, Man and Cybernetics*, 9(1):62–66, January 1979.

[67] S. T. Roweis. Nonlinear dimensionality reduction by locally linear embedding. *Science*, 290(5500):2323–2326, December 2000.

[68] C. Sommer, C. Straehle, U. Kothe, and F.A. Hamprecht. Ilastik: Interactive learning and segmentation toolkit. In *2011 IEEE International Symposium on Biomedical Imaging: From Nano to Macro*, pages 230–233, March 2011.

[69] Leo Breiman. Random forests. *Machine Learning*, 45(1):5–32, October 2001.

[70] A. J. Mozer, N. S. Sariciftci, L. Lutsen, D. Vanderzande, R. Österbacka, M. Westerling, and G. Juška. Charge transport and recombination in bulk heterojunction solar cells studied by the photoinduced charge extraction in linearly increasing voltage technique. *Applied Physics Letters*, 86(11):112104, March 2005.

[71] G. Juška, K. Arlauskas, M. Viliūnas, and J. Kovčka. Extraction current transients: New method of study of charge transport in microcrystalline silicon. *Physical review letters*, 84(21):4946, 2000.

[72] Sebastian Bange, Marcel Schubert, and Dieter Neher. Charge mobility determination by current extraction under linear increasing voltages: Case of nonequilibrium charges and field-dependent mobilities. *Physical Review B*, 81(3), January 2010.

[73] Carsten Deibel. Charge carrier dissociation and recombination in polymer solar cells. *physica status solidi (a)*, 206(12):2731–2736, 2009.

[74] Carsten Leinweber. Untersuchung der transporteigenschaften von organischen halbleitern mittls CELIV, 2013.

[75] G. Juška, K. Arlauskas, M. Viliūnas, and J. Kočka. Extraction current transients: New method of study of charge transport in microcrystalline silicon. *Physical Review Letters*, 84(21):4946–4949, May 2000.

[76] A. Baumann, J. Lorrmann, D. Rauh, C. Deibel, and V. Dyakonov. A new approach for probing the mobility and lifetime of photogenerated charge carriers in organic solar cells under real operating conditions. *Advanced Materials*, 24(32):4381–4386, 2012.

[77] Jens Lorrmann, Bekele Homa Badada, O. Inganas, Vladimir Dyakonov, and Carsten Deibel. Charge carrier extraction by linearly increasing voltage: Analytic framework and ambipolar transients. *Journal of Applied Physics*, 108(11):113705–113705, 2010.

[78] Lars Mueller. Charge transport in organic solar cells studied by (photo-) CELIV, 2014.

[79] D. J. Gundlach, L. Zhou, J. A. Nichols, T. N. Jackson, P. V. Necliudov, and M. S. Shur. An experimental study of contact effects in organic thin film transistors. *Journal of Applied Physics*, 100(2):024509, July 2006.

[80] Weiying Gao and Antoine Kahn. Controlled p-doping of zinc phthalocyanine by coevaporation with tetrafluorotetracyanoquinodimethane: A direct and inverse photoemission study. *Applied Physics Letters*, 79(24):4040–4042, 2001.

[81] Ze-Lei Guan, Jong Bok Kim, He Wang, Cherno Jaye, Daniel A. Fischer, Yueh-Lin Loo, and Antoine Kahn. Direct determination of the electronic

structure of the poly(3-hexylthiophene):phenyl-[6,6]-c61 butyric acid methyl ester blend. *Organic Electronics*, 11(11):1779–1785, November 2010.

[82] Gang Li, Vishal Shrotriya, Jinsong Huang, Yan Yao, Tom Moriarty, Keith Emery, and Yang Yang. High-efficiency solution processable polymer photovoltaic cells by self-organization of polymer blends. *Nature Materials*, 4(11):864–868, November 2005.

[83] Zhenan Bao, Ananth Dodabalapur, and Andrew J. Lovinger. Soluble and processable regioregular poly(3hexylthiophene) for thin film fieldeffect transistor applications with high mobility. *Applied Physics Letters*, 69(26):4108–4110, December 1996.

[84] P. Pingel and D. Neher. Comprehensive picture of p-type doping of p3ht with the molecular acceptor f4tcnq. *Physical Review B*, 87(11):115209, March 2013.

[85] E. F. Aziz, A. Vollmer, S. Eisebitt, W. Eberhardt, P. Pingel, D. Neher, and N. Koch. Localized charge transfer in a molecularly doped conducting polymer. *Advanced Materials*, 19(20):3257–3260, 2007.

[86] Lingyun Zhu, Eung-Gun Kim, Yuanping Yi, and Jean-Luc Bredas. Charge transfer in molecular complexes with 2,3,5,6-tetrafluoro-7,7,8,8-tetracyanoquinodimethane (f4-TCNQ): A density functional theory study. *Chemistry of Materials*, 23(23):5149–5159, 2011.

[87] B. Maennig, J. Drechsel, D. Gebeyehu, P. Simon, F. Kozlowski, A. Werner, F. Li, S. Grundmann, S. Sonntag, M. Koch, K. Leo, M. Pfeiffer, H. Hoppe, D. Meissner, N. S. Sariciftci, I. Riedel, V. Dyakonov, and J. Parisi. Organic p-i-n solar cells. *Applied Physics A*, 79(1):1–14, June 2004.

[88] Wei Zhao and Antoine Kahn. Charge transfer at n-doped organic-organic heterojunctions. *Journal of Applied Physics*, 105(12), 2009.

[89] Jan Meiss, Andre Merten, Moritz Hein, Christoph Schuenemann, Stefan Schäfer, Max Tietze, Christian Uhrich, Martin Pfeiffer, Karl Leo, and Moritz Riede. Fluorinated zinc phthalocyanine as donor for efficient vacuum-deposited organic solar cells. *Advanced Functional Materials*, 22(2):405–414, January 2012.

[90] H. Brinkmann, C. Kelting, S. Makarov, O. Tsaryova, G. Schnurpfeil, D. Woehrle, and D. Schlettwein. Fluorinated phthalocyanines as molecular semiconductor thin films. *physica status solidi (a)*, 205(3):409–420, 2008.

[91] C. Schünemann, C. Elschner, A. A. Levin, M. Levichkova, K. Leo, and M. Riede. Zinc phthalocyanine — influence of substrate temperature, film thickness, and kind of substrate on the morphology. *Thin Solid Films*, 519(11):3939–3945, 2011.

[92] CC Wu, CI Wu, JC Sturm, and A Kahn. Surface modification of indium tin oxide by plasma treatment: An effective method to improve the efficiency, brightness, and reliability of organic light emitting devices. *Applied Physics Letters*, 70(11):1348–1350, 1997.

[93] Joachim Mayer, Lucille A. Giannuzzi, Takeo Kamino, and Joseph Michael. TEM sample preparation and FIB-induced damage. *MRS Bulletin*, 32(05):400–407, May 2007.

[94] N.D. Bassim, B.T. De Gregorio, A.L.D. Kilcoyne, K. Scott, T. Chou, S. Wirick, G. Cody, and R.M. Stroud. Minimizing damage during FIB sample preparation of soft materials: FIB SAMPLE PREPARATION OF SOFT MATERIALS. *Journal of Microscopy*, 245(3):288–301, March 2012.

[95] Rebecca Saive, Lars Mueller, Eric Mankel, Wolfgang Kowalsky, and Michael Kroeger. Doping of TIPS-pentacene via focused ion beam (FIB) exposure. *Organic Electronics*, 14(6):1570–1576, June 2013.

[96] L. A. Giannuzzi, B. W. Kempshall, S. M. Schwarz, J. K. Lomness, B. I. Prenitzer, and F. A. Stevie. FIB lift-out specimen preparation techniques. In Lucille A. Giannuzzi and Fred A. Stevie, editors, *Introduction to Focused Ion Beams*, pages 201–228. Springer US, January 2005.

[97] National Research Council (U S.) Committee on Nuclear Science. *Studies in Penetration of Charged Particles in Matter*. National Academies, 1964.

[98] Diana Nanova, Anne Katrin Kast, Martin Pfannmöller, Christian Müller, Lisa Veith, Irene Wacker, Michaela Agari, Wilfried Hermes, Peter Erk, Wolfgang Kowalsky, Rasmus R. Schröder, and Robert Lovrinčić. Unraveling the nanoscale morphologies of mesoporous perovskite solar cells and their correlation to device performance. *Nano Letters*, April 2014.

[99] R. W. Ditchfield, D. T. Grubb, and M. J. Whelan. Electron energy loss studies of polymers during radiation damage. *Philosophical Magazine*, 27(6):1267–1280, June 1973.

[100] Christian Krekeler. Personal communication, 2014.

[101] G. Grancini, M. De Bastiani, N. Martino, D. Fazzi, H.-J. Egelhaaf, T. Sauermann, M. R. Antognazza, G. Lanzani, M. Caironi, L. Franco, and A. Petrozza. The critical role of interfacial dynamics in the stability of organic photovoltaic devices. *Physical Chemistry Chemical Physics*, 16(18):8294–8300, April 2014.

[102] Andreas Distler, Peter Kutka, Tobias Sauermann, Hans-Joachim Egelhaaf, Dirk M. Guldi, Daniele Di Nuzzo, Stefan C. J. Meskers, and René A. J. Janssen. Effect of PCBM on the photodegradation kinetics of polymers for organic photovoltaics. *Chemistry of Materials*, 24(22):4397–4405, November 2012.

[103] Sergey Arnautov, Elena Nechvolodova, Sergei Lomakin, and Alexander Shchegolikhin. Photo- and thermal-oxidative stability of novel material for photovoltaics: MEH-PPV/TNF blends. *Renewable Energy*, 33(2):259–261, February 2008.

[104] H. Neugebauer, C. Brabec, J. C. Hummelen, and N. S. Sariciftci. Stability and photodegradation mechanisms of conjugated polymer/fullerene plastic solar cells. *Solar Energy Materials and Solar Cells*, 61(1):35–42, February 2000.

[105] Matthew O. Reese, Alexandre M. Nardes, Benjamin L. Rupert, Ross E. Larsen, Dana C. Olson, Matthew T. Lloyd, Sean E. Shaheen, David S. Ginley, Garry Rumbles, and Nikos Kopidakis. Photoinduced degradation of polymer and polymer–fullerene active layers: Experiment and theory. *Advanced Functional Materials*, 20(20):3476–3483, 2010.

[106] Sylvain Chambon, Agnès Rivaton, Jean-Luc Gardette, and Muriel Firon. Photo- and thermal degradation of MDMO-PPV:PCBM blends. *Solar Energy Materials and Solar Cells*, 91(5):394–398, March 2007.

[107] Thomas Tromholt, Morten Vesterager Madsen, Jon E. Carlé, Martin Helgesen, and Frederik C. Krebs. Photochemical stability of conjugated polymers, electron acceptors and blends for polymer solar cells resolved in terms of film thickness and absorbance. *Journal of Materials Chemistry*, 22(15):7592–7601, March 2012.

[108] Daniel Rhinow and Werner Kühlbrandt. Electron cryo-microscopy of biological specimens on conductive titanium–silicon metal glass films. *Ultramicroscopy*, 108(7):698–705, June 2008.

[109] Radosav S. Pantelic, Jannik C. Meyer, Ute Kaiser, and Henning Stahlberg. The application of graphene as a sample support in transmission electron microscopy. *Solid State Communications*, 152(15):1375–1382, August 2012.

[110] Jun-Jie Yin, Fang Lao, Peter P. Fu, Wayne G. Wamer, Yuliang Zhao, Paul C. Wang, Yang Qiu, Baoyun Sun, Gengmei Xing, Jinquan Dong, Xing-Jie Liang, and Chunying Chen. The scavenging of reactive oxygen species and the potential for cell protection by functionalized fullerene materials. *Biomaterials*, 30(4):611–621, February 2009.

[111] H. Sirringhaus, P. J. Brown, R. H. Friend, M. M. Nielsen, K. Bechgaard, B. M. W. Langeveld-Voss, A. J. H. Spiering, R. a. J. Janssen, E. W. Meijer, P. Herwig, and D. M. de Leeuw. Two-dimensional charge transport in self-organized, high-mobility conjugated polymers. *Nature*, 401(6754):685–688, October 1999.

[112] R.j. Kline, M.d. McGehee, E.n. Kadnikova, J. Liu, and J.m.j. Fréchet. Controlling the field-effect mobility of regioregular polythiophene by changing the molecular weight. *Advanced Materials*, 15(18):1519–1522, 2003.

[113] Jeffrey A. Merlo and C. Daniel Frisbie. Field effect transport and trapping in regioregular polythiophene nanofibers. *The Journal of Physical Chemistry B*, 108(50):19169–19179, December 2004.

[114] R. Joseph Kline, Michael D. McGehee, Ekaterina N. Kadnikova, Jinsong Liu, Jean M. J. Fréchet, and Michael F. Toney. Dependence of regioregular poly(3-hexylthiophene) film morphology and field-effect mobility on molecular weight. *Macromolecules*, 38(8):3312–3319, April 2005.

[115] Yi-Kang Lan and Ching-I Huang. Charge mobility and transport behavior in the ordered and disordered states of the regioregular poly(3-hexylthiophene). *The Journal of Physical Chemistry B*, 113(44):14555–14564, 2009.

[116] Brendan O'Connor, R. Joseph Kline, Brad R. Conrad, Lee J. Richter, David Gundlach, Michael F. Toney, and Dean M. DeLongchamp.

Anisotropic structure and charge transport in highly strain-aligned regioregular poly(3-hexylthiophene). *Advanced Functional Materials*, 21(19):3697–3705, 2011.

[117] Carl Poelking and Denis Andrienko. Effect of polymorphism, regioregularity and paracrystallinity on charge transport in poly(3-hexylthiophene) [p3ht] nanofibers. *Macromolecules*, 46(22):8941–8956, November 2013.

[118] G. Juska, K. Arlauskas, M. Viliunas, and J. Kocka. Extraction current transients: New method of study of charge transport in microcrystalline silicon. *Physical Review Letters*, 84(21):4946–4949, May 2000.

[119] Attila Mozer, Niyazi Sariciftci, Almantas Pivrikas, Ronald Österbacka, Gytis Juška, Lutz Brassat, and Heinz Bässler. Charge carrier mobility in regioregular poly(3-hexylthiophene) probed by transient conductivity techniques: A comparative study. *Physical Review B*, 71(3), January 2005.

[120] Maarten J. M. Wirix, Paul H. H. Bomans, Heiner Friedrich, Nico A. J. M. Sommerdijk, and Gijsbertus de With. Three-dimensional structure of p3ht assemblies in organic solvents revealed by cryo-TEM. *Nano Letters*, February 2014.

[121] Edward J. W. Crossland, Kim Tremel, Florian Fischer, Khosrow Rahimi, Günter Reiter, Ullrich Steiner, and Sabine Ludwigs. Anisotropic charge transport in spherulitic poly(3-hexylthiophene) films. *Advanced Materials*, 24(6):839–844, 2012.

[122] Lucia Hartmann, Kim Tremel, Sureeporn Uttiya, Edward Crossland, Sabine Ludwigs, Navaphun Kayunkid, Christelle Vergnat, and Martin Brinkmann. 2d versus 3d crystalline order in thin films of regioregular poly(3-hexylthiophene) oriented by mechanical rubbing and epitaxy. *Advanced Functional Materials*, 21(21):4047–4057, 2011.

[123] C. P. Jarrett, R. H. Friend, A. R. Brown, and D. M. de Leeuw. Field effect measurements in doped conjugated polymer films: Assessment of charge carrier mobilities. *Journal of Applied Physics*, 77(12):6289–6294, 1995.

[124] J. Blochwitz, M. Pfeiffer, T. Fritz, and K. Leo. Low voltage organic light emitting diodes featuring doped phthalocyanine as hole transport material. *Applied Physics Letters*, 73(6):729–731, 1998.

[125] Felix Deschler, Daniel Riedel, Andras DeÃ¡k, Bernhard Ecker, Elizabeth von Hauff, and Enrico Da Como. Imaging of morphological changes and phase segregation in doped polymeric semiconductors. *Synthetic Metals*, 199:381–387, January 2015.

[126] Duc T. Duong, Chenchen Wang, Erin Antono, Michael F. Toney, and Alberto Salleo. The chemical and structural origin of efficient p-type doping in p3ht. *Organic Electronics*, 14(5):1330–1336, May 2013.

[127] Jian Gao, John D. Roehling, Yongle Li, Hua Guo, Adam J. Moulé, and John K. Grey. The effect of 2,3,5,6-tetrafluoro-7,7,8,8-tetracyanoquinodimethane charge transfer dopants on the conformation and aggregation of poly(3-hexylthiophene). *Journal of Materials Chemistry C*, 1(36):5638, 2013.

[128] Daniela Donhauser, Martin Pfannmöller, Levin Dieterle, Katrin Schultheiß, Rasmus R. Schröder, Wolfgang Kowalsky, and Michael Kröger. Observation of filamentous nanostructures in organic-inorganic composite thin films deposited by co-evaporation. *Advanced Functional Materials*, 23(17):2130–2136, May 2013.

[129] A. Zen, J. Pflaum, S. Hirschmann, W. Zhuang, F. Jaiser, U. Asawapirom, J. P. Rabe, U. Scherf, and D. Neher. Effect of molecular weight and annealing of poly(3-hexylthiophene)s on the performance of organic field-effect transistors. *Advanced Functional Materials*, 14(8):757–764, 2004.

[130] Wanli Ma, Jin Young Kim, Kwanghee Lee, and Alan J. Heeger. Effect of the molecular weight of poly(3-hexylthiophene) on the morphology and performance of polymer bulk heterojunction solar cells. *Macromolecular Rapid Communications*, 28(17):1776–1780, September 2007.

[131] Achmad Zen, Marina Saphiannikova, Dieter Neher, Jörg Grenzer, Souren Grigorian, Ullrich Pietsch, Udom Asawapirom, Silvia Janietz, Ullrich Scherf, Ingo Lieberwirth, and Gerhard Wegner. Effect of molecular weight on the structure and crystallinity of poly(3-hexylthiophene). *Macromolecules*, 39(6):2162–2171, March 2006.

[132] Meyoung Ju Joung, Chul Am Kim, Seung Youl Kang, Kyu-Ha Baek, Gi Heon Kim, Seong Deok Ahn, In Kyu You, Jin Hee Ahn, and Kyung Soo Suh. The application of soluble and regioregular poly(3-hexylthiophene) for organic thin-film transistors. *Synthetic Metals*, 149(1):73–77, February 2005.

[133] Navaphun Kayunkid, Sureeporn Uttiya, and Martin Brinkmann. Structural model of regioregular poly(3-hexylthiophene) obtained by electron diffraction analysis. *Macromolecules*, 43(11):4961–4967, 2010.

[134] Martin Brinkmann. Structure and morphology control in thin films of regioregular poly(3-hexylthiophene). *Journal of Polymer Science Part B: Polymer Physics*, 49(17):1218–1233, 2011.

[135] T. J. Prosa, M. J. Winokur, Jeff Moulton, Paul Smith, and A. J. Heeger. X-ray structural studies of poly(3-alkylthiophenes): an example of an inverse comb. *Macromolecules*, 25(17):4364–4372, 1992.

[136] Kyo Jin Ihn, Jeff Moulton, and Paul Smith. Whiskers of poly(3-alkylthiophene)s. *Journal of Polymer Science Part B: Polymer Physics*, 31(6):735–742, 1993.

[137] P. Scherrer. Bestimmung der größe und der inneren struktur von kolloidteilchen mittels röntgenstrahlen. *Nachrichten von der Gesellschaft der Wissenschaften zu Göttingen, Mathematisch-Physikalische Klasse*, 1918:98–100, 1918.

[138] Wibren D. Oosterbaan, Veerle Vrindts, Solenn Berson, Stéphane Guillerez, Olivier Douhéret, Bart Ruttens, Jan D'Haen, Peter Adriaensens, Jean Manca, Laurence Lutsen, and Dirk Vanderzande. Efficient formation, isolation and characterization of poly(3-alkylthiophene) nanofibres: probing order as a function of side-chain length. *Journal of Materials Chemistry*, 19(30):5424–5435, July 2009.

[139] R. A. Young and D. B. Wiles. Profile shape functions in rietveld refinements. *Journal of Applied Crystallography*, 15(4):430–438, August 1982.

[140] Marcin Wojdyr. *Fityk* : a general-purpose peak fitting program. *Journal of Applied Crystallography*, 43(5):1126–1128, October 2010.

[141] Zhiyong Wu, Albrecht Petzold, Thomas Henze, Thomas Thurn-Albrecht, Ruth H. Lohwasser, Michael Sommer, and Mukundan Thelakkat. Temperature and molecular weight dependent hierarchical equilibrium structures in semiconducting poly(3-hexylthiophene). *Macromolecules*, 43(10):4646–4653, 2010.

[142] R. Joseph Kline, Michael D. McGehee, and Michael F. Toney. Highly oriented crystals at the buried interface in polythiophene thin-film transistors. *Nature Materials*, 5(3):222–228, March 2006.

[143] R. J. Kline and M. D. McGehee. Morphology and charge transport in conjugated polymers. *Journal of Macromolecular Science, Part C: Polymer Reviews*, 46(1):27–45, January 2006.

[144] Alberto Salleo. Charge transport in polymeric transistors. *Materials Today*, 10(3):38–45, March 2007.

[145] Minh Trung Dang, Lionel Hirsch, Guillaume Wantz, and James D. Wuest. Controlling the morphology and performance of bulk heterojunctions in solar cells. lessons learned from the benchmark poly(3-hexylthiophene):[6,6]-phenyl-c61-butyric acid methyl ester system. *Chemical Reviews*, 113(5):3734–3765, 2013.

[146] Zhenan Bao, Ananth Dodabalapur, and Andrew J. Lovinger. Soluble and processable regioregular poly(3-hexylthiophene) for thin film field-effect transistor applications with high mobility. *Applied Physics Letters*, 69(26):4108–4110, December 1996.

[147] Hoichang Yang, Scott W. LeFevre, Chang Y. Ryu, and Zhenan Bao. Solubility-driven thin film structures of regioregular poly(3-hexyl thiophene) using volatile solvents. *Applied Physics Letters*, 90(17):172116, April 2007.

[148] Jui-Fen Chang, Baoquan Sun, Dag W. Breiby, Martin M. Nielsen, Theis I. Sölling, Mark Giles, Iain McCulloch, and Henning Sirringhaus. Enhanced mobility of poly(3-hexylthiophene) transistors by spin-coating from high-boiling-point solvents. *Chemistry of Materials*, 16(23):4772–4776, November 2004.

[149] Jianhua Liu, Mohammad Arif, Jianhua Zou, Saiful I. Khondaker, and Lei Zhai. Controlling poly(3-hexylthiophene) crystal dimension: Nanowhiskers and nanoribbons. *Macromolecules*, 42(24):9390–9393, 2009.

[150] Jucheol Park, Sung Heo, Jae-Gwan Chung, Heekoo Kim, HyungIk Lee, Kihong Kim, and Gyeong-Su Park. Bandgap measurement of thin dielectric films using monochromated STEM-EELS. *Ultramicroscopy*, 109(9):1183–1188, August 2009.

[151] Serap Günes, Helmut Neugebauer, and Niyazi Serdar Sariciftci. Conjugated polymer-based organic solar cells. *Chemical Reviews*, 107(4):1324–1338, 2007.

[152] Martin Heeney, Weimin Zhang, David J. Crouch, Michael L. Chabinyc, Sergey Gordeyev, Rick Hamilton, Simon J. Higgins, Iain McCulloch, Peter J. Skabara, David Sparrowe, and Steve Tierney. Regioregular poly(3-hexyl)selenophene: a low band gap organic hole transporting polymer. *Chemical Communications*, (47):5061–5063, November 2007.

[153] Amy M. Ballantyne, Lichun Chen, Justin Dane, Thomas Hammant, Felix M. Braun, Martin Heeney, Warren Duffy, Iain McCulloch, Donal D. C. Bradley, and Jenny Nelson. The effect of poly(3-hexylthiophene) molecular weight on charge transport and the performance of polymer:fullerene solar cells. *Advanced Functional Materials*, 18(16):2373–2380, 2008.

[154] Se Hyun Kim, Kihyon Hong, Keun Hyung Lee, and C. Daniel Frisbie. Performance and stability of aerosol-jet-printed electrolyte-gated transistors based on poly(3-hexylthiophene). *ACS Applied Materials & Interfaces*, 5(14):6580–6585, 2013.

[155] Rodrigo Noriega, Jonathan Rivnay, Koen Vandewal, Felix P. V. Koch, Natalie Stingelin, Paul Smith, Michael F. Toney, and Alberto Salleo. A general relationship between disorder, aggregation and charge transport in conjugated polymers. *Nature Materials*, 12(11):1038–1044, August 2013.

[156] Jui-Fen Chang, Jenny Clark, Ni Zhao, Henning Sirringhaus, Dag Breiby, Jens Andreasen, Martin Nielsen, Mark Giles, Martin Heeney, and Iain McCulloch. Molecular-weight dependence of interchain polaron delocalization and exciton bandwidth in high-mobility conjugated polymers. *Physical Review B*, 74(11), September 2006.

[157] Rui Zhang, Bo Li, Mihaela C. Iovu, Malika Jeffries-EL, Geneviève Sauvé, Jessica Cooper, Shijun Jia, Stephanie Tristram-Nagle, Detlef M. Smilgies, David N. Lambeth, Richard D. McCullough, and Tomasz Kowalewski. Nanostructure dependence of field-effect mobility in regioregular poly(3-hexylthiophene) thin film field effect transistors. *Journal of the American Chemical Society*, 128(11):3480–3481, 2006.

[158] Jean-Marie Verilhac, Gilles LeBlevennec, David Djurado, François Rieutord, Mustapha Chouiki, Jean-Pierre Travers, and Adam Pron. Effect of

macromolecular parameters and processing conditions on supramolecular organisation, morphology and electrical transport properties in thin layers of regioregular poly(3-hexylthiophene). *Synthetic Metals*, 156(11–13):815–823, June 2006.

[159] R. C. G. Naber, M. Mulder, B. de Boer, P. W. M. Blom, and D. M. de Leeuw. High charge density and mobility in poly(3-hexylthiophene) using a polarizable gate dielectric. *Organic Electronics*, 7(3):132–136, June 2006.

[160] Wibren D. Oosterbaan, Jean-Christophe Bolsée, Linjun Wang, Veerle Vrindts, Laurence J. Lutsen, Vincent Lemaur, David Beljonne, Christopher R. McNeill, Lars Thomsen, Jean V. Manca, and Dirk J. M. Vanderzande. On the relation between morphology and FET mobility of poly(3-alkylthiophene)s at the polymer/SiO2 and polymer/air interface. *Advanced Functional Materials*, 24(14):1994–2004, 2014.

[161] Wibren D. Oosterbaan, Jean-Christophe Bolsée, Abay Gadisa, Veerle Vrindts, Sabine Bertho, Jan D'Haen, Thomas J. Cleij, Laurence Lutsen, Christopher R. McNeill, Lars Thomsen, Jean V. Manca, and Dirk Vanderzande. Alkyl-chain-length-independent hole mobility via morphological control with poly(3-alkylthiophene) nanofibers. *Advanced Functional Materials*, 20(5):792–802, 2010.

[162] A. M. C. Ng, K. Y. Cheung, M. K. Fung, A. B. Djurisic, and W. K. Chan. Spectroscopic ellipsometry characterization of polymer-fullerene blend films. *Thin Solid Films*, 517(3):1047–1052, December 2008.

[163] R. F. Egerton. Values of k-shell partial cross-section for electron energy-loss spectrometry. *Journal of Microscopy*, 123(3):333–337, 1981.

[164] Patrick Pingel, Lingyun Zhu, Kue Surk Park, Jörn-Oliver Vogel, Silvia Janietz, Eung-Gun Kim, JÃ¼rgen P. Rabe, Jean-Luc BrÃ©das, and Norbert Koch. Charge-transfer localization in molecularly doped thiophene-based donor polymers. *The Journal of Physical Chemistry Letters*, 1(13):2037–2041, 2010.

[165] Diana Nanova, Sebastian Beck, Andreas Fuchs, Tobias Glaser, Christian Lennartz, Wolfgang Kowalsky, Annemarie Pucci, and Michael Kroeger. Charge transfer in thin films of donor–acceptor complexes studied by infrared spectroscopy. *Organic Electronics*, 13(7):1237–1244, July 2012.

[166] J. S. Chappell, A. N. Bloch, W. A. Bryden, M. Maxfield, T. O. Poehler, and D. O. Cowan. Degree of charge transfer in organic conductors by infrared absorption spectroscopy. *Journal of the American Chemical Society*, 103(9):2442–2443, 1981.

[167] Tobias Glaser, Sebastian Beck, Bernd Lunkenheimer, Daniela Donhauser, Andreas Köhn, Michael Kröger, and Annemarie Pucci. Infrared study of the moo3 doping efficiency in cbp. *Organic Electronics*, 14(2):575 – 583, 2013.

[168] Peter J. Brown, Henning Sirringhaus, Mark Harrison, Maxim Shkunov, and Richard H. Friend. Optical spectroscopy of field-induced charge in self-organized high mobility poly(3-hexylthiophene). *Phys. Rev. B*, 63:125204, Mar 2001.

[169] K. E. Ziemelis, A. T. Hussain, D. D. C. Bradley, R. H. Friend, J. Rühe, and G. Wegner. Optical spectroscopy of field-induced charge in poly(3-hexyl thienylene) metal-insulator-semiconductor structures: Evidence for polarons. *Phys. Rev. Lett.*, 66:2231–2234, Apr 1991.

[170] R. Oesterbacka, C. P. An, X. M. Jiang, and Z. V. Vardeny. Two-dimensional electronic excitations in self-assembled conjugated polymer nanocrystals. *Science*, 287(5454):839–842, 2000.

[171] Brian A. Collins, John R. Tumbleston, and Harald Ade. Miscibility, crystallinity, and phase development in p3ht/PCBM solar cells: Toward an enlightened understanding of device morphology and stability. *The Journal of Physical Chemistry Letters*, 2(24):3135–3145, 2011.

[172] Christoph J. Brabec, Martin Heeney, Iain McCulloch, and Jenny Nelson. Influence of blend microstructure on bulk heterojunction organic photovoltaic performance. *Chemical Society Reviews*, 40(3):1185, 2011.

[173] Ji Sun Moon, Jang Jo, and Alan J. Heeger. Nanomorphology of PCDTBT:PC70bm bulk heterojunction solar cells. *Advanced Energy Materials*, 2(3):304–308, March 2012.

[174] J. Liu, Y. Shi, and Y. Yang. Solvation-induced morphology effects on the performance of polymer-based photovoltaic devices. *Advanced Functional Materials*, 11(6):420–424, 2001.

[175] E. Buchaca-Domingo, A. J. Ferguson, F. C. Jamieson, T. McCarthy-Ward, S. Shoaee, J. R. Tumbleston, O. G. Reid, L. Yu, M.-B. Madec,

M. Pfannmöller, F. Hermerschmidt, R. R. Schröder, S. E. Watkins, N. Kopidakis, G. Portale, A. Amassian, M. Heeney, H. Ade, G. Rumbles, J. R. Durrant, and N. Stingelin. Additive-assisted supramolecular manipulation of polymer:fullerene blend phase morphologies and its influence on photophysical processes. *Materials Horizons*, December 2013.

[176] Kristin Schmidt, Christopher J. Tassone, Jeremy R. Niskala, Alan T. Yiu, Olivia P. Lee, Thomas M. Weiss, Cheng Wang, Jean M. J. Fréchet, Pierre M. Beaujuge, and Michael F. Toney. A mechanistic understanding of processing additive-induced efficiency enhancement in bulk heterojunction organic solar cells. *Advanced Materials*, 26(2):300–305, January 2014.

[177] W. Ma, C. Yang, X. Gong, K. Lee, and A. J. Heeger. Thermally stable, efficient polymer solar cells with nanoscale control of the interpenetrating network morphology. *Advanced Functional Materials*, 15(10):1617–1622, 2005.

[178] G. Li, Y. Yao, H. Yang, V. Shrotriya, G. Yang, and Y. Yang. "solvent annealing" effect in polymer solar cells based on poly(3-hexylthiophene) and methanofullerenes. *Advanced Functional Materials*, 17(10):1636–1644, 2007.

[179] Yuhang Liu, Jingbo Zhao, Zhengke Li, Cheng Mu, Wei Ma, Huawei Hu, Kui Jiang, Haoran Lin, Harald Ade, and He Yan. Aggregation and morphology control enables multiple cases of high-efficiency polymer solar cells. *Nature Communications*, 5, November 2014.

[180] Gordon J. Hedley, Alexander J. Ward, Alexander Alekseev, Calvyn T. Howells, Emiliano R. Martins, Luis A. Serrano, Graeme Cooke, Arvydas Ruseckas, and Ifor D. W. Samuel. Determining the optimum morphology in high-performance polymer-fullerene organic photovoltaic cells. *Nature Communications*, 4, December 2013.

[181] F. Padinger, R.s. Rittberger, and N.s. Sariciftci. Effects of postproduction treatment on plastic solar cells. *Advanced Functional Materials*, 13(1):85–88, 2003.

[182] J. Peet, J. Y. Kim, N. E. Coates, W. L. Ma, D. Moses, A. J. Heeger, and G. C. Bazan. Efficiency enhancement in low-bandgap polymer solar cells by processing with alkane dithiols. *Nature Materials*, 6(7):497–500, July 2007.

[183] D. Wynands, M. Levichkova, M. Riede, M. Pfeiffer, P. Baeuerle, R. Rentenberger, P. Denner, and K. Leo. Correlation between morphology and performance of low bandgap oligothiophene:c60 mixed heterojunctions in organic solar cells. *Journal of Applied Physics*, 107(1):014517–014517–6, January 2010.

[184] Steffen Pfuetzner, Jan Meiss, Annette Petrich, Moritz Riede, and Karl Leo. Thick c60:ZnPc bulk heterojunction solar cells with improved performance by film deposition on heated substrates. *Applied Physics Letters*, 94(25):253303, June 2009.

[185] Christian Koerner, Chris Elschner, Nichole Cates Miller, Roland Fitzner, Franz Selzer, Egon Reinold, Peter Bäuerle, Michael F. Toney, Michael D. McGehee, Karl Leo, and Moritz Riede. Probing the effect of substrate heating during deposition of DCV4t:c60 blend layers for organic solar cells. *Organic Electronics*, 13(4):623–631, April 2012.

[186] Konstantinos Fostiropoulos and Wolfram Schindler. Donor–acceptor nanocomposite structures for organic photovoltaic applications. *physica status solidi (b)*, 246(11-12):2840–2843, 2009.

[187] R. Banerjee, J. Novák, C. Frank, C. Lorch, A. Hinderhofer, A. Gerlach, and F. Schreiber. Evidence for kinetically limited thickness dependent phase separation in organic thin film blends. *Physical Review Letters*, 110(18):185506, May 2013.

[188] Jun Ren, Sheng Meng, and Efthimios Kaxiras. Theoretical investigation of the c60/copper phthalocyanine organic photovoltaic heterojunction. *Nano Research*, 5(4):248–257, April 2012.

[189] Barry P. Rand, Jiangeng Xue, Soichi Uchida, and Stephen R. Forrest. Mixed donor-acceptor molecular heterojunctions for photovoltaic applications. i. material properties. *Journal of Applied Physics*, 98(12):124902, December 2005.

[190] Tobias Mönch, Peter Guttmann, Jan Murawski, Chris Elschner, Moritz Riede, Lars Müller-Meskamp, and Karl Leo. Investigating local (photo-)current and structure of ZnPc:c60 bulk-heterojunctions. *Organic Electronics*, 14(11):2777–2788, November 2013.

[191] Ying Zhou, Tetsuya Taima, Tetsuhiko Miyadera, Toshihiro Yamanari, and Yuji Yoshida. Structural modifications of zinc phthalocyanine thin

films for organic photovoltaic applications. *Journal of Applied Physics*, 111(10):103117, May 2012.

[192] Debjit Datta, Vibha Tripathi, Pranjal Gogoi, Suman Banerjee, and Satyendra Kumar. Ellipsometric studies on thin film CuPC: C60 blends for solar cell applications. *Thin Solid Films*, 516(20):7237–7240, August 2008.

[193] Huai-Xin Wei, Yan-Qing Li, Xiang-Yu Chen, Chun-Sing Lee, and Jian-Xin Tang. Annealing-induced phase separation in small-molecular bulk heterojunctions. *Organic Electronics*, 15(11):2810–2816, November 2014.

[194] James B. Gilchrist, Toby. H. Basey-Fisher, Sharon C'E. Chang, Frank Scheltens, David W. McComb, and Sandrine Heutz. Uncovering buried structure and interfaces in molecular photovoltaics. *Advanced Functional Materials*, 24(41):6473–6483, 2014.

[195] P. C. Minor, M. Gouterman, and A. B. P. Lever. Electronic spectra of phthalocyanine radical anions and cations. *Inorganic Chemistry*, 24(12):1894–1900, 1985.

[196] E. Ortí, J. L. Brédas, and C. Clarisse. Electronic structure of phthalocyanines: Theoretical investigation of the optical properties of phthalocyanine monomers, dimers, and crystals. *The Journal of Chemical Physics*, 92(2):1228–1235, January 1990.

[197] N. El Khatib, B. Boudjema, M. Maitrot, H. Chermette, and L. Porte. Electronic structure of zinc phthalocyanine. *Canadian Journal of Chemistry*, 66(9):2313–2324, September 1988.

[198] Tebello Nyokong, Zbigniew Gasyna, and Martin J. Stillman. Analysis of the absorption and magnetic circular dichroism spectra of zinc phthalocyanine and the .pi.-cation-radical species [ZnPc(1-)].cntdot.+. *Inorganic Chemistry*, 26(7):1087–1095, 1987.

[199] Lawrence Edwards and Martin Gouterman. Porphyrins: XV. vapor absorption spectra and stability: Phthalocyanines. *Journal of Molecular Spectroscopy*, 33(2):292–310, February 1970.

[200] Amira Hajri, Sarra Touaiti, and Bassem Jamoussi. Preparation of organic zn-phthalocyanine-based semiconducting materials and their optical and electrochemical characterization. *Advances in OptoElectronics*, 2013:e321563, May 2013.

[201] Charles Weiss, Hiroshi Kobayashi, and Martin Gouterman. Spectra of porphyrins: Part III. self-consistent molecular orbital calculations of porphyrin and related ring systems. *Journal of Molecular Spectroscopy*, 16(2):415–450, June 1965.

[202] B. H. Schechtman and W. E. Spicer. Near infrared to vacuum ultraviolet absorption spectra and the optical constants of phthalocyanine and porphyrin films. *Journal of Molecular Spectroscopy*, 33(1):28–48, January 1970.

[203] Johannes Zimmermann. Eine infrarotspektroskopische Studie an organischen Materialien bezüglich molekularer Orientierung und dem Nachweis chemischer Reaktionen, 2014.

[204] A. S. Davydov. *Theory of absorption spectra of molecular crystals.* Department of Chemistry, University of California, 1949.

[205] J. Tauc, R. Grigorovici, and A. Vancu. Optical properties and electronic structure of amorphous germanium. *physica status solidi (b)*, 15(2):627–637, 1966.

[206] Ingmar Bruder, Jan Schöneboom, Robert Dinnebier, Antti Ojala, Stefan Schäfer, Rüdiger Sens, Peter Erk, and Jürgen Weis. What determines the performance of metal phthalocyanines (MPc, m = zn, cu, ni, fe) in organic heterojunction solar cells? A combined experimental and theoretical investigation. *Organic Electronics*, 11(3):377–387, March 2010.

[207] Ingmar Bruder, Antti Ojala, Christian Lennartz, Sudhakar Sundarraj, Jan Schöneboom, Rüdiger Sens, Jaehyung Hwang, Peter Erk, and Jürgen Weis. Theoretical and experimental investigation on the influence of the molecular polarizability of novel zinc phthalocyanine derivatives on the open circuit voltage of organic hetero-junction solar cells. *Solar Energy Materials and Solar Cells*, 94(2):310–316, February 2010.

[208] G. Gensterblum, J. J. Pireaux, P. A. Thiry, R. Caudano, J. P. Vigneron, Ph. Lambin, A. A. Lucas, and W. Krätschmer. High-resolution electron-energy-loss spectroscopy of thin films of c60 on si(100). *Physical Review Letters*, 67(16):2171–2174, 1991.

[209] E. Sohmen, J. Fink, and W. Krätschmer. Electron energy-loss spectroscopy studies on c60 and c70 fullerite. *Zeitschrift für Physik B Condensed Matter*, 86(1):87–92, February 1992.

[210] P. L. Hansen, P. J. Fallon, and W. Krätschmer. An EELS study of fullerite — c60/c70. *Chemical Physics Letters*, 181(4):367–372, June 1991.

[211] Sven Larsson, Andrey Volosov, and Arne Rosén. Optical spectrum of the icosahedral c60- "follene-60". *Chemical Physics Letters*, 137(6):501–504, July 1987.

[212] W. Krätschmer, Lowell D. Lamb, K. Fostiropoulos, and Donald R. Huffman. Solid c60: a new form of carbon. *Nature*, 347(6291):354–358, September 1990.

[213] E. Taft and H. Philipp. Optical properties of graphite. *Physical Review*, 138(1A):A197–A202, April 1965.

[214] Hiromichi Kataura, Yasushi Endo, Yohji Achiba, Koichi Kikuchi, Takaaki Hanyu, and Shigeo Yamaguchi. Dielectric constants of c60 and c70 thin films. *Journal of Physics and Chemistry of Solids*, 58(11):1913–1917, November 1997.

[215] D. Faiman, S. Goren, E. A. Katz, M. Koltun, N. Melnik, A. Shames, and S. Shtutina. Structure and optical properties of c60 thin films. *Thin Solid Films*, 295(1–2):283–286, February 1997.

[216] P. Simon, B. Maennig, and H. Lichte. Conventional electron microscopy and electron holography of organic solar cells. *Advanced Functional Materials*, 14(7):669–676, 2004.

[217] William I. F. David, Richard M. Ibberson, Judy C. Matthewman, Kosmas Prassides, T. John S. Dennis, Jonathan P. Hare, Harold W. Kroto, Roger Taylor, and David R. M. Walton. Crystal structure and bonding of ordered c60. *Nature*, 353(6340):147–149, September 1991.

[218] Vishal Shrotriya, Jianyong Ouyang, Ricky J. Tseng, Gang Li, and Yang Yang. Absorption spectra modification in poly(3-hexylthiophene):methanofullerene blend thin films. *Chemical Physics Letters*, 411(1–3):138–143, August 2005.

[219] Koen Vandewal, Kristofer Tvingstedt, Abay Gadisa, Olle Inganäs, and Jean Manca. Relating the open-circuit voltage to interface molecular properties of donor acceptor bulk heterojunction solar cells. *Physical Review B*, 81(12):125204, March 2010.

[220] Dirk Veldman, Stefan C. J. Meskers, and René A. J. Janssen. The energy of charge-transfer states in electron donor–acceptor blends: Insight into the energy losses in organic solar cells. *Advanced Functional Materials*, 19(12):1939–1948, 2009.

[221] Benoit Mandelbrot. How long is the coast of britain? Statistical self-similarity and fractional dimension. *Science*, 156(3775):636–638, May 1967.

[222] W. Ma, C. Yang, and A. J. Heeger. Spatial fourier-transform analysis of the morphology of bulk heterojunction materials used in "plastic" solar cells. *Advanced Materials*, 19(10):1387–1390, 2007.

[223] T. McAfee, E. Gann, H. Ade, and D. B. Dougherty. Thermally induced dewetting in ultrathin c60 films on copper phthalocyanine. *The Journal of Physical Chemistry C*, 117(49):26007–26012, 2013.

[224] Jia Gao, Kamal Asadi, Jian Bin Xu, and Jin An. Controlling of the surface energy of the gate dielectric in organic field-effect transistors by polymer blend. *Applied Physics Letters*, 94(9):093302, 2009.

[225] Yusuke Tajima, Takanori Matsuura, Youhei Numata, Daisuke Yamazaki, Hiroaki Kawamura, and Hiroki Osedo. Surface free energy and wettability determination of various fullerene derivative films on amorphous carbon wafer. *Japanese Journal of Applied Physics*, 47(7R):5730, 2008.

[226] S Bommel, N Kleppmann, C Weber, H Spranger, P Schäfer, Jiří Novak, SV Roth, F Schreiber, SHL Klapp, and S Kowarik. Unravelling the multilayer growth of the fullerene c60 in real time. *Nature communications*, 5, 2014.

[227] E. M. Schulson. Electron channelling patterns in scanning electron microscopy. *Journal of Materials Science*, 12(6):1071–1087, June 1977.

[228] Dale E. Newbury, David C. Joy, Patrick Echlin, Charles E. Fiori, and Joseph I. Goldstein. Electron channeling contrast in the SEM. In *Advanced Scanning Electron Microscopy and X-Ray Microanalysis*, pages 87–145. Springer US, January 1986.

[229] H. X. Wei, J. Li, Z. Q. Xu, Y. Cai, J. X. Tang, and Y. Q. Li. Thermal annealing-induced vertical phase separation of copper phthalocyanine: Fullerene bulk heterojunction in organic photovoltaic cells. *Applied Physics Letters*, 97(8):083302, August 2010.

[230] Takeshi Hasegawa. A novel measurement technique of pure out-of-plane vibrational modes in thin films on a nonmetallic material with no polarizer. *The Journal of Physical Chemistry B*, 106(16):4112–4115, 2002.

[231] Michael Brendel, Stefan Krause, Andreas Steindamm, Anna Katharina Topczak, Sudhakar Sundarraj, Peter Erk, Steffen Hoehla, Norbert Fruehauf, Norbert Koch, and Jens Pflaum. The effect of gradual fluorination on the properties of fnznpc thin films and fnznpc/c60 bilayer photovoltaic cells. *Advanced Functional Materials*, pages n/a–n/a, 2015.

[232] Philip Schulz, Sarah R. Cowan, Ze-Lei Guan, Andres Garcia, Dana C. Olson, and Antoine Kahn. NiOX/MoO3 bi-layers as efficient hole extraction contacts in organic solar cells. *Advanced Functional Materials*, 24(5):701–706, 2014.

[233] Vibha Tripathi, Debjit Datta, G. S. Samal, Asha Awasthi, and Satyendra Kumar. Role of exciton blocking layers in improving efficiency of copper phthalocyanine based organic solar cells. *Journal of Non-Crystalline Solids*, 354(19–25):2901–2904, May 2008.

[234] Bo Yu, Lizhen Huang, Haibo Wang, and Donghang Yan. Efficient organic solar cells using a high-quality crystalline thin film as a donor layer. *Advanced Materials*, 22(9):1017–1020, 2010.

[235] Heliatek GmbH Pfeiffer, Martin. Personal communication, 2014.

[236] Andreas F. Bartelt, Christian Strothkämper, Wolfram Schindler, Konstantinos Fostiropoulos, and Rainer Eichberger. Morphology effects on charge generation and recombination dynamics at ZnPc:c60 bulk heterojunctions using time-resolved terahertz spectroscopy. *Applied Physics Letters*, 99(14):143304, October 2011.

[237] Zheng Xu, Li-Min Chen, Guanwen Yang, Chun-Hao Huang, Jianhui Hou, Yue Wu, Gang Li, Chain-Shu Hsu, and Yang Yang. Vertical phase separation in poly(3-hexylthiophene): Fullerene derivative blends and its advantage for inverted structure solar cells. *Advanced Functional Materials*, 19(8):1227–1234, 2009.

[238] Tao He, Matthias Stolte, Christian Burschka, Nis Hauke Hansen, Thomas Musiol, Daniel Kaelblein, Jens Pflaum, Xutang Tao, Jochen Brill, and Frank WÃ¼rthner. Single-crystal field-effect transistors of new cl2-NDI

polymorph processed by sublimation in air. *Nature Communications*, 6, January 2015.

[239] Huanli Dong, Xiaolong Fu, Jie Liu, Zongrui Wang, and Wenping Hu. 25th anniversary article: Key points for high-mobility organic field-effect transistors. *Advanced Materials*, 25(43):6158–6183, 2013.

[240] Hiromi Minemawari, Toshikazu Yamada, Hiroyuki Matsui, Jun/'ya Tsutsumi, Simon Haas, Ryosuke Chiba, Reiji Kumai, and Tatsuo Hasegawa. Inkjet printing of single-crystal films. *Nature*, 475(7356):364–367, July 2011.

[241] Anna Loiudice, Aurora Rizzo, Mariano Biasiucci, and Giuseppe Gigli. Bulk heterojunction versus diffused bilayer: The role of device geometry in solution p-doped polymer-based solar cells. *The Journal of Physical Chemistry Letters*, 3(14):1908–1915, 2012.

[242] Eric L. Hanson, Jing Guo, Norbert Koch, Jeffrey Schwartz, and Steven L. Bernasek. Advanced surface modification of indium tin oxide for improved charge injection in organic devices. *Journal of the American Chemical Society*, 127(28):10058–10062, 2005. PMID: 16011369.

[243] Fatemeh Ghani, Andreas Opitz, Patrick Pingel, Georg Heimel, Ingo Salzmann, Johannes Frisch, Dieter Neher, Argiri Tsami, Ullrich Scherf, and Norbert Koch. Charge transfer in and conductivity of molecularly doped thiophene-based copolymers. *Journal of Polymer Science Part B: Polymer Physics*, 53(1):58–63, 2015.

[244] Pabitra K. Nayak, Germa Garcia-Belmonte, Antoine Kahn, Juan Bisquert, and David Cahen. Photovoltaic efficiency limits and material disorder. *Energy Environ. Sci.*, 5:6022–6039, 2012.

[245] Long Chen, Ko Furukawa, Jia Gao, Atsushi Nagai, Toshikazu Nakamura, Yuping Dong, and Donglin Jiang. Photoelectric covalent organic frameworks: Converting open lattices into ordered donor acceptor heterojunctions. *Journal of the American Chemical Society*, 136(28):9806–9809, 2014. PMID: 24963896.

[246] Kjell Cnops, Barry P. Rand, David Cheyns, Bregt Verreet, Max A. Empl, and Paul Heremans. 8.4% efficient fullerene-free organic solar cells exploiting long-range exciton energy transfer. *Nature Communications*, 5, March 2014.

B. Journal Publications, Conference Presentations, Supervised Theses

Journal Publications

1. Nanova D., Scherer M., Schell F., Kast A.K., Zimmermann J., Glaser T., Krekeler C., Pucci A., Schroeder R.R., Kowalsky W. and Lovrincic R.: *Stack Architecture dictates Fullerene Crystallinity and Device Efficiency in Small Molecule Solar Cells.* Submitted, 2015.

2. Nanova D., Kast A. K., Pfannmöller M., Müller C., Veith L., Wacker I., Agari M., Hermes W., Erk P., Kowalsky W, Schröder R. R. and Lovrincic, R.: *Unraveling the Nanoscale Morphologies of Mesoporous Perovskite Solar Cells and Their Correlation to Device Performance.* Nano letters, 14(5), 2735-2740, 2014.

3. Spahr H., Reinker J., Bülow T., Nanova D., Johannes H. H., and Kowalsky W.: *Regimes of leakage current in ALD-processed Al2O3 thin-film layers.* Journal of Physics D: Applied Physics, 46(15), 155302, 2013.

4. Nanova D., Beck S., Alt M., Glaser T., Pucci A., Schultheiß K., Dieterle L., Schröder R. R., Pflaum J., Kowalsky W. and Kroeger M.: *Phase separation in ternary charge-transfer-complexes.* Applied Physics A, 112(4):1019-1025, 2012.

5. Nanova D., Beck S., Fuchs A., Glaser T., Lennartz C., Kowalsky W., Pucci A. and Kroeger M.: *Charge transfer in thin films of donor–acceptor complexes studied by infrared spectroscopy.* Organic Electronics, 13(7), 1237-1244., 2012.

Conference Presentations (selection)

1. D. Nanova, F. Schell, A. K. Kast, M. Scherer, R. R. Schröder, R. Lovrincic, W. Kowalsky: *Imaging the Phase Separation in Small Molecule Bulk Heterojunction Organic Solar Cells;* Talk; MRS Fall Meeting 2014, Boston, USA.

2. D. Nanova, A. K. Kast, C Mueller, I. Wacker, M. Agari, W. Hermes, P. Erk, R. R. Schröder, W. Kowalsky, R. Lovrincic*: Applications of Analytical Transmission Electron Microscopy*; Talk; Columbia University, Group of Prof. Xiaoyang Zhu; 2014; New York, USA.

3. D. Nanova, A. K. Kast, C Mueller, I. Wacker, M. Agari, W. Hermes, P. Erk, R. R. Schröder, W. Kowalsky, R. Lovrincic*: Analytical Transmission Electron Microscopy on Hybrid Solar Cells Based on Perovskites*; Poster; MRS Spring Meeting 2014, San Francisco, USA.

4. D. Nanova, A. K. Kast, C Mueller, I. Wacker, M. Agari, W. Hermes, P. Erk, R. R. Schröder, W. Kowalsky, R. Lovrincic*: Analytical Transmission Electron Microscopy on Hybrid Solar Cells Based on Perovskites*; Talk; DPG Spring Meeting 2014, Dresden, Germany.

5. D. Nanova, A. K. Kast, M. Pfannmöller, R. Lovrincic, R. R. Schröder, W. Kowalsky: *Morphology of donor-acceptor blends studied by analytical TEM*; Talk; JSAP-MRS Joint Symposia 2013, Kyoto, Japan.

6. D. Nanova, M. Pfannmöller, R. R. Schröder, R. Lovrincic, W. Kowalsky*: Morphology and interdiffusion in organic donor-acceptor blends studied by analytical TEM*; Poster; Electronic Structure and Processes at Molecular-Based Interfaces 2013, Weizmann Institute of Science, Rehovot, Israel.

7. D. Nanova, D. Daume, J. Ostermann, R. Saive, L. Dieterle, M. Pfannmöller, R. R. Schröder, W. Kowalsky, M. Kröger: *Morphology and interdiffusion in organic donor-acceptor blends studied by analytical TEM*; Poster; International Symposium on Organic Electronics 2012, OIST, Okinawa, Japan.

8. D. Nanova, M. Kröger, J. Pflaum, K. Schultheiss, R. R. Schröder, T. Glaser, S. Beck, M. Alt, A. Pucci, W. Kowalsky: *Phase separation in organic ternary charge transfer complexes*; Talk; DPG Spring Meeting 2012, Berlin, Germany.

Supervised Master Theses

- Felix Schell, Heidelberg University: *Morphology of small molecule organic solar cells from transmission electron microscopy.*
- Lars Müller, Heidelberg University: *Charge Transport in Organic Solar Cells Studied by (Photo-) CELIV.*
- Carsten Leinweber, Heidelberg University: *Untersuchung der Ladungstransporteigenschaften von organischen Halbleitern mittels CELIV.*
- Claus Ripp, Heidelberg University: *Elektronische und optische Eigenschaften organischer Charge-Transfer-Komplexe.*

Danksagung

An dieser Stelle möchte ich mich bei allen bedanken, die mich im Laufe der Promotion begleitet und unterstützt haben. Insbesondere danke ich

Prof. Wolfgang Kowalsky für die Möglichkeit, in seiner Arbeitsgruppe am InnovationLab zu promovieren, und für die hervorragende Betreuung während der gesamten Zeit. Für die Unterstützung der Teilnahme an zahlreichen internationalen Konferenzen weltweit möchte ich mich besonders bedanken.

Prof. Albrecht Winnacker für die bereitwillige Übernahme des Zweitgutachtens.

Dr. Robert Lovrincic für die ausgezeichnete wissenschaftliche Betreuung und die gute Zusammenarbeit. Ein besonderer Dank gilt ihm auch für das Korrekturlesen dieser Arbeit.

Prof. Rasmus Schröder für die Betreuung seitens TEM. Dr. Martin Pfannmöller und Anne Kast für die tolle Zusammenarbeit am Kronos. Ohne sie wäre vieles am Kronos nicht möglich gewesen.

Dr. Tobias Glaser für die Bereitstellung der IR-Messungen und den spannenden Diskussionen, die die Zusammenarbeit sehr angenehm gemacht haben.

meinen Studenten, insbesondere Lars Müller und Felix Schell, die eine hervorragende Arbeit geleistet haben.

meinen Kollegen am iL, insbesondere meinen Bürokollegen (aktuelle und ehemalige), die immer für gute Laune und eine tolle Arbeitsatmosphäre gesorgt haben.

Dr. Janusz Schinke und Michaela Sauer für das rundum Sorglospaket am iL.

Prof. Volker Metag, Dr. Mariana Nanova, Dr. Anthony Morfa, Hans Boy und Ilse Gamp für das Korrekturlesen.

meinen Eltern, meiner Schwester und Tobit für die bedingungslose Unterstützung in jeder Hinsicht. DANKE!